Mesoscale Modeling of Deformation and Microstructure Evolution in Ni-Based Superalloys

Submitted in partial fulfillment of the requirements of the degree of

Doctor of Philosophy

by

Suketaben Amrutbhai Chaudhary

Roll number: 204116004

Supervisor:

Prof. Anirban Patra

Co-Supervisor:

Prof. P J Guruprasad
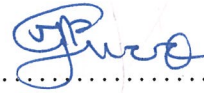

Metallurgical Engineering and Materials Science
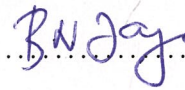
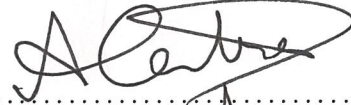INDIAN INSTITUTE OF TECHNOLOGY BOMBAY

November 2025

Thesis Approval

This thesis entitled **"Mesoscale Modeling of Deformation and Microstructure Evolution in Ni-Based Superalloys"** by **"Suketaben Amrutbhai Chaudhary"** is approved for the degree of **Doctor of Philosophy**.

Examiners:

....

....

....

Supervisor(s):

....

....

....

Chairman:

....

Date: Nov. 28, 2025

Place: IIT BOMBAY

Declaration

I declare that this written submission represents my ideas in my own words and where others ideas or words have been included, I have adequately cited and referenced the original sources. I also declare that I have adhered to all principles of academic honesty and integrity and have not misrepresented or fabricated or falsified any idea/data/fact/source in my submission. I understand that any violation of the above will be cause for disciplinary action by the Institute and can also evoke penal action from the sources which have thus not been properly cited or from whom proper permission has not been taken when needed.

Sukety

....
(Signature)

Suketaben Amrutbhai chaudhary
....
(Name of the student)

204116004
....
(Roll No.)

Date: Nov. 28, 2025

Place: IIT BOMBAY

Abstract

Ni-based superalloys are used in gas turbine engine blades, discs and other high temperature components due to their excellent creep and fatigue resistance at elevated temperatures. However, their complex microstructure, consisting of the γ matrix and $\gamma^{'}$ precipitates, leads to orientation- and temperature-dependent deformation behavior. A detailed understanding and accurate modeling of these deformation mechanisms is therefore essential to predict performance and optimize alloy design under demanding thermo–mechanical conditions. The broad objectives of this thesis are towards the development of mesoscale modeling tools for predicting processing-microstructure-mechanical property correlations in single crystal and polycrystalline Ni-based superalloys. Different aspects of these correlations have been studied via novel models developed in the different chapters of this thesis.

We have developed a coupled phase field-crystal plasticity model in Chapter 3 to simulate the microstructure evolution during aging heat treatment and the post-aging mechanical properties of single-crystal Ni-based superalloys. The model has been used to predict the precipitation kinetics at different aging temperatures and for Ni-Al alloys with different compositions. The model is extensively validated by comparison of the predicted precipitate size and volume fraction during aging with available literature data, as well as the predicted tension-compression asymmetry in the post-aged microstructures with the literature data.

We have developed a microstructure-sensitive dislocation density-based crystal plasticity finite element framework in Chapter 4 for simulating the orientation- and temperature-dependent deformation of single crystal Ni-based superalloys. Constitutive equations for substructure and microstructure evolution are developed to simulate the deformation behavior during tensile, cyclic, and creep loading of single crystal Ni-based superalloys. The model has consideration for dislocation climb around the precipitates, Orowan looping around precipitates, and microstructure evolution during isotropic coarsening and rafting, in addition to models for dislocation strengthening and evolution. The orientation

and temperature-dependent tensile, cyclic, creep, and creep-fatigue response of two single crystal Ni-based superalloys (CMSX-4 and PWA-1484) are predicted and validated with experimental results from the literature.

We have developed a microstructure-sensitive crystal plasticity model in Chapter 5 to that accounts for the individual deformation of the γ and primary $\gamma^{'}$ phases in a polycrystalline Ni-based superalloy and their effect on the overall deformation and failure initiation characteristics. The model accounts for solute solution strengthening due to the various elements present in the matrix and the precipitate phase, strengthening due to secondary and tertiary $\gamma^{'}$ precipitates present in the matrix (γ) phase, and Taylor hardening due to dislocation forests that evolve during deformation. The solute atom concentrations for both the matrix and primary $\gamma^{'}$ phase have been determined using Energy Dispersive X-ray spectroscopy (EDS). Electron Back Scatter Diffraction (EBSD) microstructures and these solute concentration values serve as input to the crystal plasticity model. The model is calibrated to the experimental stress-strain data at 293 K and 923 K and validated by predicting the mechanical response at 523 K and 723 K. Further, interrupted tensile tests have been conducted using Scanning Electron Microscopy (SEM) and EBSD to gain insights into the microstructure evolution during tensile deformation. The simulated EBSD microstructures are correlated with the experimental deformed microstructures to identify areas of misorientation development and the microstructural features contributing to these.

We have developed a micromechanical model for precipitate shearing in Chapter 6 to predict the cyclic deformation and softening of polycrystalline Ni-based superalloys. A slip-system level backstress model is developed to account for the initial kinematic hardening, while the precipitate shearing model accounts for microstructure evolution due to dislocation-precipitate interactions, their eventual shearing, and the change in the precipitate strengthening due to secondary and tertiary $\gamma^{'}$ precipitates. The model is used to predict cyclic softening in two different polycrystalline superalloys with different precipitate morphologies.

We have implemented various Fatigue Indicator Parameters (FIPs) into our crystal plasticity framework in Chapter 7 to predict possible sites of crack initiation during cyclic deformation of polycrystalline superalloys. Based on the model predictions, FIPs were found to mainly localize along the annealing twin boundaries, grain and phase boundaries, which may eventually act as possible locations of crack initiation during cyclic deformation.

Keywords: Ni-based superalloys; crystal plasticity; phase field; creep; fatigue; misorientation; precipitates; cyclic softening

Contents

List of Figures

List of Tables

Chapter 1

Introduction

1.1 Motivation

Nickel-based superalloys are a class of compositionally complex alloys, which are widely used to manufacture structural components that require superior elevated temperature mechanical properties (Geddes et al., 2010). The most prominent application is in the manufacturing of gas turbines for advanced aero-engines, turboshaft engines for helicopters, nuclear power plants, and marine propulsion (Akca et al., 2015). Nickel-based superalloys constitute approximately 50% of the weight of the materials used in advanced aircraft engines (Akca et al., 2015). This application is primarily due to their properties such as heat resistance, high melting points, and the ability to maintain mechanical and chemical stability at elevated temperatures (Betteridge et al., 1974). In addition, these alloys exhibit high toughness, relatively high creep, thermal fatigue resistance, and corrosion resistance (Geddes et al., 2010). Such properties are crucial for effective and efficient performance in demanding aerospace environments (Akca et al., 2015).

Broadly speaking, Ni-based superalloys may be further classified into single crystal and polycrystalline superalloys. Generally, single crystal Ni-based superalloys offer excellent high-temperature creep strength and are the material of choice for turbine blades and vanes. Also, polycrystalline Ni-based superalloys are used as materials for stationary components like turbine disks due to their ability to withstand high thermo-mechanical loads (Fischer et al., 2019). These components generally operate in temperatures ranging from room temperature to very high temperatures (>1000 °C) and they are exposed to complex mechanical loading combined with thermal transients such as creep with thermal and/or fatigue (Shenoy, 2006). Ni-based superalloys also find application in the oil and

gas industry, space vehicles, space vehicles, nuclear reactors, cryogenic applications, heat exchanger tubing, chemical processing vessels, and military electric motors (Pollock and Tin, 2006). Over the years, several generations of superalloys have been developed, with each new generation offering improved resistance to high temperatures (Locq and Caron, 2011). The recent advancements in these materials involve the addition of costly alloying elements such as rhenium and ruthenium to enhance their performance characteristics (Akca et al., 2015).

The properties of these Ni-based superalloys are based on the microstructure and chemical composition (Thornton et al., 2023). The chemical composition is generally chosen to achieve corrosion resistance, strength, creep, and fatigue properties (Kuo et al., 2009). The strengthening in these alloys is typically achieved through the precipitation of intermetallic compounds within a face-centered cubic (FCC) matrix (Gell and Duhl, 1986), $\gamma^{'}$ precipitates being the dominant ones. Generally, these alloys consist of a two-phase microstructure: the Ni-rich solid solution, with FCC crystal structure having the $Fm-3m$ space group (Sun et al., 2023) (γ phase), and coherent L12-type, long-range ordered intermetallic Ni_3Al precipitates $\gamma^{'}$ phase, having the $Pm\bar{3}m$ space group (Raju et al., 2015; Murakumo et al., 2004). The primary shear (slip) systems in both phases are based on the $111 < 1\bar{1}0 >$ family and $001 < 1\bar{1}0 >$ cube slip systems get activated at high temperature for $\gamma^{'}$ phase. Figure 1.1 shows the two-phase microstructure of a representative single crystal Ni-based superalloy (Pollock and Tin, 2006). In this regard, their mechanical properties have been enhanced/optimized by tailoring key microstructural parameters, including the size and morphology of the $\gamma^{'}$ precipitates and the grain size via heat treatment (Mughrabi et al., 1997; Furrer et al., 2003; Chen et al., 2023; Kumar et al., 2025). Directional solidification or single crystal processing are crucial techniques that eliminate grain boundaries, thereby enhancing creep resistance in high-temperature applications (Reed, 2008). The grain size may vary for powder metallurgy processed alloys (micron scale) used in turbine discs applications to single crystal alloys (actual size of component) used in turbine blades (Antolovich, 2015).

A high factor of safety, frequent inspection, and replacement intervals are needed for superalloy-based engine components because of insufficient knowledge of the material behavior, which is expensive and inefficient (Rodas and Neu, 2018). Failure in these materials during cyclic and creep loading is essentially a weakest link phenomenon, which is affected by the microstructure variability (e.g., distribution of precipitates, grain morphology, and orientation that may arise due to processing conditions). These are some
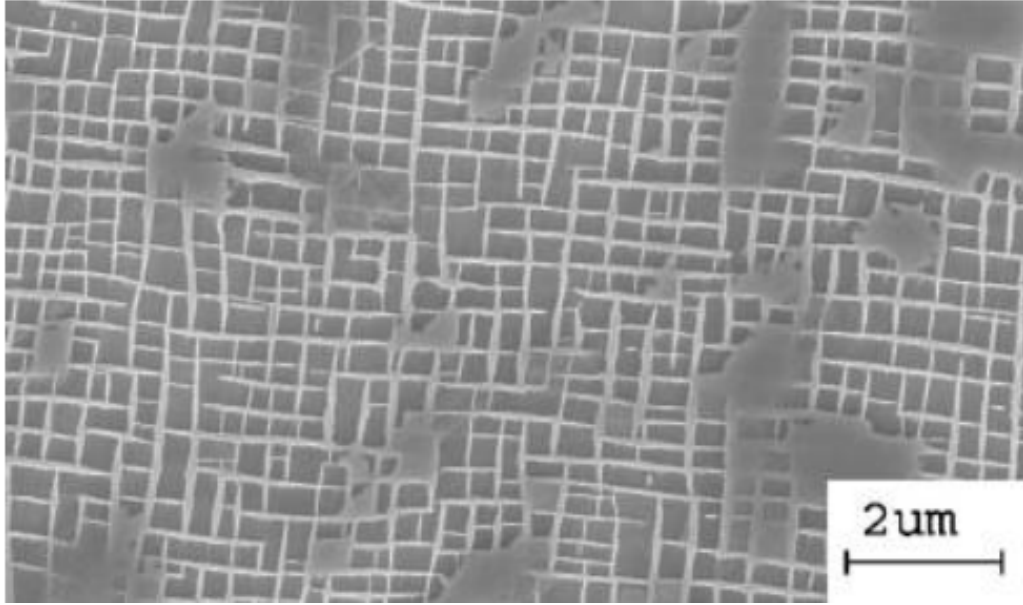
FIGURE 1.1: Two-phase microstructure of single crystal Ni-based superalloys Pollock and Tin (2006)).

of the primary concerns for industries manufacturing gas turbine components, where significant interest lies in quantifying the effect of microstructure variability and reducing the uncertainty of the turbine blade component failure. Thermo-mechanical deformation (and eventually failure) of turbine disks made of Ni-based superalloy is microstructure-dependent phenomenon. Experiments provide accurate and valuable information, but it is costly, time-consuming, and unfeasible to characterize these variabilities for the range of microstructure and loading conditions. Alternatively, these issues can be addressed by experimentally validated modeling techniques (Ma et al., 2008; Shenoy et al., 2008; Staroselsky and Cassenti, 2011; Vattré and Fedelich, 2011; Zhu et al., 2012; Le Graverend et al., 2014; Ghorbanpour et al., 2017; Gupta and Bronkhorst, 2021; Agaram et al., 2021; Keshavarz et al., 2022; Lu et al., 2023; Fan et al., 2024; Wang et al., 2024; Gao et al., 2025), which can predict the effect of the microstructure on the mechanical properties. Development of such models forms the primary objectives of the present thesis.

Literature studies have developed phase-field models to predict the microstructure evolution during solution and aging treatment (Wen et al., 2006; Kundin et al., 2012; Ta et al., 2014; Wu et al., 2019a; Lin et al., 2019; Le Graverend and Harikrishnan, 2019; Yu et al., 2020b; Le Graverend and Harikrishnan, 2021; Yang et al., 2021; Ali et al., 2023; Wang et al., 2025a). Wen et al. (2006) conducted isothermal phase-field simulations for several Ni–Al alloys at different temperatures and simulated realistic heat treatments corresponding to

two isothermal experiments. Kundin et al. (2012) studied the microstructural changes during heat treatment using phase-field multi-component considering elastic driving forces in the presence of a lattice misfit and validated the model using experimental results for CMSX-4 and CMSX-6. Ta et al. (2014) coupled MICRESS and CALPHAD thermo-dynamic and atomic mobility databases to simulate three-dimensional (3-D) phase-field simulations of microstructural evolution in Ni-Al alloy during the precipitation process. Wu et al. (2019a) coupled phase-field and continuum dislocation dynamics to study the evolution of dislocation and $\gamma/\gamma^{'}$ microstructures to study the creep deformation of single crystal Nickel-based superalloys. Le Graverend and Harikrishnan (2019) used a phase-field informed crystal plasticity model to study the effect of the sign of misfit between γ and $\gamma^{'}$ phases on the size, shape and distribution of precipitates during the heat treatment and on the direction of rafting and performed the tensile tests on cuboidal, rafted, and topologically inverted microstructure generated by phase-field. Similarly, Le Graverend and Harikrishnan (2021) used this microstructure to study the effect of misfit strain on tensile and cyclic test on microstructure generated using phase-field study and observed smaller macroscopic yield stress and strain hardening as well as smaller stress triaxiality with higher magnitude of lattice misfit for cuboidal microstructure. Yang et al. (2021) investigated the microstructural evolution and element distribution from solidification to the SHT process using multiphase-field simulation coupled with thermodynamic calculation. Further, Wang et al. (2025a) used a 3D phase-field model to study growth behavior of precipitates under aging conditions at 850 K and revealed that the initial nucleation conditions significantly affect the equilibrium phase morphology, size and spatial distribution, while the final equilibrium volume fractions remain constant. Although many literature studies have simulated the microstructure evolution using phase–field model, very few studies have studied the microstructure evolution during the heat treatment considering varying cooling rates, temperature gradients or multi-step heat treatments.

Further, several constitutive models have been proposed in the literature to predict the mechanical response of single crystal Ni-based superalloys (Cuitino and Ortiz, 1993; Allan, 1995; Ma et al., 2008; Cormier and Cailletaud, 2010; Staroselsky and Cassenti, 2011; Vattré and Fedelich, 2011; Fedelich et al., 2012; Zhu et al., 2012; Le Graverend et al., 2014; Barba et al., 2018; Ali et al., 2020a; Gupta and Bronkhorst, 2021; Keshavarz et al., 2022; Pei et al., 2022; Lu et al., 2023; Fan et al., 2024; Gao et al., 2025). Early works by Cuitino and Ortiz (1993) and Allan (1995) developed crystal plasticity models to study the anisotropic mechanical response of single crystal Ni-based superalloys. Ma et al. (2008) developed a crystal plasticity framework with dislocation density evolution, incorporating mechanisms such as dislocation climb within precipitates and creep flow formulation and predicted the

creep behavior for [001] crystallographic orientation. Staroselsky and Cassenti (2011) and Vattré and Fedelich (2011) have also developed crystal plasticity models to predict the temperature- and strain rate-dependence, and directional hardening in order to predict creep, cyclic and creep-fatigue interactions in superalloy single crystals over a range of deformation histories. The microstructure evolution during rafting and it's effect on creep deformation has been studied in several literature (Fedelich et al., 2012; Zhu et al., 2012; Fan et al., 2024). further refined these models by integrating experimental observations with computational simulations to enhance predictive capabilities. Le Graverend et al. (2014) developed microstructure-sensitive constitutive model to study creep, fatigue and creep-fatigue interactions. Further, Pei et al. (2022), Lu et al. (2023) and Gao et al. (2025) have expanded the understanding of high-temperature deformation mechanisms, including the effects of γ/γ' phase interactions, rafting phenomena, and environmental degradation. Though, there are many studies in the literature which study the deformation of single crystal Ni-based superalloys, very few crystal plasticity modeling frameworks have predicted the tensile, cyclic, creep responses and creep-fatigue interactions for various orientation and temperature for single crystal Ni-based superalloys using a single model.

Further, several studies focus on understanding the deformation of polycrystalline Ni-based superalloys (Manonukul and Dunne, 2004; Shenoy et al., 2008; Castelluccio and McDowell, 2014; Ghorbanpour et al., 2017; Prithivirajan and Sangid, 2020; Bandyopadhyay and Sangid, 2019; Agaram et al., 2021; Zhang et al., 2022b; Li et al., 2022a; Liu et al., 2024; Toursangsaraki et al., 2024; Wang et al., 2024). Manonukul and Dunne (2004) developed a crystal plasticity finite element framework with consideration for grain morphology and crystal orientations for predicting the cyclic plasticity of a Ni-based alloy. A physically based microstructure sensitive, rate-dependent crystal plasticity framework was proposed by Shenoy et al. (2008), to simulate the mechanical behavior of the polycrystalline Ni-based superalloy during cyclic loading. Castelluccio and McDowell (2014) proposed a mesoscale crystal plasticity framework to estimate the initiation and early-stage growth of fatigue cracks of a powder-processed Ni-based superalloy, RR1000. A dislocation density-based crystal plasticity framework was proposed by Ghorbanpour et al. (2017) for predicting the room temperature deformation of an Inconel superalloy, while estimating the constitutive model parameters using lower length scale calculations. Bandyopadhyay et al. (2019) have performed crystal plasticity finite element simulations for RR1000 under fatigue loading to study two failure modes (inclusion- and matrix-driven failures). Agaram et al. (2021) proposed a crystal plasticity framework for modeling the cyclic softening due to precipitate shearing. Zhang et al. (2022b) investigated the effect of microstructure and temperature on the low cycle fatigue behavior by EBSD analysis and CPFE simulations of a Ni-based

superalloy. Further, Liu et al. (2024), Toursangsaraki et al. (2024) and Wang et al. (2024) have contributed to the development of crystal plasticity models to study of effect of microstructural features on macroscopic deformation under complex loading conditions. The temperature-dependent heterogeneous deformation of polycrystalline Ni-based superalloys, including the effect of orientation and microstructural features for tensile and cyclic loading conditions, has not been studied extensively in the literature.

While several modeling studies already exist in the literature, gaps can still be identified. These include: (a) physically-based constitutive models that can account for the effect of microstructure (precipitate size, shape, distribution, grain morphology, etc.) on the mechanical properties, and (b) an integrated modeling framework for correlating processing-microstructure-mechanical properties of Ni-based superalloys. The present thesis aims to address these gaps by developing constitutive models for predicting the microstructure evolution during processing (specifically, heat treatment) and the microstructure-sensitive mechanical properties of single crystal and polycrystalline Ni-based superalloys by accounting for the underlying physics.

1.2 Thesis Outline

The thesis is structured in the following fashion.

A review of the literature on processing-microstructure-mechanical property correlations in Ni-based superalloys is given in Chapter 2. In this review, we briefly discuss the processing of single crystal and polycrystalline Ni-based superalloys, specifically about the variation in microstructural attributes with different processing and heat treatments, and their effect on the underlying mechanical properties. Gaps in the literature in predicting and correlating these relationships are also summarized, and the objectives of the thesis are presented to address these gaps.

A coupled phase field-crystal plasticity framework is presented in Chapter 3 to study the effect of heat treatment on the microstructure evolution of single crystal Ni-based superalloys. The model is used to predict the growth of the precipitates under isothermal aging at different temperatures. Further, the temperature-dependent mechanical properties of a heat-treated single crystal superalloy (CMSX-4) are predicted using a crystal plasticity finite element framework, thus demonstrating the model's capability for predicting the processing-microstructure-mechanical property correlations.

Chapter 4 develops a microstructure-sensitive crystal plasticity constitutive model to simulate thermo-mechanical deformation in single crystal Ni-based superalloys. Physically-based constitutive models have been developed for various mechanisms such as slip system-level backstress, crystallographic dislocation climb, and dislocation-precipitate interactions. Further, microstructure evolution models during rafting have also been developed. The model has been used to predict the tensile, creep, and cyclic response of two different superalloys, CMSX-4 and PWA-1484, over a wide range of loading conditions, which demonstrates the predictive capabilities of the model.

A mesoscale crystal plasticity model is developed in Chapter 5 for a powder metallurgy-processed polycrystalline Ni-based superalloy that accounts for the individual deformation of the matrix (γ phase, with homogenized distribution of $\gamma_s^{'}$ and $\gamma_t^{'}$ precipitates) and primary $\gamma^{'}$ phase and their effect on the local and aggregate deformation characteristics. Physically-based constitutive models are developed to account for microstructure-specific strengthening mechanisms and predict the macroscopic mechanical response for a range of deformation temperatures. The combined modeling and experimental framework is then used to study competitive misorientation developments at various microstructural features, namely annealing twin boundaries, phase interfaces (between the γ and $\gamma^{'}$ precipitates) and grain boundaries and their role in heterogeneous deformation (and potential failure) in the measured Electron Back Scatter Diffraction (EBSD) microstructures of these superalloys.

In Chapter 6, a micromechanical constitutive model is proposed that accounts for precipitate shearing during deformation to predict the cyclic deformation and softening behavior of polycrystalline Ni-based superalloys. The physically-based shearing model has consideration for dislocation-precipitate interactions, the volume conservation of precipitates, as well as the geometric shape of precipitates. The shearing model, coupled with a precipitate strengthening model, can also account for the transition in precipitate strengthening from strong pair to weak pair coupling. Application of the model has been demonstrated to predict the cyclic hardening and softening behavior of two different polycrystalline Ni-based superalloys, with different initial microstructures. Further, the model can also predict the microstructure and substructure evolution during cyclic deformation.

In Chapter 7, different Fatigue Indicator Parameters (FIPs) are implemented in the crystal plasticity framework to predict the fatigue crack initiation sites during fatigue loading. Room temperature cyclic deformation simulations have been performed on the EBSD microstructures, and a statistical analysis of the FIPs is performed to study the competitive role of different microstructural features on the FIPs. Based on the statistical analysis,

higher FIP localization is observed at the twin boundaries, indicating a higher propensity for failure, as compared to the grain boundaries and phase interfaces.

Finally, the thesis is summarized and major conclusions listed, along with recommendations for future work, in Chapter 8.

Chapter 2

Background

As discussed in Chapter 1, Ni-based superalloys are widely used in applications that require superior elevated temperature properties like high strength, high toughness, relatively high creep resistance, and thermal fatigue resistance. These properties are highly dependent on the microstructure of these alloys, which is, in turn, sensitive to the processing of the alloys. In this regard, a review of the inter-relationships between processing, microstructure, and mechanical properties has been presented in this Chapter.

2.1   Single Crystal Superalloys

Single crystal Ni-based superalloys are widely used in manufacturing advanced aero-engine components, such as turbine blades, owing to their mechanical properties at elevated temperatures. These superalloys usually consist of Cr, Co, Al, Mo, Ti, Ta, W, Re, Ru, and Nb as alloying elements, with Ni as the base metal. The development of single crystal superalloys has evolved through five generations, with ongoing efforts currently focused on the development of a sixth-generation alloy (Satyanarayana and Eswara Prasad, 2016). PWA1480, Rene N4, and SRR99 are first-generation superalloys. 3 wt. % Re was added for second-generation superalloys (PWA1484, CMSX-4 and Rene N5), which was further increased to 6 wt. % in third-generation superalloys (CMSX-10 and Rene N6) (Reed, 2008). Further, the fourth-generation superalloys (MC-NG and EPM-102) were developed by the addition of Ru to the third-generation superalloys, with further increase in Ru content for fifth-generation superlloys (TMS-162 and TMS-172) (Reed, 2008; Satyanarayana and Eswara Prasad, 2016). Subsequently, efforts are being made by changing the alloy composition for sixth-generation superalloys to further improve the mechanical properties

and phase stability (Satyanarayana and Eswara Prasad, 2016). The mechanical properties and the underlying microstructure greatly depend on the composition as well as the processing of these superalloys.

2.1.1 Processing and Heat Treatment

The processing of superalloys involves the initial fabrication of large ingots by vacuum induction melting, followed by investment casting, or extrusion and forging processes (Akca et al., 2015). Vacuum induction melting (VIM) is generally performed in a refractory crucible to consolidate the primary elemental constituents and/or recycle (revert) alloy into a base alloy (Akca et al., 2015). Compared to traditional electric arc melting in air or slag environments, VIM is effective in the removal of low-melting-point contaminants (Akca et al., 2015). After achieving the desired alloy composition, the solidified ingot is subjected to consolidation processes or addition melting, depending upon the application of the material (Akca et al., 2015). The first gas turbine engine blade was manufactured by extrusion and forging operations (Wright and Smith, 1986). These manufacturing techniques have been found to have limitations. For example, the blades tend to be relatively heavy because making them in a hollow form is not feasible without performing additional machining steps. Further, the blades are susceptible to cracking and incipient melting (a localized melting below the melting point temperature at grain boundaries or segregated regions) due to the hot working temperature (Reed, 2008). In response to these limitations, investment casting emerged as the preferred manufacturing method and remains the industry standard today. Investment casting, also known as the lost-wax process, is a key method for producing nickel-based superalloy components with complex geometries. Ceramic molds containing alumina, silica, and/or zirconia are prepared using the progressive buildup of ceramic layers around a wax pattern of the cast component and melting out the wax to form a mold. The mold is poured with remelted superalloys in a preheated vacuum chamber. The mold is removed once the alloy has cooled to room temperature, forming microstructures with either columnar or equiaxed grains, or single crystals (Akca et al., 2015). In equiaxed casting, the furnace is generally switched off after pouring the molten metal, whereas in advanced methods like the conventional Bridgman crystal-growing method, the mold is withdrawn at a controlled rate from the furnace to produce directionally solidified or single crystal structures. Once cooled, the ceramic shell is broken away, and any core is leached out chemically (Reed, 2008).

Heat treatment plays a critical role in optimizing the microstructure, eliminating defects, and enhancing the mechanical properties of the castings by controlling the morphology and

the distribution of the $\gamma^{'}$ precipitate phase (Wilson et al., 2003; Sahu et al., 2021). Heat treatment helps in developing a uniform $\gamma/\gamma^{'}$ microstructure, relieving residual stresses developed during directional solidification, eliminating casting defects, and improving the creep, fatigue, and oxidation resistance. Traditionally, two-step heat treatments, a solutionizing treatment (also sometimes referred to as solution treatment), followed by aging treatment, are used for Ni-based superalloys. During solutionizing, the alloy is heated above the $\gamma^{'}$ solvus temperature, leading to the dissolution of $\gamma^{'}$ precipitates and elimination of interdendritic microstructures, such that a homogenized microstructure is generated (Wilson et al., 2003). It reduces dendritic segregation and prepares the alloy for optimal $\gamma^{'}$ precipitation. During the subsequent aging process, $\gamma^{'}$ re-precipitates to form the typical microstructure of superalloys. Two-step aging is often performed to obtain the desired size, shape and morphology of $\gamma^{'}$ precipitates (Wilson et al., 2003). Figure 2.1 shows a schematic of the solutionizing treatment and the two-step aging treatment used for CMSX-4 single crystal Ni-based superalloy (Sengupta et al., 1994). First, a series of solutionizing treatments at progressively higher temperatures was performed. Initially, the specimen was held at 1276 $^{\circ}C$ for 2 h, followed by treatments at 1287 $^{\circ}C$ for 2 h, 1296 $^{\circ}C$ for 3 h, 1304 $^{\circ}C$ for 3 h, 1315 $^{\circ}C$ for 2 h, 1321 $^{\circ}C$ for 2 h, 1324 $^{\circ}C$ for 2 h and finally air cooled. Subsequently, a high-temperature aging process was conducted at 1080 $^{\circ}C$ for 4 h, followed by air cooling. This was followed by a final aging treatment at 871 $^{\circ}C$ for 20 h, after which the materials were air cooled again.

2.1.2 Microstructure

The composition plays an important role in the microstructure of these alloys, and generally, more than ten alloying elements are present in Ni-based superalloys. Most alloys contain significant amounts of Al, Cr, Co and Ti. Further, other elements such as Re, W, Ta, Hf, Ru, Mo, Nb and Zr are also present in some alloys (Reed, 2008). Elements such as Co, Cr, Ru, Mo, Re, and W have atomic radii similar to Ni and act as the γ phase stabilizer. Elements such as Al, Ta and Ti have atomic radii greater than Ni, promoting the formation of the $\gamma^{'}$ ordered phases such as $Ni_3(Al, Ta, Ti)$ (Reed, 2008). The microstructure of a typical superalloy thus consists of γ and $\gamma^{'}$ phases.

γ **phase**: This phase has a FCC crystal structure and forms the matrix phase in which other phases reside. A representative microstructure of a single crystal superalloy is shown in Figure 2.2(b).
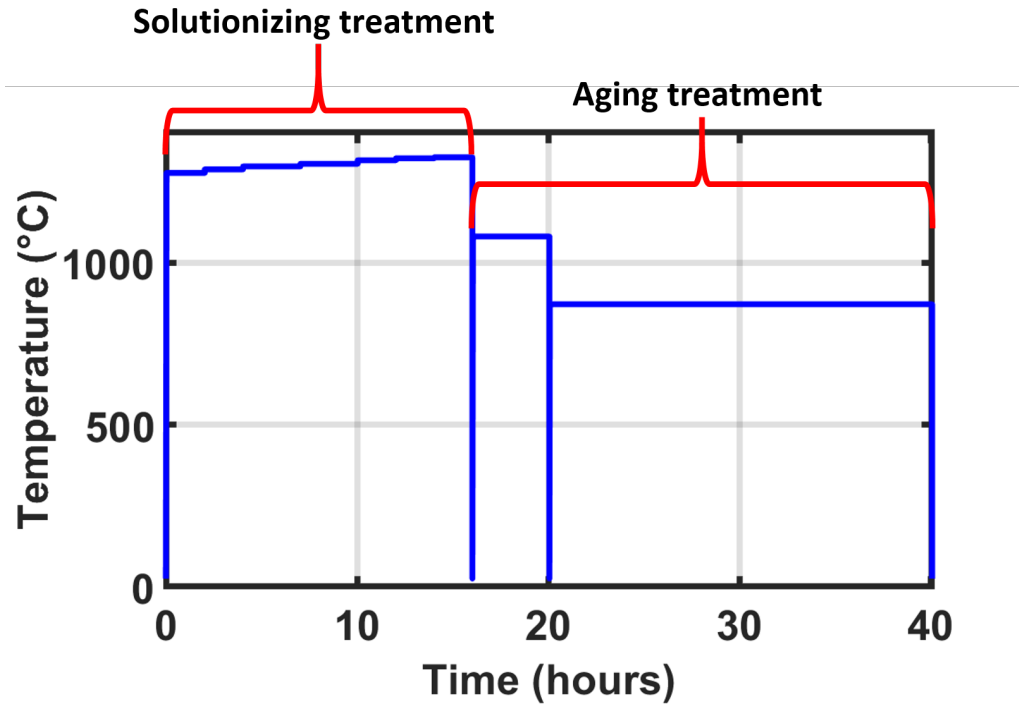
FIGURE 2.1: Solutionizing and aging treatments of single crystal Ni-based superalloy, CMSX-4. Adapted from (Sengupta et al., 1994).
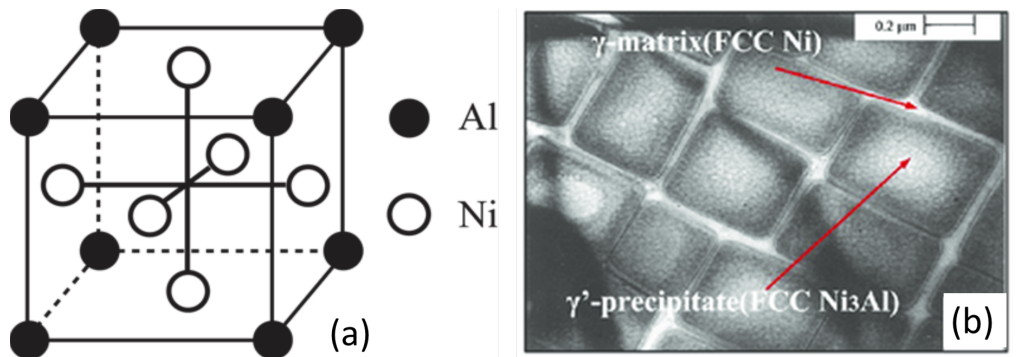
FIGURE 2.2: (a) L_{12} crystal structure of $\gamma^{'}$ phase and (b) Microstructure of single crystal Ni-based superalloys, with cuboidal $\gamma^{'}$ precipitates in the γ matrix. Adapted from (Vattré, 2009) and (Huang et al., 2014).

$\boldsymbol{\gamma'}$ **phase**: The γ' phase, with a stoichiometric composition of Ni_3Al and cuboidal morphology, is the primary strengthening phase in superalloys (Satyanarayana and Eswara Prasad, 2016). Often, this phase is referred as the precipitate phase. These single crystal superalloys have a high precipitate volume fraction, around 70% for some modern alloys (Satyanarayana and Eswara Prasad, 2016). γ' phase has a $L1_2$ crystal structure as shown in Figure 2.2(a) and is coherent with the γ matrix. The lattice parameters for γ and γ' phases are nearly similar, and the chemical compatibility of the two phases allows γ' to precipitate homogeneously throughout the matrix (Satyanarayana and Eswara Prasad, 2016). γ' precipitates impart strengthening to the superalloy due to their strength and high volume fraction, γ' fault energy, and coherency strengthening (Satyanarayana and Eswara Prasad, 2016). Initially, the small γ' precipitates have a spherical shape. During heat treatment, as the volume fraction of γ' increases, the morphology changes from spherical to cuboidal. Cuboidal γ' precipitates homogenized with the γ phase can be seen in Figure 2.2(a).

The deformation behavior of nickel-based superalloys is governed by the interactions between the constituent γ and the γ' phases. Plastic deformation primarily occurs in the γ matrix via dislocation glide on the $111<1\bar{1}0>$ slip systems, while the γ' phase imparts strength to the superalloys via precipitate strengthening. Further, solute solution strengthening due to the various alloying elements also contributes to the enhanced strength of the superalloys.

2.1.3 Process-Structure-Mechanical Property Relationships

The effect of processing and heat treatment parameters on the microstructure and resultant mechanical properties is discussed in this section. The casting method and parameters, such as mold geometry, play a major role in influencing the properties of superalloys (Selvaraj et al., 2021). Directional solidification is widely used in the production of single crystal superalloys. Various parameters such as temperature gradients, solidification rate, and cooling rate influence the directionally solidified microstructure and ultimately the mechanical properties (Selvaraj et al., 2021; Szeliga et al., 2016).

As mentioned earlier, γ' precipitates strengthen these superalloys, and their morphology, size, and volume fraction significantly influence the mechanical properties. The effect of the heat treatment process on the microstructure and mechanical properties has been studied extensively in the literature (Caron and Khan, 1983; Bhowal et al., 1990; Grosdidier et al., 1998; Fuchs, 2002; Yu et al., 2007; Tian et al., 2008, 2014; Liang et al., 2016; Wang

et al., 2019c; Du et al., 2021; Wang et al., 2020; Strutt et al., 2023; He et al., 2023). A supersaturated solid solution is first obtained through solutionizing heat treatment, which provides the best condition for the further aging process. Heat treatment results are affected by solutionizing heat treatment parameters such as temperature, holding time, and cooling rate. Du et al. (2021) studied the effect of solutionizing treatment on creep properties and found that creep life increases with solutionizing treatment time until a threshold limit. Tian et al. (2008) performed solutionizing heat treatment at different temperatures and indicated great dependence of creep life on solutionizing temperature. Lee et al. (2013) found that the fraction of eutectic phase decreases with an increase in the solutionizing temperature. Yu et al. (2007) studied the effect of different solutionizing treatments on microstructure and stress rupture life of DD32 single crystal superalloy and concluded that solutionizing treatment temperature has a more significant role on microstructure as compared to the hold time. Wang et al. (2020) investigated the influence of cooling rate on the microstructure and elevated temperature tensile properties. The as-cast superalloy was heated in a stepwise manner to its solutionizing temperature ($1315~^\circ C$) and held for 4 h at this temperature. The material was then cooled to room temperature at four different cooling rates, furnace cooling 1 ($0.5~^\circ C/s$) (FC1), furnace cooling 2 ($0.6~^\circ C/s$) (FC2), air cooling ($72~^\circ C/s$)(AC), and water cooling ($138~^\circ C/s$) (WC). The SEM micrographs after four different heat treatments are shown in Figure 2.3. It can be seen that the cooling rate has a significant effect on the distribution, shape, and size of $\gamma^{'}$ precipitates. With an increase in cooling rate, the size of the $\gamma^{'}$ precipitate was found to be smaller and uniform, and the shape of the precipitates also changed from cuboidal to irregular curved surfaces. Further, the tensile stress-strain response at $980~^\circ C$ varied significantly for these four different cooling rates. The elastic modulus was also significantly lower at low cooling rates as compared with AC and WC. The yield stress and ultimate tensile strength also vary with cooling rates.

Following the solutionizing treatment, generally, a two-stage aging treatment is performed. The aging temperature and time influence the microstructure of superalloys. Wang et al. (2019a) performed different heat treatments, thus varying the precipitation temperature and time, and determined the optimum microstructure of DD5 superalloy. Grosdidier et al. (1998) studied dissolution of the γ phase and precipitation of CMSX-2 during heat treatment and concluded that the shape of the precipitate changes from spherical to cuboidal to dendritic from nucleation to growth as a function of time. Further, Yu et al. (2007) optimized the heat treatment in terms of the volume fraction, size and morphology of precipitates by altering the aging time and temperature to obtain maximum stress rupture life. Feng et al. (2021) studied the effect of aging time and temperature and concluded

FIGURE 2.3: Effect of different cooling rates on microstructure and tensile stress–strain response at 980 $^\circ C$. Here, FC1: furnace cooling 1(0.5 $^\circ C/s$), FC2: furnace cooling 2 (0.6 $^\circ C/s$), AC: air cooling (72 $^\circ C/s$) and WC: water cooling (138 $^\circ C/s$). Adapted from (Wang et al., 2020).

that at low aging time, the precipitate size increases first, then decreases, and finally increases with increasing aging temperature, whereas at high aging time, precipitate size gradually increases with aging temperature. Sengupta et al. (1994) performed different heat treatments to produce different γ' sizes and distribution phases and studied the effect of γ' sizes on the tensile properties of CMSX-4. It has been observed that the tensile behavior of CMSX-4 is influenced by the size and distribution of γ' precipitates, which are controlled through specific heat treatment processes. During long-term aging, precipitate size increases with aging temperature and time (Nabarro, 1996). The effect of aging time on the tensile stress-strain response and creep response is shown in Figure 2.4. As can be seen, the mechanical property degrades with long aging hours.

FIGURE 2.4: (a) Stress-strain response of the aged material with different aging times at 1100 $^\circ C$ (adapted from Yang et al. (2020)). (b) Creep response of the material aged at 1000 $^\circ C$ for different aging times, followed by loading at 1140 $^\circ C$ and 137 MPa (adapted from Huang et al. (2020)).

The materials used in gas turbine blades must exhibit long-term microstructural stability, excellent mechanical strength at elevated temperatures, and superior resistance to

creep for a good high-performance operation (Shang et al., 2022). As $\gamma^{'}$ precipitates provide significant strengthening, the size, fraction, and distribution of precipitates influence the properties and performance. Compared to irregularly shaped precipitates, uniformly shaped and well-aligned cuboidal precipitates increase the strength of single crystal superalloys (Caron and Khan, 1983). Smaller $\gamma^{'}$ precipitates improve the yield strength (Grant et al., 2013) and enhance the fatigue performance (Le Graverend et al., 2010). Caron et al. (1988) observed that a precipitate size between 0.35–0.5 μm offers maximum creep strength along [001] orientation, in contrast, orientations near the [111]–[011] showed a significant reduction in creep life. However, around 0.2 μm precipitate size, the [111] orientation shows improvement in creep life, becoming the most creep-resistant. Ali et al. (2020b) explored the effect of the size of $\gamma^{'}$ precipitate on the hardness and creep properties of single crystal superalloys using both experiments and crystal plasticity simulations. It has been observed that smaller $\gamma^{'}$ precipitates increase hardness and improve creep resistance. Furthermore, during long-term high-temperature operation, the microstructure of these alloys gradually deteriorates over time (Cheng et al., 2009; Dan et al., 2015), which has a great effect on their mechanical properties. Thus, the blade life depends not only on the initial high-temperature properties of the superalloy but also on the microstructure stability throughout service (Yang et al., 2020). To understand the effect of thermal exposure on mechanical performance, various experiments were conducted on aged superalloys, focusing on tensile and compressive properties (Leidermark et al., 2010; Zhixun et al., 2015). Xia et al. (2007) observed a reduction in both tensile and compressive yield strengths with increased aging time, due to $\gamma^{'}$ precipitate coarsening and a reduction in their volume fraction. In addition, the life of the stress rupture was found to degrade over time and at higher temperatures (Xia et al., 2007; Acharya and Fuchs, 2004), mainly due to the coarsening of the $\gamma^{'}$ phase, the formation of the Topologically Close-Packed (TCP) phases and the accumulation of dislocations (Shi et al., 2012; Liu et al., 2010). Long-term aging also affected very high cycle fatigue behavior due to microstructural deterioration (Cervellon et al., 2017). Lapin et al. (2009) found that the room-temperature Vickers hardness and the 0.2% yield strength at 950 $^{\circ}C$ decrease as the volume fraction of $\gamma^{'}$ precipitates decreases and their average size increases.

The combined effects of composition, processing, microstructure, and service conditions thus govern their mechanical properties and performance.

TABLE 2.1: Effect of chemical composition on properties of polycrystalline Ni-based superalloys (Akca et al., 2015).

Alloy	Composition(wt.%)	Applications
Inconel Alloy 600	76Ni-15Cr-8Fe	Nuclear reactors; chemical industry
Nimonic Alloy 75	80Ni-20Cr-Ti-C	Gas turbines; furnace components; heat treatment equipment
Alloy 601	61Ni-Al-Si	Chemical processing; pollution control; aerospace; power generation
Alloy X750	Ni-Al-Ti	Gas turbines; rocket engines; nuclear reactors; pressure vessels; aircraft structures
Alloy 718	55Ni-21Cr-5Nb-3Mo	Aircraft and land-based gas turbines; cryogenic tankage
Alloy X	48Ni-22Cr-18Fe-9Mo-W	high-temperature flat-rolled products for aerospace
Waspaloy	60Ni-19Cr-4Mo-3Ti-1.3Al	Jet engine components
Alloy 718Plus	Bal.Ni-18.53Cr-9.26Co-8.82Fe-5.34Nb-2.85Mo-1.55Al-0.80Ti-1.08W-0.024C-0.011P-0.007P (Li et al., 2021)	Jet engine; turbine, steam generator (Li et al., 2021)
Nimonic 90	54Ni-18-21Cr-15-21Co-2-3Ti-1-2Al	Turbine blades; discs; hot-working tools
Alloy 720Li	57.4Ni-16Cr-14.7Co-5Ti-2.5Al-3Mo-1.25W-0.01C-0.015B-0.03Zr (Wise et al., 2024)	Turbine discs

2.2 Polycrystalline Superalloys

Polycrystalline Ni-based superalloys are generally used in the manufacturing of turbine discs. The primary alloying element composition affects the properties, microstructure, and application of these superalloys. Some prevalent polycrystalline Ni-based superalloys with primary composition and applications are listed in the Table 2.1.

2.2.1 Processing and Heat Treatment

Depending on the alloy chemistry and other factors, polycrystalline superalloys are fabricated either by cast and wrought processing C&W or by PM (Reed, 2008). Alloys such as IN718 and Waspaloy are generally processed by C&W process, as the composition

of strengthening elements Al, Ti, and Nb is relatively low and PM processing is costly compared to the C&W process (Reed, 2008).

The processing for both routes starts with VIM, where alloying elements are poured into the crucible and the electrode is formed by pouring the molten alloy into a mold (Galpin, 2022). In C&W processing, VIM is followed by electroslag remelting and vacuum arc remelting to remove impurities and to form a billet (Galpin, 2022). In addition, the billets are processed by thermomechanical processing such as rolling, extrusion, or controlled heating before undergoing forging operations (Reed, 2008). The level of segregation increases during melt processing in heavily alloyed grades such as Rene 95 and RR1000, and cracking can occur during thermal-mechanical processing. Thus, PM processing is preferred for such alloys (Reed, 2008). Alloys with a high $\gamma^{'}$ fraction and several element additions, for safety-critical components, where element segregation must be minimized, are generally treated using PM processing (Galpin, 2022).

In PM processing, VIM is followed by remelting and inert gas atomization to produce the metal powder (Reed, 2008). Then the metal powder is sieved to remove large non-metallic inclusions that may be present due to processing (Reed, 2008). The sieved powder is consolidated using Hot Isostatic Pressing (HIP) by packing powder into steel cans (Galpin, 2022). The solid billets are formed by subjecting steel cans to high temperature and pressure for a longer period, depending on the alloy composition (Galpin, 2022). The concentration of the inclusions is generally lower for products processed by PM as compared to the C&W route, although PM processing is costly and significantly more complex (Reed, 2008).

As with single crystal superalloys, the heat treatment generally involves two steps: solutionizing treatment and aging treatment. The solutionizing treatment dissolves the $\gamma^{'}$ precipitates and helps to obtain the appropriate grain size and prepares a supersaturated solid solution for the aging process. The aging treatment adjusts the size, volume fraction, and distribution of $\gamma^{'}$ precipitates (Gai et al., 2022). Figure 2.5 shows the heat treatment of a representative powder metallurgy superalloy, N18, which includes solutionizing and two-step annealing treatments. The solutionizing treatment applied to the alloy consists of 1165 $^{\circ}C$ for 4 h, followed by two-step aging at 700 $^{\circ}C$ for 24 h and finally at 800 $^{\circ}C$ for 4 h (Flageolet et al., 2004).
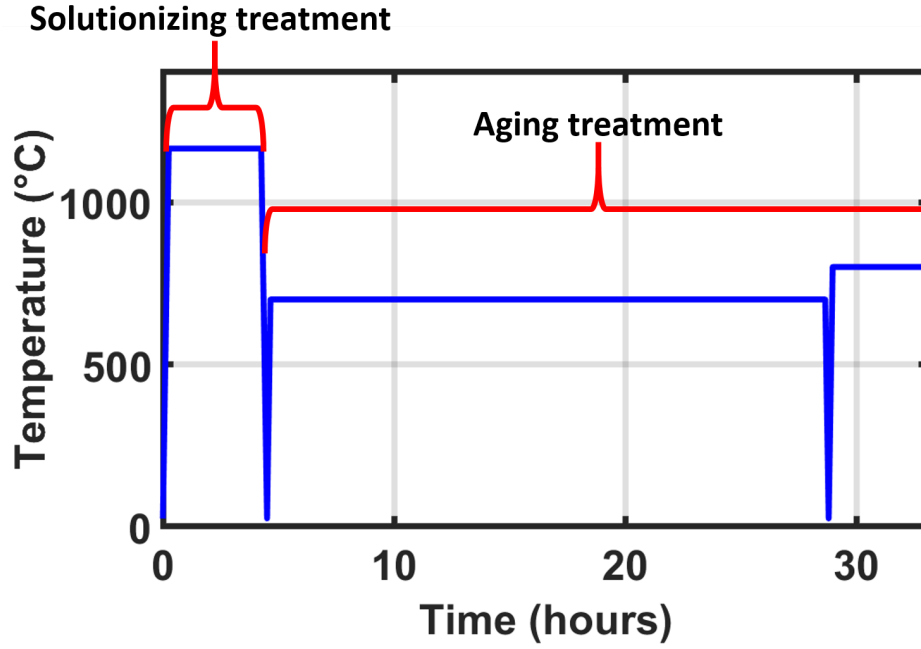
FIGURE 2.5: Heat treatment of polycrystalline Ni-based superalloy (N18). Adopted from (Flageolet et al., 2004).

2.2.2   Microstructure

Similar to single crystal superalloys, the microstructure of polycrystalline superalloys consists of two primary phases, the γ phase with FCC crystal structure and an ordered $L1_2$ type $\gamma^{'}$ phase. The γ phase is a continuous solid solution strengthened phase that usually contains a high percentage of elements such as Cr, Fe, Co, Mo, and W (Thellaputta et al., 2017). The $\gamma^{'}$ precipitates, often coherent with the γ phase, are rich in elements like Al, Ti, and Ta (Reed, 2008). Further, $\gamma^{'}$ precipitates are generally classified as primary, secondary, and tertiary precipitates depending on their size, a schematic of which is shown in Figure 2.6 (Galpin, 2022). Under sub-solvus solutionizing heat treatment, the micrometer-sized primary $\gamma^{'}$ precipitates are generally formed at the grain boundaries (Reed, 2008). In addition, sub-micron-sized secondary and nanometer-sized tertiary precipitates are present inside the γ grains, and their typical sizes are ∼100 nm and ∼20 nm, respectively (Galpin, 2022). Further, $\gamma^{''}$ precipitates also form in the presence of Fe, where Ni and Nb combine to form Ni$_3$Nb with body-centered tetragonal structure in Ni-Fe alloys (Thellaputta et al., 2017). This phase provides high strength at low to intermediate temperatures and is unstable at temperatures above 650 $°C$ (Thellaputta et al., 2017). Carbide and boride particles are also found in polycrystalline superalloys, depending on

their chemical composition (Reed, 2008). These particles often form along grain boundaries, as both carbon (C) and boron (B) tend to segregate in these regions (Reed, 2008). The most commonly observed carbides are the cuboidal MC type, where M can be Ti, Ta, Nb, or Hf (Charpagne et al., 2016). Boride particles are typically of the M_3B_2 type, with M generally consisting of a combination of Mo and Cr (Thellaputta et al., 2017).
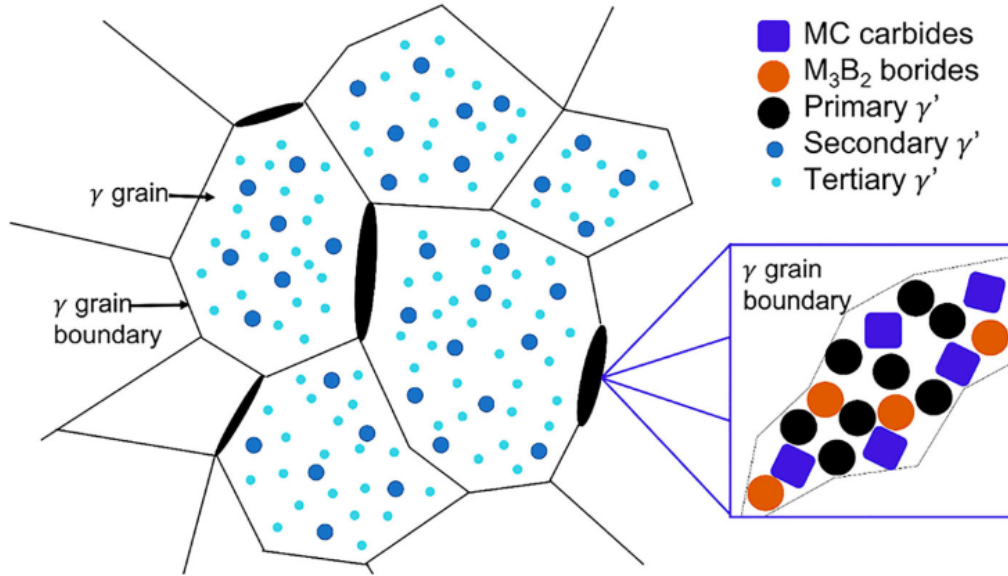
FIGURE 2.6: Schematic of the different precipitates present in polycrystalline Ni-based superalloys. Adopted from (Galpin, 2022).

2.2.3 Process-Structure-Mechanical Property Relationships

The manufacturing process and the following heat treatment process have a significant effect on the microstructure and mechanical properties of polycrystalline Ni-based superalloys. The choice between C&W and PM processing largely depends on the application requirements in terms of the geometry, service conditions and mechanical performance. PM processing is especially advantageous for processing highly alloyed compositions that are prone to cracking during conventional forging. Although for components that do not operate under demanding conditions, the properties offered by PM processing are generally not required. In such cases, low-cost C&W alloys are used (Wise et al., 2024).

Significant research has been conducted to explore the balance between cost and performance for traditional C&W alloys like 718Plus and PM-based alloys such as RR1000 (Hardy et al., 2020). One way is to modify the composition of the existing highly alloyed commercial materials to develop derivatives that are better suited to manufacture by C&W

processing, such as Alloy 720Li (Keefe et al., 1992) and René 65 (Heaney et al., 2014). Both of these advanced alloys show improved properties over Alloy 718Plus (Wise et al., 2024). Due to its high alloy content, it is generally viewed as the upper limit for cast and wrought processing, before transitioning to powder metallurgy becomes necessary; Alloy 720Li is one of the most highly alloyed materials that can be processed via C&W processing (Wise et al., 2024). Furrer and Fecht (1999) showed the effect of the manufacturing route on the grain size of U720Li alloy, as can be seen in Figure 2.7. C&W alloy tends to exhibit rapid and non-uniform grain coarsening, whereas PM alloys generally show more gradual and uniform grain growth (Furrer and Fecht, 1999). The rate at which the average and as-large-as grain sizes vary significantly between the C&W and PM processing of U720Li, as can be seen in Figure 2.7. The grain size influences strength, creep, and fatigue properties of the material (Furrer and Fecht, 1999).
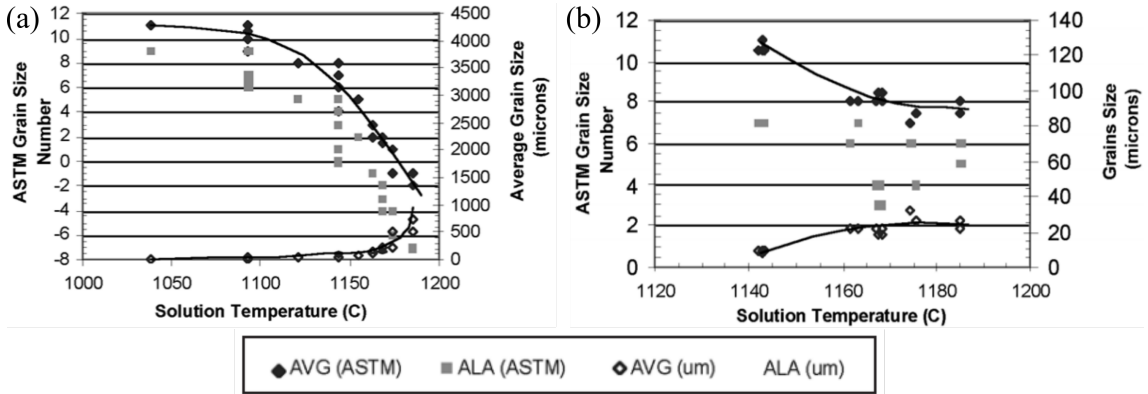
FIGURE 2.7: Variation of grain size with heat treatment for one hour at various solutionizing temperatures via (a) C&W and (b) PM route of U720Li alloy. Here, AVG denotes "average" and ALA denotes "as large as". Adopted from (Furrer and Fecht, 1999).

Further, the size and distribution of the $\gamma^{'}$ precipitates are crucial in these superalloys, as precipitation of the $\gamma^{'}$ phase is the main contributor to their high-temperature strength (Nembach and Neite, 1985). Characteristics of the $\gamma^{'}$ precipitate are mainly controlled by the heat treatment (solutionizing treatment and aging treatment). The $\gamma^{'}$ solvus temperature lies between 1050 $^{\circ}C$ and 1200 $^{\circ}C$ for most turbine disc alloys depending on the chemical composition (Reed, 2008). The temperature of the solutionizing treatment plays an important role in the microstructure of these alloys. If the solutionizing temperature is sub-solvus, the grain-pinning effect caused by undissolved $\gamma^{'}$ precipitates restricts γ grain-growth, while the γ grains are comparatively coarser, if the solutionizing temperature is super-solvus (Reed, 2008). Super-solvus heat treatment eliminates primary $\gamma^{'}$ precipitates, while sub-solvus heat treatment generates a bimodal microstructure with

primary, secondary, and tertiary $\gamma^{'}$ precipitates (Reed, 2008). Wan et al. (2018) studied the effect of solutionizing heat treatment from 1130 $^{\circ}C$ to 1150 $^{\circ}C$ on the microstructures and tensile properties of U720Li alloy and showed that a solutionizing temperature of 1130 $^{\circ}C$ to 1140 $^{\circ}C$ leads to fine secondary $\gamma^{'}$ precipitates, resulting in higher strength as compared to 1140 $^{\circ}C$. Atabay et al. (2021) performed sub- and super-solvus heat treatment for Rene 41 alloy and concluded that fine $\gamma^{'}$ precipitates in sub-solvus specimens show the highest elongation. Kozar et al. (2009) found that alloys subjected to super-solvus heat treatment gain their strength from resistance to $\gamma^{'}$ precipitate shearing. In contrast, sub-solvus heat-treated alloys not only benefited from precipitation strengthening, but also exhibited enhanced strength due to the Hall–Petch effect. You et al. (2017) investigated the effect of solutionizing temperatures and strengthening mechanisms for Inconel 718, and their study revealed that the $\gamma^{'}$ phase precipitates at higher temperatures than the $\gamma^{''}$ phase. Radis et al. (2009) studied the microstructural and $\gamma^{'}$ phase distribution during continuous cooling of Udimet 720Li after solutionizing treatment, and developed a kinetics model to describe the precipitation of $\gamma^{'}$ phases during cooling. Mostafaei et al. (2016) investigated the effect of solutionizing treatment and aging on the microstructure and mechanical performance of Alloy 625. Wang et al. (2016b) focused on the effect of solutionizing temperature and holding time on $\gamma^{'}$ phase dissolution in IN100 and DS Rene125, providing insight into the kinetic aspects influencing dissolution during solutionizing treatment. Mitchell et al. (2008) explored how cooling rates affect the microstructure and hardness in nickel-based superalloys. Gai et al. (2022) performed solutionizing heat treatment at temperatures ranging from 1100 $^{\circ}C$ to 1140 $^{\circ}C$ to get optimized microstructures and mechanical properties of GH4151 alloy. Figure 2.8 shows the microstructure after solutionizing treatment at different temperatures for 2 h and their effect on the yield strength of GH4151 alloy. The average grain size is similar for specimens treated at 1100 $^{\circ}C$ and 1120 $^{\circ}C$ and increases with solutionizing treatment for 1130 $^{\circ}C$ and 1140 $^{\circ}C$ temperatures. The area fraction of primary $\gamma^{'}$ precipitates decreases, and the size of spherical secondary $\gamma^{'}$ precipitates increases with an increase in solutionizing temperature. Further, the highest yield strength is observed for specimens solutionized at 1130 $^{\circ}C$ for both room and 750 $^{\circ}C$ temperatures.

Further, single or two-step aging is generally performed for optimizing the $\gamma^{'}$ precipitate size. The influence of aging temperature, time, and cooling rate on the microstructure has been studied for different polycrystalline superalloys. Jackson and Reed (1999) optimized the heat treatment to 24 h at $700^{\circ}C$ as compared to the conventional aging treatment for Udimet 720Li alloy, consisting of 24 hours at $650^{\circ}C$ followed by 16 hours at $760^{\circ}C$ to obtain highest tensile and creep properties of Udimet 720Li alloy. Microstructure evolution
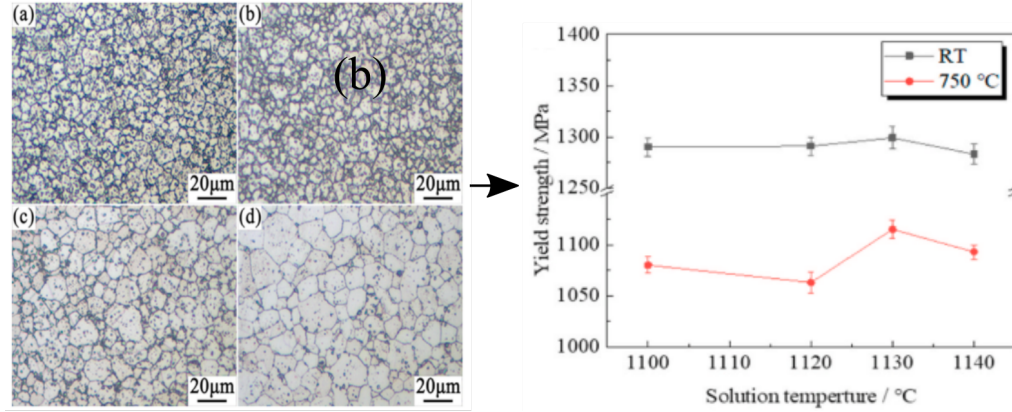
FIGURE 2.8: Effect of solutionizing temperature ((a) 1100 °C, (b) 1120 °C, (c) 1130 °C, (d) 1140 °C) on the microstructure and yield strength of GH4151 alloy at room temperature and 750 °C. Adopted from (Gai et al., 2022).

during various heat treatment processes of IN738LC alloy was studied by Balikci et al. (1997). Kearsey et al. (2012) studied the effect of heat treatment on the microstructure, particularly $\gamma^{'}$ size, grain size, and phase fraction, and mechanical properties such as low cycle fatigue (LCF) life, fatigue crack growth rate (FCGR) properties, and dwell FCGR behavior. Joseph et al. (2017) investigated the effect of heat treatment on the microstructure and properties of Haynes 282 and found out that standard two-step aging (1010 °C/2 h +788 °C/8 h) produced fine $\gamma^{'}$ and discrete grain boundary carbides, resulting in excellent strength and ductility at room temperature. Hao et al. (2020) studied the effect of heat treatment on the microstructure and $\gamma^{'}$ phase characteristics and consequently on the mechanical properties of the FGH4096 M superalloy. The results showed that a high volume fraction of uniformly sized and dense distribution $\gamma^{'}$ precipitates significantly contributed to increased tensile strength and hardness. Shin et al. (2019) compared a single-step heat treatment using three different cooling rates after solutionizing annealing with a two-step process of Haynes 282. Their results showed that slower cooling rates led to larger $\gamma^{'}$ precipitates, and the single-step treatment could achieve a good balance of strength and ductility. Xia et al. (2018) concluded that the shape and size of the $\gamma^{'}$ phase significantly influence the stress rupture life and hardness of nickel-based superalloys. Xu et al. (2018) studied the effect of three solutionizing treatment temperatures—1080 °C, 1150 °C, and 1210 °C and found that heat treatment at 1150 °C for 4 hours followed by air cooling led to a uniform distribution of fine $\gamma^{'}$ precipitates and stress rupture life increases with solutionizing temperature. Yıldız et al. (2017) have investigated the influence of cooling rate for various superalloys and found that higher cooling rates lead to a more uniform microstructure, which enhances the strength.

Further, it should be noted that the optimized heat treatment may be different for different alloy grades to get the desired mechanical properties, owing to the different alloy compositions that lead to variation in thermal properties and different thermodynamic behavior (Wu et al., 2019a). For example, the typical heat treatment for IN100 involves sub- or super-solvus solutionizing treatment, at $982\,^{\circ}C/1h$, and aging at $732\,^{\circ}C/8h$ (Kozar et al., 2009), while maximum tensile properties for Udimet 720Li are achieved by a sub-solvus solutionizing treatment at $1120\,^{\circ}C$ or $1080\,^{\circ}C$, followed by aging at $760\,^{\circ}C/16h$ and $650^{\circ}C/24h$ (Vaunois et al., 2010). For Rene 88DT, the recommended heat treatment is generally first super-solvus solutionizing treatment followed by aging at $760^{\circ}C/8h$ (Krueger et al., 1990). (Du et al., 2018) used three steps heat treatment for IN792 superalloy, which includes : $1120^{\circ}C/2h$ followed by air cooling (AC) then $1080^{\circ}C/4h$ AC and finally $845^{\circ}C/24h$ AC . Thus, according to the alloy chemical composition, the heat treatment process varies for different alloys.

The essential mechanical properties of polycrystalline Ni-based superalloys in operating conditions, such as those required for stationary components of an aero engine, are high yield stress, tensile strength, ductility, fracture toughness, resistance to crack initiation and propagation, and creep resistance (Reed, 2008). Less emphasis is given on creep resistance due to their relatively lower operating temperatures as compared to single crystal superalloys (Reed, 2008). Achieving optimal mechanical performance depends significantly on the microstructure, which is mainly influenced by the chemical composition of the alloy and the applied heat treatment. In nickel-based disk alloys, the key microstructural factors include grain size, the volume fraction, size and distribution of γ' precipitates, as well as boride/carbide precipitation along grain boundaries (Cui et al., 2009).

Grain size has a pronounced effect on the mechanical properties of these alloys. Williams and Starke Jr (2003) observed that grain size is inversely proportional to yield strength and resistance to fatigue crack initiation, whereas creep strength and resistance to fatigue crack growth increase with grain size in the range of 10-1000 μm. Longer fatigue life is reported for fine-grained structures as compared to coarse-grained structures under the same testing conditions. This is due to better resistance to crack initiation and early crack propagation by fine-grained structures (Gabb et al., 2005, 2011). However, a faster fatigue crack growth rate is observed for the fine-grained structures (Everitt et al., 2007; Pang and Reed, 2007, 2009) due to increased grain boundary area available for preferential environmental damage (oxidation or corrosion) Osinkolu et al. (2003) and promotion of creep at finer grain size (Yang et al., 2011).

Further, the volume fraction, morphology, and size distribution of γ' precipitates significantly influence the strengthening of these alloys. Yield strength at 650 $^\circ C$ and 1000 h creep rupture strength at 700 $^\circ C$ are strongly related to the sum of the fractions of the γ' phases (Reed, 2008). Hao et al. (2020) revealed that a high volume fraction, uniform size, and distribution of γ' precipitates significantly enhanced tensile strength and hardness. Wu et al. (2019a) observed that a higher volume fraction of fine γ' precipitates enhances yield strength and hardness, and the fine precipitates act as obstacles to dislocation movement, which provides strength. However, excessive coarsening due to high aging temperatures diminishes this effect, which leads to a decrease in yield strength and an increase in ductility. Wang et al. (2014a) observed that increasing the size and volume fraction of γ' precipitates of 718Plus alloy increases resistance to fatigue crack growth. Thus, optimal performance can be achieved by controlling the microstructure to balance strength, creep resistance, and fatigue life.

2.3 Objectives of the Present Work

Based on the literature review in the previous section, it is evident that the processing and heat treatment have a significant influence on the microstructure of Ni-based superalloys. Further, the resultant mechanical properties of both single and polycrystalline superalloys are intrinsically linked to the underlying microstructure. In order to accelerate the design of such alloys for engineering applications, appropriate modeling tools need to be developed. This lays the foundations of the present work. An integrated modeling framework which can predict the processing-dependent microstructure and the resultant mechanical properties is generally missing in the literature. While the former can be predicted using phase field models and the later using crystal plasticity models, their integration can combine the processing-microstructure-mechanical property predictions into one single framework. Towards this objective, this thesis aims to develop a coupled phase field-crystal plasticity framework for single crystal superalloys. Additionally, the objective of the thesis is to develop physically-based crystal plasticity constitutive models to predict the deformation of single crystal and polycrystalline Ni-based superalloys as a function of the microstructure and loading conditions, by accounting for the underlying deformation mechanisms. Specifically, the microstructural features of interest include the γ' precipitate size, shape, and volume fraction, and the crystallographic orientation.

Accordingly, the main objectives of this research work are summarized here, which have been addressed in the following chapters of the thesis:

- Development of a coupled phase field-crystal plasticity model to study the evolution of $\gamma^{'}$ precipitates during aging heat treatments and their effect on the ensuing mechanical properties of single crystal Ni-based superalloys.

- Development of a dislocation density-based crystal plasticity constitutive modeling framework for predicting the orientation- and temperature-dependent tensile and cyclic deformation of single crystal Ni-based superalloys.

- Development of a constitutive model for dislocation climb and microstructure evolution due to isotropic coarsening and rafting for predicting the creep deformation at elevated temperatures.

- Development of a physically-based crystal plasticity framework for modeling the tensile deformation of polycrystalline Ni-based superalloys, with consideration for the underlying microstructure comprised of primary, secondary and tertiary $\gamma^{'}$ precipitates.

- Prediction of the preferential damage initiation sites among the different microstructural features (annealing twin boundaries, phase interfaces, and grain boundaries) during tensile deformation.

- Development of a micromechanical constitutive model for precipitate shearing to predict cyclic softening during cyclic deformation of polycrystalline Ni-based superalloys.

- Prediction of FIPs and their correlation with the misorientation developments during cyclic deformation of polycrystalline Ni-based superalloys.

The broad objectives of this thesis are towards the development of modeling tools for the prediction of processing-microstructure-mechanical property correlations in Ni-based superalloys for potential use in microstructure-sensitive materials design applications as well as residual life assessment studies.

Chapter 3

Coupled Phase Field - Crystal Plasticity Model for Heat Treatment and Deformation of Single Crystal Ni-based Superalloys

3.1 Introduction

Single crystal nickel-based superalloys possess superior elevated temperature mechanical properties and performance as well as excellent microstructure stability (Geddes et al., 2010; Wei et al., 2022). This makes them amenable for use in high-temperature aerospace applications, such as gas turbine blades (Wei et al., 2022). The typical microstructure of single crystal superalloys is comprised of $\gamma^{'}$ precipitates in the γ matrix (Reed, 2008). The role of $\gamma^{'}$ precipitates is vital for excellent thermomechanical properties in these precipitation-strengthened superalloys. The size, shape, and volume fraction of these precipitates can be altered by heat treatment at different temperatures for varying durations. Thus, different heat treatments are commonly applied during the manufacturing of Ni-based superalloy components to achieve optimal microstructures and mechanical properties for specific applications (Lin et al., 2019).

---

[1]Significant parts of this chapter have been published in Chaudhary and Patra (2025).

27

In this regard, significant research has been performed to understand the influence of heat treatment on the microstructure and mechanical properties of Ni-based superalloys (Ai et al., 2020; Tan et al., 2021; Su et al., 2018). Wang et al. (2020) investigated the effect of cooling rate on the microstructure and tensile properties of single crystal Ni-based superalloys and revealed that as the cooling rate rises, the nucleation rate of the $\gamma^{'}$ precipitates increases, resulting in a larger number of smaller $\gamma^{'}$ precipitates. Some further investigations focus on the effect of the solution and aging heat treatments on the microstructure of Ni-based superalloys (Zhou et al., 2022; He et al., 2023). Solution treatment and aging are considered effective heat treatment methods to achieve the size, distribution, and morphology of $\gamma^{'}$ precipitates for desired mechanical properties (Li et al., 2015; He et al., 2023). Solution treatment helps to dissolve the pre-existing $\gamma^{'}$ precipitates. This leads to a microstructure with a supersaturated solid solution, which can be utilized for subsequent aging (Du et al., 2021). The desired size distribution and volume fraction of the $\gamma^{'}$ precipitates can be obtained by the aging process (Liu et al., 2021). Du et al. (2021) studied the effect of solution heat treatment on the creep properties and showed improvement in the creep life with increased solution treatment time. This was attributed to the enhanced microstructural homogenization and a more uniform $\gamma^{'}$ phase. However, excessive treatment time may lead to detrimental defects that promote stress concentration and dislocation shearing, ultimately reducing the creep resistance. While these experimental studies provide valuable insights, detailed parametric experimental studies are typically time and costly. Thus, it is essential to develop modeling frameworks that can study the microstructure evolution and its effect on the underlying mechanical properties for these alloys.

Phase field models have been widely used for simulating microstructural evolution in Ni-based superalloys, due to their ability to capture complex phase transformations, including precipitate growth and morphological changes. The phase field method has been used for accurately predicting the microstructure evolution of $\gamma^{'}$ precipitates in Ni–Al alloys during simple heat treatment processes (Wang et al., 1998; Attallah et al., 2016). Previously, phase field models have focused on understanding the effects of elastic and diffusional interactions on the morphological evolution of precipitates (Wang et al., 1998; Wen et al., 1999; Zhu et al., 2002). The phase field studies by (Lund and Voorhees, 2002; Vaithyanathan and Chen, 2002; Zhu et al., 2004) focus on the effect of elastic stresses on the coarsening kinetics of the Ni-Al system. These models have been advanced by correlating bulk free energies with thermodynamic databases (Grafe et al., 2000; Zhu et al., 2002) and both thermodynamic and mobility databases (Chen et al., 2004; Wu et al., 2004; Zhu et al., 2004). Gururajan and Abinandanan (2005) studied the microstructural

evolution in two-phase coherent solids by focusing on the role of elastic stresses arising from lattice parameter mismatch. Mukherjee et al. (2009) employed phase-field simulations to investigate the influence of elastic misfit strain and interfacial curvature on diffusion-controlled growth dynamics of a precipitate in a supersaturated matrix. Bhattacharyya and Abinandanan (2009) explored the influence of misfit strain anisotropy on microstructural evolution during the precipitation of an ordered β phase from a disordered α matrix using two-dimensional phase-field simulations. This study highlights the critical role of misfit anisotropy in determining precipitate morphology and spatial arrangement. Further, Chafle and Mukherjee (2020) studied the effect of elasticity on the coarsening of Ni-Al alloy using phase-field modeling. Ghosh et al. (2024) have re-parameterized the IN740H multicomponent Ni-based superalloy into a simplified ternary Ni-Al-Mo system using CALPHAD (CALculation of PHAse Diagram) to study the effect of molybdenum on the coarsening of precipitates. Generally speaking, the above models have not been used to simulate non-isothermal heat treatment processes in superalloys.

Wen et al. (2003) and Simmons et al. (2004) developed a 2D phase field model to study microstructural evolution during continuous cooling and were able to predict the development of a bimodal particle size distribution. Wen et al. (2006) developed a phase field model to predict the microstructure evolution under non-isothermal heat treatment processes. Further, the multiphase-field model introduced by Steinbach (Steinbach et al., 1996; Steinbach and Pezzolla, 1999; Steinbach, 2009) has been used for predicting microstructure evolution during alloy solidification processes. This modeling approach has been widely applied to superalloys, providing insights into phenomena such as dendritic growth (Warnken et al., 2009), $\gamma^{'}$ precipitation (Kundin et al., 2012; Mushongera et al., 2015), and rafting mechanisms (Zhou et al., 2007). In addition, Nestler et al. (2005); Nestler and Choudhury (2011) developed a multicomponent phase field model to simulate solidification and microstructure evolution in complex alloy systems. Further, microstructure evolution during solidification was studied in Warnken et al. (2009) and Cao et al. (2017) by coupling the phase field model with CALPHAD thermodynamic databases. Ta et al. (2014) performed quantitative 3D phase field simulations of binary Ni-Al alloys using the phase field models in MICRESS, coupled with CALPHAD databases, for analyzing the effects of alloy composition and aging temperature on the microstructure evolution. Lin et al. (2019) performed a quantitative simulation of microstructure evolution during the aging heat treatment, using the phase-field model, coupled with CALPHAD thermodynamic and atomic mobility databases, and also validated with the experimental studies. More recently, Bhure et al. (2025) provided thermal histories from melt pool modeling to a phase-field model to predict the primary dendrite arm spacing during solidification by

incorporating all the components of the CMSX-4 alloy. Thus, the phase field model, coupled with the accurate thermodynamic databases, has become an effective tool to simulate microstructure evolution during processing in Ni-based superalloys (Warnken et al., 2009; Milenkovic et al., 2012; Ta et al., 2014, 2015; Cao et al., 2017; Lin et al., 2019).

Meanwhile, crystal plasticity finite element frameworks have been developed to predict the anisotropic mechanical response as a function of the microstructure, thus allowing microstructure-mechanical property correlations in superalloys (Shenoy et al., 2005; Spanos et al., 2008; Rodas and Neu, 2018; Le Graverend, 2019; Guo et al., 2021; Ranjan et al., 2021; Chaudhary et al., 2022). While these are separate modeling techniques, phase field models, coupled with plasticity models (crystal plasticity or otherwise), can be used for the prediction of the microstructure evolution as well as mechanical properties within a single framework.

In this regard, several works have modeled plasticity at the scale of individual dislocations, which are incorporated into phase field models (Rodney and Finel, 2000; Wang et al., 2001; Koslowski et al., 2002; Zhou et al., 2007; Wu and Sandfeld, 2016a, 2017; Gao et al., 2019; Varma et al., 2023, 2024; Mann et al., 2024), drawing an analogy of dislocation loops and platelet precipitates with eigen strains. Plasticity in evolving microstructures has been extended to larger length scales through the use of mesoscale plasticity models that consider viscous rate effects and plastic anisotropy. Coupled phase field-mesoscale plasticity models have been developed for microstructure evolution during heat treatment (Wen et al., 2006; Rettig et al., 2015; Yang et al., 2021) and rafting (Gururajan and Abinandanan, 2007; Gaubert et al., 2008, 2010; Zhao et al., 2014; Harikrishnan and le Graverend, 2018; Wu et al., 2020; Yang et al., 2024; Wang et al., 2025b). Gaubert et al. (2010) coupled the phase field model with an elasto-viscoplastic model to study the microstructure evolution, specifically rafting, during creep deformation, by including elastic anisotropy and inhomogeneity. Cottura et al. (2012) incorporated strain gradient viscoplasticity into a phase field model to predict the rafting in Ni-based superalloys. Further, a dislocation density-based crystal plasticity model, coupled with the phase field model, was developed for diffusion-controlled transformations to enhance the prediction of microstructure evolution during diffusive phase transformations (Cottura et al., 2016). Further, (Wu et al., 2017, 2019b) used a coupled phase-field dislocation dynamics model to show the effect of $\gamma/\gamma^{'}$ precipitates on creep deformation of single crystal Ni-based superalloys. Wu and Sandfeld (2016a,b, 2017) also used a coupled phase-field/continuum dislocation dynamics model to study the effect of initial dislocation density and external stress on primary creep and dislocation-assisted rafting. Le Graverend and Harikrishnan (2019) performed tensile

deformation simulations using the crystal plasticity framework on cuboidal, rafted, and topologically inverted microstructures generated using 3D multiphase-field simulations. Le Graverend and Harikrishnan (2021) studied the effect of lattice strain using phase field and crystal plasticity to show that larger lattice misfits in cuboidal microstructures reduce the yield stress, strain hardening, and stress triaxiality. Further, Jogi et al. (2024) developed a phase field model incorporating both interfacial and elastic anisotropy to simulate dendritic and split γ' precipitates.

As can be seen, there are several coupled phase field-elasto-plasticity modeling studies that focus on the microstructure evolution during creep, i.e., rafting. However, literature studies that simulate the microstructure evolution during the processing/heat treatment, such as varying cooling rates, temperature gradients, or multi-step heat treatments using such coupled approaches, are relatively few. Also, the influence of thermal processing on the development of microstructural and deformation heterogeneity has not been extensively studied for superalloys. Additionally, rapid cooling during the heat treatment process results in the development of residual stresses that influence the mechanical properties of single-crystal Ni-based superalloys (Attallah et al., 2016). These stresses can either improve or degrade the material's performance, depending on their nature and distribution. A key challenge is to model these effects accurately to optimize the heat treatment processes for enhanced mechanical properties and performance via predictive modeling. The present work aims to address some of these issues.

A phase field model is developed and coupled with an existing dislocation density-based crystal plasticity model (Ranjan et al., 2021), to predict the microstructure evolution during the heat treatment of single crystal Ni-based superalloys and their resultant mechanical properties. Specifically, heat treatment simulations are performed for representative single crystal superalloy microstructures, with different initial compositions, to predict the effect of heat treatment temperature and time on the volume fraction and size of γ' precipitates. Model predictions are compared with available literature data. Further, representative heat treatment simulations are also performed for a commercial single crystal superalloy, CMSX-4, and its subsequent mechanical properties are predicted in terms of the temperature-dependent tension-compression asymmetry of yield behavior using the previously developed crystal plasticity model (Ranjan et al., 2021).

The broad objectives of this work are towards the development of an integrated modeling framework for the prediction of processing-microstructure-mechanical property correlations in single crystal Ni-based superalloys.

3.2 Model Description

An integrated phase field-crystal plasticity model has been developed to study the aging kinetics and microstructure evolution during heat treatment. The aging heat treatment is performed on a solutionized microstructure using the phase field model. Further, the crystal plasticity model is used for deformation simulations under tensile and compressive loading on the heat-treated microstructures to predict the temperature-dependent mechanical properties.

3.2.1 Phase Field Model

The phase field method has been extensively used for modeling microstructure evolution during solidification, dissolution, precipitation, and coarsening in various alloy systems (Steinbach, 2009). This method is based on the evolution of one or more non-conserved order parameters, which are used to represent the phase transformations in the system. The free energy of the system is generally formulated as a function of this order parameter, and any other chemical concentration or deformation energy-dependent terms, the total sum of which is minimized to solve for the evolution of phases for a given set of thermal/mechanical boundary conditions.

In the present case, a binary Ni-Al alloy system is assumed to represent the microstructure of single crystal Ni-based superalloys. This system is comprised of two phases: γ phase, which is a solid solution of aluminum in nickel, and $\gamma^{'}$ phase, which is an ordered phase with four distinct variants, determined by the position of Al atoms within the Ni_3Al unit cell (Wu et al., 2019b). The phase field formulation has been adapted from Qin and Bhadeshia (2009); Zhou et al. (2010), and is based on the Kim-Kim-Suzuki (KKS) model (Kim et al., 1999). The two-phase microstructure is described in terms of four continuous order parameters, $0 \leq \phi_i \leq 1, i \in (1,4)$, that evolve over space and time in this phase field model. Here, $\phi_i = 0$ represents the γ phase, $\phi_i = 1$ represents the ith-variant of the $\gamma^{'}$ phase, and $0 < \phi_i < 1$ represents either the $\gamma/\gamma^{'}$ interface or interfaces of the different $\gamma^{'}$ variants, such as an anti-phase boundary (APB) (Wu et al., 2017). A detailed description of the four variants of the ordered parameters is provided in Wu et al. (2017). Finally, the conserved variable, c, is used to represent the concentration of solute (Al) in the Ni system.

3.2.1.1 Evolution of the order parameter, ϕ_i

Evolution of the order parameter, ϕ_i, is adopted from Qin and Bhadeshia (Qin and Bhadeshia, 2009), where a phase field model was proposed to study the effect of interface anisotropy on the morphology of crystals for cubic crystals. The governing equation for the evolution of the phase field parameter is written as (Qin and Bhadeshia, 2009):

$$\frac{\partial \phi_i}{\partial t} = -L \left(\nabla . \left(|\nabla \phi_i|^2 \, \epsilon \, (\hat{n}) \, \frac{\partial \epsilon \, (\hat{n})}{\partial \nabla \phi_i} \right) + \nabla . \left(\epsilon \, (\hat{n})^2 \, \nabla \phi_i \right) + \frac{\partial F}{\partial \phi_i} \right) \tag{3.1}$$

where, L denotes the phase field mobility. $\epsilon(\hat{n})$ describes the interface anisotropy and is given as (Qin and Bhadeshia, 2009):

$$\epsilon \, (\hat{\boldsymbol{n}}) = \epsilon_0 \left(1 + \frac{\epsilon_1}{\epsilon_0} \left(n_x^2 n_y^2 + n_y^2 n_z^2 + n_z^2 n_x^2 \right) + \frac{\epsilon_2}{\epsilon_0} \left(n_x^2 n_y^2 n_z^2 \right) + \frac{\epsilon_3}{\epsilon_0} \left(n_x^2 n_y^2 + n_y^2 n_z^2 + n_z^2 n_x^2 \right)^2 \right) \tag{3.2}$$

where, ϵ_0, ϵ_1, ϵ_2, and ϵ_3 are anisotropy coefficients that control the morphology of the precipitates. $\epsilon_0 = \sqrt{\frac{3\eta k_0}{2.2}}$ is adopted from Qin and Bhadeshia (Qin and Bhadeshia, 2009), where η is the interface width and k_0 is a coefficient related to ϵ_0. $\boldsymbol{n}$ is the interface normal vector, which is of the form:

$$\boldsymbol{n} = \frac{\nabla \phi_i}{|\nabla \phi_i|} \tag{3.3}$$

Thus, $n_j = \frac{\psi_j}{\sqrt{\sum_j \psi_j^2}}$, where $\psi_j = \partial \phi_i / \partial x_j$.

The total free energy functional, F, includes contributions from the chemical, f_{chem}, bulk, f_{bulk}, and deformation energy, f_{def}, integrated over the volume domain Ω, i.e.,

$$F = \int_{\Omega} \left(f_{chem} + f_{bulk} + f_{def} \right) dV \tag{3.4}$$

The chemical free energy for the two-phase material is given as:

$$f_{chem} = \frac{1}{V_m} \left((1 - h \, (\phi_i)) \, f_{\gamma} + h \, (\phi_i) \, f_{\gamma'} \right) \tag{3.5}$$

where, V_m is the molar volume and $h(\phi_i)$ is an interpolation function described later. Further, f_{γ} and $f_{\gamma'}$ are the equilibrium chemical free energies of γ and γ', respectively. These are approximated by two parabolic functions as (Zhou et al., 2010):

$$f_{\gamma} = (f_0)_{\gamma} \left(c_{\gamma} - c_{\gamma}^e \right)^2 \tag{3.6}$$

$$f_{\gamma'} = (f_0)_{\gamma'} \left(c_{\gamma'} - c_{\gamma'}^e \right)^2 \tag{3.7}$$

where, $(f_0)_\gamma$ and $(f_0)_{\gamma'}$ are representative of the second derivative of the chemical free energy near the equilibrium concentration of γ and γ' phases, respectively. c_γ and $c_{\gamma'}$ are the concentrations of Al in the γ and γ' phases, respectively, and c_γ^e and $c_{\gamma'}^e$ are the equilibrium concentrations of Al in the respective phases. The local composition, c, is calculated as (Zhou et al., 2010):

$$c = \left((1 - h(\phi_i)) c_\gamma + h(\phi_i) c_{\gamma'} \right) \tag{3.8}$$

The condition, $df_\gamma/dc_\gamma = df_{\gamma'}/dc_{\gamma'}$ needs to be satisfied for local equilibrium between the two phases, which leads to $c_{\gamma'} = c_\gamma + (c_{\gamma'}^e - c_\gamma^e)$ (Zhou et al., 2010). In these equations, the interpolation function, $h(\phi_i)$, is given as (Zhu et al., 2004):

$$h(\phi_i) = \sum_{i=1}^{4} \left[\phi_i^3 (6\phi_i^2 - 15\phi_i + 10) \right] \tag{3.9}$$

Here, $h(\phi_i)$ is a switching function used to distinguish between the γ and γ' phases. $h(\phi_i) = 0$ for γ phase, $h(\phi_i) = 1$ for γ' phase, while in the interfacial regions of this diffuse interface model, $h(\phi_i)$ may have values between 0 and 1.

Further, the bulk free energy is given as (Zhou et al., 2010):

$$f_{bulk} = \omega \left(\sum_{i=1}^{4} \phi_i^2 (1 - \phi_i)^2 + \theta \sum_{i=1}^{4} \sum_{j \neq i}^{4} \phi_i^2 \phi_j^2 \right) \tag{3.10}$$

where, ω is a coefficient related to the γ/γ' interface energy and width, and θ is a parameter associated with the APB energy.

Energy dissipation due to the elastic and inelastic work is represented by:

$$f_{def} = (1 - h(\phi_i)) \left(\frac{1}{2} (\boldsymbol{\sigma} : \boldsymbol{E})_\gamma \right) + h(\phi_i) \left(\frac{1}{2} (\boldsymbol{\sigma} : \boldsymbol{E})_{\gamma'} \right) \tag{3.11}$$

where, $\boldsymbol{\sigma}$ is the Cauchy stress, and $\boldsymbol{E}$ is the strain due to elastic and inelastic deformation, represented by $\boldsymbol{E} = \boldsymbol{E}^t - \boldsymbol{E}^m$. Here, $\boldsymbol{E}^t$ is the total strain. The misfit strain due to lattice misfit between the two phases, $\boldsymbol{E}^m$, is calculated as:

$$\boldsymbol{E}^m = (1 - h(\phi_i)) \left(\frac{2 \left(a_{\gamma'} - a_\gamma \right)}{\left(a_{\gamma'} + a_\gamma \right)} \right) \boldsymbol{I} + h(\phi_i) \left(\frac{2 \left(a_\gamma - a_{\gamma'} \right)}{\left(a_{\gamma'} + a_\gamma \right)} \right) \boldsymbol{I} \tag{3.12}$$

where, a_γ and $a_{\gamma'}$ represents the lattice parameters of γ and γ' phase, respectively. The stresses and strains are available from the mesoscale deformation model, which is described

in Section 3.2.2.

3.2.1.2 Evolution of Al concentration, c

Minimization of system's free free energy serves as the driving force for the evolution of the conserved variable, c, which represents the concentration of Al in the Ni-Al binary solid solution. The Cahn-Hilliard equation for the same is given as Cahn (1962),

$$\frac{\partial c}{\partial t} = \nabla \cdot M \nabla \frac{\partial F}{\partial c} \tag{3.13}$$

where M is the chemical mobility.

3.2.2 Crystal Plasticity Framework

The crystal plasticity framework is adapted from Ranjan et al. Ranjan et al. (2021), where it was used to predict the temperature-dependent, anisotropic mechanical properties of single crystal superalloys. In this framework, the finite deformation gradient, $\boldsymbol{F}$, is multiplicatively decomposed into the elastic, $\boldsymbol{F}^e$, inelastic, $\boldsymbol{F}^i$, and misfit, $\boldsymbol{F}^m$, parts Musinski and McDowell (2015), i.e.,

$$\boldsymbol{F} = \boldsymbol{F}^e \cdot \boldsymbol{F}^i \cdot \boldsymbol{F}^m \tag{3.14}$$

where, $\boldsymbol{F}^e$ accounts for the elastic deformation and rigid rotation, $\boldsymbol{F}^i$ accounts for the shear due to inelastic deformation, and $\boldsymbol{F}^m$ accounts for the deformation due to misfit strain. $\boldsymbol{F}^e$ is related to the elastic Green strain tensor, $\boldsymbol{E}^e$, as, $\boldsymbol{E}^e = (1/2)(\boldsymbol{F}^{eT} \cdot \boldsymbol{F}^e - \boldsymbol{I})$, which is further related to Piola–Kirchhoff stress, $\boldsymbol{S} = \boldsymbol{C}_{eff} : \boldsymbol{E}^e$, where $\boldsymbol{C}_{eff}$ is effective elasticity tensor and is given as (Ranjan et al., 2021):

$$C_{eff}{}^{ijkl} = \left((1 - \phi) \, C_m{}^{ijkl-1} + \phi C_p{}^{ijkl-1} \right)^{-1} \tag{3.15}$$

where, $\boldsymbol{C_m}$ and $\boldsymbol{C_p}$ represent the anisotropic fourth order elasticity tensors of the matrix phase, γ, and the precipitate phase, $\gamma^{'}$, respectively. $\phi = \sum_i \phi_i$ is obtained from the phase field model and is used to distinguish between the two phases and the interfacial regions. The second Piola-Kirchoff stress tensor, $\boldsymbol{S}$, is obtained as: $\boldsymbol{S} = \boldsymbol{C_{eff}} : \boldsymbol{E^e}$. In the current configuration, the Cauchy stress, $\boldsymbol{\sigma}$ is related to $\boldsymbol{S}$ as: $\boldsymbol{S} = det(\boldsymbol{F}^e)\boldsymbol{F}^{e^{-1}} \cdot \boldsymbol{\sigma} \cdot \boldsymbol{F}^{e^{-T}}$.

$\boldsymbol{F}^i$ is related to the inelastic velocity gradient, $\boldsymbol{L}^i$ as, $\dot{\boldsymbol{F}}^i = \boldsymbol{L}^i \cdot \boldsymbol{F}^i$. Further, $\boldsymbol{L}^i$ is the tensor sum of the crystallographic shearing rate over all possible slip systems and given as:

$$\boldsymbol{L}^i = (1 - \phi) \sum_{\alpha=1}^{N_s} \dot{\gamma}^\alpha \boldsymbol{s}_0^\alpha \otimes \boldsymbol{m}_0^\alpha + \phi \sum_{\beta=1}^{N_p} \dot{\gamma}^\beta \boldsymbol{s}_0^\beta \otimes \boldsymbol{m}_0^\beta \tag{3.16}$$

Here, $\boldsymbol{s}_0^\zeta$ and $\boldsymbol{m}_0^\zeta$ represent the unit vectors along the slip and slip plane normal directions for slip system, ζ, in the reference configuration, respectively. Further, N_s and N_p represent the total number of slip systems in the γ and γ' phase, respectively. We have considered twelve octahedral $\{111\} < 110 >$ slip systems in the γ phase and twenty four octahedral $\{111\} < 110 >$ slip systems (considering forward and backward directions), along with six cube $\{100\} < 110 >$ slip systems, in the γ' phase. The cube slip systems are expected to be activated at higher temperatures. Note that while Ranjan et al. Ranjan et al. (2021) considered the deformation of the homogenized crystal, comprised of the γ and γ' phases, we have explicitly considered the deformation of the individual phases in the present work.

The constitutive equations for the temperature-dependent flow rule, dislocation strengthening and dislocation density evolution are adopted from Ranjan et al. (2021). The crystallographic shearing rate, $\dot{\gamma}^\alpha$, on slip system α is modeled using a Kocks-type thermally activated flow rule (Equation 3.17) (Kocks et al., 1975). Crystallographic shearing rate due to the dislocation glide is given as,

$$\dot{\gamma}_j^\alpha = \begin{cases} \dot{\gamma}_{0j}^\alpha exp\left[-\frac{\Delta F_j^\alpha}{kT}\left(1 - \left(\frac{|\tau_j^\alpha - \chi_j^\alpha| - s_{aj}^\alpha}{s_{tj}^\alpha}\right)^{p_j^\alpha}\right)^{q_j^\alpha}\right] sgn\left(\tau_j^\alpha\right); \left|\tau_j^\alpha\right| > s_{aj}^\alpha, \alpha \in \text{oct}, j \in \gamma \\ \\ \dot{\gamma}_{0j}^\alpha exp\left[-\frac{\Delta F_j^\alpha}{kT}\left(1 - \left(\frac{(\tau_j^\alpha) - s_{aj}^\alpha}{s_{tj}^\alpha}\right)^{p_j^\alpha}\right)^{q_j^\alpha}\right]; \tau_j^\alpha > s_{aj}^\alpha, \alpha \in \text{oct}, j \in \gamma' \\ \\ \dot{\gamma}_{0j}^\alpha exp\left[-\frac{\Delta F_{gj}^\alpha}{kT}\left(1 - \left(\frac{|\tau_j^\alpha - \chi_j^\alpha| - s_{aj}^\alpha}{s_{tj}^\alpha}\right)^{p_j^\alpha}\right)^{q_j^\alpha}\right] sgn\left(\tau_j^\alpha\right); \left|\tau_j^\alpha\right| > s_{aj}^\alpha, \alpha \in \text{cube}, j \in \gamma' \\ \\ 0; \text{ otherwise} \end{cases} \tag{3.17}$$

where, $\dot{\gamma}_{0j}^\alpha$ is the reference strain rate, ΔF_j^α is the activation energy for dislocation glide, k is the Boltzmann constant, T is the absolute temperature, τ_j^α is the driving stress for dislocation glide, s_{aj}^α is the athermal slip resistance, s_{tj}^α is the thermal slip resistance, and

p_j^α and q_j^α are shape parameters for the activation energy curve. Here, octahedral slip in the γ and the γ' phases is represented as $\alpha \in \text{oct}, j \in \gamma$ and $\alpha \in \text{oct}, j \in \gamma'$, respectively, while cube slip in the γ' phase is represented as $\alpha \in \text{cube}, j \in \gamma'$.

The driving stress for dislocation glide depends on the resolved shear stress, which includes both Schmid and non-Schmid contributions, depending on the type of slip system (Equation 3.18). Further, driving stress for dislocation glide is given as,

$$\tau_j^\alpha = \begin{cases} \boldsymbol{s}^\alpha \cdot \boldsymbol{\sigma} \cdot \boldsymbol{m}^\alpha; \alpha \in \text{oct}, j \in \gamma \\\\ \boldsymbol{s}^\alpha \cdot \boldsymbol{\sigma} \cdot \boldsymbol{m}^\alpha + \left(a_1 \boldsymbol{s}_{pe}^\alpha \cdot \boldsymbol{\sigma} \cdot \boldsymbol{m}_{pe}^\alpha + a_2 \boldsymbol{s}_{se}^\alpha \cdot \boldsymbol{\sigma} \cdot \boldsymbol{m}_{se}^\alpha \\\ +a_3 \boldsymbol{s}_{cb}^\alpha \cdot \boldsymbol{\sigma} \cdot \boldsymbol{m}_{cb}^\alpha \right) exp\left(-\frac{\epsilon_p^i}{\epsilon_o^i}\right); \alpha \in \text{oct}, j \in \gamma' \\\\ \boldsymbol{s}^\alpha \cdot \boldsymbol{\sigma} \cdot \boldsymbol{m}^\alpha; \alpha \in \text{cube}, j \in \gamma' \end{cases} \tag{3.18}$$

where, $\boldsymbol{s}^\alpha$ and $\boldsymbol{m}^\alpha$ are the slip and slip plane normal directions, respectively. $\left(\boldsymbol{s}_{pe}^\alpha, \boldsymbol{m}_{pe}^\alpha\right)$, $(\boldsymbol{s}_{se}^\alpha, \boldsymbol{m}_{se}^\alpha)$ and $(\boldsymbol{s}_{cb}^\alpha, \boldsymbol{m}_{cb}^\alpha)$ are unit vectors along the slip and slip plane normal directions associated with the primary edge, secondary edge, and cube planes, respectively, ϵ_p^i is the effective inelastic strain in the precipitate phase and ϵ_o^i is a material constant.

The athermal slip resistance, s_a^α (Equation 3.19), represents the resistance to dislocation glide from long-range stress fields and has contributions from the Hall–Petch effect and dislocation-based Taylor hardening. The contribution of each deformation mechanism is determined by the phase and the specific type of slip system. The thermal slip resistance, s_t^α (Equation 3.20), represents the ability of dislocations to overcome short-range stresses through thermal vibrations. The athermal, s_{aj}^α, and thermal, s_{tj}^α, slip resistances is are written as:

$$s_{aj}^\alpha = \tau_{th}^\alpha + k_{\rho j} G_j b_j \sqrt{\left(\sum_{\xi=1}^{N_m} A^{\alpha\xi} \rho_j^\xi\right)}; \alpha \in \text{oct,cube}, j \in \gamma, \gamma' \tag{3.19}$$

$$s_{tj}^\alpha = \tau_{0j}^\alpha; \alpha \in \text{oct,cube}, j \in \gamma, \gamma' \tag{3.20}$$

where, τ_{th}^α is the threshold resistance, G_j is the shear modulus, b_j is the Burgers vector magnitude, $k_{\rho j}$ is the dislocation barrier strength, $A^{\alpha\xi}$ is the matrix of slip system dislocation interaction coefficients, and ρ^ξ is the dislocation density on the slip system ξ.

The dislocation density is given as the sum of the mobile, ρ_{Mj}^ξ, and immobile, ρ_{Ij}^ξ, dislocation densities, i.e., $\rho_j^\xi = \rho_{Mj}^\xi + \rho_{Ij}^\xi$. Further, the rates of evolution of the mobile and

immobile dislocation densities are given as:

$$\dot{\rho}_{Mj}^{\alpha} = \frac{k_{mj}^{\alpha}}{b_j \lambda_j^{\alpha}} \left| \dot{\gamma}_j^{\alpha} \right| - \frac{2R_c}{b_j} \rho_{Mj}^{\alpha} \left| \dot{\gamma}^{\alpha} \right| - \frac{k_{tj}^{\alpha}}{b_j \lambda_j^{\alpha}} \left| \dot{\gamma}_j^{\alpha} \right|; \alpha \in \text{oct,cube}, j \in \gamma, \gamma' \tag{3.21}$$

$$\dot{\rho}_{Ij}^{\alpha} = \frac{k_{tj}^{\alpha}}{b_j \lambda_j^{\alpha}} \left| \dot{\gamma}_j^{\alpha} \right| - k_{dj}^{\alpha} \rho_{Ij}^{\alpha} \left| \dot{\gamma}_j^{\alpha} \right|; \alpha \in \text{oct,cube}, j \in \gamma, \gamma' \tag{3.22}$$

where, k_{mj}^{α} is the material parameter associated with dislocation multiplication at pre-existing segments, R_c is the critical capture radius for annihilation of dislocation dipoles, k_{tj}^{α} is the material parameter associated with trapping of mobile dislocations at barriers, and k_{dj}^{α} is the material parameter associated with dynamic recovery of immobile dislocations. The effective mean free path is given as,

$$\frac{1}{\lambda^{\alpha}} = \begin{cases} \sqrt{\rho_j} + \frac{1}{\bar{w}}; \alpha \in \text{oct}, j \in \gamma \\ \\ \sqrt{\rho_j}; \alpha \in \text{oct,cube}, j \in \gamma' \end{cases} \tag{3.23}$$

where, $\bar{w}$ is the channel width. The reader is referred to Ranjan et al. Ranjan et al. (2021) for a detailed description of these models.

The integrated phase field-crystal plasticity model has been implemented in the form of two separate material models, with the phase field variables and displacements as degrees of freedom, in the open-source finite element solver, Multiphysics Object Oriented Simulation Environment (MOOSE) (Permann et al., 2020). The Kim-Kim-Suzuki (KKS) model (Kim et al., 1999) is already implemented in the MOOSE framework (Schwen et al., 2021). Additionally, we have implemented the interfacial anisotropy model Qin and Bhadeshia (2009) as given in Equations 3.1, 3.2, and 3.3. The crystal plasticity model distinguishes between the two phases using the phase field variable, $\phi = \sum_i \phi_i$, while the phase field model minimizes the total free energy using the contribution from the deformation, f_{def}, obtained from the crystal plasticity model. Both these models are allowed to operate concurrently during the heat treatment simulations, while only the crystal plasticity model is utilized during the post-heat treatment deformation simulations. Further, it will be shown later from our model predictions that the effect of plasticity on the microstructure evolution during aging is negligible. Subsequent to this verification, inelastic deformation has been artificially disabled by setting a very high critical resolved shear stress on all slip systems, thus allowing only anisotropic elastic deformation in the crystal plasticity model during aging. This leads to a significant reduction in computational costs for our simulations.

In the present framework, the temperature, T, is varied uniformly in the entire simulation domain and there is no consideration for heat transfer (conduction, convection, etc.) or associated temperature gradients. This is a reasonable assumption given the relatively small sizes of the simulation domains considered. The thermodynamic free energies, equilibrium concentrations, lattice parameters in the phase field model and the strengthening parameters in the crystal plasticity vary as a function of temperature, T. In future work, the framework may be easily coupled with the existing heat conduction and convection modules in MOOSE for simulating thermal gradients in larger microstructures, for example, to simulate dendritic microstructures.

3.2.2.1 Model Parameters

In the later sections, the application of the model has been demonstrated for two different alloy systems, a commercial single crystal superalloy, CMSX-4, and a binary Ni-Al alloy, with (5.9-6.96 wt.%Al) concentrations. The chemical composition of the CMSX-4 is given in Table 3.1. Table 3.2 lists the phase field parameters that are the same for both alloys,

TABLE 3.1: Chemical composition of CMSX-4 (in wt. %) (Reed, 2008).

Alloy	Cr	Co	Mo	W	Al	Ti	Ta	Re	Hf	Ni
CMSX-4	6.5	9.6	0.6	6.4	5.6	1.0	6.5	3.0	0.1	Bal.

while Table 3.3 lists the phase field parameters that are different for the two alloy systems.

The coefficient related to the $\gamma/\gamma^{'}$ interface energy and width, ω, has been used as a calibration parameter. Further, Zhou et al. (Zhou et al., 2010) showed that the parameter, $\theta = 10$, in the bulk free energy term, ensures that the APB energy is greater than twice the $\gamma/\gamma^{'}$ interfacial energy, thus preventing the coalescence of $\gamma^{'}$ domains. The coefficient related to interface anisotropic coefficient, k_0, and the other interface anisotropic coefficients (ϵ_1/ϵ_0, ϵ_2/ϵ_0 and ϵ_3/ϵ_0), control the morphology of the precipitates. We have calibrated these parameters to predict a cuboidal precipitate morphology during aging. The temperature-dependent lattice parameters for γ and $\gamma^{'}$ phases are adopted from Huang et al. (Huang et al., 2018). The chemical mobility is assumed to be constant and adopted from Wu et al. Wu et al. (2019b).

In our simulations, the interface width is set to be equal to the initial size of the precipitates. Further, the temperature-dependent second derivative of the chemical free energy near equilibrium composition, molar volume, and equilibrium concentration of Al in γ and $\gamma^{'}$ are adopted from Ardell Ardell (2021), where representative values have been given

for binary Ni-Al alloys. The Gibbs free energy coefficients for CMSX-4 are taken from Tsukada et al. (Tsukada et al., 2011). The equilibrium concentration of Al in γ and γ' phases for CMSX-4, $c_\gamma^e = 0.0711$ at.% and $c_{\gamma'}^e = 0.1664$ at.% are taken from Kundin et al. Kundin et al. (2012). As a first-order approximation, the Gibbs free energy and equilibrium concentrations for CMSX-4 are assumed to remain constant over the temperature ranges considered in this study.

TABLE 3.2: Phase field model parameters common for both CMSX-4 and Ni-Al alloy.

Parameter	Value
Coefficient related to interface energy and width, ω	$4 \times 10^7 \text{J/m}^3$
Coefficient related to APB energy, θ	10
Interfacial anisotropy coefficients, ϵ_1/ϵ_0, ϵ_2/ϵ_0, ϵ_3/ϵ_0	5, 1, 1
Lattice parameter of γ, a_γ	$4.569790585487995 \times 10^{-8}T^2 - 1.09660104402762 \times 10^{-5}T + 3.592354535180594$Å
Lattice parameter of γ', $a_{\gamma'}$	$2.862103961503188 \times 10^{-8}T^2 + 1.370720453370645 \times 10^{-5}T + 3.583046315245131$Å
Chemical mobility, M	$1.5 \times 10^{-26} \text{m}^5/\text{Js}$

TABLE 3.3: Phase field model parameters that are distinct for CMSX-4 and Ni-Al alloy.

Parameter	CMSX-4	Ni-Al
Interface width, η	60nm	5nm
Coefficient related to interfacial anisotropy, k_0	0.123J/m^2	$5.010 \times 10^{-3} \text{J/m}^2$
Molar volume, V_m	–	$3.1836 \times 10^{-10}T + 6.7487 \times 10^{-6} \text{m}^3/\text{mol}$
Coefficient related to free energy of γ phase, $(f_0)_\gamma$	$2.58 \times 10^8 \text{J/m}^3$	$-6.8338 \times 10^{-5}T^2 + 0.2127T + 203.3014 \text{kJ/mol}$
Coefficient related to free energy of γ' phase, $(f_0)_{\gamma'}$	$3.11 \times 10^8 \text{J/m}^3$	$-6.8338 \times 10^{-5}T^2 + 0.2127T + 203.3014 \text{kJ/mol}$
Equilibrium concentration of Al in γ phase, c_γ^e	0.0711 at.%	$0.055027exp(8.124 \times 10^{-4}T)$ at.%
Equilibrium concentration of Al in γ' phase: $c_{\gamma'}^e$	0.1664 at.%	$-1.505 \times 10^{-13}T^4 + 7.444 \times 10^{-10}T^3 - 1.313 \times 10^{-6}T^2 + 9.653 \times 10^{-4}T - 0.02008$ at.%

The crystal plasticity framework has been used previously to predict the non-Schmid yield behavior of Ni_3Al crystal and CMSX-4, single crystal Ni-based superalloys in the temperature range 260–1304 K Ranjan et al. (2021). The associated temperature-dependent single crystal elastic constants are given in Table 3.4 and the crystal plasticity model parameters for CMSX-4 are given in Table 3.5. Note that the crystal plasticity parameters are directly taken from Ranjan et al. (2021).

In addition, $\tau_{0,oct}^\alpha$ is calibrated to fit the experimental data of the tension-compression asymmetry of CMSX-4, given as:

TABLE 3.4: Temperature-dependent elastic constants for the γ and γ' phases (Keshavarz et al., 2016).

Parameter	Value
γ	$C_{11} = (298.0 - 0.096T)\,\text{GPa}$
	$C_{12} = (191.0 - 0.057T)\,\text{GPa}$
	$C_{44} = (139.0 - 0.035T)\,\text{GPa}$
γ'	$C_{11} = (325.0 - 0.096T)\,\text{GPa}$
	$C_{12} = (209.0 - 0.057T)\,\text{GPa}$
	$C_{44} = (144.0 - 0.035T)\,\text{GPa}$

TABLE 3.5: Crystal plasticity model parameters for the γ and γ' phases adopted from Ranjan et al. (2021).

Parameters	$\alpha \in$ oct, $j \in$ m (γ)	$\alpha \in$ oct, $j \in$ p $\left(\gamma'\right)$	$\alpha \in$ cube, $j \in$ p $\left(\gamma'\right)$
Glide flow rule: $\dot{\gamma}_{0j}\,(\text{s}^{-1})$, ΔF_j^α, p_j^α, q_j^α	1×10^2, $0.35Gb^3$, 0.3, 1.7	1, $1.5Gb^3$, 0.3, 1.7	1×10^{-2}, $4.5Gb^3$, 1, 1
Dislocation hardening: $k_{\rho j}^\alpha$, $A^{\alpha\alpha}$, $A^{\alpha\zeta}$	0.31, 1, 1×10^{-4}	0.31, 1, 1×10^{-4}	0.31, 1, 1×10^{-4}
Initial dislocation densities: $\rho_M^0\,(\text{m}^{-2})$ $\rho_I^0\,(\text{m}^{-2})$	1×10^{11}, 1×10^{11}	1×10^{10}, 1×10^{10}	1×10^{10}, 1×10^{10}
Dislocation evolution: k_{mj}^α, R_c, k_{tj}^α, k_{dj}^α	0.15, 6b, 0.12, 1000	0.07, 6b, 0.065, 600	0.07, 6b, 0.065, 6
Thermal slip resistance: s_{tj}^α (MPa)	10	5	5
Burgers vector magnitude: b (nm)	0.249	0.249	0.249

$$\tau_{0,j}^\alpha(\text{MPa}) = \begin{cases} 4.409 \times 10^2 + 7.095 \times 10^{-2}T - 3.817 \times 10^{-5}T^2; T \leq 923\text{K}; \\ 5.961 \times 10^4 - 1.698 \times 10^2 T + 1.642 \times 10^{-1}T^2 - 5.297 \times 10^{-5}T^3; T > 923\text{K} \end{cases} \quad ; \alpha \in \text{oct}, j \in \gamma$$

(3.24)

3.3 Model Predictions

The model is used to predict the microstructure evolution in single crystal superalloys subjected to aging heat treatments.

Three different case studies have been simulated to demonstrate the model's predictive capabilities.

- The first case study involves 2D and 3D simulations of two-stage aging heat treatment of a commercial single crystal superalloy, CMSX-4, followed by prediction of the tension-compression asymmetry during quasi-static mechanical loading of the heat-treated microstructure. Model predictions of precipitate size evolution are compared with the experimental data from Sengupta et al. (1994), while the predicted mechanical properties are compared with the experimental data from Allan (1995). Both 2D and 3D simulations are performed and their equivalence is demonstrated.

- The second case study involves 2D simulations of coarsening in larger microstructures of CMSX-4 during isothermal aging at 1223 K. Model predictions of the precipitate size and volume fraction evolution are compared with the experimental data from Lapin et al. (2009). Further, the effect of varying the cooling rate on the microstructure evolution is also demonstrated.

- The third case study involves 2D simulations of short term aging of a Ni-Al system with composition in the range (12-14 at.%Al) in the temperature range 823-988 K. Experimental data from Plotnikov et al. (2014) and Ardell (1968) have been used to compare model predictions of the precipitate size evolution as a function of the aging time.

3.3.1   Case Study I

3.3.1.1   Prediction of Precipitation Kinetics for CMSX-4

In this case study, the model is used to predict the microstructure evolution subjected to high temperature aging at 1353 K for 4 h, followed by air cooling, and then followed by aging at 1144 K for 20 h. This heat treatment regime is schematically shown in Figure 3.1(a) and is commonly used for CMSX-4 (Sengupta et al., 1994). As reported in Sengupta et al. (1994), this aging heat treatment, after the solution treatment (which has not been simulated), for CMSX-4 leads to an average γ' precipitate average size of 0.3 μm, with cube shape. In the phase field model, the temperature dependence of the mobility parameter, L, has been calibrated by predicting the response for this heat treatment. Here, L is the parameter which has been calibrated to predict the microstructure evolution for the heat treatments in case studies I and II. Specifically, L has been calibrated for the simulation

at 1143 K and 1353 K for heat treatment of case study I and 1223 K isothermal heat treatment for case study II. The calibrated value of the mobility parameter was then fit to an Arrhenius equation of the following form:

$$L = 6.324 \times 10^{-3} exp\left(-\frac{3.9025 \times 10^{-19}}{kT}\right) \text{m}^3\text{J}^{-1}\text{s}^{-1}; 1144\text{K} \leq T \leq 1353\text{K} \qquad (3.25)$$

where, T is the absolute temperature and k is the Boltzmann constant. The calibrated value of the phase-field mobility parameter, L, is plotted as a function of temperature in Figure 3.1(b).
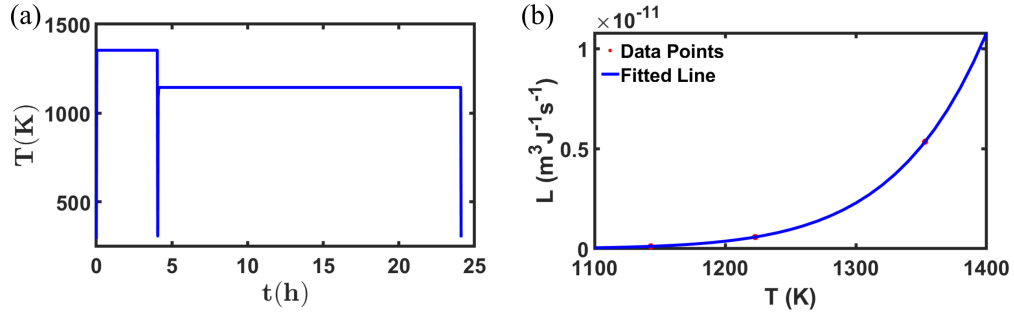
FIGURE 3.1: (a) Schematic of the aging heat treatment, as also used by Sengupta et al. (1994), for CMSX-4. (b) Calibrated value of the phase field mobility, L, as a function of temperature, T, along with the fit to the Arrhenius equation.

2D and 3D simulation domains of $0.75 \times 0.75 \mu$m and $0.75 \times 0.75 \times 0.75 \mu$m were used, considering the "expected" final volume fraction and size of the precipitates. Note that simulations with different domain sizes have been performed in the subsequent case studies to verify that the evolution of precipitate size/volume fraction is not domain size dependent. For the present case study, the simulation domain was meshed using either 2D square-shaped or 3D hexahedral elements, with linear interpolation, and an element size of 0.0375 μm. The two-phase misconstrue is represented by four order parameters, ϕ_i due to which a minimum of four γ' nuclei are required to model the γ/γ' interface or the antiphase boundaries. Thus, Four γ' nuclei in the 2D domain, and eight γ' nuclei in the 3D domain, were instantiated with [001] crystallographic orientation with an initial radius of 0.03 μm and an interface width of 0.06 μm. Note that while MOOSE allows for mesh adaptivity, we have not used the same in our simulations for computational efficiency. Different sets of simulations have been performed, considering only elasticity and considering both elasticity and crystal plasticity in the 2D and 3D domains. Periodic boundary conditions were applied to all the faces of the cube, while the bottom left corner was fixed in all degrees of freedom to prevent rigid body motion.

Figure 3.2 shows the aged microstructure, in terms of the phase field variable, c_{Al}(at.%), after heat treatment for 25 h for the different (a,b) 2D, and (c,d, e,f) 3D simulations, with and without plasticity. Note that elasticity has been considered in all the simulations. While the final microstructure after heat treatment has been shown in Figure 3.2, the evolution of the microstructure in the 2D simulation (with plasticity) at intermediate time steps is shown in Figure 3.3 after (a) 0.1 h, (b) 0.5 h, (c) 1 h and (d) 5 h. The different 2D and 3D simulations result in similar precipitate evolution characteristics as in Figure 3.3 and hence they are not shown separately.

These results show the evolution of precipitates to the cuboidal shape from the initial circular/spherical nuclei. $\gamma^{'}$ precipitates start to grow from smaller nuclei during aging. During aging, the precipitate growth is generally governed by the minimization of the free energy of the system. As $\gamma^{'}$ precipitates grow, they tend to adopt more stable morphologies, evolving from circular/spherical to square/cuboidal shapes, thus lowering the surface energy associated with the interfaces (Ardell, 1968). Here, the free energy of the system and the equilibrium concentration depend on the heat treatment temperature. Thus, the precipitation kinetics are also expected to be affected by the heat treatment temperature.

As can be seen from Figure 3.2, the predictions of the precipitate shape, with and without plasticity, are almost the same from both 2D and 3D simulations. This is because only hydrostatic stresses develop due to the misfit strains during aging (Luo et al., 2022). Since the deviatoric stress components are absent, no plastic deformation occurs in these microstructures. Given this observation, all subsequent simulations presented here are performed only with elasticity, and without crystal plasticity, to save computational costs. Crystal plasticity simulations are generally more computationally intensive due to the iterative decomposition of the total deformation gradient into the elastic and inelastic parts, and the associated matrix inversions (cf. Patra et al. (2023)). Nonetheless, anisotropic crystalline elasticity is considered in all simulations.

It can be seen from Figure 3.3(a-d) that the size of the precipitates increases with aging time, increasing from an initial size of 60 nm to 300 nm. It is worth noting that the precipitate size saturates to 300 nm within the initial 5 h of aging, along with a saturation in the volume fraction. This is also evident from the line plots in Figure 3.3 (e,f), which show the evolution of the precipitate size and the volume fraction as a function of aging time, respectively, from the different 2D and 3D simulations. There is no experimental result to directly validate this predicted trend. The predicted size of the precipitates at the end of the heat treatment is comparable with the experimental observations reported by Sengupta et al. (1994), where the precipitate size after heat treatment was measured to be around
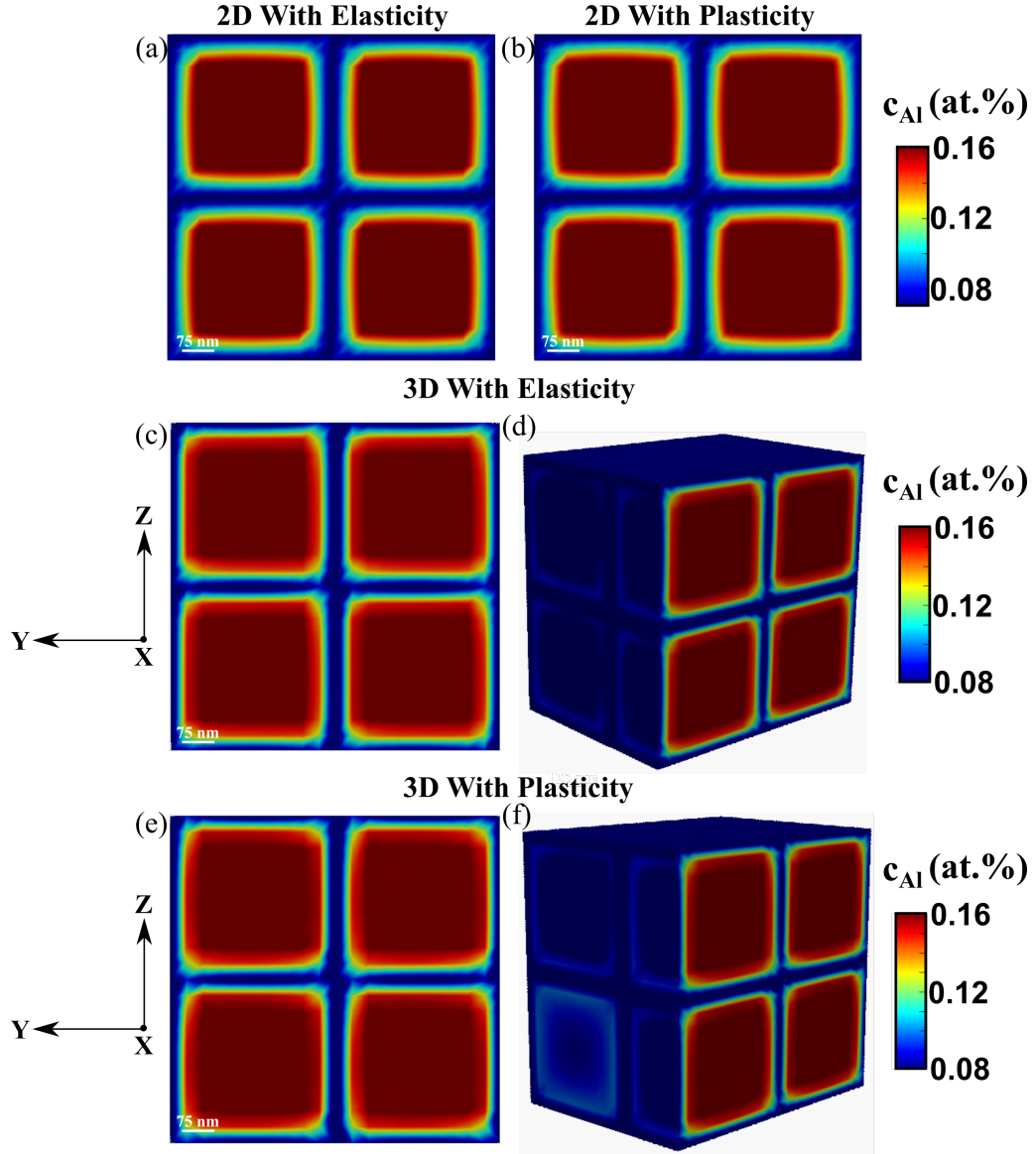
FIGURE 3.2: Predicted precipitate morphology in CMSX-4 shown in terms of the field variable, c(at.%), after the aging heat treatment as predicted in the (a) 2D domain with elasticity, (b) 2D domain with plasticity, (c,d) 3D domain with elasticity, and (e,f) 3D domain with plasticity. For the 3D simulations, the YZ plane at an intermediate section is shown in (c) and (e), while the isometric view is shown in (d) and (f).

300 nm. The precipitate size increases linearly with aging time initially during the growth stage, and as the volume fraction reaches a steady state, the size of the precipitates remains almost constant. The volume fraction of the precipitates (Figure 3.3(d)) also increases in the growth stage, until the concentration of Al reaches the equilibrium concentration in the γ and γ' phases. Subsequently, the volume fraction remains almost constant in the steady-state region. The steady-state volume fraction of the simulation reaches 0.62, which is close to the volume fraction reported for CMSX-4 (i.e., 0.70) (Sengupta et al., 1994). The multi-component phase field model and temperature-dependent phase field parameters can be further calibrated to improve this prediction. Further, mesh adaptivity could also be used to refine the predictions, especially in the interfacial regions, however at higher computational costs. Finally, line plots of the evolution of precipitate sizes and volume fractions as a function of time from the different 2D and 3D simulations, with and without consideration of plasticity, follow similar trends. This is in line with the earlier observations of the same from the contour plots shown in Figure 3.2.

3.3.1.2 Prediction of Tension-Compression Asymmetry

The size, volume fraction, and morphology of the precipitates affect the mechanical properties of the single crystal superalloys. The aged microstructure predicted by the phase field model is used as an input for the deformation simulations, where only crystal plasticity is considered. This aged microstructure is shown in Figure 3.4(a) and is representative of a CMSX-4 single crystal superalloy oriented for [0 0 1] loading. In these simulations, the material is loaded at a quasi-static strain rate of 10^{-3}s^{-1} at different deformation temperatures. A schematic of the symmetric boundary conditions used in these deformation simulations is also shown in Figure 3.4(a)), such that displacements normal to the three adjacent faces on the rear side are set to zero and all degrees of freedom are restricted on the corner node at the back. Further, displacement-controlled loading, either in tension or compression, at the prescribed strain rate, is applied along the [0 0 1] direction on the top face.

Figure 3.4(b) shows the predicted tensile and compressive 0.2 % yield stress for different temperatures, as compared with the corresponding experimental data from Allan (Allan, 1995). Overall, the model predictions are in good agreement with the experimental data for all the temperatures. The precipitate phase in these superalloys demonstrates anomalous yield behavior (increase in yield stress with temperature and tension-compression asymmetry), which is generally attributed to the formation of Kear-Wilsdorf (KW) locks and temperature-dependent cross-slip phenomena (Paidar et al., 1984; Shenoy et al., 2008;
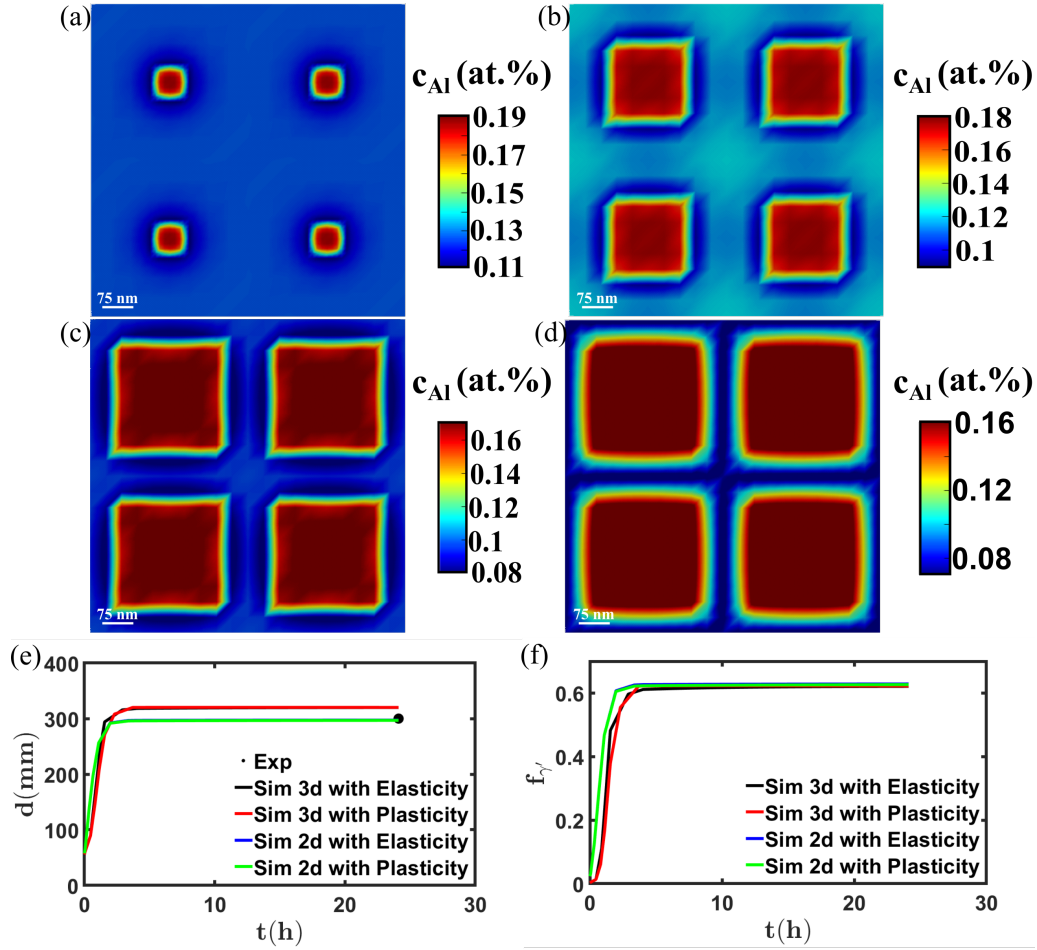
FIGURE 3.3: Predicted precipitate morphology in CMSX-4 shown in terms of the field variable, c(at.%), after (a) 0.1 h, (b) 0.5 h, (c) 1 h, (d) 5 h from the 2D simulation with plasticity. Predicted evolution of precipitate (e) size, and (f) volume fraction during heat treatment from the 2D and 3D simulations with elasticity and with plasticity. The experimentally reported precipitate size (Sengupta et al., 1994) at the end of the heat treatment is also shown using the black symbol in (e).

Ranjan et al., 2021). As a result, the super-dislocations may dissociate into two super partials, which may further split into Shockley partials, thus creating complex stacking faults and anti-phase boundaries (Keshavarz et al., 2016). Further, cross-slip of dislocations onto the <001> cube plane may also hinder subsequent dislocation glide. As a result, the individual Shockley partials must constrict for dislocation glide to occur (Ghorbanpour et al., 2020; Ranjan et al., 2021). In our crystal plasticity model, the driving force for dislocation glide with consideration for non-Schmid stresses (cf. Equation 3.18) accounts for the constriction of the dislocation core (cf. Ranjan et al. (2021)). This is a loading orientation- and temperature-dependent phenomenon.

While Ranjan et al. Ranjan et al. (2021) had predicted the temperature-dependent tension-compression anisotropy of CMSX-4 using a homogenized model, we have shown the same here for the aged microstructure, which was predicted using the coupled phase field-crystal plasticity simulation, with the explicit evolution of the γ and γ' phases. This demonstrates the capability of the model to predict processing-microstructure-mechanical property correlations in single crystal Ni-based superalloys.
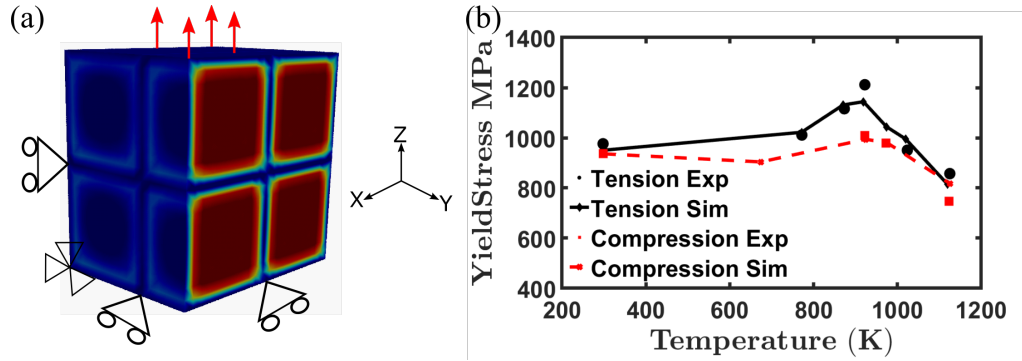
FIGURE 3.4: (a) Schematic of loading and boundary conditions shown on the aged CMSX-4 microstructure oriented for [0 0 1] loading, as predicted by the coupled phase field-crystal plasticity model. (b) Predicted 0.2% offset yield stress during quasi-static tensile and compressive loading as a function of the loading temperature using the crystal plasticity model and comparison with the corresponding experimental data from Allan (1995) (shown in symbols), highlighting the tension-compression asymmetry.

3.3.2   Case Study II

3.3.2.1   Microstructure Evolution During Isothermal Aging

The model is further used to predict the microstructure evolution of CMSX-4 during long-term isothermal aging at 1223 K. Model predictions of the average precipitate size and volume fraction have been compared with the experimental data given in Lapin et al. (2009), which used this aging treatment after the solution treatment for CMSX-4. Note that no additional fitting was performed for the phase field mobility parameter and the model predictions for this case study serve as validation of the fitted parameter.

For this case study, larger 2D simulation domains of $5 \times 5\mu$m, $4 \times 4\mu$m and $3 \times 3\mu$m were considered, with different numbers of initial nuclei in the different domains. The reason for considering three different simulation domains was to establish the invariance of the model predictions to the size of the simulation domain. The domain was meshed with a mesh size of 0.05 μm using square-shaped elements with linear interpolation. To ensure accurate mesh discretization, the element size must be smaller than the characteristic interface

width, allowing for proper resolution of interfacial gradients. Typical grid sizes in phase-field modelling of Ni-based superalloys lie in the tens of nanometres in the literature (Zhou et al., 2010; Le Graverend and Harikrishnan, 2019, 2021). 728, 500, and 265 $\gamma^{'}$ nuclei, with circular shape, were randomly instantiated in the $5 \times 5\mu$m, $4 \times 4\mu$m, and $3 \times 3\mu$m simulation domains, respectively. An initial diameter of 0.06 μm and [001] crystallographic orientation was assigned for all nuclei. Further, an interface width of 0.06 μm was used in all the simulations. Periodic boundary conditions were applied on the lateral faces, while the bottom left corner was constrained in the displacement degrees of freedom to prevent rigid body motion. There was no consideration for plasticity in these simulations, and only elasticity was allowed. As we have shown earlier, model predictions with and without plasticity do not show appreciable differences in the precipitate morphology or size.

Figure 3.5 shows the microstructure evolution after aging at 1 h, 500 h, and 2000 h for the three different microstructures. During the initial stages, the size of the precipitate increases, and the shape becomes square. However, it can be seen that the phenomenon of precipitate coarsening becomes dominant during the later stages. During this period, the larger precipitates increase in size at the expense of the smaller ones. This is generally referred to as Ostwald ripening (Voorhees, 1985) and is thermodynamically driven by the decrease in the "total" surface area of the system. As a result, the number of precipitates decreases, but the average precipitate size increases. Qualitatively, these predicted microstructures agree with the experimental counterparts reported in (Lapin et al., 2009; Kundin et al., 2012).

Figure 3.6(a) shows the predicted evolution of the average precipitate size with time, while Figure 3.6(b) shows the evolution of the precipitate volume fraction with time, as compared with the respective experimental data from Lapin et al. (2009). Predictions from all three simulations are plotted here. The size of the precipitates increases with aging time from an initial size of 60 nm to 490 nm (Figure 3.6(a)). The predicted size of the precipitates is qualitatively comparable with experimental observations reported by Lapin et al. (2009). While there are some differences in the precipitate size from the different simulations, their long-term evolution behavior appears to be qualitatively similar. Moreover, the predicted precipitate size evolution approaches the experimental values using larger simulation domains. It can be seen from Figure 3.6(b) that the volume fraction of the precipitates increases rapidly during the growth stage as Al atoms diffuse and contribute to the formation of the $\gamma^{'}$ phase. This increase continues until the Al concentration in both the γ matrix and the γ' precipitates reaches equilibrium. Subsequently, the system enters a steady-state regime, where the volume fraction of precipitates saturates and does
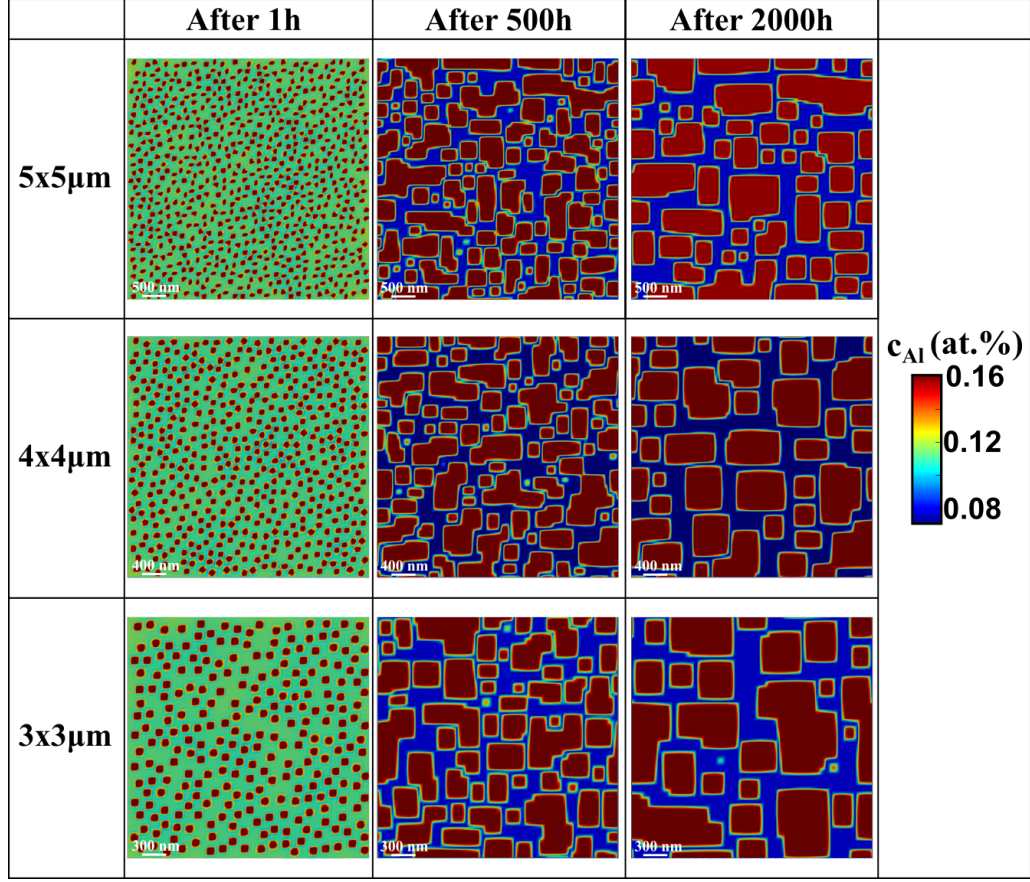
FIGURE 3.5: Predicted precipitate morphology in CMSX-4 shown in terms of the field variable, c(at.%), as a function of time during aging at 1223 K for different simulation domain sizes.

not vary appreciably with time. The predicted volume fraction of the $\gamma^{'}$ phase after 2000 h is 0.62, which is slightly under-predicted as compared to the experimentally reported value of 0.7 (Lapin et al., 2009). As the precipitate volume fraction saturates, a further increase in precipitate size occurs primarily due to coarsening, where larger precipitates grow at the expense of smaller ones. We note that there is an under-prediction of the precipitate volume during long term aging. This could be due to the fact that the exact free energy functions of CMSX-4 have not been used in the present work, rather they have been approximated as a two component system (cf. Table 3.3).

Nonetheless, these results demonstrate the capability of the model to predict the long-term microstructure evolution during aging in single crystal Ni-based superalloys. In future work, the model applications could also be extended to rafting simulations in the presence of external loads.
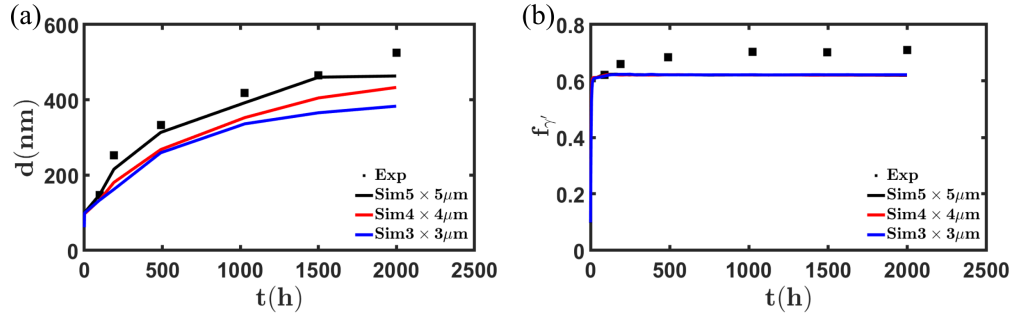
FIGURE 3.6: Predicted evolution of (a) average precipitate size, and (b) volume fraction during isothermal aging at 1223 K from the 2D simulations with different domain sizes as compared with the experimental data from Lapin et al. (2009).

3.3.2.2 Effect of Cooling Rate on Microstructure Evolution

The model is also used to predict the effect of the cooling rate on precipitate evolution for CMSX-4. As mentioned earlier, the temperature was assumed to be the same in the entire simulation domain, without consideration for temperature gradients. 2D simulation domains of $3 \times 3\mu$m were considered with 265 randomly instantiated nuclei. The domain was meshed using square-shaped elements with a mesh size of 0.05 μm and an initial precipitate size of 0.06 $3 \times 3\mu$m, with [001] crystallographic orientation. All other model parameters and boundary conditions are the same as previous section.

The cooling simulations have been performed starting from an initial temperature of 1353 K, under the assumption of an initial solutionized microstructure. These microstructures were subject to four different cooling rates, namely 10 K/s, 1 K/s, 0.1 K/s and 0.01 K/s, respectively, until a temperature of 300 K is reached. Figure 3.7 (a) shows the schematic evolution of the temperature as a function of time, which are applied as boundary conditions in these simulations. The corresponding evolution of the volume fraction of precipitates with time is shown in Figure 3.7 (b). Figures 3.7 (c), (d), (e) and (f) show the corresponding morphology of the precipitates after cooling to room temperature with cooling rates of 10 K/s, 1 K/s, 0.1 K/s and 0.01 K/s, respectively.

These simulations indicate that the cooling rate plays a critical role on the volume fraction and size of the $\gamma^{'}$ precipitates. Coarse, cuboidal $\gamma^{'}$ precipitates are observed at relatively slower cooling rates. On the other hand, the morphology of the precipitates is irregular and circular in shape as the cooling rate increases. Further, the simulations with higher cooling rates exhibit a lower volume fraction of $\gamma^{'}$ precipitates, which are also smaller in size. While there are no experimental studies to quantitatively compare our model predictions, these results compare qualitatively with the experimental studies on CMSX-2 Grosdidier et al.

(1998) and UDIMET 720Li Radis et al. (2009). It was observed in both these studies that the precipitate size increases as the cooling rate decreases. The former study Grosdidier et al. (1998) also noted that the precipitate volume fraction increased with a decrease in cooling rate. Essentially, sufficient time is not available for the nucleation and growth of the precipitates at higher cooling rates, with a very low volume fraction of precipitates formed after cooling at 1 K/s and 10 K/s. While nucleation is not considered explicitly, the predicted trends are attributed to the growth kinetics in our model.
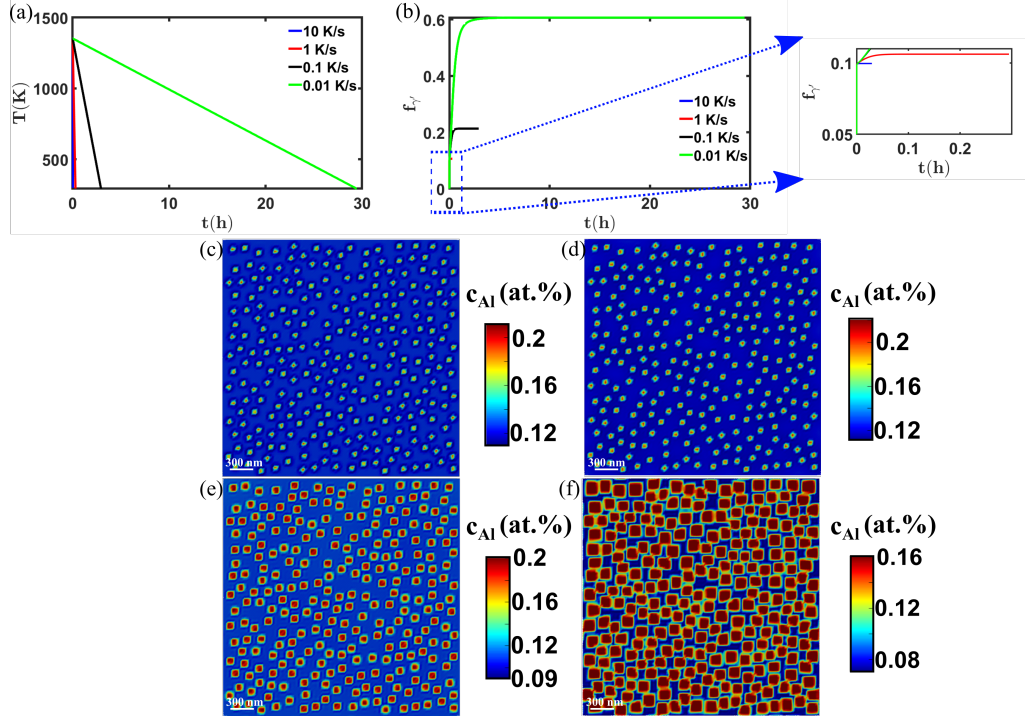
FIGURE 3.7: (a) Temperature versus time history for the simulations with different cooling rates. (b) Predicted precipitate volume fraction as a function of cooling time from the simulations with different cooling rates. Predicted precipitate morphology shown in terms of the field variable, c(at.%), after cooling to room temperature for the cooling rates: (c) 10 K/s, (d) 1 K/s, (e) 0.1 K/s, (f) 0.01 K/s in a simulation domain of $3 \times 3\mu$m.

3.3.3 Case Study III

This case study presents predictions of isothermal aging for Ni-Al alloys at relatively lower temperatures and for different durations. Relevant experimental data for the coarsening kinetics of γ' precipitates for Ni-12.5 at.%Al at 823 K and 873 K are taken from Plotnikov et al. (2014), while similar isothermal aging data for Ni-13.53 at.%Al at 898 K and 988 K are taken from Ardell (1968).

2D domains of $0.5 \times 0.5 \mu$m were considered for all cases, with the mesh size of 0.0025 μm. 29 γ' nuclei were randomly instantiated, with an initial radius of 4 nm and an interface width of 5 nm. Note that a smaller initial nucleus size was used in these simulations, in order to accurately capture the initial growth kinetics of precipitate evolution. All nuclei were assigned a [001] crystallographic orientation. Similar boundary conditions were used, as in the previous case studies. Except for the mobility parameter, L, the same phase field parameters as used in the previous case studies are used to simulate this heat treatment. The mobility parameter was calibrated to predict the experimentally observed precipitate size during the heat treatments, and the temperature-dependent value of L is reported at the end of this section.

During isothermal aging of Ni–Al alloys, the γ' precipitates nucleate and grow from the supersaturated γ matrix due to a strong chemical driving force. While we have simulated the latter here, the nucleation process is assumed to have occurred before our aging simulations. The morphology of the aged precipitates at 823 K and 873 K after 256 h for Ni-12.5 at.%Al and at 898 K after 93 h and 988 K after 25 h for Ni-13.53 at.%Al are plotted in Figure 3.8. It can be seen that the morphology of the precipitates evolves with different aging temperatures and durations. Starting from the initial circular shape, the morphology of the precipitates at 823 K is still circular for these relatively smaller γ' precipitates, whereas the precipitate morphology changes from circular to square shape at higher temperatures. Plotnikov et al. Plotnikov et al. (2014) also reported that the shape of the precipitates evolves from spherical to cuboidal after 100 h, while Ardell Ardell (1968) reported the shape of the precipitates to be cuboidal after aging.

The volume fraction of the precipitates is plotted as a function of the aging time for the different simulations in Figure 3.9. It can be seen that the volume fraction increases almost linearly with time during the initial stages for all cases, and the respective rates depend on the aging temperature. During this stage, the precipitates grow by drawing solute from the γ matrix. This leads to a gradual increase in the γ' volume fraction, which approaches a steady-state value over time. At lower aging temperatures, the diffusion of aluminum is expected to be relatively slower, whereas the rate of diffusion is expected to be higher at higher temperatures. As a result, rapid growth occurs at higher temperatures, and the volume fraction approaches the equilibrium value more quickly. This is observed for the simulation at 988 K, where saturation in the volume fraction occurs at a relatively shorter time as compared to the other simulations at lower temperatures.

The evolution of the average precipitate size with aging time for the different aging temperatures and alloy compositions is shown in Figure 3.10 (a) and (b), as compared with the
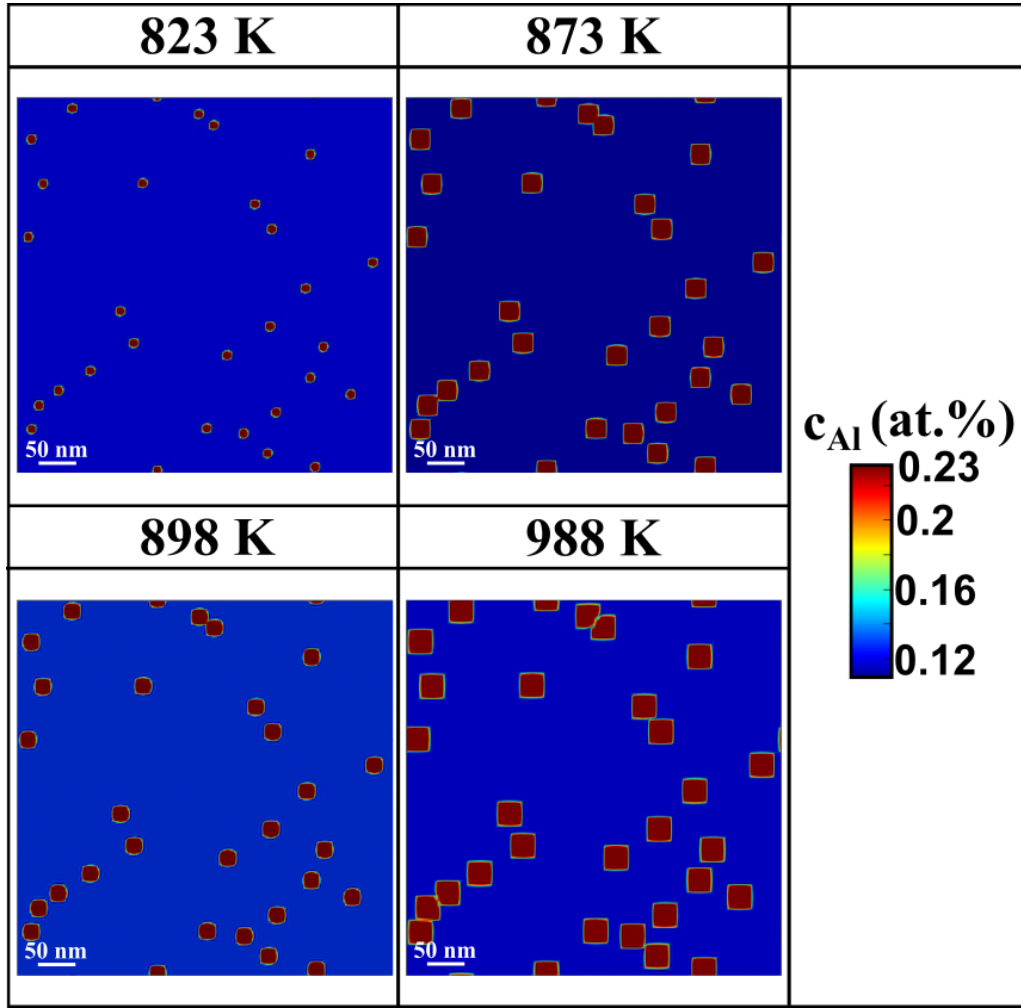
FIGURE 3.8: Predicted precipitate morphology in two different Ni-Al systems shown in terms of the field variable, c(at.%), after isothermal aging at (a) 823 K for 256 h, (b) 873 K for 256 h for Ni-12.5 at.%Al, and at (c) 898 K for 93 h, (d) 988 K for 25 h for Ni-13.53 at.%Al.

respective experimental data from Plotnikov et al. (2014); Ardell (1968). As can be seen, the model is able to predict the experimentally measured precipitate size with reasonable accuracy in all cases. The average precipitate size remains relatively small even after prolonged aging, in the range of 10–30 nm after several hours at 823 K and 873 K. At 988 K, the precipitates grow rapidly in size initially, and this growth rate decreases after 20 h. In our model, the phase field mobility, L, has been calibrated to obtain this experimentally observed behavior. The temperature dependence of the phase field mobility, L, has then been fit to an Arrhenius-type model according to the following equation:

$$L = 2.3424 exp\left(-\frac{3.9025 \times 10^{-19}}{kT}\right) \text{m}^3\text{J}^{-1}\text{s}^{-1}; 823\text{K} \leq T \leq 988\text{K} \qquad (3.26)$$
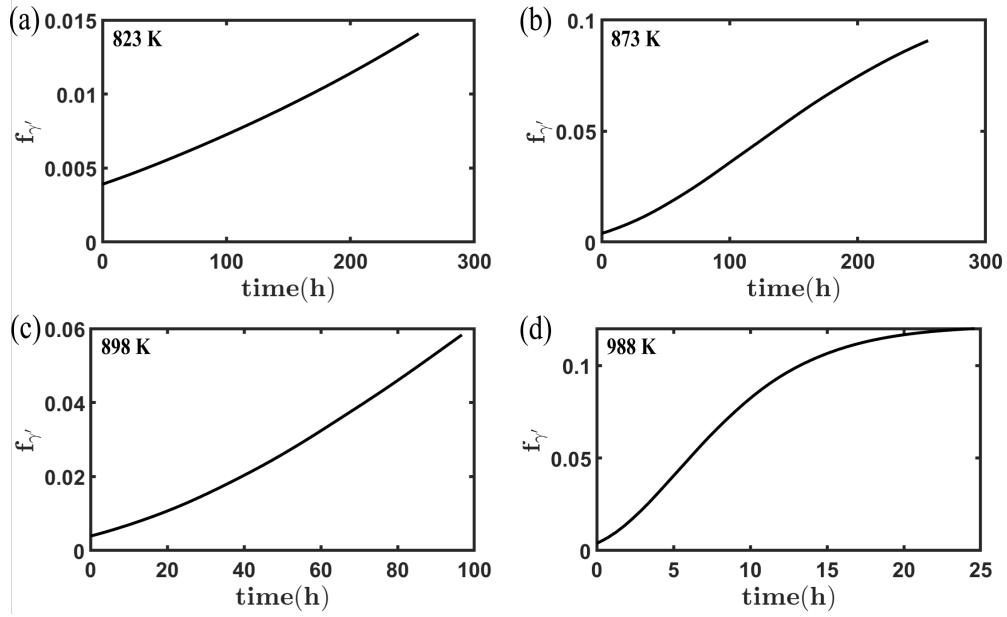
FIGURE 3.9: Evolution of the volume fraction of precipitates during isothermal aging at (a) 823 K, (b) 873 K for Ni-12.5 at.%Al, and (c) 898 K, (d) 988 K for Ni-13.53 at.%Al.
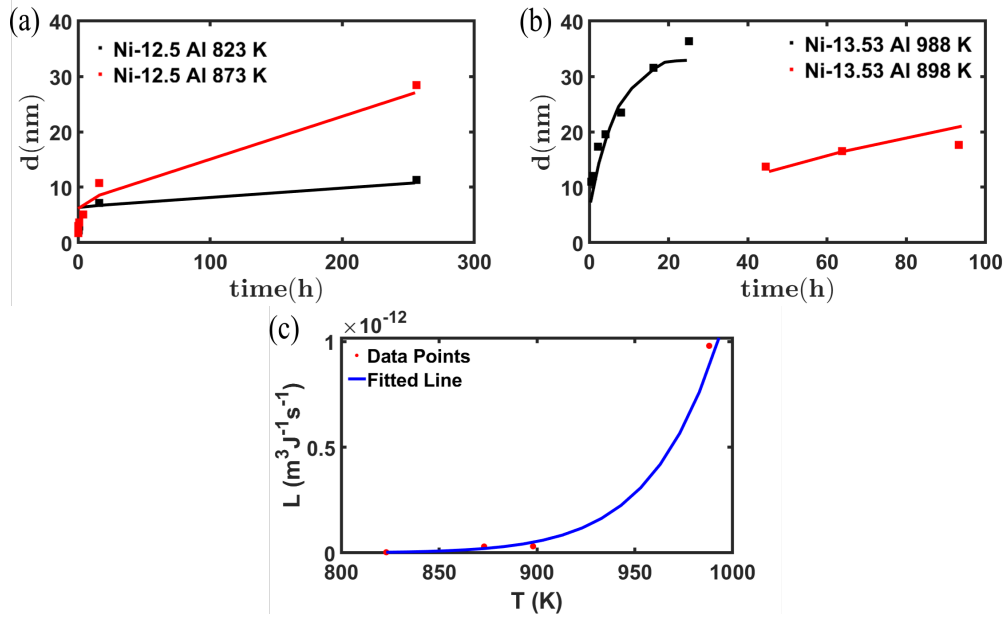
FIGURE 3.10: Predicted evolution of the average precipitate size during isothermal aging at (a) 823 K and 873 K for Ni-12.5 at.%Al, and at (b) 898 K and 988 K for Ni-13.53 at.%Al as compared with the respective experimental data from (Plotnikov et al., 2014; Ardell, 1968). Experimental data are shown using symbols, while the model predictions are shown using lines. (c) Calibrated value of the phase-field mobility, L, as a function of temperature, T.

This mobility parameter, L, is plotted as a function of temperature in Figure 3.10(c), along with the fitted equation. While the value of the term within the exponential, physically representative of the activation energy for mobility, is the same as used earlier for CMSX-4, the pre-exponential term has a higher value in the present case.

Note that these aging temperatures are significantly lower than those used previously for CMSX-4. The results presented in this case study demonstrate the applicability of the model for predicting the precipitate morphology and sizes for relatively lower aging temperatures and different alloy compositions.

3.4   Concluding Remarks

A phase field model is developed and integrated with a dislocation density-based crystal plasticity framework to predict the microstructure evolution during aging heat treatment and the mechanical properties of the aged microstructures of single crystal Ni-based superalloys. The phase field model, which has been adapted from (Qin and Bhadeshia, 2009; Zhou et al., 2010), and is based on the Kim-Kim-Suzuki (KKS) model (Kim et al., 1999), accounts for the anisotropic growth and coarsening of precipitates during aging. Specifically, the interfacial anisotropy in the phase field model is used to model the morphological evolution of precipitates from an initial spherical/circular shape to a cuboidal/square shape, which is a characteristic feature of γ' precipitate growth in superalloys. The crystal plasticity model has been adopted from (Ranjan et al., 2021) and is used to predict the mechanical properties of the aged microstructures.

Application of the model has been demonstrated in the form of three case studies, which are listed in the following:

- The first case study simulates the two stage aging of a commercial single crystal superalloy, CMSX-4. Verification of the model predictions have been performed using 2D and 3D simulations, considering only elasticity and with plasticity. Model predictions of the precipitate morphology and volume fraction, from the 2D and 3D simulations, with and without plasticity, are similar and comparable with the experimental values from the literature. Further, the mechanical properties of the 3D aged microstructures have predicted in the form of the temperature-dependent tension-compression asymmetry, which also shows a good comparison with experimental data from the literature.

- The second case study simulates long term aging of CMSX-4 in relatively larger 2D microstructures. The model predicts a saturation in the average precipitate volume fraction and subsequent coarsening. The model is able to qualitatively predict the average precipitate size and volume fraction, as observed in the experiments. Further, the effect of varying the cooling rate on the microstructure evolution is also demonstrated.

- The third case study simulates aging in 2D microstructures of Ni-Al alloys, with different compositions, at relatively lower temperatures. The model is able to predict the evolution in the precipitate morphology from circular to square shapes, as well as the experimentally observed evolution of average precipitate size for different alloy compositions.

As a first order approximation, we have assumed a binary Ni–Al system, with parabolic free energy functions, for the γ and γ' phases in the present work. While this approach captures the essential thermodynamic features governing phase evolution, it might not fully reproduce the quantitative microstructural evolution observed in multicomponent Ni-based superalloys such as CMSX-4. In future work, this framework may be enhanced by incorporating CALPHAD-based multi-component Gibbs free energy functions to improve the predictive fidelity. The crystal plasticity model used for predicting the mechanical properties also does not have consideration for the alloy chemistry at present. For example, solid solution strengthening is expected to be composition dependent and may influence the strength of both the γ and γ' phases. Further, this framework can also be coupled with heat transfer models in the future to simulate realistic heat treatments and dendritic microstructures. These model considerations will allow the use of the modeling framework for alloy design. Note that only the γ and γ' phases are considered in our model for single crystal Ni-based superalloys. The single crystal superalloys may also have carbides and borides (Lamm and Singer, 2007; Reed, 2008; Steuer et al., 2015; Liu et al., 2022). The effect of these are not considered in our model due to their relatively low volume fractions and negligible influence on the mechanical properties.

Overall, this integrated phase field-crystal plasticity framework offers a powerful tool for studying the processing-microstructure-mechanical property correlations in single crystal Ni-based superalloys. The precipitate morphology and size in these alloys depend on the heat treatment and influence the post-processing mechanical properties. Integrating the two different modeling techniques into one framework offers the scope for computational design of single crystal superalloys by optimizing heat treatment processes to improve the

mechanical properties. However, significant experimental validation and uncertainty quantification are required before the adoption of these models in industrial design processes, which also requires certification at various levels. These may be explored in future work.

Chapter 4

Crystal Plasticity Constitutive Modeling of Tensile, Creep and Cyclic Deformation in Single Crystal Ni-based Superalloys

4.1 Introduction

Nickel-based superalloys are widely used in applications that require superior elevated temperature properties like high strength, high toughness, relatively high creep resistance, and thermal fatigue resistance (Geddes et al., 2010). Turbine blades and turbine discs of modern gas turbines, burner cans and vanes are some engineering applications where Ni-based superalloys are used (Antolovich, 1996). The mechanical properties of Ni-based superalloys are governed by their underlying microstructure. Generally, these alloys comprise of a two-phase microstructure: a Ni-rich solid solution, with FCC crystal structure, called the γ phase, and coherent $L1_2$-type, long-range ordered intermetallic Ni_3Al precipitates, called the $\gamma^{'}$ phase (Murakumo et al., 2004). Several factors influence the deformation behavior of these alloys: (i) Orowan looping of matrix dislocations around precipitates (Fedelich et al., 2009); (ii) interface coherency stress (Tinga et al., 2008); (iii) activation of cube slip in the $\gamma^{'}$ phase (Tinga et al., 2009b; Wang et al., 2016a); and (iv) shearing of precipitates by super dislocations, which leads to the formation of APBs (Allan,

---

[1] Significant parts of this chapter have been published in Chaudhary et al. (2022).

59

1995; Keshavarz and Ghosh, 2015a). These factors contribute to anisotropic, orientation- and temperature-dependent deformation in Ni-based superalloys (Ranjan et al., 2021). Contrary to conventional metals and alloys, these superalloys show an anomalous yield behavior, with little or no decrease in yield strength with temperature up to a certain value, after which yield strength decreases. This makes them suitable for use in elevated temperature applications (Westbrook, 1957; Flinn, 1960; Shenoy et al., 2008). Further, rafting, directional coarsening of cuboidal γ' phase into lamellar structures, usually occurs at temperatures above 900 °C, which significantly affects the creep deformation of superalloy single crystals (Fan et al., 2015).

Creep deformation of single crystal superalloys is anisotropic and depends on the stress, temperature, and loading orientation (Sims et al., 1987; Stouffer and Dame, 1996; Xia et al., 2020). Single crystal superalloys show tertiary creep behavior, along with a small amount of steady-state creep at temperatures greater than 850 °C (Ghosh et al., 1990; Reed, 2008; Titus et al., 2012). Deformation near [001] crystal orientations primarily occurs due to the glide/climb of dislocations on the octahedral slip systems $\{111\} < 1\bar{1}0 >$ (Pollock and Argon, 1994). Glide/climb of dislocations on the $\{001\} < 1\bar{1}0 >$ cube slip systems have been observed near the [111] crystal orientation at high temperatures (Sun and Hazzledine, 1996; Matan et al., 1999a). Although the role of cube slip on deformation is not yet fully understood, but experimental observations by (Clement et al., 1991; Österle et al., 2000; Tinga et al., 2009b; Wang et al., 2016a) are indicative of the activation of cube slip near the [111] orientations. Rafting of γ' precipitates was first observed in Ni-based superalloys by Webster and Sullivan (1967). It strongly depends on the elastic constants of γ/γ' phases, the sign of applied stress and lattice misfits (Chang and Allen, 1991; Ignat et al., 1993; Pollock and Argon, 1994; Nabarro, 1996; Svoboda and Lukas, 1996; Laberge et al., 1997; Ohashi et al., 1997; Henderson et al., 1998; Mughrabi and Tetzlaff, 2000; Epishin et al., 2000; Titus et al., 2012; Mughrabi, 2014). Experimental studies have revealed that rafting occurs parallel (or perpendicular) to the loading axis under compression (or tension) for alloys with negative lattice misfit (Lukáš et al., 1996). It was also reported that rafting does not occur during creep loading along the [111] orientation (Liu et al., 2008; Yu et al., 2013).

Several continuum crystal plasticity models have been developed to predict the temperature and orientation-dependent deformation behavior of Ni-based superalloys (Ghosh et al., 1990; Qin and Bassani, 1992; Allan, 1995; Brehm and Glatzel, 1999; MacLachlan and Knowles, 2000; Ma et al., 2008; Shenoy et al., 2008; Tinga et al., 2009a; Staroselsky and Cassenti, 2011; Vattré and Fedelich, 2011; Le Graverend et al., 2014; Keshavarz and

Ghosh, 2015a; Keshavarz et al., 2016; Ghorbanpour et al., 2017; Rodas and Neu, 2018; Yu et al., 2020c; Agaram et al., 2021; Gupta and Bronkhorst, 2021; Ranjan et al., 2021). A power law model, with consideration for the shearing of the $\langle 112 \rangle$ super-partials, was proposed by MacLachlan and Knowles (2000). This model was able to predict the creep response for the [001] and [111] loading orientations. Ma et al. (2008) proposed a dislocation density-based crystal plasticity model, with consideration for climb in the precipitates and a creep flow rule. Model predictions were in good agreement for all the creep stages for the [001] orientations. Le Graverend et al. (2014) developed a microstructure-sensitive model to investigate non-isothermal creep, fatigue, and creep-fatigue response. However, this model is only valid for the creep of single crystal alloys with negative lattice misfit under tension. Keshavarz and Ghosh (2015a) proposed a dislocation density-based non-Schmid crystal plasticity model to predict anomalous thermo-mechanical behavior for Ni_3Al single crystals. Gupta and Bronkhorst (2021) proposed a crystal plasticity model with separate flow rules for the γ and γ' phases that includes the effects of strengthening mechanisms like Orowan hardening, γ' contribution to initial slip resistance, and Anti-Phase Boundary (APB) shearing of γ' phase.

A number of studies have proposed crystal viscoplasticity models to capture the creep-fatigue interactions. Rodas and Neu (2018) has extended the model proposed by Ma et al. (2008) to predict 3-D creep-fatigue interactions by adding backstress formulations, strain rate sensitivity exponent, and dislocation evolution. The effect of orientation on the mechanical response of single crystal alloys has been modeled and compared with experiments by (Sabnis et al., 2013; Su et al., 2020). Crystal plasticity constitutive models have also been proposed for polycrystalline Ni-based superalloys (Shenoy, 2006; Shenoy et al., 2008; Zhang et al., 2015a; Ghorbanpour et al., 2017; Phan et al., 2017; León-Cázares et al., 2020a; Sun et al., 2020; Agaram et al., 2021; Fernandez-Zelaia et al., 2022). Further, macroplasticity models have also been proposed to predict the thermo-mechanical deformation of Ni-based superalloys (Chaboche et al., 2013; Lindström et al., 2022).

In addition to the mechanical properties, the microstructure of Ni-based superalloys evolves during creep deformation at elevated temperatures, as well. The morphology of the γ' precipitate changes from cuboidal geometry to elongated rafts during directional coarsening, and the γ channels widen along the direction of loading. Different models have been proposed to model the evolution of channel width due to rafting (Epishin et al., 2009; Fedelich et al., 2009; Tinga et al., 2009a; Le Graverend et al., 2014; Fan et al., 2015; Desmorat et al., 2017; Wu et al., 2019c; Guo et al., 2021). Epishin et al. (2009) have modeled the channel width evolution during rafting using a modified Arrhenius equation that accounts for

temperature- and stress-dependence. Tinga et al. (2009a) extended this model to a multiaxial stress state within a crystal plasticity formulation to simulate tensile and cyclic tests. Fedelich et al. (2009) proposed a dimensionless parameter to capture the isotropic and direction coarsening of channel width. Fan et al. (2015) further extended this model to predict the rafting characteristics under various loading conditions like double shear creep and rafting without external stress. Although their model is orientation-dependent, the applicability of the model to capture channel width and creep response along different orientations (e.g., [111] loading) was not demonstrated. Desmorat et al. (2017) proposed a model considering the effect of isotropic and directional coarsening on viscoplastic behavior at higher temperatures, which includes a tensorial description of channel width evolution. It should also be noted that several recent studies have focused on phase field modeling of microstructure evolution during creep deformation (Gaubert et al., 2015; Wu et al., 2017; Ali et al., 2020a; Zhang et al., 2020; Le Bouar et al., 2022). These spatially resolved simulations provide detailed information regarding the microstructural evolution; however, they are computationally expensive.

As can be seen, significant research has been directed at constitutive modeling of deformation in these alloys. However, there are only a few frameworks proposed for unified modeling of the effects of temperature- and strain rate-dependence, and directional hardening to predict creep, cyclic and creep-fatigue interactions in superalloy single crystals over a range of deformation histories (cf. (Staroselsky and Cassenti, 2011; Vattré and Fedelich, 2011; Rodas and Neu, 2018)). Further, microstructure evolution during creep has also not been addressed explicitly in some of these works. The present work aims to address these gaps in the literature by developing a physically-based constitutive framework for unified modeling of the above-mentioned phenomena.

We propose a microstructure-sensitive crystal plasticity constitutive model to simulate thermo-mechanical deformation in single crystal Ni-based superalloys. Description of the proposed crystal plasticity framework and constitutive equations for microstructure evolution during creep are first given in Section 4.2. Details of the constitutive model parameters fit to the available experimental data for tensile, cyclic, and creep response for two different superalloys, CMSX-4 and PWA-1484, are then given in Section 4.3. Finally, the model is validated by comparison of the predicted response with the available experimental data for the creep-fatigue loading for these alloys.

4.2 Crystal Plasticity Framework

The constitutive modeling framework is based on the prior work of Ranjan et al. (2021), where a crystal plasticity model was proposed to model the homogenized response of the microstructure comprising the γ matrix and γ' precipitate. Ranjan et al. (2021) modeled the effect of non-Schmid stresses on the orientation- and temperature-dependent yield stress for single crystal Ni-based superalloys. In the present work, we extend this framework by proposing constitutive models for backstress evolution, climb-enhanced glide, and microstructure evolution during elevated temperature deformation to predict the creep, cyclic, and creep-fatigue interactions.

4.2.1 Finite Deformation Kinematics

This framework is based on the multiplicative decomposition of the deformation gradient, $\boldsymbol{F}$, into the elastic deformation gradient, $\boldsymbol{F^e}$, and the inelastic deformation gradient, $\boldsymbol{F^i}$ (Asaro and Rice, 1977):

$$\boldsymbol{F} = \boldsymbol{F^e} \cdot \boldsymbol{F^i} \tag{4.1}$$

Here, $\boldsymbol{F^e}$ accounts for the lattice distortion and the rigid body rotation that carries the intermediate isoclinic configuration to the current, deformed configuration and $\boldsymbol{F^i}$ accounts for the effects of inelastic deformation on a undeformed lattice, mapping the reference configuration to an intermediate configuration in which the lattice has the same orientation.

The second Piola-Kirchoff stress in the intermediate configuration is given by $\boldsymbol{S} = \boldsymbol{C_{eff}} : \boldsymbol{E^e}$, where, $\boldsymbol{C_{eff}}$ is the fourth rank elasticity tensor and $\boldsymbol{E^e}$ is the elastic Green strain tensor. The effective elasticity tensor for the homogenized material is given by (Ranjan et al., 2021):

$$\boldsymbol{C_{eff}^{ijkl}} = \left(\left(1 - f_{\gamma'}\right) \boldsymbol{C_m^{ijkl-1}} + f_{\gamma'} \boldsymbol{C_p^{ijkl-1}} \right)^{-1} \tag{4.2}$$

where, $\boldsymbol{C_m^{ijkl}}$ and $\boldsymbol{C_p^{ijkl}}$ represent the anisotropic fourth order elasticity tensors of the matrix phase, γ, and the precipitate phase, γ', respectively. The second Piola-Kirchoff stress is related to the Cauchy stress, $\boldsymbol{\sigma}$, in current configuration by $\boldsymbol{S} = det\left(\boldsymbol{F^e}\right) \boldsymbol{F^{e-1}} \cdot \boldsymbol{\sigma} \cdot \boldsymbol{F^{e-T}}$.

The inelastic deformation gradient is given by $\dot{\boldsymbol{F^i}} = \boldsymbol{L^i} \cdot \boldsymbol{F^i}$, where $\boldsymbol{L^i}$ is the inelastic velocity gradient. $\boldsymbol{L^i}$ is modeled as the tensor sum of crystallographic shearing rates and

climb rates across all possible deformation systems and is given by:

$$
\begin{aligned}
\boldsymbol{L^i} = \left(1 - f_{\gamma'}\right) \sum_{\alpha=1}^{N_m} \dot{\gamma}_g^{\alpha} \boldsymbol{s}_{0m}^{\alpha} \otimes \boldsymbol{m}_{0m}^{\alpha} + f_{\gamma'} \sum_{\beta=1}^{N_p} \dot{\gamma}_g^{\beta} \boldsymbol{s}_{0p}^{\beta} \otimes \boldsymbol{m}_{0p}^{\beta} \\
+ \left(1 - f_{\gamma'}\right) \sum_{\alpha=1}^{N_m} \dot{\gamma}_c^{\alpha} \boldsymbol{s}_{0m}^{\alpha} \otimes \boldsymbol{s}_{0m}^{\alpha} + f_{\gamma'} \sum_{\beta=1}^{N_p} \dot{\gamma}_c^{\beta} \boldsymbol{s}_{0p}^{\beta} \otimes \boldsymbol{s}_{0p}^{\beta}
\end{aligned}
\tag{4.3}
$$

Here, $\dot{\gamma}_g^{\alpha}$ and $\dot{\gamma}_c^{\alpha}$ are the crystallographic strain rates due to glide and climb on deformation system α, respectively, and N_m and N_p denote the total number of deformation systems for matrix and precipitate phase, respectively. Further, the slip system direction and plane normal in the reference configuration are given by $\boldsymbol{s}_0^{\alpha}$ and $\boldsymbol{m}_0^{\alpha}$, respectively. The subscripts, m and p, denote the corresponding quantities for the matrix and the precipitate phase, respectively. The dominant deformation mechanism (dislocation glide or climb) generally depends on the loading conditions and the deformation temperature. Constitutive equations for dislocation glide and climb contributing to the total velocity gradient have been discussed later. Further, the relative contribution of these mechanisms has also been predicted for different loading conditions later in the manuscript.

The model considers deformation on the octahedral $\{111\} < 1\bar{1}0 >$ deformation systems for the matrix phase. Further, to account for non-Schmid effects, the model explicitly accounts for forward and backward slip on the octahedral $\{111\} < 1\bar{1}0 >$ slip systems in the precipitate phase. In addition, the cube $\{100\} < 011 >$ slip systems are also considered for the precipitate phase, which are expected to get activated at elevated temperatures (cf. (Allan, 1995; Keshavarz and Ghosh, 2015a; Ranjan et al., 2021)). The slip systems for octahedral and cube slip are adopted from Qin and Bassani (1992) and listed in Table 4.1 and 4.2.

Further, dislocation climb perpendicular to the slip plane is modeled based on the climb kinematics proposed by Geers et al. (2014), where the climb projection tensor was introduced to model the additional strain rate due to dislocation climb in a small deformation plasticity framework for coupled glide and climb. Here, we have extended the same to a finite deformation framework. Note that other forms of constitutive equations for modeling combined glide and climb have also been proposed by (Lebensohn et al., 2010; Patra and McDowell, 2012; Phan et al., 2017; Wen et al., 2017, 2020).

In the following sections, we refer to the deformation systems α in the phase j using the following notation: $\alpha \in$ oct, cube and $j \in$ m,p. Here, 'oct' represents the octahedral slip

TABLE 4.1: Octahedral and cube slip systems in $\gamma^{'}$ phase (Qin and Bassani 1992)

α	Type	$(m^\alpha)[s^\alpha]$	$\left(m_{pe}^\alpha\right)\left[s_{pe}^\alpha\right]$	$(m_{se}^\alpha)[s_{se}^\alpha]$	$(m_{cb}^\alpha)[s_{cb}^\alpha]$
1	Octahedral	$(111)[01\bar{1}]$	$(111)[\bar{2}11]$	$(1\bar{1}\bar{1})[\bar{2}\bar{1}\bar{1}]$	$(100)[01\bar{1}]$
2	Octahedral	$(111)[\bar{1}01]$	$(111)[1\bar{2}1]$	$(\bar{1}1\bar{1})[\bar{1}\bar{2}\bar{1}]$	$(010)[\bar{1}01]$
3	Octahedral	$(111)[1\bar{1}0]$	$(111)[11\bar{2}]$	$(\bar{1}\bar{1}1)[\bar{1}\bar{1}\bar{2}]$	$(001)[1\bar{1}0]$
4	Octahedral	$(1\bar{1}\bar{1})[0\bar{1}1]$	$(1\bar{1}\bar{1})[\bar{2}\bar{1}1]$	$(111)[\bar{2}11]$	$(100)[0\bar{1}1]$
5	Octahedral	$(1\bar{1}\bar{1})[\bar{1}0\bar{1}]$	$(1\bar{1}\bar{1})[12\bar{1}]$	$(\bar{1}1\bar{1})[\bar{1}112]$	$(0\bar{1}0)[\bar{1}0\bar{1}]$
6	Octahedral	$(1\bar{1}\bar{1})[110]$	$(1\bar{1}\bar{1})[1\bar{1}2]$	$(\bar{1}\bar{1}1)[\bar{1}112]$	$(00\bar{1})[110]$
7	Octahedral	$(\bar{1}1\bar{1})[011]$	$(\bar{1}1\bar{1})[21\bar{1}]$	$(\bar{1}\bar{1}1)[2\bar{1}1]$	$(\bar{1}00)[011]$
8	Octahedral	$(\bar{1}1\bar{1})[10\bar{1}]$	$(\bar{1}1\bar{1})[\bar{1}\bar{2}\bar{1}]$	$(111)[1\bar{2}1]$	$(010)[10\bar{1}]$
9	Octahedral	$(\bar{1}1\bar{1})[\bar{1}\bar{1}0]$	$(\bar{1}1\bar{1})[\bar{1}12]$	$(1\bar{1}\bar{1})[1\bar{1}2]$	$(00\bar{1})[\bar{1}\bar{1}0]$
10	Octahedral	$(\bar{1}\bar{1}1)[0\bar{1}\bar{1}]$	$(\bar{1}\bar{1}1)[2\bar{1}1]$	$(\bar{1}1\bar{1})[21\bar{1}]$	$(\bar{1}00)[0\bar{1}\bar{1}]$
11	Octahedral	$(\bar{1}\bar{1}1)[101]$	$(\bar{1}\bar{1}1)[\bar{1}21]$	$(1\bar{1}\bar{1})[1\bar{1}2]$	$(0\bar{1}0)[101]$
12	Octahedral	$(\bar{1}\bar{1}1)[\bar{1}10]$	$(\bar{1}\bar{1}1)[\bar{1}\bar{1}\bar{2}]$	$(111)[11\bar{2}]$	$(001)[\bar{1}10]$
13	Octahedral	$(111)[0\bar{1}1]$	$(111)[\bar{2}11]$	$(1\bar{1}\bar{1})[\bar{2}\bar{1}\bar{1}]$	$(100)[0\bar{1}1]$
14	Octahedral	$(111)[10\bar{1}]$	$(111)[1\bar{2}1]$	$(\bar{1}1\bar{1})[\bar{1}\bar{2}\bar{1}]$	$(010)[10\bar{1}]$
15	Octahedral	$(111)[\bar{1}10]$	$(111)[11\bar{2}]$	$(\bar{1}\bar{1}1)[\bar{1}\bar{1}\bar{2}]$	$(001)[\bar{1}10]$
16	Octahedral	$(1\bar{1}\bar{1})[01\bar{1}]$	$(1\bar{1}\bar{1})[\bar{2}\bar{1}1]$	$(111)[\bar{2}11]$	$(100)[01\bar{1}]$
17	Octahedral	$(1\bar{1}\bar{1})[101]$	$(1\bar{1}\bar{1})[12\bar{1}]$	$(\bar{1}1\bar{1})[\bar{1}112]$	$(0\bar{1}0)[101]$
18	Octahedral	$(1\bar{1}\bar{1})[\bar{1}\bar{1}0]$	$(1\bar{1}\bar{1})[1\bar{1}2]$	$(\bar{1}\bar{1}1)[\bar{1}112]$	$(00\bar{1})[\bar{1}\bar{1}0]$
19	Octahedral	$(\bar{1}1\bar{1})[0\bar{1}\bar{1}]$	$(\bar{1}1\bar{1})[21\bar{1}]$	$(\bar{1}\bar{1}1)[2\bar{1}1]$	$(\bar{1}00)[0\bar{1}\bar{1}]$
20	Octahedral	$(\bar{1}1\bar{1})[\bar{1}01]$	$(\bar{1}1\bar{1})[\bar{1}\bar{2}\bar{1}]$	$(111)[1\bar{2}1]$	$(010)[\bar{1}01]$
21	Octahedral	$(\bar{1}1\bar{1})[110]$	$(\bar{1}1\bar{1})[\bar{1}12]$	$(1\bar{1}\bar{1})[1\bar{1}2]$	$(00\bar{1})[110]$
22	Octahedral	$(\bar{1}\bar{1}1)[011]$	$(\bar{1}\bar{1}1)[2\bar{1}1]$	$(\bar{1}1\bar{1})[21\bar{1}]$	$(\bar{1}00)[011]$
23	Octahedral	$(\bar{1}\bar{1}1)[\bar{1}0\bar{1}]$	$(\bar{1}\bar{1}1)[\bar{1}21]$	$(1\bar{1}\bar{1})[1\bar{1}2]$	$(0\bar{1}0)[\bar{1}0\bar{1}]$
24	Octahedral	$(\bar{1}\bar{1}1)[1\bar{1}0]$	$(\bar{1}\bar{1}1)[\bar{1}\bar{1}\bar{2}]$	$(111)[11\bar{2}]$	$(001)[1\bar{1}0]$
25	Cube	$(100)[011]$	-	-	-
26	Cube	$(100)[01\bar{1}]$	-	-	-
27	Cube	$(010)[101]$	-	-	-
28	Cube	$(010)[10\bar{1}]$	-	-	-
29	Cube	$(001)[110]$	-	-	-
30	Cube	$(001)[1\bar{1}0]$	-	-	-

systems, while 'cube' represents the cube slip systems. Further, 'm' represents the matrix phase, while 'p' represents the precipitate phase.

4.2.2 Kinetics of Deformation

4.2.2.1 Dislocation Glide

Thermally-activated dislocation glide can be modeled using an Arrhenius-type activation energy-based model for crystalline materials (Kocks et al., 1975). A similar flow rule is

TABLE 4.2: Octahedral slip systems in γ phase

α	Type	$(m^\alpha)[s^\alpha]$
1	Octahedral	$(111)[01\bar{1}]$
2	Octahedral	$(111)[\bar{1}01]$
3	Octahedral	$(111)[1\bar{1}0]$
4	Octahedral	$(1\bar{1}\bar{1})[0\bar{1}1]$
5	Octahedral	$(1\bar{1}\bar{1})[\bar{1}0\bar{1}]$
6	Octahedral	$(1\bar{1}\bar{1})[110]$
7	Octahedral	$(\bar{1}1\bar{1})[011]$
8	Octahedral	$(\bar{1}1\bar{1})[10\bar{1}]$
9	Octahedral	$(\bar{1}1\bar{1})[\bar{1}\bar{1}0]$
10	Octahedral	$(\bar{1}\bar{1}1)[0\bar{1}\bar{1}]$
11	Octahedral	$(\bar{1}\bar{1}1)[101]$
12	Octahedral	$(\bar{1}\bar{1}1)[\bar{1}10]$

used in this framework for modeling the crystallographic shearing rate due to glide (Ranjan et al., 2021), with additional consideration for the slip system-level backstress:

$$\dot{\gamma}_g^\alpha = \begin{cases} \dot{\gamma}_{0j}^\alpha exp\left[-\dfrac{\Delta F_{gj}^\alpha}{kT}\left(1-\left(\dfrac{\left|\tau_j^\alpha-\chi_j^\alpha\right|-s_{aj}^\alpha}{s_{tj}^\alpha}\right)^{p_j^\alpha}\right)^{q_j^\alpha}\right] sgn\left(\tau_j^\alpha-\chi_j^\alpha\right); \left|\tau_j^\alpha-\chi_j^\alpha\right| > s_{aj}^\alpha, \alpha \in \text{oct}, j \in \text{m} \\[3em] \dot{\gamma}_{0j}^\alpha exp\left[-\dfrac{\Delta F_{gj}^\alpha}{kT}\left(1-\left(\dfrac{\left(\tau_j^\alpha-\chi_j^\alpha\right)-s_{aj}^\alpha}{s_{tj}^\alpha}\right)^{p_j^\alpha}\right)^{q_j^\alpha}\right]; \left(\tau_j^\alpha-\chi_j^\alpha\right) > s_{aj}^\alpha, \alpha \in \text{oct}, j \in \text{p} \\[3em] \dot{\gamma}_{0j}^\alpha exp\left[-\dfrac{\Delta F_{gj}^\alpha}{kT}\left(1-\left(\dfrac{\left|\tau_j^\alpha-\chi_j^\alpha\right|-s_{aj}^\alpha}{s_{tj}^\alpha}\right)^{p_j^\alpha}\right)^{q_j^\alpha}\right] sgn\left(\tau_j^\alpha-\chi_j^\alpha\right); \left|\tau_j^\alpha-\chi_j^\alpha\right| > s_{aj}^\alpha, \alpha \in \text{cube}, j \in \text{p} \\[3em] 0; \text{ otherwise} \end{cases}$$

$$(4.4)$$

where, $\alpha \in \text{oct}, j \in \text{m}$ denotes octahedral slip in the matrix phase, $\alpha \in \text{oct}, j \in \text{p}$ denotes octahedral slip in the precipitate phase, and $\alpha \in \text{cube}, j \in \text{p}$ denotes cube slip in the precipitate phase. Further, $\dot{\gamma}_{0j}^\alpha$ is the pre-exponential factor, ΔF_{gj}^α is the activation energy for dislocation glide in the absence of external stress, k is the Boltzmann constant, T is the absolute temperature, τ_j^α is the driving stress for dislocation glide, χ_j^α is the slip system-level backstress, s_{aj}^α is the athermal slip resistance, s_{tj}^α is the thermal slip resistance to dislocation glide, and p_j^α and q_j^α are parameters used to model the shape of the activation enthalpy function.

Based on the non-Schmid model proposed by Ranjan et al. (2021), the driving stress for dislocation glide, τ_j^α, is a function of the resolved shear stress (Schmid and non-Schmid stresses depending on the type of slip system), i.e.,

$$
\tau_j^\alpha =
\begin{cases}
\boldsymbol{s}^\alpha \cdot \boldsymbol{\sigma} \cdot \boldsymbol{m}^\alpha; \alpha \in \text{oct}, j \in \text{m} \\[2em]
\boldsymbol{s}^\alpha \cdot \boldsymbol{\sigma} \cdot \boldsymbol{m}^\alpha + \left(a_1 \boldsymbol{s}_{pe}^\alpha \cdot \boldsymbol{\sigma} \cdot \boldsymbol{m}_{pe}^\alpha + a_2 \boldsymbol{s}_{se}^\alpha \cdot \boldsymbol{\sigma} \cdot \boldsymbol{m}_{se}^\alpha \right. \\
\left. + a_3 \boldsymbol{s}_{cb}^\alpha \cdot \boldsymbol{\sigma} \cdot \boldsymbol{m}_{cb}^\alpha \right) exp\left(-\frac{\epsilon_p^i}{\epsilon_o^i} \right); \alpha \in \text{oct}, j \in \text{p} \\[2em]
\boldsymbol{s}^\alpha \cdot \boldsymbol{\sigma} \cdot \boldsymbol{m}^\alpha; \alpha \in \text{cube}, j \in \text{p}
\end{cases}
\tag{4.5}
$$

where, $(\boldsymbol{s}^\alpha, \boldsymbol{m}^\alpha)$ are unit vectors along the slip and slip plane normal on the primary slip plane, α, $\left(\boldsymbol{s}_{pe}^\alpha, \boldsymbol{m}_{pe}^\alpha \right)$, $(\boldsymbol{s}_{se}^\alpha, \boldsymbol{m}_{se}^\alpha)$ and $(\boldsymbol{s}_{cb}^\alpha, \boldsymbol{m}_{cb}^\alpha)$ are the unit vectors along slip and slip plane normal associated with the primary edge, secondary edge and cube planes, ϵ_p^i is the effective inelastic strain in the precipitate phase and ϵ_o^i is a material constant. The choice of the primary and secondary edge slip planes are motivated by crystallographic considerations of the formation of APB and the cross-slip planes onto which the super-dislocation core may spread (Paidar et al., 1984). The reader is referred to a comprehensive discussion of the underlying mechanisms by Ranjan et al. (2021). Beyond yield, dislocation glide is expected to be driven only by resolved shear stress on the primary slip plane. This is modeled using the exponential decay of non-Schmid stresses subsequent to yield (Ranjan et al., 2021). Further, also note that the non-Schmid stress components are present only for the octahedral slip systems in the precipitate phase. This is motivated by prior experimental and modeling studies, which point to the absence of the same for cube slip in the precipitate phase and octahedral slip in the matrix phase (Allan, 1995; Keshavarz and Ghosh, 2015a; Ranjan et al., 2021). Tension-compression asymmetry observed during yield is generally an effect of non-Schmid slip (Qin and Bassani, 1992; Patra et al., 2014). The experimental data for $\gamma^{'}$ (Ni₃Al) (Heredia and Pope, 1991a) and CMSX-4 (Allan, 1995) indicate that while there is clear evidence of tension-compression asymmetry for loading orientations in which the octahedral slip systems may be active ([001], for example), such effects are not present at higher temperatures for the $[1\bar{1}1]$ and [011] loading orientations, where cube slip may get activated. Hence, we have not considered non-Schmid behavior of the cube slip systems.

4.2.2.2 Dislocation Climb

In the absence of sufficient driving force due to external stresses, dislocations may not be able to overcome the barriers to glide, and such barriers may be overcome by climb. This deformation mechanism may be expected to be dominant at elevated temperatures and low stresses. The consideration for climb is motivated by experimental microstructure observations (Pollock and Argon, 1994; Li et al., 2022b), which indicate the same during high temperature deformation of single crystal Ni-based superalloys. For example, dislocation glide in the γ phase may get impeded at the γ/γ' interface, when stresses are not sufficient to penetrate or cut through the γ' precipitates. In order to accommodate the imposed deformation, these dislocations may climb along the γ/γ' interface by a thermally-activated process (see schematic in Figure 4.1(a)). Dislocation climb may also occur in the matrix and precipitate phases when encountered with other obstacles, such as dislocation networks, etc.

The crystallographic strain rate due to dislocation climb is modeled using a phenomenological power law model. Such models are generally of the form: $\dot{\gamma}_c = \rho b v$ and $v \propto \sigma^n$, where the symbols have their usual meaning (Mesarovic, 2017). Accordingly, we model the corresponding crystallographic strain rate as:

$$\dot{\gamma}_c^\alpha = \dot{\gamma}_{0cj}^\alpha exp\left(-\frac{\Delta F_{cj}^\alpha}{kT}\right) \rho_{Mj}^\alpha \left(\left|\sigma_j^\alpha\right|\right)^{n_j^\alpha} sgn\left(\sigma_j^\alpha\right); \alpha \in \text{oct,cube}, j \in \text{m,p} \qquad (4.6)$$

where $\dot{\gamma}_{0cj}^\alpha$ is a material constant, F_{cj}^α is the activation energy for diffusion-mediated processes contributing to dislocation climb. ρ_{Mj}^α is the density of mobile dislocations, σ_j^α is the resolved normal stress (perpendicular to the slip plane), and n_j^α is the climb exponent. Since climb is generally a diffusion-mediated process, we have assumed that there is no stress threshold for thermally-activated dislocation climb.

The driving stress for dislocation climb, σ_j^α, is given by:

$$\sigma_j^\alpha = \boldsymbol{s}^\alpha \cdot \boldsymbol{\sigma} \cdot \boldsymbol{s}^\alpha; \alpha \in \text{oct,cube}, j \in \text{m,p} \qquad (4.7)$$

This stress is the resolved normal stress perpendicular to the slip plane (Geers et al., 2014) and is motivated by crystallographic considerations for the Peach-Koehler force for dislocation climb (Peach and Koehler, 1950).
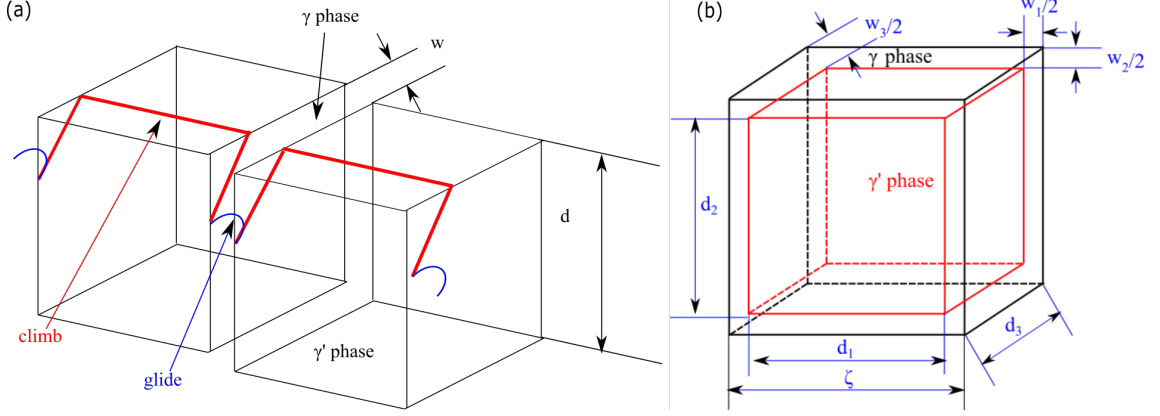
FIGURE 4.1: (a) Schematic of climb-enhanced glide, and (b) 3-D Unit Cell Model (UCM) for $\gamma/\gamma^{'}$ phases.

4.2.3 Slip Resistance and Substructure Evolution

The resistance to dislocation glide due to the long-range stress fields is modeled using the athermal slip resistance, s_a^α, and has dominant contributions from existing dislocations (Taylor hardening) and Orowan hardening due to bowing of dislocations around the precipitates (only in the matrix phase). Their contribution depends on the type of slip system and phase (Ranjan et al., 2021), and is given as:

$$s_{aj}^\alpha = \begin{cases} \tau_{th}^\alpha + k_{oro}\frac{G_j b_j}{\bar{w}} + k_{\rho j}G_j b_j\sqrt{\left(\sum_{\xi=1}^{N_m} A^{\alpha\xi}\rho_j^\xi\right)}; \alpha \in \text{oct}, j \in \text{m} \\ \\ \tau_{th}^\alpha + k_{\rho j}G_j b_j\sqrt{\left(\sum_{\xi=1}^{N_m} A^{\alpha\xi}\rho_j^\xi\right)}; \alpha \in \text{oct,cube}, j \in \text{p} \end{cases} \tag{4.8}$$

Here, τ_{th}^α is the threshold resistance, G_j is the shear modulus, b_j is the Burgers vector magnitude, $k_{\rho j}$ is the dislocation barrier strength, $A^{\alpha\xi}$ is the matrix of slip system dislocation interaction coefficients and ρ^ξ is the dislocation density in the slip system ξ. k_{oro} is a material constant associated with Orowan hardening, and $\bar{w}$ is the effective width of the matrix channel, with consideration for rafting during creep deformation. The constitutive equation for modeling the evolution of $\bar{w}$ due to rafting is discussed later.

Dislocations overcome the short-range stress due to lattice thermal vibrations, which is given by the thermal slip resistance, s_{tj}^α,

$$s_{tj}^\alpha = \tau_{0j}^\alpha; \alpha \in \text{oct,cube}, j \in \text{m,p} \tag{4.9}$$

Here, τ_{0j}^α is a material constant. Note that this term may have contributions from the intrinsic slip resistance and the solute solution strengthening in these superalloys. As a first-order approximation, this term is assumed to be invariant with deformation.

Constitutive equations governing the evolution of mobile and immobile dislocations have been adapted from (Patra and McDowell, 2012; Ranjan et al., 2021) and are given in Equations (4.10) and (4.11), respectively.

$$\dot{\rho}_{Mj}^\alpha = \frac{k_{mj}^\alpha}{b_j\lambda_j^\alpha}\left|\dot{\gamma}_{gj}^\alpha\right| - \frac{2R_c}{b_j}\rho_{Mj}^\alpha\left|\dot{\gamma}^\alpha\right| - \frac{k_{tj}^\alpha}{b_j\lambda_j^\alpha}\left|\dot{\gamma}_{gj}^\alpha\right| - \frac{1}{b_j l_{gj}^\alpha}\left|\dot{\gamma}_{cj}^\alpha\right|; \alpha \in \text{oct,cube}, j \in \text{m,p} \quad (4.10)$$

$$\dot{\rho}_{Ij}^\alpha = \frac{k_{tj}^\alpha}{b_j\lambda_j^\alpha}\left|\dot{\gamma}_{gj}^\alpha\right| - k_{dj}^\alpha\rho_{Ij}^\alpha\left|\dot{\gamma}_{gj}^\alpha\right| + \frac{1}{b_j l_{gj}^\alpha}\left|\dot{\gamma}_{cj}^\alpha\right|; \alpha \in \text{oct,cube}, j \in \text{m,p} \quad (4.11)$$

The first term in the mobile dislocation evolution rate (Equation (4.10)) accounts for the multiplication of mobile dislocations at pre-existing dislocation segments (Essmann and Mughrabi 1979), where k_{mj}^α denotes the dislocation multiplication constant. The annihilation of dislocation dipoles within a capture radius, R_c, is modeled using the second term. Trapping of mobile dislocation segments at other dislocations is modeled using the third term, where k_t^α is the dislocation trapping constant. The effective free path of dislocation trapping λ_j^α is given by Equation (4.12). The migration rate of mobile dislocations (due to climb) is modeled using the last term, where $l_{gj}^\alpha \approx \lambda^\alpha$ is the average distance swept by glide dislocations on the slip plane (Patra and McDowell, 2012). The effective mean free path of dislocations, λ^α, is generally given as the harmonic mean of the individual obstacle mean free paths (Krausz and Krausz, 1996; Austin and McDowell, 2011) and is given by:

$$\frac{1}{\lambda^\alpha} = \begin{cases} \sqrt{\rho_j} + \frac{1}{w}; \alpha \in \text{oct}, j \in \text{m} \\ \\ \sqrt{\rho_j}; \alpha \in \text{oct,cube}, j \in \text{p} \end{cases} \quad (4.12)$$

While the mean free path for the precipitates is primarily a function of the dislocation density, the channel width may also play a role in limiting the dislocation mean free path for the matrix phase. The trapping of mobile dislocations increases the immobile dislocation density as given in the first term of Equation (4.11). The annihilation of dislocations by dynamic recovery is represented by the second term in Equation (4.11), where k_{dj}^α is the dynamic recovery constant. Migration of mobile dislocation density increases the immobile dislocation density as given in the third term in Equation (4.11).

4.2.4 Backstress

Backstress in single crystal Ni-based superalloys under cyclic loading originates from the accumulation and rearrangement of dislocations, particularly around the $\gamma^{'}$ precipitates, which act as strong obstacles to dislocation motion. This internal stress field opposes the applied load during reversal. The model for backstress evolution is adapted from Shenoy et al. (2008), and is given as a function of the dislocation density, i.e.,

$$\chi_j^\alpha = \left(k_{\chi 1}^\alpha G_j b_j \sqrt{\rho_j^\alpha} sgn \left(\tau_j^\alpha - \chi_j^\alpha \right) - k_{\chi 2}^\alpha \chi_j^\alpha \right) \left| \dot{\gamma}_j^\alpha \right|; \alpha \in \text{oct,cube}, j \in \text{m,p} \qquad (4.13)$$

Here, $k_{\chi 1}^\alpha$ and $k_{\chi 2}^\alpha$ are material constants. The first term in this model represents the directional hardening due to the accumulation of dislocations. The second term is a recovery term similar to the Armstrong-Frederick model. Here, both octahedral and cube slip systems are included, although backstress is primarily expected to play a role in affecting slip for the octahedral slip systems (Shenoy et al., 2008).

4.2.5 Microstructure Evolution During Creep Deformation

The microstructure evolution during high-temperature creep deformation is assumed to be governed by two primary mechanisms: isotropic coarsening (homothetic growth of single $\gamma^{'}$ precipitates) (Epishin et al., 2009; Fedelich et al., 2009; Le Graverend et al., 2014) and directional coarsening (rafting) (Henderson et al., 1998; Matan et al., 1999b). Isotropic coarsening does not change the internal stress state in the structure, it is just a change of scale (Fedelich et al., 2009). On the other hand, directional coarsening (rafting) relaxes the internal stresses significantly (Fedelich et al., 2009). Based on prior modeling works (Fedelich et al., 2009; Tinga et al., 2009a; Fan et al., 2015; Guo et al., 2021), two geometric parameters, matrix channel width, w_i, and precipitate size, d_i, are required to describe the current state of $\gamma^{'}$ morphology along the ith direction. These two parameters are schematically described in terms of the geometric model as shown in Figure 4.1(b). The relationship between these parameters is as follows (Fedelich et al., 2009; Guo et al., 2021):

$$\zeta = w_1 + d_1 = w_2 + d_2 = w_3 + d_3 \qquad (4.14)$$

where ζ is the microstructure periodicity and directions 1, 2, and 3 correspond to the [001], [010], and [001] directions of the reference crystal.

The matrix channel width is assumed to evolve according to two mechanisms: isotropic coarsening and rafting (Fan et al., 2015). As a first-order approximation, dissolution of the γ' phase (evolution of volume fraction of γ' phase) is not considered as the volume fraction of the precipitates has been found to be invariant up to ≈ 980 °C (Serin et al., 2004). Accordingly, the volume fraction of the γ' phase, $f_{\gamma'}$, is assumed to be constant during isothermal creep deformation.

4.2.5.1 Isotropic Coarsening

The driving force for isotropic coarsening is due to the reduction of overall interfacial energy (Baldan, 2002). It is generally assumed that this phenomenon is independent of the stress state and only a function of time and temperature (Tinga et al., 2009a; Fedelich et al., 2012). Isotropic coarsening occurs due to Ostwald ripening during the rafting process. During isotropic coarsening, the smaller precipitates disappear along with an increase in the size of the larger precipitates, due to which the microstructure coarsens at a global scale and increases the microstructure periodicity (Tinga et al., 2009a). Following prior works (Tinga et al., 2009a; Le Graverend et al., 2014; Fan et al., 2015), we model isotropic coarsening using the Lifschitz-Slyosov-Walter (LSW) theory (Glicksman and Fradkov, 1995). According to LSW theory, the microstructure periodicity, $\zeta(t)$, increases with time, t, according to the following:

$$\zeta(t)^3 - \zeta_0^3 = Kt \tag{4.15}$$

where, $\zeta_0 = w_0 + d_0$ is the initial microstructure periodicity, and K is a temperature-dependent material constant. w_0 is the initial channel width and d_0 is the initial precipitate size. The rate of evolution of the microstructure periodicity is given by:

$$\dot{\zeta} = \frac{K}{3}\left(\zeta_0^3 + Kt\right)^{\frac{-2}{3}} \tag{4.16}$$

Moreover, it is assumed that the precipitate size and channel width increase proportionally from their initial value as:

$$\frac{\dot{w}_{iso}}{\dot{\zeta}} = \frac{w_0}{\zeta_0} \tag{4.17}$$

where $\dot{w}_{iso}$ is the rate of evolution of channel width due to isotropic coarsening and w_0 is the initial channel width.

4.2.5.2   Directional Coarsening (Rafting)

Rafting is the morphological change of the $\gamma^{'}$ precipitate from cuboidal geometry to elongated rafts at elevated temperatures. During rafting, the γ channels widen in the direction of applied stress for alloys with negative lattice misfit subjected to tension (Lukáš et al., 1996) and give way to dislocation accumulation and motion due to the Orowan mechanism. It must be noted that rafting may occur parallel or perpendicular to the loading axis, depending on the lattice misfit and the direction of applied stress. For negative misfit δ and positive stresses σ, ($\sigma \times \delta < 0$), rafts would form perpendicular to the loading axis (N-type rafts), whereas for ($\sigma \times \delta > 0$) rafts would form parallel to the loading axis, i.e., γ channels widen perpendicular to the direction of applied stress (P-type rafts) (Mughrabi, 2014). However, our proposed model is valid only for alloys with negative lattice misfit subjected to tension.

We propose to model the rafting kinetics using a modified form of the Johnson-Mehl-Avrami-Kolmogorov (JMAK) equation (Porter and Easterling, 2009). The JMAK equation has been extensively used to model the kinetics of isothermal phase transformations in various metallurgical applications (Ohring, 1998; Jiang et al., 2014; Yang et al., 2020). The original JMAK model has been modified here to account for temperature- and stress-dependence to model the microstructure evolution during rafting.

If rafting is considered as an evolution of $\gamma^{'}$ precipitate morphology from the cuboidal structure to the rafted structure at a constant temperature, then the rate of increase of channel width in the direction of applied stress (rafting direction) is given by:

$$(\dot{w}_3)_{raft} = A_0 \left(w_f - w_3 \right) exp \left(-\frac{\Delta F_r - \bar{\sigma} \Delta V}{kT} \right) \tag{4.18}$$

where, A_0 is the Avrami constant, ΔF_r is the associated activation energy, $\bar{\sigma}$ is the von Mises effective stress, and ΔV is the activation volume. Note that while this constitutive model is similar in form to those proposed by (Fedelich et al., 2009; Tinga et al., 2009a; Fan et al., 2015), our form of constitutive model allows a more direct physical interpretation in terms of the activation energy for rafting and its reduction due to the current stress state. Infinite $\gamma^{'}$ plates like rafts will form perpendicular to the direction of loading for a fully rafted microstructure (Fedelich et al., 2009). As a result, the channel width evolves from w_0 (initial channel width) to w_f (channel width for a fully rafted microstructure) (Fedelich et al., 2009). The instantaneous volume fraction of the precipitate is given as (Serin et al., 2004),

$$f_{\gamma'} = \left(1 - \frac{w_3}{\zeta} \right) \left(1 - \frac{w_2}{\zeta} \right) \left(1 - \frac{w_1}{\zeta} \right) \tag{4.19}$$

where w_1 and w_2 are the channel widths along directions transverse to the loading direction. For loading in the [001] direction, $w_1 = w_2$. For a fully rafted microstructure, $w_1 = w_2 = 0, w_3 = w_f$. Thus,

$$f_{\gamma'} = 1 - \frac{w_f}{\zeta_0} \tag{4.20}$$

$$w_f = \left(1 - f_{\gamma'}\right) \zeta_0 \tag{4.21}$$

Here, w_f remains constant as $f_{\gamma'}$ and ζ_0 is constant. However, due to precipitate dissolution, the volume fraction of γ' precipitates may decrease with an increase in temperature after a critical temperature. Accordingly, the initial microstructure periodicity parameter, ζ_0, may vary for other alloys. The total increase of channel width in the direction of rafting at any given time is the summation of an increase in channel width due to isotropic coarsening (Equation 4.17) and the increase of channel width due to rafting (Equation 4.18) (Fan et al., 2015), i.e.,

$$\dot{w}_3 = (\dot{w}_3)_{raft} + (\dot{w})_{iso} \tag{4.22}$$

From (Equation 4.19),

$$w_1 = w_2 = \zeta \left(1 - \sqrt{\frac{f_{\gamma'}}{1 - \frac{w_3}{\zeta}}} \right) \tag{4.23}$$

Note that the above description of channel width evolution holds only for a crystal loaded along the [0 0 1] direction. However, the orientation dependence of rafting needs to be considered for creep loading along different orientations. In order to accomplish this, we adopt the tensorial description of channel width proposed by Desmorat et al. (2017), i.e.,

$$\boldsymbol{w}' = \boldsymbol{Q}^T \cdot \boldsymbol{w} \cdot \boldsymbol{Q} \tag{4.24}$$

Here, $\boldsymbol{w}'$ is the second rank tensor of channel width in the rotated configuration, $\boldsymbol{Q}$ is the rotation tensor and $\boldsymbol{w}$ is a second order tensor of channel width with diagonal elements as w_1, w_2 and w_3, and the non-diagonal elements are zero. Depending on the applied rotation, the rotated channel width tensor, $\boldsymbol{w}'$, may of course have non-diagonal components. We adopt the same formulation in our work, with $\boldsymbol{Q}$ directly obtained from the rotation tensor corresponding to the Euler angles in the Bunge notation. Note that this is the same rotation tensor that we use for the rotation of the elastic stiffness tensor as well.

Finally, the effective channel width, $\bar{w}$, is calculated as the L^2 norm of the channel width tensor (Desmorat et al., 2017), i.e.,

$$\bar{w} = ||\boldsymbol{w}'|| \tag{4.25}$$

As mentioned earlier, the effect of rafting on creep deformation is incorporated in the crystal plasticity model by Orowan strengthening in the matrix phase (Equation 4.8).

These equations comprise the full set of equations for modeling the thermo-mechanical deformation of Ni-based superalloys. A fully implicit Newton-Raphson scheme is implemented for the time integration of the constitutive model. The constitutive model has been implemented as a material model and interfaced with the open-source finite element library, MOOSE (Permann et al., 2020).

4.2.6 Model Parameters

Complex physical mechanisms are involved in the deformation of Ni-based superalloys, and their representation in the constitutive equations makes the calibration of the numerous model parameters non-trivial.

In the present work, we have demonstrated the application of the model to predict thermo-mechanical deformation in two different single crystal superalloys, CMSX-4 and PWA-1484. These materials are similar in composition, with small differences in the alloy element content between them (Rodas and Neu, 2018). First, we calibrated the model parameters for CMSX-4 by fitting them to the available experimental data for tension tests and cyclic tests for different temperatures, orientations, and strain rate conditions. Subsequently, we estimated the parameters pertaining to creep deformation for different temperatures, orientations, and stress conditions. A similar procedure was followed for estimating the model parameters for PWA-1484. The chemical composition of CMSX-4 and PWA-1484 is given in Table 4.3.

TABLE 4.3: Chemical composition of CMSX-4 (in wt. %) (Reed, 2008).

Alloy	Cr	Co	Mo	W	Al	Ti	Ta	Re	Hf	Ni
CMSX-4	6.5	9.6	0.6	6.4	5.6	1.0	6.5	3.0	0.1	Bal.
PWA1484	5.0	10.0	2.0	6.0	5.6	-	9.0	3.0	0.1	Bal.

The temperature-dependent elastic constants for γ and $\gamma^{'}$ phases are given in Table 4.4.

Some of the parameters related to slip resistance and substructure evolution (k_{oro}, $k_{\rho j}^{\alpha}$, $A^{\alpha\alpha}$, $A^{\alpha\zeta}$, ρ_{M}^{0}, ρ_{I}^{0}, k_{mj}^{α}, R_{c}, k_{tj}^{α}, k_{dj}^{α}) were adopted directly from Ranjan et al. (2021). Here, k_{oro} (material constant associated with Orowan hardening) varies between 0.238 and 2.15 (Tinga et al., 2008; Ranjan et al., 2021). Accordingly, $k_{oro} = 0.25$ is assumed in our model. The initial dislocation densities (ρ_{M}^{0}, ρ_{I}^{0}) are assumed to be very low ($1 \times 10^{10} m^{-2}$) for

TABLE 4.4: Temperature-dependent elastic constants for the γ and $\gamma^{'}$ phases (Keshavarz et al., 2016).

Parameter	Value
γ	$C_{11} = (298.0 - 0.096T)\,\text{GPa}$
	$C_{12} = (191.0 - 0.057T)\,\text{GPa}$
	$C_{44} = (139.0 - 0.035T)\,\text{GPa}$
$\gamma^{'}$	$C_{11} = (325.0 - 0.096T)\,\text{GPa}$
	$C_{12} = (209.0 - 0.057T)\,\text{GPa}$
	$C_{44} = (144.0 - 0.035T)\,\text{GPa}$

an undeformed $\gamma^{'}$ phase Ranjan et al. (2021). Further, the range of initial dislocation density for γ phase has been experimentally reported of order $10^{11} - 10^{12} m^{-2}$ (Jacome et al., 2013; Pollock and Argon, 1992). Accordingly, somewhat higher initial dislocation density ($1 \times 10^{11} m^{-2}$) has been assumed for γ phase Ranjan et al. (2021). The dislocation hardening parameters ($k_{\rho j}^{\alpha}$, $A^{\alpha\alpha}$, $A^{\alpha\zeta}$) are chosen to have physically representative values (Ranjan et al., 2021). The material constants (k_{mj}^{α}, R_c, k_{tj}^{α}, k_{dj}^{α}) are calibrated by fitting the model to the experimental hardening response. Values of these constants are in the same range as earlier studies (Patra and McDowell, 2012; Patra et al., 2014; Ranjan et al., 2021). The magnitude of the Burgers vector was taken from Keshavarz and Ghosh (2015a). The temperature-dependent material parameter, τ_{0j}^{α}, in Equation (4.9) was obtained by fitting to the tension test data. Here, we initially started with the values given by Ranjan et al. (2021) and then adjusted according to the fit to the experimental tensile test data. While the material considered in this prior study was the same, differences in processing history might have contributed to a different initial threshold slip resistance. A single set of the flow parameters was chosen for deformation at all the different temperatures and strain rates. Model parameters related to kinematic hardening, $k_{\chi 1}^{\alpha}$ and $k_{\chi 2}^{\alpha}$, were obtained by fitting the model to the available cyclic test data. A parametric study for $k_{\chi 1}^{\alpha}$ and $k_{\chi 2}^{\alpha}$ was performed by maintaining the ratio $k_{\chi 1}^{\alpha}/k_{\chi 2}^{\alpha} = 1.055$. This is in the range of literature values (0.47 to 2) for similar kinematic hardening models (Shenoy et al., 2008; Agaram et al., 2021). Essentially, a ratio close to unity for these two kinematic hardening parameters implies lower kinematic hardening and vice versa.

Based on the best fit, the activation energy for dislocation climb, F_{cj}^{α}, was set to $8.46 \times 10^{-19} J$ for octahedral slip and $1.28 \times 10^{-18} J$ for cube slip. $n_m^{\alpha} = 5$ was used for the creep exponent of the matrix phase, and $n_p^{\alpha} = 10$ was used for the creep exponent of the precipitate phase. This is in the range of creep exponents calculated from experimental data for similar superalloys (Sharma et al., 2008; Huang et al., 2016). $\dot{\gamma}_{0c}$ was obtained based on the best fit to the experimental data. Note that all model parameters related

to creep were assumed to be temperature-invariant. All the temperature-invariant model parameters for inelastic deformation are listed in Tables 4.5, 4.6, and the temperature-dependent model parameters are listed in Table 4.7.

Further, the initial microstructure parameters, $f_{\gamma'}$, $d_{\gamma'}$ and w_0, were adopted from Tinga et al. (2009b). Directional coarsening parameters (ΔF_r and ΔV) were set to $6.64 \times 10^{-20} J$ and $6.64 \times 10^{-28} m^3$, respectively. This is in the range given by Tinga et al. (2009a). The isotropic coarsening parameter K and directional coarsening parameter, A_0, were determined by performing a parametric study and comparing with the experimental channel width data (not presented here). The initial microstructure, isotropic coarsening, and directional coarsening parameters are listed in Table 4.8.

TABLE 4.5: Temperature-invariant flow rule related model parameters for the γ and γ' phases.

Parameters	Material	$\alpha \in$ oct, $j \in$ p $\left(\gamma'\right)$	$\alpha \in$ cube, $j \in$ p $\left(\gamma'\right)$	$\alpha \in$ oct, $j \in$ m (γ)
Glide flow rule:	CMSX-4	1.5×10^{-2},	1×10^{-3},	1×10^{-5},
$\dot{\gamma}_{0j}\ (s^{-1})$,		$1.4Gb^3$, 0.3, 1.45	$0.5Gb^3$, 0.5, 1	$0.25Gb^3$, 0.9, 1
$\Delta F_{gj}^{\alpha}, p_j^{\alpha}, q_j^{\alpha}$	PWA-1484	1.5×10^{-2},	1×10^{-3},	1×10^{-5},
		$1.4Gb^3$, 0.3, 1.45	$0.5Gb^3$, 0.5, 1	$0.25Gb^3$, 0.9, 1
Climb flow rule:	CMSX-4	8.46×10^{-19},	1.28×10^{-18},	8.46×10^{-19},
$\Delta F_{cj}^{\alpha}\ (J)$,		3.84×10^{-15}, 10	5.72×10^{-2}, 10	4.5, 5
$\dot{\gamma}_{0cj}^{\alpha}\ (MPa \times s/mm)^{-1}$,	PWA-1484	6.42×10^{-19},	1.38×10^{-18},	6.42×10^{-19},
n_j^{α}		3.84×10^{-15}, 10	93.9, 10	2.4×10^{-5}, 5

After obtaining a reasonable fit with the experimental data for CMSX-4 for various loading conditions, we performed calibration of the model to the available experimental data for PWA-1484. Most of the model parameters for PWA-1484 were assumed to be the same as CMSX-4. This is reasonable, given that the chemical composition of both the alloys is comparable (Rodas and Neu, 2018). Note that the hardening and the dislocation evolution parameters are assumed to be the same for both alloys as given in a Table 4.6. However, the parameters, τ_{0j}^{α} and $\dot{\gamma}_{0j}$ had to be modified based on a fit to the experimental tension test data for PWA-1484. Further, F_{cj}^{α} and $\dot{\gamma}_{0c}$ were also calibrated by fitting them to the experimental creep test data for PWA-1484.

TABLE 4.6: Temperature-invariant hardening and backstress related model parameters for the γ and γ' phases. The same parameters are used for both CMSX-4 and PWA-1484.

Parameters	$\alpha \in$ oct, $j \in$ p $\left(\gamma'\right)$	$\alpha \in$ cube, $j \in$ p $\left(\gamma'\right)$	$\alpha \in$ oct, $j \in$ m (γ)
Orowan hardening: k_{oro}	-	-	0.25
Dislocation hardening: $k_{\rho j}^{\alpha}$, $A^{\alpha\alpha}$, $A^{\alpha\zeta}$	$0.31, 1, 1 \times 10^{-4}$	$0.31, 1, 1 \times 10^{-4}$	$0.31, 1, 1 \times 10^{-4}$
Initial dislocation densities: $\rho_M^0 \left(m^{-2}\right)$ $\rho_I^0 \left(m^{-2}\right)$	$1 \times 10^{10}, 1 \times 10^{10}$	$1 \times 10^{10}, 1 \times 10^{10}$	$1 \times 10^{11}, 1 \times 10^{11}$
Dislocation evolution: k_{mj}^{α}, R_c, k_{tj}^{α}, k_{dj}^{α}	$0.07, 6b, 0.065, 600$	$0.07, 6b, 0.065, 1 \times 10^6$	$7.096 \times 10^{-3}, 6b, 1.35 \times 10^{-2}, 3000$
Threshold slip resistance: τ_{th}^{α}	71.5	31.5	1.5
Burgers vector magnitude: $b(nm)$	0.249	0.249	0.249
Backstress: $k_{\chi1}^{\alpha}$, $k_{\chi2}^{\alpha}$	9500, 9000	9500, 9000	9500, 9000

TABLE 4.7: Temperature-dependent model parameters for the γ and γ' phases.

Parameter	T(K)	$\alpha \in$ oct $j \in$ p $\left(\gamma'\right)$		$\alpha \in$ cube $j \in$ p $\left(\gamma'\right)$		$\alpha \in$ oct $j \in$ m (γ)	
		CMSX-4	PWA-1484	CMSX-4	PWA-1484	CMSX-4	PWA-1484
$\tau_{0j}^{\alpha} (MPa)$	1123-1143	674.25	674.25	411.6	411.6	265.71	275.7076
$\tau_{0j}^{\alpha} (MPa)$	1223-1273	554.18	554.18	286.10	186.10	228.45	153.4454

TABLE 4.8: Microstructural parameters for CMSX-4 and PWA-1484. Note that in the absence of relevant experimental data for PWA-1484, the same microstructural parameters have been assumed, as for CMSX-4.

Parameters	Value
Volume fraction: f_γ, $f_{\gamma'}$	0.28, 0.72
Precipitate size: $d_\gamma (mm)$, $d_{\gamma'} (mm)$	$1, 0.5 \times 10^{-3}$
Initial channel width: $w_0 (mm)$	0.06×10^{-3}
Directional coarsening: A_0, $\Delta F_r (J)$, $\Delta V (m^3)$	$1 \times 10^{-9}, 6.64 \times 10^{-20}, 6.64 \times 10^{-28}$
Isotropic coarsening: $K \left(mm^3/s\right)$	3×10^{-16}

4.3 Results and discussion

We have used the constitutive model to predict the tensile, cyclic, and creep deformation behavior of CMSX-4 and PWA-1484 for various loading conditions. All simulations were performed with single-element calculations. Symmetric boundary conditions were applied on the three adjacent faces of the cell, implying that the displacement normal to these three faces was fixed to be zero, and the corner node common to these three faces was fixed to prevent rigid body rotation. In the laboratory coordinate system, the crystal was loaded along the z-direction for all the cases (cf. Figure 5(a) in (Ranjan et al., 2021) for a schematic). While displacement-controlled loading was applied for the tensile and cyclic tests at the prescribed strain rates, stress-controlled loading was applied for the creep tests at the prescribed stress values. For displacement-controlled loading, a constant nominal strain rate was maintained throughout the simulation. For creep tests performed under stress-controlled loading, the stress was initially ramped up to the desired stress level at a constant stress rate within the initial 10 s of the simulation and then held constant for the remaining duration of the simulation. A hexahedral finite element, with linear interpolation, was used for all simulations. Although all the simulations have been performed using a single element, the same can easily be performed for a larger number of finite elements and complex geometries. We have verified the same by performing two additional simulations of tension and creep using 27 elements and comparing the predicted response with the single element predictions. These results are shown in the Figure 4.15. As can be seen, there is no significant difference between the predictions for the two cases. Further, loading orientations used in the present work are shown in Figure 4.2 and Euler angles (in Bunge notation) for this loading orientation are given in Table 4.9.

TABLE 4.9: Euler angles (in Bunge notation) for loading orientations used in the present work.

Orientation no.	Crystal orientation	Euler angles (degrees)
1	[001]	[0, 0, 0]
2	[011]	[0, -45, 0]
3	[$\bar{1}$11]	[45, -54.736, 0]
4	[$\bar{1}$23]	[255.4, 36.7, 333.43]

We have gathered relevant experimental data for CMSX-4 and PWA-1484 from different sources in the literature. These are in the temperature range of 1123-1273 K, which is generally also the operating temperature of these alloys in aerospace applications (Allan, 1995; Ali et al., 2020a). The different sets of experimental conditions are listed in Table 4.10 along with the test temperatures. The experimental data sets for tension tests, cyclic
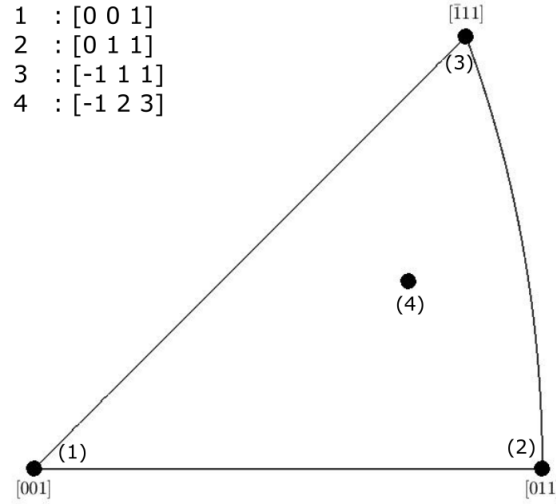
FIGURE 4.2: Loading orientations used in the present work.

tests, and creep tests were used for calibration, while the relaxation data sets were used for model validation. While it is possible that the different sources may have used materials with different processing histories for their experiments, this is unavoidable since there is no single data set that contains all the different conditions used for calibration and prediction in our work.

TABLE 4.10: List of the experimental data used for model prediction and validation.

Alloy	Test	Experimental data	T(K)
CMSX-4	Tension tests	(Vattré and Fedelich, 2011)	1123, 1223
CMSX-4	Cyclic tests	(Vattré and Fedelich, 2011)	1123, 1223
CMSX-4	Creep tests	(Vattré and Fedelich, 2011)	1123
CMSX-4	Creep tests	(MacLachlan et al., 2001)	1223
CMSX-4	Creep tests	(MIURA et al., 2003)	1273
CMSX-4	Relaxation tests	(Vattré and Fedelich, 2011)	1123, 1223
PWA-1484	Tension tests	(Staroselsky and Cassenti, 2010)	1255
PWA-1484	Cyclic tests	(Staroselsky and Cassenti, 2011)	1143
PWA-1484	Creep tests	(Staroselsky and Cassenti, 2011)	1143, 1255
PWA-1484	Creep tests	(Staroselsky and Cassenti, 2010)	1200
PWA-1484	Relaxation tests	(Staroselsky and Cassenti, 2011)	1255

4.3.1 Tensile loading

The constitutive model was fit to the experimental tension test data at different temperatures and strain rates. Figure 4.3 compares the true stress-strain curves for CMSX-4 at different strain rates and 1123 K for (a) [001] and (b) [$\bar{1}$11] loading orientation and 1223 K

for (c) [001] and (d) [$\bar{1}$11] loading orientation, respectively. Figure 4.4 compares the true stress-strain curves for PWA-1484 at 1255 K for (a) [001] and (b) [$\bar{1}$11] loading orientation. A reasonable fit was obtained for loading at the different strain rates, temperatures, and crystal orientations for both materials. The model can capture both the temperature and strain rate sensitivity effects for CMSX-4. This is primarily due to the Kocks-type thermally activated flow rule (cf. Equation 4.4), which can account for such effects via the activation enthalpy, shape parameters, and the pre-exponential factor. In addition, the temperature-dependent slip resistance (cf. Equation 4.9 and Table 4.7) is also used to capture the experimentally observed temperature dependence of the yield stress. Limited experimental data are available for PWA-1484, and hence such predictions are not possible. Deviations from exact single crystal orientations in the experiments (cf. Vattré and Fedelich (2011)) could also be a source of discrepancy between the model predictions and experimental data. Further, our model does not predict the initial softening subsequent to yield, as experimentally observed for CMSX-4. This is especially evident for both the [001] and [1$\bar{1}$1] loading at higher strain rates. Microstructure degradation effects could be contributing to this phenomenon. This is also linked to the formation of Kear-Wilsdorf (KW) locks due to cross-slip (Paidar et al., 1984). Initially, the yield strength increases as dislocations are hindered by these locks. However, once the dislocations begin to shear through these barriers, the resistance to their motion decreases, leading to a reduction in the flow stress required for further glide. As discussed in Section 4.3.9, discrepancies between the experiments and simulations can be addressed by adding the effect of coherency stresses (lattice misfit), precipitate dissolution, and the effect of APB energy on precipitate shearing. Ranjan et al. (2021) have shown that such effects can be captured by accounting for the decay of non-Schmid stresses subsequent to the initiation of plastic deformation (cf. Equation (4.5)). However, we have neglected such effects as a first-order approximation in the present work, where the main focus is on predicting the cyclic and creep response. The ability of the model to predict the orientation-dependent yield stress of CMSX-4 over a wide range of temperatures (from room temperature to 1123 K) has also been demonstrated in Ranjan et al. (2021).

The difference in the flow stress for the two different orientations under identical loading conditions may be attributed to the elastic anisotropy and the activation of different slip systems. Plastic deformation in the [001] orientation is governed by the octahedral {111} < 110 > slip systems, while for the [$\bar{1}$11] orientation, it is dominated by the cube {100} < 110 > slip systems. The tensile response of CMSX-4 for the [001] loading orientation exhibits three stages of deformation. The elastic regime (stage 1) is followed by dislocation glide in γ channel (stage 2) and finally γ' precipitate shearing (stage 3), which is nearly a

horizontal stress-plateau (Vattré et al., 2010; Gupta and Bronkhorst, 2021). For loading along the [$\bar{1}11$] orientation, the elastic regime (stage 1) is followed by a low hardening phase (stage 3), where stress drops from the upper yield point, and stage 2 is missing for loading along the [111] orientation (Vattré et al., 2010). In our simulations, the stress drop is missing for both orientations, although it has been shown earlier that such effects can be captured by the constitutive model (Ranjan et al., 2021). Note that the constitutive model is still capturing the effects of precipitate evolution on the Orowan stress, although its effect on the macroscopic stress is not significant. This is described in 4.3.5. Finally, it is observed that there is a significant drop in the flow stress (150-200 MPa) from 1123 K to 1223 K for a given orientation and strain rate. This could be correlated with the non-Schmid deformation mechanisms, which are operative up to about 1123 K and contribute to the strength plateau (cf. (Allan, 1995; Keshavarz and Ghosh, 2015a; Ranjan et al., 2021). Presumably, the strength of the alloy drops significantly, as the contribution of non-Schmid stresses (due to APB formation) is reduced beyond this temperature.
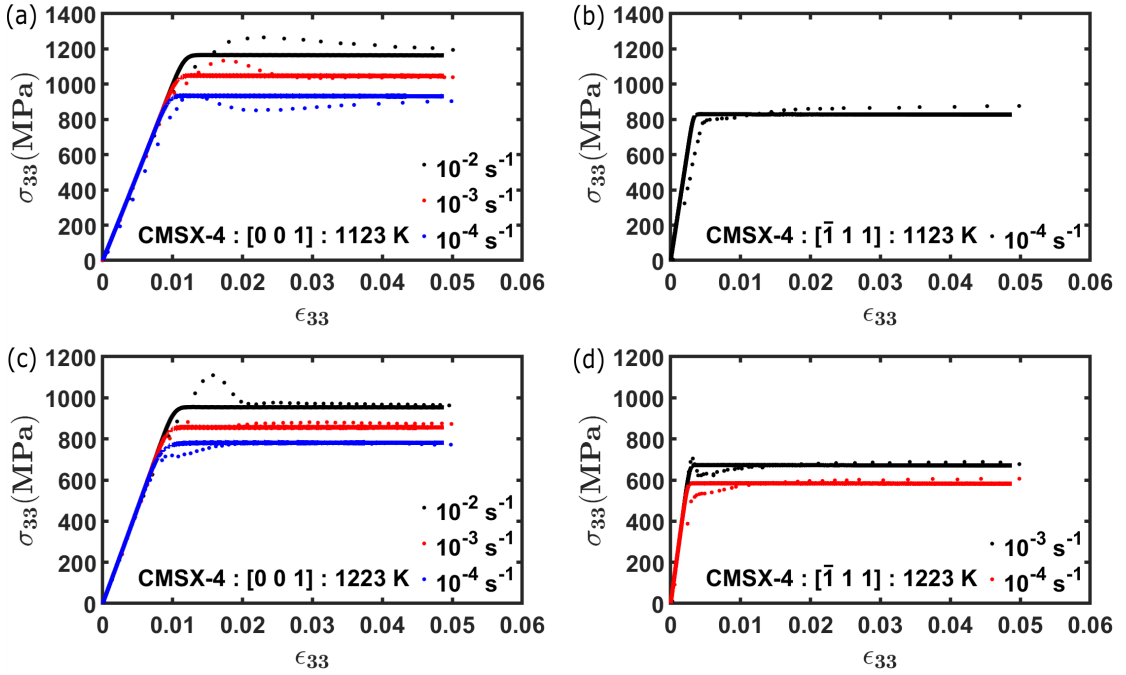
FIGURE 4.3: Simulated true stress-strain curves for different strain rates at 1123 K for (a) [001] and (b) [$\bar{1}11$] loading orientations, and at 1223 K for (c) [001] and (d) [$\bar{1}11$] loading orientations as compared with the experimental data for CMSX-4 (Vattré and Fedelich, 2011). The simulated data is plotted with solid lines, while the experimental data is plotted with symbols.
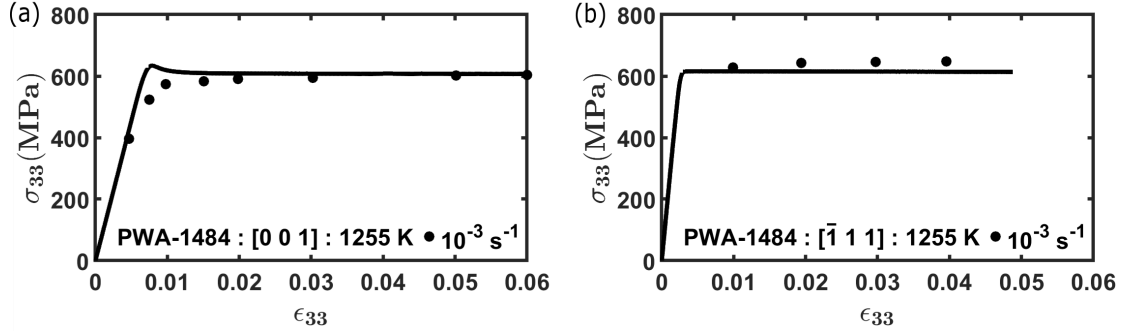
FIGURE 4.4: Simulated true stress-strain curves at 1255 K for (a) [001] and (b) [$\bar{1}$11] orientations as compared with the experimental data for PWA-1484 (Staroselsky and Cassenti, 2010). The simulated data is plotted with solid lines, while the experimental data is plotted with symbols.

4.3.2 Cyclic loading

The constitutive model was fit to the experimental data for cyclic tests for CMSX-4 and PWA-1484 with different strain amplitudes and at different temperatures. Figure 4.5 shows a comparison of model predictions of the cyclic stress-strain curves with the corresponding experimental data for CMSX-4 loaded along different orientations ([001], [011], [$\bar{1}$11]) at different strain rates and temperatures. Figure 4.6 compares the simulated cyclic stress-strain curves with the experimental data for PWA-1484 loaded along different orientations ([001], [$\bar{1}$11], [$\bar{1}$23]) at 1143 K. All the simulated stress-strain curves are plotted for twenty cycles for CMSX-4. For PWA-1484, the number of cycles for the different tests is shown in the corresponding figures.

Model predictions for CMSX-4 agree qualitatively with the experimental data. There is some discrepancy in the predicted flow stress for the [$\bar{1}$11] cyclic loading cases at 1123 K (see Figure 4.5(c) and (d)), which may be due to the model's inability to accurately capture the strain rate sensitivity of the material for the [$\bar{1}$11] orientation. Given that the model is able to predict the tensile response for this orientation with reasonable accuracy, this discrepancy could be indicative of the temperature- and strain rate-dependence of the backstress evolution, which has not been considered in the present work. Cube slip is expected to dominate for these loading conditions. For the other loading conditions, the model predicts a wider hysteresis loop as compared to the experiments, although the peak stresses are predicted with reasonable accuracy. In all the cases, the simulated stress-strain curves were found to converge after two or three cycles towards a stabilized hysteresis loop.

A similar observation was noted in the experimental study of Vattré and Fedelich (2011) as well.

The model predicts the cyclic response for PWA-1484 with higher accuracy (see Figure 4.6) as compared to CMSX-4. While details of the experimental conditions for PWA-1484 are not entirely known, deviation from ideal orientations of the test specimens for CMSX-4 (cf. (Vattré and Fedelich, 2011)) could have contributed to some of this discrepancy in the predicted mechanical response. Further, repeatability of the experimental tests over multiple specimens has not been discussed in the experimental references in Table 5 as well. This could be an additional source of discrepancy.. The amount of plastic deformation (width of the loop) is remarkably similar between the experiments and simulations. The hysteresis loop is wider for the $[\bar{1}11]$ orientation, as compared to similar loading conditions along the $[001]$ orientation. This could be due to higher elastic stiffness along the $[\bar{1}11]$ orientation, which leads to a more pronounced yielding (Staroselsky and Cassenti, 2010). The hysteresis loop for loading along $[\bar{1}23]$ orientation is significantly wider due to the relatively lower yield stress, as compared to the $[001]$ orientation. As a result, activation of slip on multiple $111<1\bar{1}0>$ slip systems leads to higher plastic deformation as compared to $[001]$ loading.The low-cycle fatigue life of specimens along the $[\bar{1}23]$ orientation is expected to be shorter than that of specimens oriented along the $[001]$ direction. Note that while the $[001]$ and $[\bar{1}11]$ orientations were used for model calibration, the $[\bar{1}23]$ loading orientation was used for validation of the cyclic response for PWA-1484 in Figure 4.6 (c). Given that the model is able to predict the cyclic response for this loading orientation, it points to the ability of the model to predict the orientation-dependent activation of different deformation modes.

4.3.3   Creep loading

The constitutive model was fit to the experimental creep data for CMSX-4 and PWA-1484. Figure 4.7 compares model predictions of the creep strain with the experimental data for CMSX-4 loaded along different orientations ($[001]$ and $[\bar{1}11]$) over a range of stresses and temperatures. Figure 4.8 compares the same for PWA-1484 loaded along different orientations for different temperatures and stresses.

It is observed that the model predictions are in general qualitative agreement with the experiments. As discussed earlier, steady state secondary creep is generally absent/minimal in both the experiments and simulations (cf. 4.1). Further, the tertiary creep behavior, which may lead to eventual failure via rupture, is captured by our model. There is some
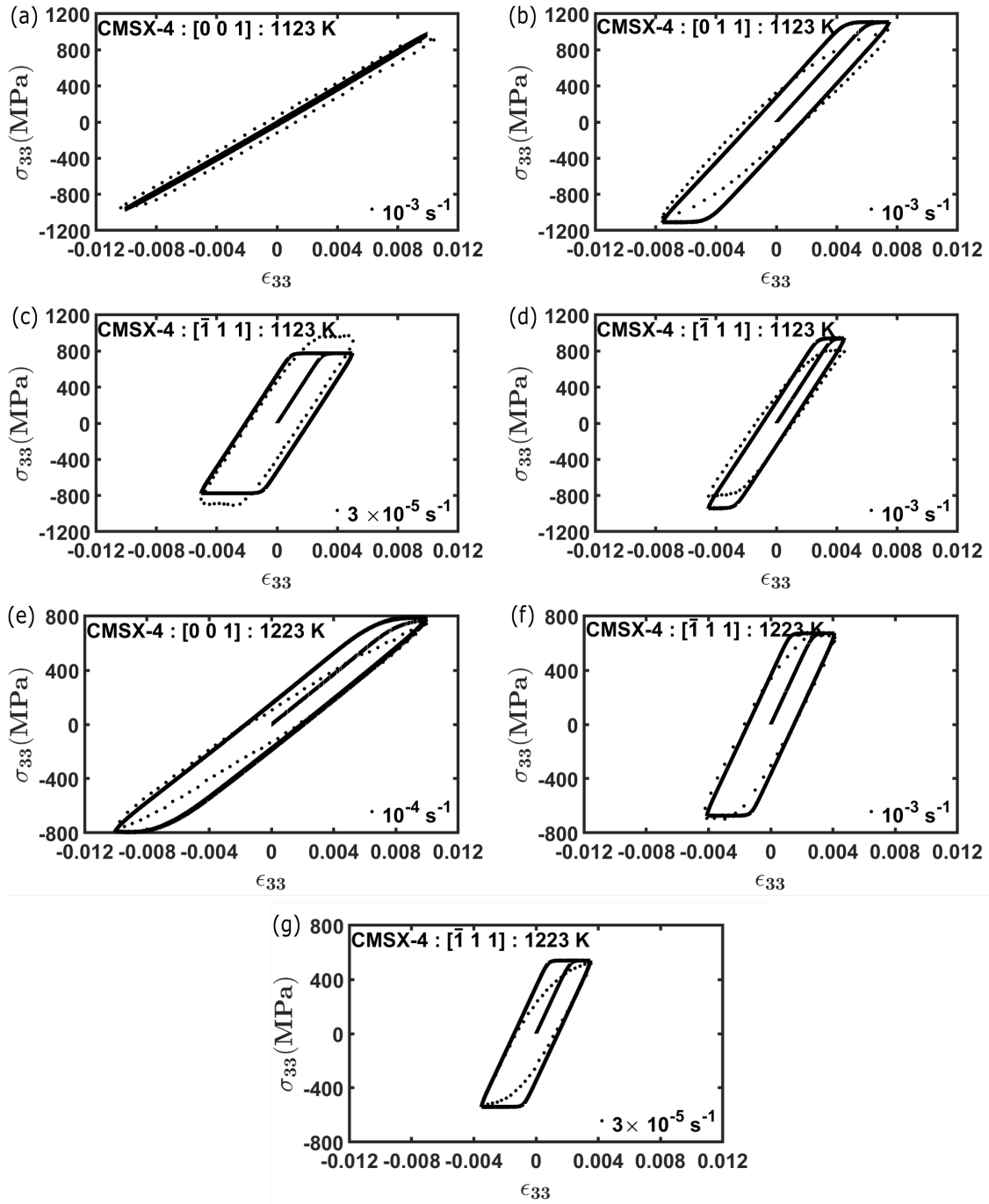
FIGURE 4.5: Simulated true stress-strain curves for different strain rates at 1123 K for (a) [001], (b) [011] and (c), (d) [$\bar{1}$11] orientations, and at 1223 K for (e) [001] and (f), (g) [$\bar{1}$11] orientations as compared with the experimental data for CMSX-4 (Vattré and Fedelich, 2011). The simulated data is plotted with solid lines, while the experimental data is plotted with symbols.
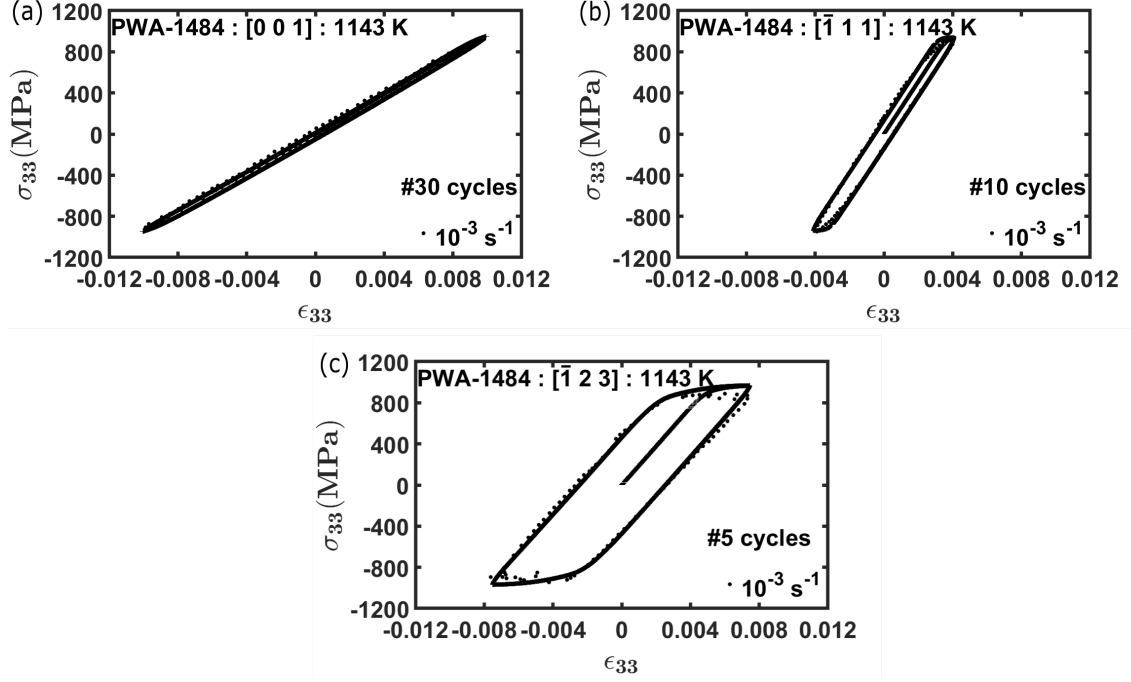
FIGURE 4.6: Simulated true stress-strain curves at 1143 K for (a) [001], (b) [$\bar{1}$11] and (c) [123] orientations as compared with the experimental data for PWA-1484 (Staroselsky and Cassenti, 2011). The simulated data is plotted with solid lines, while the experimental data is plotted with symbols.

discrepancy in predicted creep strains for the lower stresses (180 MPa and 250 MPa) at 1223 K for CMSX-4 (see Figure 4.7(c) and (d)). It should also be pointed out that variability in the creep response may be expected from experiments even for identical loading conditions. Hence, our focus has been on predicting the overall creep trends with temperature and applied stress. As can be seen, the tertiary creep strains are generally comparable with experiments for higher stress values. However, we note that other mechanisms, such as damage, may also be prevalent during the later stages of creep. Presumably, our model is not able to capture the tertiary creep rates accurately (as compared to the experiments) due to the neglect of such mechanisms in the constitutive model. As can be seen, the model under-predicts the tertiary creep rates for CMSX-4 for [0 0 1] loading and over-predicts the tertiary creep rates for [$\bar{1}$ 1 1] loading (for some cases at 1223 K) at higher temperatures. Similar trends are also observed for [0 0 1] loading for PWA-1484. While the reasons for this are not entirely clear, this could be attributed to the above-mentioned neglect of damage in our constitutive model.

It is natural to expect that mechanisms governing the evolution of creep strains over the range of stresses, temperatures, and loading orientations may change from one test case

to another. These are discussed in the context of the various deformation mode activities in Section 4.3.6.
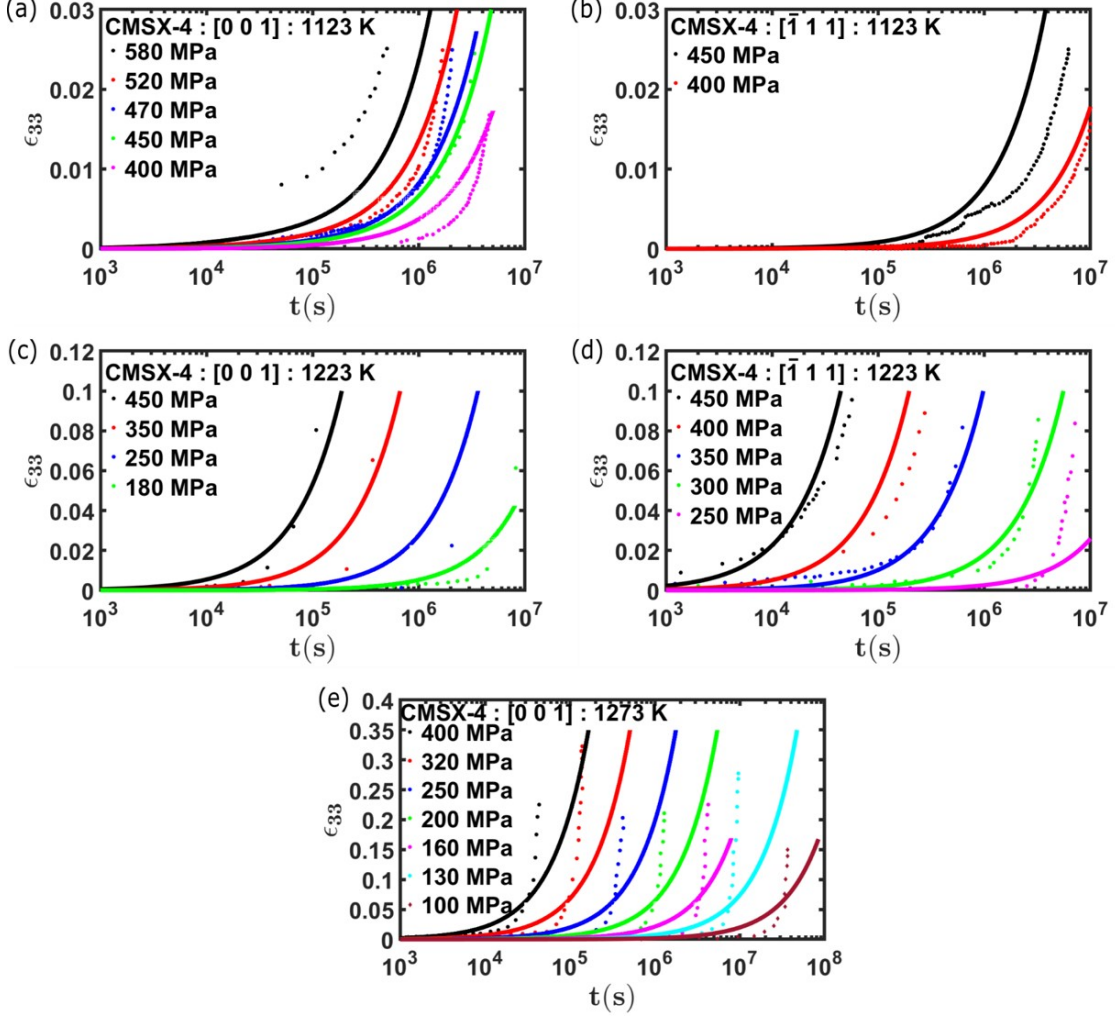
FIGURE 4.7: Simulated creep strain versus time for different stresses at 1123 K for (a) [001] and (b) [$\bar{1}$11] orientations, and at 1223 K for (c) [001] and (d) [$\bar{1}$11] orientations, and at 1273 K for (e) [001] orientation as compared with the experimental data for CMSX-4 (Vattré and Fedelich, 2011). The simulated data is plotted with solid lines, while the experimental data is plotted with symbols.

4.3.4 Channel width evolution

The channel width evolution of CMSX-4 is studied using the constitutive model described in Section 4.2.5 along with values of the model parameters in Table 4.8. Figure 4.9 compares the simulated channel width along the direction of loading with the available experimental data at 1223 K (Fedelich et al., 2009) for different applied stresses and two different
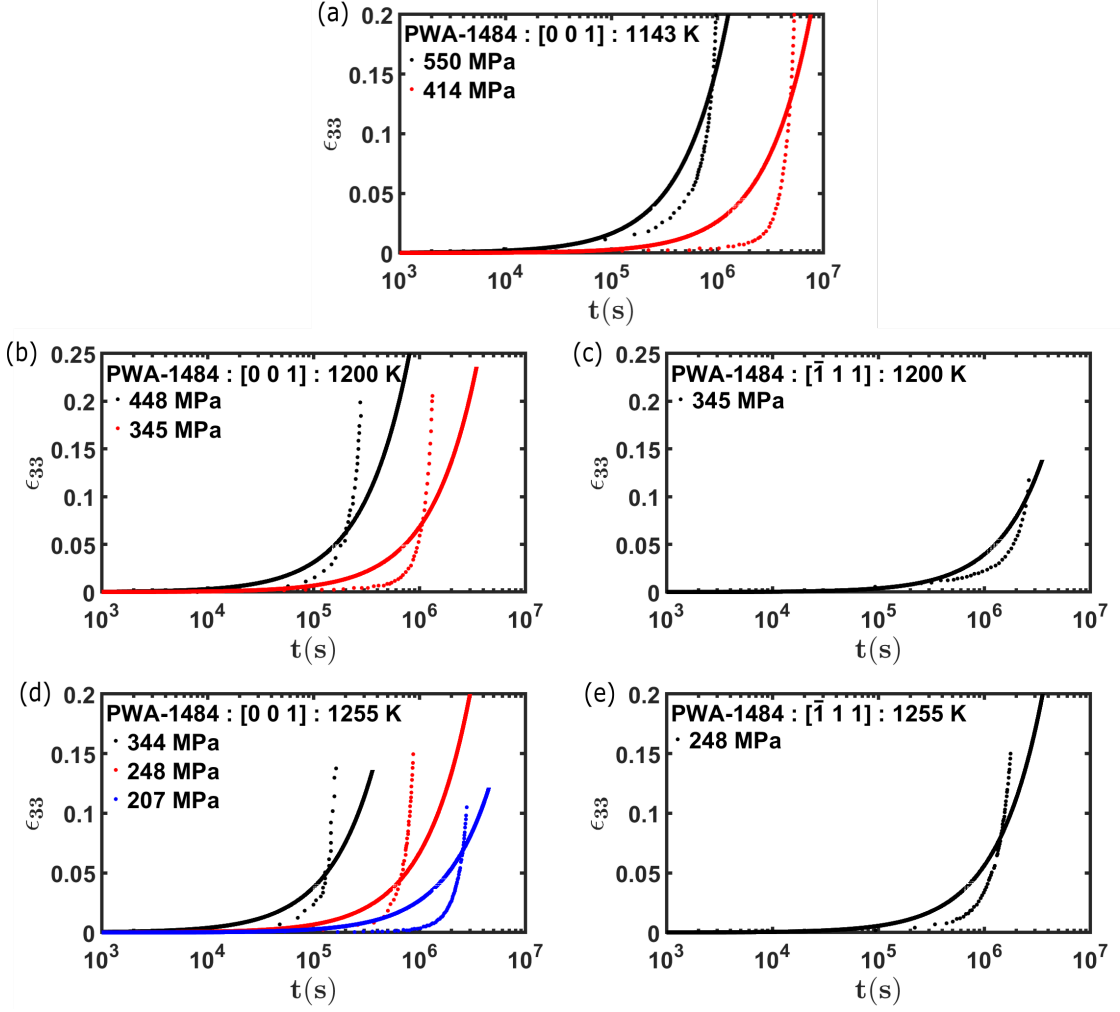
FIGURE 4.8: Simulated creep strain versus time for different stresses at (a) 1143 K, (b) 1200 K, and (d) for [001] orientation, and (c) 1200 K and (e) 1255 K for $[\bar{1}11]$ orientation as compared with the experimental data for PWA-1484 (Staroselsky and Cassenti, 2011). The simulated data is plotted with solid lines, while the experimental data is plotted with symbols.

loading orientations. It can be seen from Figure 4.9 (a) that the channel width increases both with applied stress and loading time for loading along the [001] direction, as also indicated by the limited experimental data. This has contributions from both isotropic coarsening and rafting. However, the channel width does not evolve with stress for creep loading along the $[\bar{1}11]$ orientation. This is due to the inherent geometric orientation of the channel for the $[\bar{1}11]$ single crystal, which does not allow rafting (Liu et al., 2008). In our framework, this effect is captured due to the rotation of the channel width tensor as a function of the loading orientation (cf. Equation (4.24)). For the $[\bar{1}11]$ orientation, the primary contribution to the evolution of channel width is due to isotropic coarsening.

The channel width evolution has several effects on the material's response: (a) the Orowan stress decreases as the channel width increases (Equation (4.8)), which increases the matrix slip rate (Fedelich et al., 2009), and (b) coherency between the precipitate and matrix phase reduces during rafting, which makes precipitate shearing easier (Tinga et al., 2009a). While coherency stresses have not been explicitly accounted for in our model, the effect on Orowan stress has been modeled using appropriate constitutive equations in the present work. When deformation is dominated by precipitate shearing and/or matrix slip (tensile tests, creep tests at higher stresses), rafting causes an increase in the crystallographic slip rate. On the other hand, rafting increases the load-bearing capacity of the material when dislocation climb dominates deformation (creep at lower stresses) (Tinga et al., 2009a).

Before moving further, it should be noted that experimental data for channel width are not available for PWA-1484. Hence, relevant model parameters calibrated to CMSX-4 are used for PWA-1484 predictions as well, with the inherent assumption of similar channel width evolution.

There are some differences in the underlying deformation mechanisms for creep under $[0\ 0\ 1]$ and $[\bar{1}\ 1\ 1]$ loading. Based on model predictions for CMSX-4, the contribution of dislocation glide to deformation is higher as compared to dislocation climb at higher stresses for the $[\bar{1}\ 1\ 1]$ orientation (Figure 4.12), which may have led to higher tertiary creep rates for $[\bar{1}\ 1\ 1]$ loading as compared to $[0\ 0\ 1]$ loading. For the $[0\ 0\ 1]$ orientation, the Orowan stress decreases with an increase in rafting (cf. Figure 4.11). This may have led to stress relaxation within the γ channels and an accompanying decrease in the glide rate. This may have caused a decrease in the tertiary creep rate during the later stages of creep deformation for the $[0\ 0\ 1]$ orientation as compared to the $[\bar{1}\ 1\ 1]$ orientation.
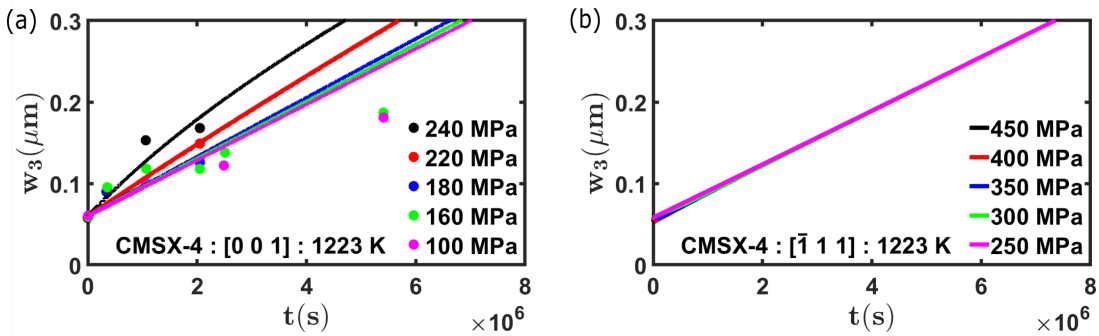
FIGURE 4.9: Evolution of channel width during creep loading at 1223 K for (a) [001] and (b) [$\bar{1}$11] orientations. The simulated data is plotted with solid lines, while the experimental data (Fedelich et al., 2009) is plotted with symbols.

Further, we have varied the channel width parametrically to study its effect on the macroscopic response. For this study, three simulations with varying channel width (keeping the volume fraction of precipitate constant at 0.72) were performed for both tensile and creep loading of a [0 0 1] CMSX-4 crystal at 1223 K. These results are shown in Figure 4.10. The γ' phase fraction plays a key role in governing the mechanical properties of single crystal Ni-based superalloys. A higher γ' volume fraction enhances tensile and creep strength by hindering dislocation motion (Reed, 2008). The effect of a change in channel width on the macroscopic behavior is significant for tensile loading, with an increase in flow stress as the channel width decreases. This is primarily an effect of the increase in the Orowan stress (cf. Equation 4.8) with a decrease in channel width. However, no significant effect was observed on the creep response with varying channel width.
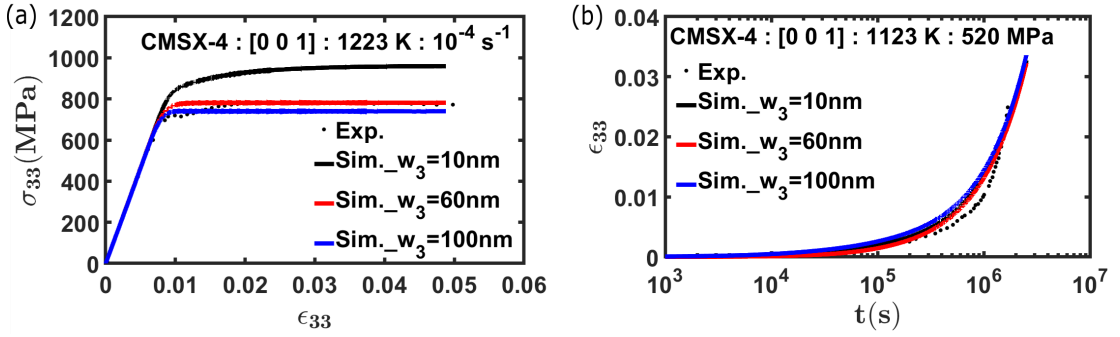
FIGURE 4.10: Influence of initial channel width value on the macroscopic response during (a) tensile loading at a strain rate of 10^{-4} s^{-1} at 1223 K, and (b) creep loading at 520 MPa at 1123 K stress for [001] orientation for CMSX-4.

4.3.5 Evolution of Orowan stress during tensile and creep loading

Figure 4.11 shows the evolution of Orowan stress with respect to time for tensile and creep loading, respectively. The Orowan stress decreases with an increase in time for both cases, although the drop in stress for tensile loading is abrupt at the beginning of inelastic deformation, when dislocation glide has not yet set in. This is primarily due to the increase in channel width due to rafting, which can lead to stress softening for low-strain-rate tensile loading (Desmorat et al., 2017). Our model predicts that the Orowan stress is almost constant (after the initial drop) even at the lowest strain rate (at $10^{-4}s^{-1}$) as these tests are not long enough to allow for microstructure degradation. This may also explain the stress plateau observed during stage 3 tensile loading (cf. Section 4.3.1). Initially, deformation occurs due to dislocation climb until the critical resolved stress for glide does

not reach the threshold value, after which dislocation glide dominates the deformation. A sudden drop in the Orowan stress is observed when slip gets activated.
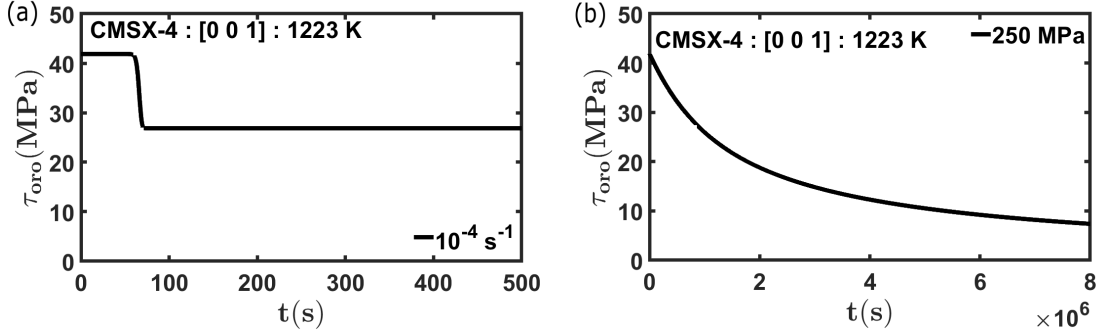
FIGURE 4.11: Evolution of Orowan stress with time for (a) tensile loading at $10^{-4}s^{-1}$ strain rate and (b) creep loading at 250 MPa stress for CMSX-4.

4.3.6 Relative slip activity

Figure 4.12 shows the contribution of different deformation modes as a function of von Mises effective strain for loading in tension, cyclic and creep conditions for the [001] and the [$\bar{1}$11] orientations at 1123 K. Note that the cyclic tests were conducted for a strain amplitude of 0.01.

As can be seen, octahedral slip in the matrix phase is dominant for loading along the [001] orientation, while the contribution from cube slip in the precipitate phase is higher for loading along the [$\bar{1}$11] orientation. Also, deformation occurs primarily by dislocation glide for tensile and cyclic loading, whereas for creep loading, deformation occurs primarily by dislocation climb. Note that some climb activity is observed even during tensile and cyclic loading during the initial transients, until the threshold to initiate deformation by slip is reached. Further, glide activity is also observed during the initial phases of creep deformation, until the creep stresses have been relaxed by dislocation climb. While there is some experimental transmission electron microscopy evidence showing the presence of both octahedral and cube dislocations in the precipitate phase at elevated temperatures (Wang et al., 2014b; Ding et al., 2021), there is no clear indication in the literature about whether these dislocations were formed due to glide or climb. Moreover, the relative fraction of different types of dislocations is also difficult to estimate using such techniques. Based on the fit to the experimental macroscopic response, our model predictions indicate that octahedral glide in the precipitate phase, although present to a small extent for tensile and cyclic loading, is rather limited.

Rafting also plays an important role during creep deformation. Dislocation slip occurs in the γ matrix at the onset of creep deformation, which increases the dislocation density. The material hardens as a result, and the creep strain rate decreases as further dislocation multiplication and motion are hindered by existing dislocations in the narrow γ channels (Xu et al., 2023). This corresponds to the steady state, secondary creep. These γ channels widen due to isotropic coarsening and rafting at elevated temperatures. Consequently, the glide of dislocations in the γ channels becomes relatively easier (Liu et al., 2025). This also causes an increase in the creep strain rate and corresponds to the initiation of tertiary creep. Thus, the microstructure degradation caused by isotropic coarsening and rafting is one of the primary contributors to the acceleration of creep rate during the later stages of deformation (Fan et al., 2015).

4.3.7 Creep-fatigue interactions

In the previous sections, the constitutive model has been calibrated to predict the tensile, cyclic, and creep response of CMSX-4 and PWA-1484 for a wide range of loading conditions. Here, we use the model to predict the creep-fatigue interactions for both alloys as validation test cases.

Figure 4.13 compares model predictions of tensile or cyclic relaxation in terms of the stress-strain as compared with the corresponding experimental data for CMSX-4 for different orientations ([001] and [$\bar{1}$11]) and different strain rates at 1123 K and 1223 K (Vattré and Fedelich, 2011). Strain-controlled relaxation tests were performed with strain holds of different time intervals during cyclic/tensile loading. The loading histories are given in the form of strain versus time plots in Figures 4.13 and 4.14. The model is able to qualitatively predict the experimentally observed relaxation behavior for CMSX-4. There is some variation in the predicted flow stress, as compared with the experimental data at 1123 K for [$\bar{1}$11] orientation. As mentioned earlier, this might be due to the model's inability to capture the the temperature- and strain rate-sensitivity of the backstress evolution for the [$\bar{1}$11] orientation at very low strain rates. Similar to the cyclic loading data in Figure 4.5, the effects appear to be more severe for [$\bar{1}$11] loading as compared to the [001] loading. Future work could consider the said temperature- and strain rate sensitivity to improve the model's predictive capabilities. Further, as can be seen in the experimental data in Figure 4.13(c), there is some cyclic softening observed; the constitutive model for which has not been proposed here. As was seen earlier, the peak stresses during cyclic loading are not predicted accurately by the model, although qualitative concurrence is still present. Mechanisms responsible for cyclic softening include precipitate shearing, precipitate dissolution,
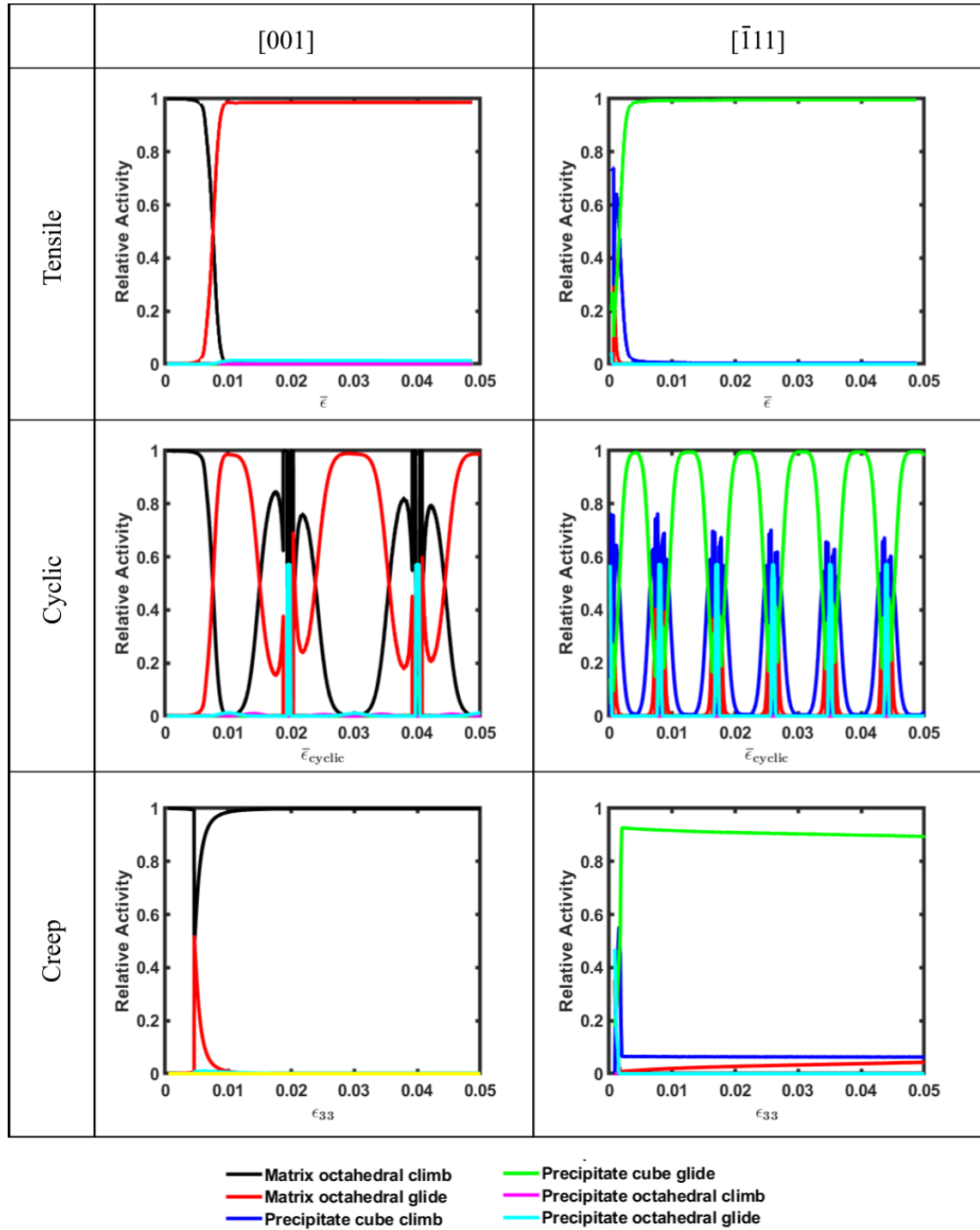
FIGURE 4.12: Relative activity of different deformation modes as a function of applied strain for tension, cyclic, and creep loading along [001] and [$\bar{1}$11] orientations at 1123 K.

precipitate disordering, and loss of coherency between the precipitates and the matrix (Antolovich et al., 1981; Sundararaman et al., 1989; Humphreys and Hatherly, 2012; Phillips et al., 2013; Zhang et al., 2019c; León-Cázares et al., 2020a). Recent works on constitutive modeling of Ni-based superalloys have considered such effects (León-Cázares et al., 2020a; Agaram et al., 2021), and similar models could be included in future work.
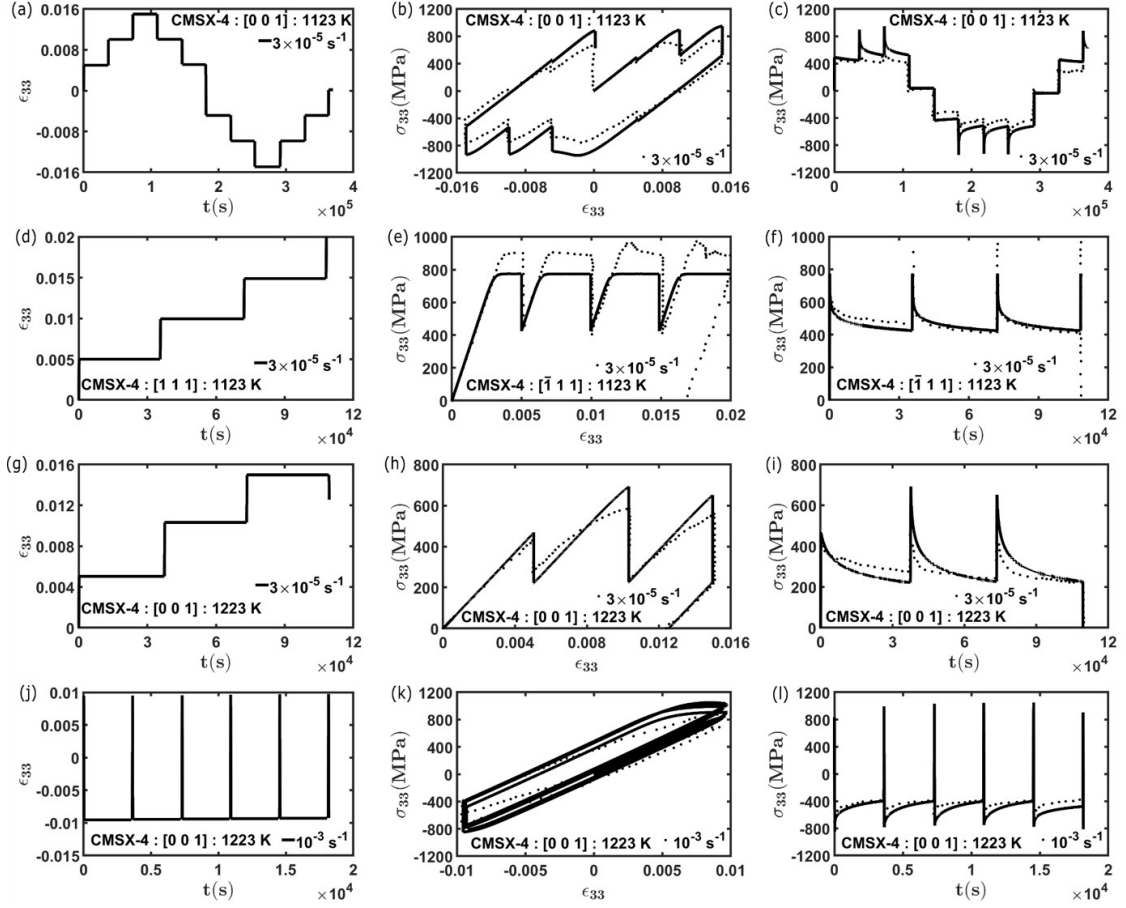
FIGURE 4.13: Strain versus time for strain-controlled relaxation test for (a) [001] orientation at 1123 K, and (d) [$\bar{1}$11] orientation at 1123 K, and (g-j) [001] orientation at 1223 K. The corresponding simulated creep-fatigue behavior as a function of (b) strain and (c) time for [001] orientation at 1123 K, and (e) strain and (f) time for [$\bar{1}$11] orientation at 1123 K, and (h-k) strain and (i-l) time for [001] orientation at 1223 K as compared with the experimental data for CMSX-4 (Vattré and Fedelich, 2011). The simulated data is plotted with solid lines, while the experimental data is plotted with symbols.

Figure 4.14 compares the simulated cyclic relaxation stress-strain curve with the corresponding experimental data for PWA-1484 for [001] orientation at 1255 K for strain amplitudes 0.005 and 0.008 (Staroselsky and Cassenti, 2010). A strain hold of 5 minutes was applied both in tension and compression at the maximum strain for each cycle. Further, note that the number of cycles is different in both cases. Model predictions agree

qualitatively with the experimental results for PWA-1484. However, the peak stresses are not predicted accurately here as well. This could be due to the fact that the strain amplitudes are very small in both these cases, and the initiation of plastic deformation is not predicted accurately. It can be seen that the model predicts the width of the hysteresis loop better at higher strain amplitude, which is expected to have higher plastic strain.
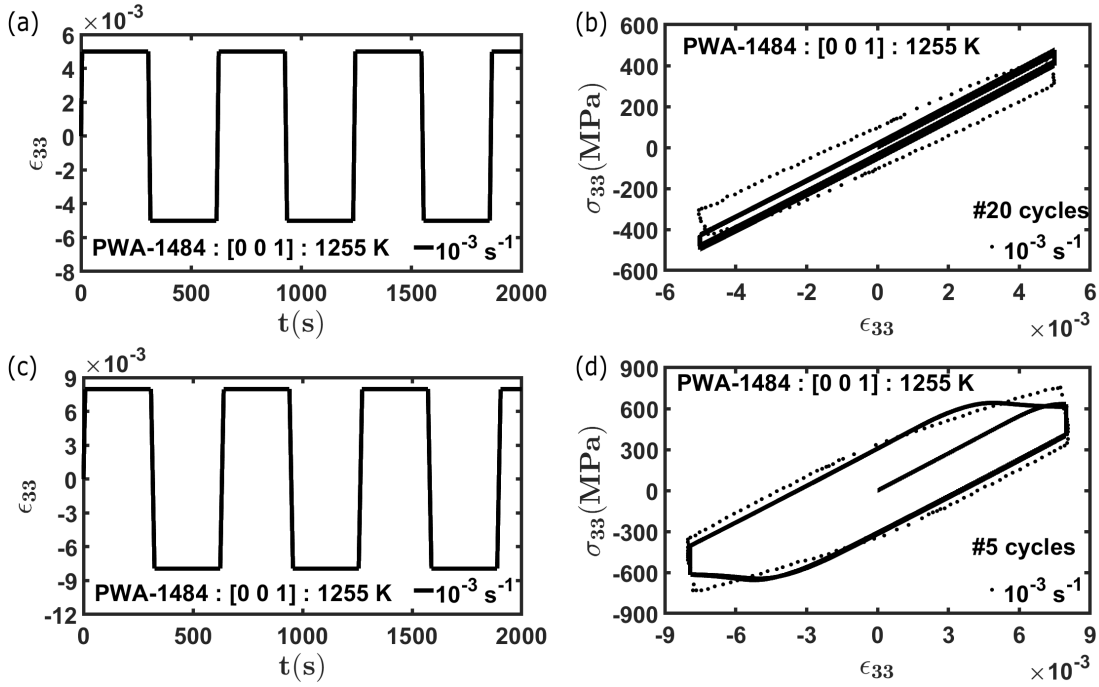
FIGURE 4.14: (a), (c) Strain versus time for strain-controlled relaxation test for [001] orientation at 1255 K and two different strain amplitudes. The corresponding simulated creep-fatigue behavior as compared with the experimental data for PWA-1484 (Staroselsky and Cassenti, 2010) is shown in (b) and (d). The simulated data is plotted with solid lines, while the experimental data is plotted with symbols.

4.3.8 Simulated response with different number of elements

Figure 4.15 shows that the simulation results do not vary with the number of elements.

4.3.9 Discussion

While the constitutive model presented in this work is comprehensive enough to capture the temperature- and strain rate-sensitivity, directional hardening, and microstructure evolution during creep loading, there are certain underlying assumptions involved in these equations:
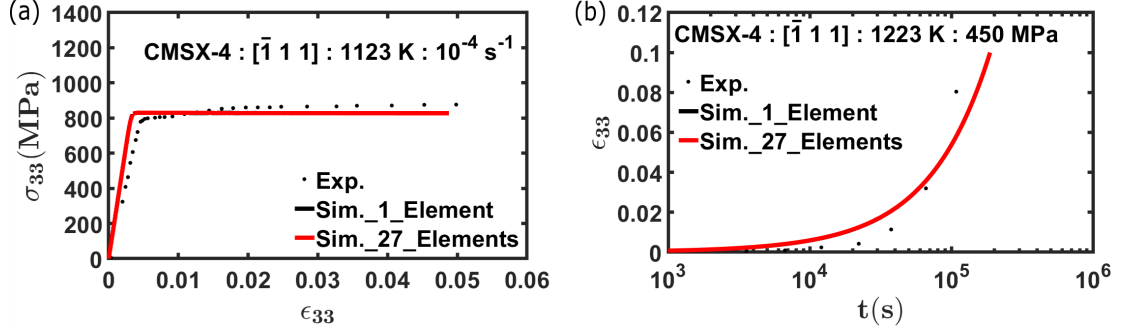
FIGURE 4.15: Simulated response with different number of elements for (a) tensile loading at $10^{-4}s^{-1}$ strain rate and (b) creep loading at 450 MPa stress for CMSX-4. No noticeable difference is observed on increasing the number of elements.

1. It has been assumed that the channel width due to rafting increases along the loading direction, which is only valid for negative lattice misfit alloys subjected to tension. With appropriate modifications, positive misfit can also be accounted for in the present framework (cf. Desmorat et al. (2017); Wu et al. (2019c)).

2. The volume fraction of γ' precipitates has been assumed to be constant in the present work. However, precipitate dissolution is expected to occur beyond a critical temperature (Desmorat et al., 2017). Based on fit to appropriate experimental data, the change in volume fraction with temperature can be empirically or phenomenologically modeled (Fan et al., 2015; Desmorat et al., 2017). Insights from phase field and kinetics models could also be used to inform such constitutive equations (Masoumi et al., 2016). This can also be accounted for with minor modifications.

3. Lattice misfit and associated coherency stresses have not been explicitly considered in our model. Coherency stresses affect the fatigue, creep, and directional coarsening (Tinga et al., 2009a). Further, these may also influence the type of rafting observed in single crystal superalloys (Guo et al., 2021). In our model, these stresses are implicitly assumed to be present in the threshold stress term, s_{aj}^{α}, and their description can be refined further in future work.

4. Finally, the effect of APB energy on precipitate shearing (Ghorbanpour et al., 2017; Li et al., 2019b; Gupta and Bronkhorst, 2021) and its temperature dependence has not been explicitly considered in our work. This may be expected to vary between alloys with different compositions. While this term is inherently assumed to be present in the temperature-dependent threshold resistance, τ_{0j}^{α} (cf. Ranjan et al. (2021)), its description can also be refined in future work.

Moreover, despite these assumptions, the model is able to predict qualitative trends of mechanical response across a wide range of loading histories for the two alloys, CMSX-4 and PWA-1484..

4.4   Conclusions

We have proposed a crystal plasticity constitutive framework for modeling the thermo-mechanical deformation of single crystal Ni-based superalloys. In this dislocation density-based framework, slip is modeled using an Arrhenius-type activation energy-based equation. A model for the evolution of the slip system-level back stress is used to predict the cyclic response. Climb of dislocations is modeled with consideration for the climb kinematics perpendicular to the slip plane and a Peach-Koehler-type crystallographic normal stress that causes climb. Further, dislocation climb is modeled using a power law type equation with temperature dependence. Material-specific hardening mechanisms such as Orowan looping around precipitates, grain/precipitate size hardening, and dislocation density-based hardening are considered in this framework. The substructure evolution is considered in terms of the mobile and immobile dislocation densities. Further, constitutive equations for rafting and isotropic coarsening of the γ' precipitates are developed to account for the microstructure evolution commonly observed in these materials during creep deformation. The constitutive model has been implemented and coupled with the open-source finite element library, MOOSE, using a fully implicit time integration scheme.

Application of the constitutive model has been demonstrated to predict the mechanical response of two different single crystal superalloys, CMSX-4 and PWA-1484, and compared with available experimental data. Specifically, the orientation-, temperature-, and rate-dependent response has been predicted under tensile loading. The cyclic and creep response has also been predicted for a range of strain amplitudes, orientations, and stresses, respectively. Insights obtained from the model have been used to understand the competitive role of various deformation mechanisms during different loading conditions. Finally, the model has been used to predict the creep-fatigue interactions in both alloys and compared with available experimental data.

This physically-based, microstructure-sensitive constitutive model accounts for a wide range of deformation mechanisms that may occur under different loading conditions during the operation cycle of these alloys in aerospace components. The model's ability to predict the mechanical response due to such competing effects at relatively low computational costs (as compared to more computationally intensive tools, such as coupled phase

field-crystal plasticity models) is one of the main advantages of this framework. Further, while mechanisms such as dislocation density-based backstress evolution, dislocation climb kinematics, orientation-dependent channel width evolution, and temperature- and stress-dependent evolution of rafting kinetics, have been individually proposed in the literature, their integration into a unified crystal plasticity constitutive framework for single crystal superalloys enhances the model's predictive capabilities significantly over a wide range of possible deformation histories. This is the primary contribution of the proposed framework.

Chapter 5

Modeling Heterogeneous Deformation of Polycrystalline Ni-based Superalloys

5.1 Introduction

Polycrystalline Ni-based superalloys, processed by the PM route, have superior high-temperature mechanical properties and find use in gas turbine engine disks (Shenoy et al., 2008; Kozar et al., 2009; Stinville et al., 2015; Zhang et al., 2022b). The properties of these alloys are dependent on the underlying microstructure (Shenoy, 2006), which generally has a two phase microstructure: γ matrix, with FCC crystal structure, and $\gamma^{'}$ precipitates, with $L1_2$-type crystal structure (Kozar et al., 2009). Further, the $\gamma^{'}$ precipitates are classified into three categories (primary, secondary, and tertiary $\gamma^{'}$) depending on their size (Boittion et al., 2010). While, the primary $\gamma^{'}$ precipitates are micron-sized and separated from the γ matrix by high-angle boundaries, the secondary and tertiary $\gamma^{'}$ precipitates are sub-micron sized, and generally coherent with the γ phase (Kozar et al., 2009). Generally, the strength of these alloys increases marginally from room temperature to 800 °C, due to the presence of long-range ordered intermetallic $\gamma^{'}$ precipitates (Kozar et al., 2009), and then starts dropping at higher temperatures. Deformation in these microstructures is essentially a multiscale phenomena: the secondary and tertiary $\gamma^{'}$ precipitates (referred hereon as $\gamma^{'}_s$ and $\gamma^{'}_t$, respectively) provide strengthening to the matrix at the sub-micron

---

[1] Significant parts of this chapter have been published in Chaudhary et al. (2023).

scales, while the primary $\gamma^{'}$ precipitate (simply referred as $\gamma^{'}_p$), annealing twin boundaries and grain boundaries influence polycrystalline deformation at the grain (micron) scale.

Significant research has been performed to study the deformation and failure mechanisms in these superalloys via experimental techniques and crystal plasticity modeling tools Castelluccio and McDowell (2014, 2016); Prithivirajan and Sangid (2020); Zhang et al. (2022b); Stinville et al. (2016); Latypov et al. (2021); Hestroffer et al. (2022). Several studies have focused on mapping the strain localization phenomena in Ni-based superalloys using high-resolution microscopy (Wang and Pan, 2015; Jiang et al., 2017; Liu et al., 2019; Charpagne et al., 2020). Crystallographic orientation-based misorientation can be obtained from EBSD and used in the analysis of heterogeneous deformation (Charpagne et al., 2021). Information related to local deformation and dislocation activity can also be obtained from the misorientation (Zhang et al., 2022b). It has been observed that the Digital Image Correlation (DIC) measured plastic strain correlates with these misorientation measures Harte et al. (2020). Recently, cross-correlation strains have also been measured to study the strain localization by using high-resolution EBSD (Wilkinson et al., 2006; Zhang et al., 2014, 2018). Generally, studies have used the strain concentration or KAM localization as an indicator of local plastic deformation and correlated with the propensity for crack initiation (Stinville et al., 2016; Jiang et al., 2017; Harte et al., 2020; Zhang et al., 2022b). Statistical and computational analyses show that the plastic strain accumulates particularly at regions near grain boundaries and interfaces near the triple junctions and sharp corners (Stinville et al., 2015; Latypov et al., 2021; Hestroffer et al., 2022). Further, annealing twins also form during the processing of polycrystalline Ni-based superalloys (Stinville et al., 2015). Crack initiation has been observed near these annealing twin boundaries during low-cycle fatigue of Ni-based superalloys (Zhang et al., 2022b; Miao et al., 2009, 2012; Stein et al., 2012; Stinville et al., 2017b).

Meanwhile, modeling frameworks have been developed with physically representative constitutive equations and considering realistic microstructures. Several CPFE frameworks have been developed to predict the heterogeneous strain fields at the grain-scale for monotonic and cyclic loading for the analysis of local deformation in polycrystalline Ni-based superalloys (Shenoy et al., 2008; Castelluccio and McDowell, 2014; Manonukul and Dunne, 2004; Ghorbanpour et al., 2017; Chen et al., 2018; Bandyopadhyay and Sangid, 2019; Prithivirajan and Sangid, 2020; Agaram et al., 2021; Zhang et al., 2022b; Eghtesad and Knezevic, 2021; Chandra et al., 2018; Kashinga et al., 2017; Luccarelli et al., 2019; Bergsmo et al., 2022; Zhang et al., 2022a, 2016). Recently, there has also been significant work on crystal plasticity modeling of additively manufactured Ni-based superalloys (Aburakhia

et al., 2022; Babamiri et al., 2022; Pilgar et al., 2022). While phenomenological hardening equations are often used in these crystal plasticity models, physically-based micromechanical models (Shenoy et al., 2008; Ghorbanpour et al., 2017; Collins and Stone, 2014; Kim et al., 2018; Wu et al., 2023; Tan et al., 2019) could also be used to improve the predictability of the modeling frameworks.

To date, most of the CPFE frameworks consider the deformation of the γ matrix and the $\gamma^{'}$ precipitates in a homogenized fashion. While this may be a reasonable approach where the precipitates are generally nanometer-sized, PM processed superalloys generally also have micron-sized $\gamma^{'}$ precipitates. These $\gamma^{'}$ precipitates may be expected to influence the deformation and failure of these alloys, in addition to the annealing twins and grain boundaries (Flageolet et al., 2005; Jiang et al., 2015a). For example, Figure 5.1 shows the SEM and TEM images of the as-received microstructure of the PM processed superalloy considered in the present study (characterization details are presented later). The microstructure shows micron-sized primary $\gamma_{p}^{'}$ precipitates and cuboidal-shaped secondary $\gamma_{s}^{'}$ and tertiary $\gamma_{t}^{'}$ precipitates embedded in the γ phase. The typical size of $\gamma_{s}^{'}$ and $\gamma_{t}^{'}$ precipitates was found to be in the range $200-300\ nm$ and $10-30\ nm$, respectively. This multiscale microstructure may contribute to strengthening and heterogeneous deformation at multiple length scales (Shenoy et al., 2008) and should be considered appropriately in constitutive models. Generally, there are not many constitutive modeling frameworks in the literature that explicitly consider experimental inputs such as phase chemistry and precipitate sizes for these superalloys. The individual deformation of $\gamma_{p}^{'}$ precipitates and their effect on the local deformation have also not been considered. Further, the competitive role of microstructural features, such as twin boundaries, grain boundaries, and matrix-precipitate interfaces, on the deformation heterogeneity (and eventual failure) of these PM processed alloys has not been studied in detail. The present work attempts to address these issues by considering these microstructural features and the associated strengthening mechanisms in a crystal plasticity constitutive framework, with the objective of studying their competitive role in the deformation and misorientation developments.

We propose a crystal plasticity framework for a PM-processed polycrystalline Ni-based superalloy. This framework accounts for the individual deformation of the matrix (γ phase, with homogenized distribution of $\gamma_{s}^{'}$ and $\gamma_{t}^{'}$ precipitates), and the $\gamma_{p}^{'}$ phase separately, with the objective of identifying their effect on the local and aggregate deformation characteristics. The framework is informed by relevant experimental measurements. The concentration of the solute species present in the matrix and $\gamma_{p}^{'}$ phases is obtained directly from EDS measurements and serves as input to the relevant strengthening models,
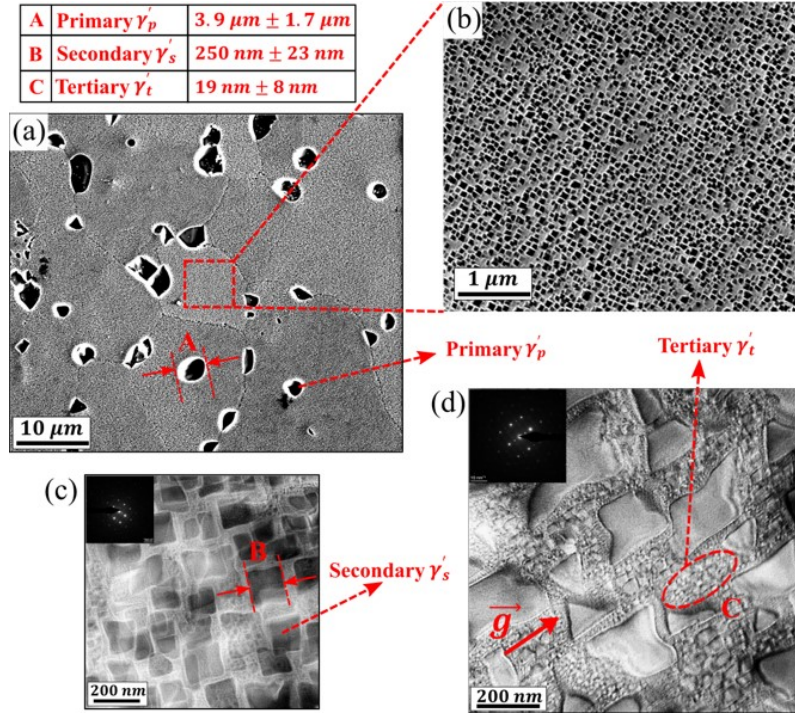
FIGURE 5.1: SEM and TEM images of the as-received material showing (a) the primary $\gamma_p^{'}$ precipitates at the grain boundaries, and (b), (c) the secondary $\gamma_s^{'}$ precipitates and (d) the tertiary $\gamma_t^{'}$ precipitates. Mean precipitate sizes are also given in the inset.

along with the EBSD microstructures. The model has been calibrated to reproduce the macroscale stress–strain response at 293 K and 923 K, and then validated by predicting the response at 523 K and 723 K. Room temperature tensile deformation simulations have been performed on the EBSD microstructures and compared with their experimental counterparts from interrupted tensile testing to study the substructure evolution. In this regard, statistical analysis of competitive misorientation development at various microstructural features, such as grain boundaries, twin boundaries, and matrix-precipitate interfaces, is performed to investigate their effects on heterogeneous deformation.

The novelty of the present work lies in the consideration of physically-based deformation mechanisms in the crystal plasticity constitutive model, in combination with synergistic experiments, which provide microstructural inputs to the model as well as serve as validation, for studying competitive deformation mechanisms in polycrystalline Ni-based superalloys.

5.2   Material and Experimental Characterization

5.2.1   Material

The material used in the present work is a polycrystalline Ni-based superalloy, processed using the PM route. The alloy was obtained from the Defence Metallurgical Research Laboratory (India) in the form of circular rods. The As-Received (AR) material did not exhibit any dominant texture components. Micro-tensile samples extracted from the AR rod were then used to study the microstructure evolution with progressive, albeit interrupted, plastic deformation.

5.2.2   Experimental Characterization

Interrupted progressive tensile tests were carried out on micro-tensile specimens having the following dimensions: 5 mm gauge length, 2 mm gauge width, 1 mm thickness, and 16 mm total length. A screw-driven Instron 3345 Universal Testing Machine (UTM), with a 5 kN load cell, was used to perform the deformation at a nominal strain rate of $10^{-4} \ s^{-1}$. The data from monotonic tensile tests were used to calibrate our crystal plasticity model, while the microstructure characterization data from interrupted tensile tests were used for comparison with model predictions of misorientation developments.

Traditional metallography, followed by sub-micron colloidal silica polishing, was used to prepare the samples. EBSD measurements were performed using a FEI Quanta 3D-FEG (Field Emission Gun) scanning electron microscope, equipped with a TSL-EDX EBSD system. A 0.1 cutoff on the Confidence Index (CI), signifying 95% accuracy in the EBSD indexed patterns, was applied during subsequent analysis. Microstructural characterization was carried out on samples deformed up to $0\%, 5\%, 10\%$ and 15% nominal strain. All scans were collected from the center of the micro-tensile specimens (identified using indented impressions), in order to avoid any edge effects.

In order to analyze the $\gamma_s^{'}$ precipitates, the polished specimens were then etched using Collins etchant, with a composition of 100 ml (38%) Hydrochloric Acid, 100 ml Ethyl Alcohol, and 5 grams Copper (II) Chloride. Subsequent SEM imaging revealed the cuboidal nature of the $\gamma_s^{'}$ precipitates, as shown in Figure 5.1(b). The SEM micrographs were acquired using a FEI Nova-Nano SEM, while SEM-EDS (Energy-Dispersive X-Ray Spectroscopy) was obtained with a commercial EDX system. The $\gamma_t^{'}$ precipitates were characterized using TEM. The TEM specimens were prepared in a Struers Tenupol-5 twin-jet
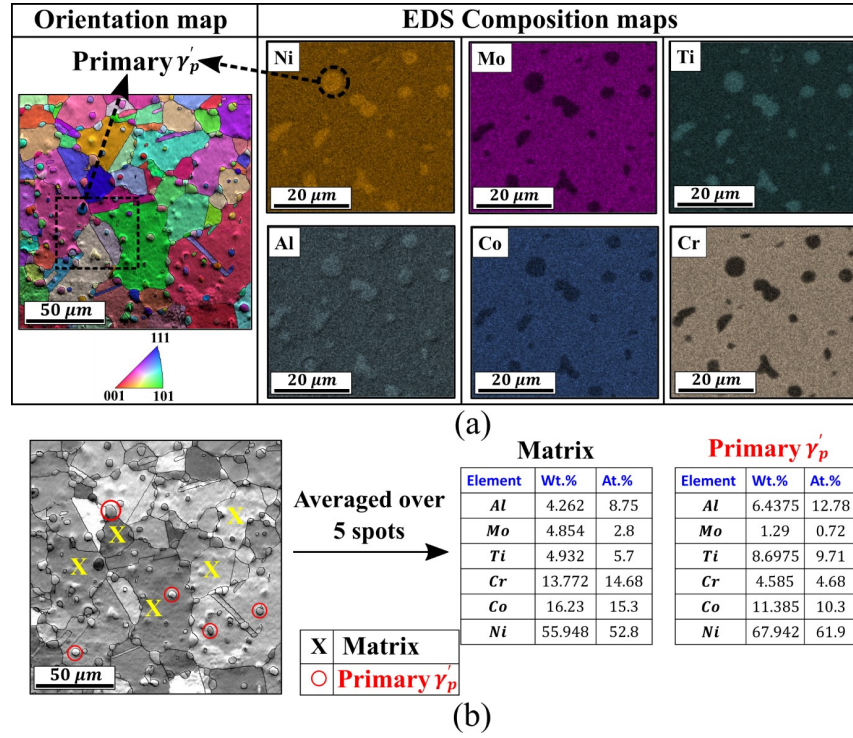
FIGURE 5.2: (a) Representative EDS composition maps, and (b) corresponding average concentrations of the constituent elements in the matrix (γ with embedded $\gamma_s^{'}$ and $\gamma_t^{'}$ precipitates) and primary $\gamma_p^{'}$ phases.

electropolisher, using a 90:10 ratio of methanol to perchloric acid, at 15 V DC, and at a stable temperature below 250 K. TEM investigations were carried out on a Thermofisher Themis-300 microscope (300 keV operating voltage) with a four-detector ChemiSTEM EDS arrangement. Further, High Angle Annular Dark Field-Scanning Transmission Electron Microscopy (HAADF-STEM) images were used to characterize the $\gamma_t^{'}$ precipitates (cf. Figure 5.1(c,d)).

SEM-EDS results for the as-received material are shown in Figure 5.2(a). This characterization was performed at 5 different spots in the matrix (γ matrix with embedded $\gamma_s^{'}$ and $\gamma_t^{'}$ precipitates) and primary $\gamma_p^{'}$ phases each to estimate the mean concentration of the constituent solute atoms in the different phases (cf. Figure 5.2(b)). The information obtained from this characterization was used to inform the crystal plasticity model. Note that SEM-EDS does not have the spatial resolution to measure compositions in the $\gamma_s^{'}$ and $\gamma_t^{'}$ precipitates, hence the compositional heterogeneity in the matrix has not been considered in the present work. Further, the TEM investigations were limited to obtaining the spatial size distribution of tertiary $\gamma_t^{'}$ precipitates, and further reference to EDS implies SEM-EDS measurements. The average chemical composition of the superalloy was determined using EDS and is given in Figure 5.2.

As will be explained later, identification of individual matrix and primary $\gamma_p^{'}$ precipitates phases from EBSD measurements is required for the CPFE simulations. However, the γ and $\gamma_p^{'}$ precipitates belong to the same space group (F-$m3m$), with nearly identical lattice parameters (cf. Figure 5.3(a)). Kinematically simulated Kikuchi patterns (generated using the TSL-OIM software) also indicate the same. The diffracting planes in electron diffraction can be calculated readily using the kinematical theory, provided the atomic positions within a unit cell are known (Cullity, 1956). Although the bandwidth and location of these kinematically simulated patterns would be identical to experiments, the intensity profiles may differ significantly. This is because the interference effects alter the resulting diffracted intensities. This makes the identification of the individual phases non-trivial. The present work uses the PRIAS (Pattern Region of Interest Analysis System) signal, overlaid with orientation measurements to resolve this issue. PRIAS considers the EBSD detector (or the phosphor screen) as a sequential array of up to 25 positional electron detectors for sample imaging (Nowell et al., 2014; Wright et al., 2015; Adams et al., 2020). Hence, the topographical contrast between these two phases, arising due to differential polishing, can be captured using PRIAS. A higher PRIAS signal, in conjunction with the point-to-point misorientation, is observed in the $\gamma_p^{'}$ phase region, when compared to the surrounding matrix (cf. Figure 5.3(b)). This has been used to distinguish the $\gamma_p^{'}$ phase from the matrix (γ, with embedded $\gamma_s^{'}$ and $\gamma_t^{'}$ precipitates). Figure 5.3(b) shows the phase map of the matrix (in red color) and the $\gamma_p^{'}$ phase (in green color). To the best of our knowledge, such a phase separation technique has not been reported previously.

5.3 Crystal Plasticity Framework

The crystal plasticity framework accounts for the role of local microstructure on the deformation behavior of PM-processed Ni-based superalloys. Specifically, the framework considers: (a) elemental concentration of the matrix and $\gamma_p^{'}$ phase (from EDS), (b) grain size, crystallographic orientation and spatial distribution of the matrix and $\gamma_p^{'}$ (from EBSD), and (c) crystallographic orientation and spatial distribution of the annealing twins (from EBSD). Appropriate constitutive models are developed for considering the role of each of these features in strengthening and deformation. The deformation length scale of interest in the present problem is at the scale of grains; hence, individual deformation of the nanometer-sized $\gamma_s^{'}$ and $\gamma_t^{'}$ is not considered explicitly. Rather, their contribution to the strengthening of the γ phase has been considered in a homogenized sense. The framework has been adapted from (Ranjan et al., 2021; Chaudhary et al., 2022), where the deformation behavior of single crystal Ni-based superalloys was studied. Constitutive equations
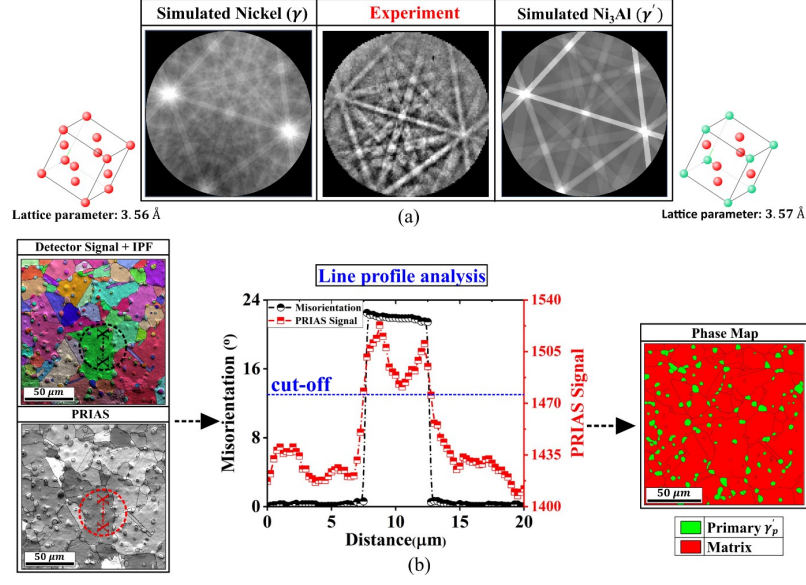
FIGURE 5.3: (a) Experimentally acquired Kikuchi patterns are compared to the kinematically simulated Kikuchi patterns for the γ as well as γ'_p phases, for a given set of Euler angles. (b) Line profile analysis of PRIAS signal, in conjunction with point-to-point misorientation data, used for identifying the γ and γ'_p phases in EBSD.

related to the basic framework, along with phase-specific strengthening mechanisms, are presented here, while additional details of substructure evolution models adopted from previous works (Ranjan et al., 2021; Chaudhary et al., 2022) are provided in the Table 5.1.

The finite deformation framework assumes the multiplicative decomposition of the deformation gradient, $\boldsymbol{F}$, into the elastic, $\boldsymbol{F^e}$, and inelastic parts, $\boldsymbol{F^i}$ (Asaro and Rice, 1977), i.e.,

$$\boldsymbol{F} = \boldsymbol{F^e} \cdot \boldsymbol{F^i} \tag{5.1}$$

Here, $\boldsymbol{F^i}$ accounts for the shear due to inelastic deformation on the undeformed lattice, mapping the reference configuration to an isoclinic, intermediate configuration, and $\boldsymbol{F^e}$ accounts for the elastic lattice distortion and the rigid body rotation that maps the intermediate configuration to the current, deformed configuration.

The framework considers the individual decomposition of the constituent phases, i.e., the γ matrix containing the secondary, γ'_s, and tertiary, γ'_t, precipitates (referred simply as the matrix), and that of the primary γ'_p precipitates, separately. The elasticity tensor for the

matrix and the primary $\gamma_p^{'}$ are given as (Ranjan et al., 2021):

$$C^{ijkl} = \begin{cases} \left(\left(1 - f_{\gamma_s^{'}} - f_{\gamma_t^{'}}\right) C_{\gamma}^{ijkl-1} + \left(f_{\gamma_s^{'}} + f_{\gamma_t^{'}}\right) C_{\gamma^{'}}^{ijkl-1} \right)^{-1} ; matrix \\ C_{\gamma^{'}}^{ijkl}; \gamma_p^{'} \end{cases} \tag{5.2}$$

where, $C_{\gamma^{'}}^{ijkl}$ and C_{γ}^{ijkl} represent the anisotropic elasticity tensor of the precipitate $(\gamma^{'})$ phase and the γ phase, respectively. $f_{\gamma_p^{'}}$, $f_{\gamma_s^{'}}$, and $f_{\gamma_t^{'}}$ represent the volume fractions of the primary, secondary, and tertiary precipitates, respectively. As a first-order approximation, the anisotropic elastic constants for these primary, secondary, and tertiary precipitates are assumed to be the same. Density functional theory calculations may be used in future work to determine the elastic constants of the individual precipitates (for example, see (Ghorbanpour et al., 2017)).

The inelastic spatial velocity gradient, $\boldsymbol{L^i}$, is related to $\boldsymbol{F^i}$ according to: $\dot{\boldsymbol{F}}^i = \boldsymbol{L^i} \cdot \boldsymbol{F^i}$. $\boldsymbol{L^i}$ due to the crystallographic shearing rates, is tensorially summed over all possible deformation systems, i.e.,

$$\boldsymbol{L^i} = \begin{cases} \sum_{\alpha=1}^{N_s} \dot{\gamma}^{\alpha} \boldsymbol{s}_0^{\alpha} \otimes \boldsymbol{m}_0^{\alpha}; matrix \\ \sum_{\alpha=1}^{N_p} \dot{\gamma}^{\alpha} \boldsymbol{s}_0^{\alpha} \otimes \boldsymbol{m}_0^{\alpha}; \gamma_p^{'} \end{cases} \tag{5.3}$$

where, $\dot{\gamma}^{\alpha}$ is the inelastic shearing rate on slip system α. The slip direction and slip plane normal in the reference (and intermediate) configuration are given by $\boldsymbol{s}_0^{\alpha}$ and $\boldsymbol{m}_0^{\alpha}$. N_s and N_p denote the total number of slip systems in the matrix and $\gamma_p^{'}$ phase, respectively. We consider 12 octahedral {111} < 110 > slip systems in the matrix phase. Further, we consider 24 octahedral {111} < 110 > slip systems (explicit forward and backward slip) and 6 cube {001} < 110 > slip systems in the $\gamma_p^{'}$ phase. The additional slip systems in the $\gamma_p^{'}$ phase are motivated by the non-Schmid deformation modes commonly observed in these L_{12} phases (Allan, 1995; Ghorbanpour et al., 2017; Ranjan et al., 2021). Forward and backward slip are expected to be influenced differently by the non-Schmid stresses in the $\gamma_p^{'}$ phase, and this is one of the primary contributors to the experimentally observed tension-compression asymmetry (Keshavarz and Ghosh, 2015a; Ghorbanpour et al., 2017; Xu et al., 2023). Thus, 24 octahedral {111} < 110 > slip systems are considered for the primary $\gamma_p^{'}$ precipitates. In FCC crystals, the octahedral {111} planes are the closed-packed planes amenable to slip. However, there is also evidence of slip on the cube {100} planes, which generally are not closed packed (Me'ric et al., 1991; Österle et al., 2000; Tinga et al., 2009b). Hence, we have considered cube slip as an additional deformation mode in the primary $\gamma_p^{'}$ phase.

Dislocation glide has been modeled using a thermally-activated Arrhenius-type model for crystalline solids (Kocks et al., 1975; Ranjan et al., 2021):

$$
\dot{\gamma}^\alpha = \begin{cases}
\dot{\gamma}_{0j}^\alpha exp\left[-\dfrac{\Delta F_j^\alpha}{kT}\left(1-\left(\dfrac{|\tau_j^\alpha|-s_{aj}^\alpha}{s_{tj}^\alpha}\right)^{p_j^\alpha}\right)^{q_j^\alpha}\right] sgn\left(\tau_j^\alpha\right); \left|\tau_j^\alpha\right| > s_{aj}^\alpha, \alpha \in \text{oct}, j \in \text{matrix} \\[3ex]
\dot{\gamma}_{0j}^\alpha exp\left[-\dfrac{\Delta F_j^\alpha}{kT}\left(1-\left(\dfrac{\tau_j^\alpha-s_{aj}^\alpha}{s_{tj}^\alpha}\right)^{p_j^\alpha}\right)^{q_j^\alpha}\right]; \tau_j^\alpha > s_{aj}^\alpha, \alpha \in \text{oct}, j \in \gamma_p' \\[3ex]
\dot{\gamma}_{0j}^\alpha exp\left[-\dfrac{\Delta F_j^\alpha}{kT}\left(1-\left(\dfrac{|\tau_j^\alpha|-s_{aj}^\alpha}{s_{tj}^\alpha}\right)^{p_j^\alpha}\right)^{q_j^\alpha}\right] sgn\left(\tau_j^\alpha\right); \left|\tau_j^\alpha\right| > s_{aj}^\alpha, \alpha \in \text{cube}, j \in \gamma_p' \\[3ex]
0; otherwise
\end{cases}
$$

(5.4)

Here, $\alpha \in \text{oct}, j \in \text{matrix}$ represents octahedral slip in the matrix phase, and $\alpha \in \text{oct}, j \in \gamma_p'$ represents octahedral slip in the γ_p' phase, while $\alpha \in \text{cube}, j \in \gamma'$ represents cube slip in the γ_p' phase. In the above equation, $\dot{\gamma}_{0j}^\alpha$ represents the reference strain rate, ΔF_j^α represents the dislocation glide activation energy, k represents the Boltzmann constant, T represents the absolute temperature, τ_j^α represents the driving stress, s_{aj}^α represents the athermal slip resistance, s_{tj}^α represents the thermal resistance, and, p_j^α and q_j^α are parameters governing the shape of the activation energy curve. Further, depending on the phase, the driving stress, τ_j^α, is a function of the Schmid and non-Schmid stresses (Ranjan et al., 2021) (Equation 5.8 in the Table 5.1).

The athermal slip resistance, s_a^α, represents the glide resistance due to the long-range stress fields of other defects and obstacles. For octahedral slip in the matrix phase, this term is assumed to have dominant contributions from the Hall-Petch effect, precipitate strengthening due to γ' precipitates, and dislocation-based Taylor hardening. For octahedral slip in the γ_p' phase, this term has contributions from the Anti-Phase Boundary (APB) energy dependent resistance, Hall-Petch strengthening, and dislocation strengthening (Chaudhary et al., 2022). For cube slip in γ_p', this term is assumed to have contributions from Hall-Petch strengthening and dislocation strengthening (Chaudhary et al., 2022). The respective contributions are given as:

$$
s_{aj}^\alpha = \begin{cases}
\tau_{ps}^\alpha + \dfrac{k_{Hj}}{\sqrt{d_\gamma}} + k_{\rho j} G_j b_j \sqrt{\left(\sum_{\xi=1}^{N_m} A^{\alpha\xi}\rho_j^\xi\right)}; \alpha \in \text{oct}, j \in \text{matrix} \\[3ex]
\tau_{APB}^\alpha + \dfrac{k_{Hj}}{\sqrt{d_{\gamma_p'}}} + k_{\rho j} G_j b_j \sqrt{\left(\sum_{\xi=1}^{N_p} A^{\alpha\xi}\rho_j^\xi\right)}; \alpha \in \text{oct}, j \in \gamma_p' \\[3ex]
\tau_{0j}^\alpha + \dfrac{k_{Hj}}{\sqrt{d_{\gamma_p'}}} + k_{\rho j} G_j b_j \sqrt{\left(\sum_{\xi=1}^{N_p} A^{\alpha\xi}\rho_j^\xi\right)}; \alpha \in \text{cube}, j \in \gamma_p'
\end{cases}
$$

(5.5)

Here, τ_{ps}^{α} represents the strengthening of the matrix due to γ_s' and γ_t' precipitates and is described below. Further, τ_{APB}^{α} represents the APB-dependent strength contribution and τ_{0j}^{α} represents the intrinsic strength of the cube slip system. G_j represents the shear modulus, b_j represents the Burgers vector magnitude, $k_{\rho j}$ represents the dislocation barrier strength, $A^{\alpha\xi}$ represents the matrix of slip system dislocation interaction coefficients and ρ^{ξ} represents the dislocation density in the slip system ξ.

Matrix strengthening due to precipitates may occur due to three mechanisms depending on the precipitate size (Kozar et al., 2009): (a) precipitate shearing by weakly coupled dislocation pairs, where the resolved shear stress increases with precipitate size up to ≈ 100 nm (applicable to γ_t' in the present case), (b) precipitate shearing by strongly coupled dislocation pairs, where the resolved shear stress decreases with precipitate sizes in the range 100 nm to 400 nm (applicable to γ_t'), and (c) Orowan looping of dislocations around precipitates for precipitate size > 400 nm (Shenoy et al., 2008; Kozar et al., 2009; Collins and Stone, 2014; Ghorbanpour et al., 2017; Gupta and Bronkhorst, 2021). Since the size of both γ_s' and γ_t' precipitates is less than 400 nm (cf. Figure 5.1), Orowan looping is assumed to be absent in the present case. Accordingly, τ_{ps}^{α} representing precipitate strengthening due to γ_s' and γ_t' and is modeled as (Collins and Stone, 2014):

$$\tau_{ps}^{\alpha} = \frac{A}{2}\left(\frac{\gamma_{APB}}{b}\right)^{\frac{3}{2}}\left(\frac{2d_{\gamma_t'}f_{\gamma_t'}}{Gb}\right)^{\frac{1}{2}} - \frac{1}{2}\left(\frac{\gamma_{APB}}{b}\right)f_{\gamma_t'} + \frac{1}{2}\left(\frac{Gb}{d_{\gamma_s'}}\right)f_{\gamma_s'}^{\frac{1}{2}}0.72w\left(\frac{\pi d_{\gamma_s'}\gamma_{APB}}{wGb2} - 1\right)^{\frac{1}{2}}$$
(5.6)

Here, A is a geometric factor, γ_{APB} is the APB energy per unit area, $d_{\gamma_s'}$ and $d_{\gamma_t'}$ are the sizes of the γ_s' and γ_t' precipitates, respectively, and w represents the elastic repulsion between the paired dislocations.

Lattice thermal vibrations overcome the short-range stress due to the thermal slip resistance, s_{tj}^{α}. This is assumed to have contributions primarily from solute solution strengthening due to the various alloying elements (Roth et al., 1997; Ghorbanpour et al., 2017), i.e.,

$$s_{tj}^{\alpha} = \frac{1}{M_j}\Sigma\left(\frac{d\sigma}{\sqrt{dC_i}}\sqrt{C_i}\right); \alpha \in \text{oct,cube}, j \in \text{matrix}, \gamma_p'$$
(5.7)

Here, M_j is the Taylor factor, C_i is atomic fraction, and $\frac{d\sigma}{\sqrt{dC_i}}$ is the strengthening coefficient for a given element. The concentrations of the various alloying elements for the matrix and γ_p' are directly obtained from experimental characterization (cf. Figure 5.2), while the strengthening coefficients have been taken from literature (Roth et al., 1997).

The framework considers the evolution of slip plane-level mobile, ρ_{Mj}^{α}, and immobile dislocation densities, ρ_{Ij}^{α}. Constitutive equations for their evolution have been adapted from (Ranjan et al., 2021; Chaudhary et al., 2022). Previously, these equations have also been used to represent substructure evolution in bcc, fcc, and hcp materials (Pokharel et al., 2019; Thool et al., 2020; Patra et al., 2023) and are given as Equations 5.9 and 5.10 in Table 5.1. The crystal plasticity model has been numerically implemented and interfaced with the Multiphysics Object-Oriented Simulation Environment (MOOSE) open-source finite element solver (Permann et al., 2020). A fully implicit Newton-Raphson algorithm has been implemented for the time step integration Patra et al. (2023).

TABLE 5.1: Constitutive equations

Constitutive Equation		Description
Driving stress for dislocation glide:		Slip direction and slip plane normal associated with the primary slip system are s^α, and m^α, respectively. Similarly, slip direction and plane normal associated with the "non-Schmid" primary edge, secondary edge and cube systems are $(s_{pe}^\alpha, m_{pe}^\alpha)$, $(s_{se}^\alpha, m_{se}^\alpha)$ and $(s_{cb}^\alpha, m_{cb}^\alpha)$, respectively. ϵ_p^i is the effective inelastic strain in the precipitate phase and ϵ_o^i is a material constant. The Schmid and non-Schmid slip systems are given in (Ranjan et al., 2021; Chaudhary et al., 2022).
$$\tau_j^\alpha = \begin{cases} s^\alpha \cdot \sigma \cdot m^\alpha; \alpha \in \text{oct}, j \in \text{matrix} \\ s^\alpha \cdot \sigma \cdot m^\alpha + \left(a_1 s_{pe}^\alpha \cdot \sigma \cdot m_{pe}^\alpha + a_2 s_{se}^\alpha \cdot \sigma \cdot m_{se}^\alpha \right. \\ \left. + a_3 s_{cb}^\alpha \cdot \sigma \cdot m_{cb}^\alpha \right) exp\left(-\frac{\epsilon_p^i}{\epsilon_o^i}\right); \alpha \in \text{oct}, j \in \gamma_p' \\ s^\alpha \cdot \sigma \cdot m^\alpha; \alpha \in \text{cube}, j \in \gamma_p' \end{cases}$$	(5.8)	
Mobile dislocation density evolution:		The first term represents dislocation multiplication at pre-existing segments, with the associated material parameter, k_{Mj}^α. The second term represents mutual annihilation of dislocation dipoles that are within a critical capture radius, R_C (Arsenlis and Parks, 2002). The third term represents trapping of mobile dislocations, thus rendering them immobile. This is a function of the mean free path of the dislocations, λ_j^α, and k_t^α is the associated material parameter. The effective mean free path, λ_j^α, is a function of the dislocation density across all slip systems and is given by, $\lambda_j^\alpha = \dfrac{1}{\sqrt{\sum_\xi \rho_j^\xi}}$; $\alpha \in$ oct,cube, $j \in$ matrix, γ_p'
$$\dot{\rho}_{Mj}^\alpha = \frac{k_{Mj}^\alpha}{b_j}\left(\sqrt{\sum_\xi \rho_j^\xi}\right)\left|\dot{\gamma}_j^\alpha\right| - \frac{2R_C}{b_j}\rho_{Mj}^\alpha\left|\dot{\gamma}_j^\alpha\right| - \frac{k_{tj}^\alpha}{b_j\lambda_j^\alpha}\left|\dot{\gamma}_j^\alpha\right|; \alpha \in \text{oct,cube}, j \in \text{matrix}, \gamma_p'$$	(5.9)	
Immobile dislocation density evolution:		The trapped mobile dislocations are rendered immobile, as given in the first term. The annihilation of dislocations by dynamic recovery is represented by the second term, and k_{dj}^α is the associated material parameter
$$\dot{\rho}_{Ij}^\alpha = \frac{k_{tj}^\alpha}{b_j\lambda_j^\alpha}\left|\dot{\gamma}_j^\alpha\right| - k_{dj}^\alpha\rho_{Ij}^\alpha\left|\dot{\gamma}_j^\alpha\right|; \alpha \in \text{oct,cube}, j \in \text{matrix}, \gamma_p'$$	(5.10)	

5.3.1 Model Parameters

The model parameters were first calibrated to predict the macroscopic stress-strain response of the polycrystalline superalloy at 293 K and 923 K and then validated by predicting the response at 523 K and 723 K. Parameters related to the initial yield were first fitted to the experimental yield stress data at 293 K and 923 K, followed by the hardening response. Physical justification for the former is provided in the following paragraphs. For the latter, the response was fitted to the experimental response by altering the dislocation evolution parameters.

The elastic constants for the γ and $\gamma^{'}$ phases were obtained from Keshavarz et al. (2016). The magnitude of the Burgers vector was taken from Keshavarz and Ghosh (2015a). All temperature-independent model parameters for inelastic deformation are listed in Table 5.4, and all microstructural parameters are listed in Table 5.5. The shape parameters for the dislocation glide enthalpy curve should lie between $0 < p_j^\alpha < 1$ and $1 < q_j^\alpha < 2$ (Kocks et al., 1975). Accordingly, we have chosen values that give a representative response. The strengthening and dislocation evolution parameters ($A^{\alpha\alpha}$, $A^{\alpha\zeta}$, ρ_M^0, ρ_I^0, R_c), were adopted directly from Ranjan et al. (2021), while other parameters ($k_{\rho j}^\alpha$, k_{dj}^α, k_{tj}^α, k_{mj}^α) were obtained based on best fit to the experimental data. The Hall-Petch coefficients, k_{Hj}^α, for γ phase and $\gamma_p^{'}$ phase were taken from Kozar et al. (2009) and Ranjan et al. (2021). Grain size (d_γ) and the size of $\gamma_p^{'}$ precipitates ($d_{\gamma_p'}$) were characterized from our experimental microstructure by the line intercept method from the EBSD microstructure using TSL-OIM software as given in Table 5.5. Our framework can account for individual grain sizes based on the EBSD mesh and their corresponding strength contribution. While we have not considered a strain gradient plasticity model, the framework provides the grain size from the finite element mesh to the constitutive model (based on the assumption of a circular grain shape), which then calculates the corresponding contribution of the Hall-Petch term for each material point. Such an approach has also been used in the literature (Zeng et al., 2016).

There is no data available in the literature regarding the APB energy-dependent strength contribution, τ_{APB}, for the superalloy under consideration. This term varies as a function of temperature and was calibrated in Ranjan et al. (2021) for a single crystal Ni-based superalloy, CMSX-4. As a first-order approximation, we have scaled the same as a function of the *representative* APB energy of the polycrystalline superalloy (which is expected to

be composition dependent), i.e.,

$$\tau_{APB}^{\alpha} = \tau_{APB}^{\alpha}|_{CMSX-4} \left(\frac{\gamma_{APB}}{\gamma_{APB}^{\alpha}|_{CMSX-4}} \right) \tag{5.11}$$

The representative APB energy, γ_{APB}, of the polycrystalline superalloy and that of CMSX-4, $\gamma_{APB}|_{CMSX-4}$, were taken from (Ma et al., 2008; Kozar et al., 2009; Ghorbanpour et al., 2017), while $\tau_{APB}^{\alpha}|_{CMSX-4}$ was taken from Ranjan et al. (2021), where it was first fit to the Ni$_3$Al yield stress data (Heredia and Pope, 1991b) and then used for predicting the asymmetric tension-compression yield behavior of CMSX-4 single crystal superalloys over a range of loading orientations and temperatures (Ranjan et al., 2021):

$$\begin{aligned} \tau_{APB}^{\alpha}|_{CMSX-4} = {} & 2.589 \times 10^{-15}T^6 - 9.269 \times 10^{-12}T^5 + 1.033 \times 10^{-8}T^4 - 2.784 \times 10^{-6}T^3 \\ & -1.452 \times 10^{-3}T^2 + 9.265 \times 10^{-1}T - 6.522 \times 10^1 \text{ MPa}; \ 260 \text{ K} \leq T \leq 1304 \text{ K} \end{aligned} \tag{5.12}$$

In this polynomial expression, the pre-factors of the temperatures vary over a wide range of magnitudes as the temperature itself goes to a sixth-order polynomial. A sixth-order polynomial was necessitated as $\tau_{APB}^{\alpha}|_{CMSX-4}$ initially increased with an increase in temperature up to about 1000 K and then reduced beyond this temperature (cf. Figure 3(a) in Ranjan et al. (2021)). We note that the APB energies are expected to vary as a function of superalloy composition. As discussed in (Ghorbanpour et al., 2017; Vamsi and Karthikeyan, 2021), this can be estimated using lower length scale calculations to arrive at more refined estimates in future work. Further, the temperature-dependent intrinsic resistance for cube slip, τ_{0j}^{α}, was estimated by (Allan, 1995), and also used by (Ranjan et al., 2021). Those values are directly used here in the following form:

$$\tau_{0j}^{\alpha} = \begin{cases} 858 \ - \ 0.577T \text{ MPa}; \ T \geq 915 \text{ K} \\ 330 \text{ MPa}; \ T < 915 \text{ K} \end{cases} \tag{5.13}$$

The geometry parameter, A, for precipitate strengthening was set to 0.72 (Collins and Stone, 2014) (cf. Equation (5.6)). The elastic repulsion parameter, w, was set to 1.4 by fitting it to experimental data by Hüther and Reppich (1979), which was further approximated to be 1 by Collins and Stone (2014). Further, sizes of the secondary, $d_{\gamma_s'}$, and tertiary precipitates, $d_{\gamma_t'}$, were estimated using the line intercept method for $d_{\gamma_s'}$ from SEM characterization and $d_{\gamma_t'}$ from TEM characterization. γ_p' volume fraction was calculated from phase maps obtained from EBSD characterization, using the TSL-EDX software. The volume fraction of γ_s' precipitates is commonly observed to lie within $0.3 - 0.5$ (Shenoy

et al., 2008; Deng et al., 2020). Characterizing the SEM images (cf. Figure 5.1(b)) by the line intercept method resulted in a similar volume fraction of $\gamma_s^{'}$ (0.41). The volume fraction of $\gamma_t^{'}$ was taken from literature (Deng et al., 2020). Coefficients for solution strengthening in nickel were adopted from Roth et al. (1997), while the solute concentrations have been obtained from our EDS measurements. The solute concentration profiles obtained from EDS have been assumed to be uniform for a phase distributed across the entire microstructure. Solute segregation at the twin and high angle grain boundaries has not been explicitly considered in the model. This could also be a potential contributor to heterogeneous deformation.

TABLE 5.2: Temperature-dependent elastic constants for γ and $\gamma^{'}$ phase (Keshavarz et al., 2016).

Parameter	Value
γ	$C_{11} = (298.0 - 0.096T)$ GPa
	$C_{12} = (191.0 - 0.057T)$ GPa
	$C_{44} = (139.0 - 0.035T)$ GPa
$\gamma^{'}$	$C_{11} = (325.0 - 0.096T)$ GPa
	$C_{12} = (209.0 - 0.057T)$ GPa
	$C_{44} = (144.0 - 0.035T)$ GPa

TABLE 5.3: Temperature-invariant strengthening coefficients and solute concentrations of the alloying elements for the matrix and $\gamma_p^{'}$ phase. The strength coefficients are taken from Roth et al. (1997), while the concentrations are from our EDS measurements.

Alloying Element	Strength Coefficient $\left(\text{MPa} \cdot \text{At.Fraction}^{-\frac{1}{2}}\right)$	Atomic Fraction (matrix)	Atomic Fraction $(\gamma_p^{'})$
Al	225	8.75	12.78
Mo	1015	2.80	0.72
Ti	775	5.70	9.71
Cr	337	14.68	4.68
Co	39.4	15.30	10.30
Ni	-	52.80	61.90

5.4 Results

We first present model predictions of the monotonic stress-strain response over a range of temperatures, as compared with experiments. We then study competitive misorientation developments at the different microstructural features, namely, annealing twin boundaries, matrix/$\gamma_p^{'}$ phase interfaces, and grain boundaries, during room temperature deformation.

TABLE 5.4: Temperature-invariant flow, strengthening and substructure parameters for γ and $\gamma_p^{'}$ phase.

Parameter	$\alpha \in$ oct, $j \in$ matrix	$\alpha \in$ oct,cube, $j \in \gamma_p^{'}$
Reference strain rate: $\dot{\gamma}_{0j}\left(s^{-1}\right)$	10^2	10^{-3}
Activation energy for dislocation glide: ΔF_j^{α}	$10Gb^3$	$10Gb^3$
Shape parameters: p_j^{α}, q_j^{α}	0.5, 1.4	0.5, 1.4
Dislocation barrier strength: $k_{\rho j}^{\alpha}$	0.45	0.45
Dislocation interaction coefficients: $A^{\alpha\alpha}$, $A^{\alpha\zeta}$	1, 0	1, 0
Initial dislocation densities: $\rho_M^0\left(m^{-2}\right)$, $\rho_I^0\left(m^{-2}\right)$	1×10^{12}, 1×10^{12}	1×10^{12}, 1×10^{12}
Hall–Petch coefficient: $k_{Hj}^{\alpha}\left(\mathrm{MPa}\sqrt{\mu m}\right)$	250	222.22
Dislocation multiplication constant: k_{Mj}^{α}	0.24	0.25
Capture radius for annihilation of mobile dislocations: R_c	6b	6b
Dislocation trapping constant: k_{tj}^{α}	0.12	0.065
Dynamic recovery constant: k_{dj}^{α}	2000	5
Burgers vector magnitude: $b(nm)$	0.249	0.249
APB energy of polycrystalline superalloy: $\gamma_{APB}\left(\frac{mJ}{m^2}\right)$	200	200
APB energy of CMSX-4: $\gamma_{APB}|_{CMSX-4}\left(\frac{mJ}{m^2}\right)$	-	111
Geometry parameter: A	0.72	-
Elastic repulsion parameter: w	1	-

TABLE 5.5: Microstructural parameters for γ and $\gamma^{'}$ phases.

Parameter	Value
$f_{\gamma_p^{'}}$, $f_{\gamma_s^{'}}$, $f_{\gamma_t^{'}}$, f_{γ}	0.09, 0.41, 0.0772, 0.4228
$d_{\gamma_p^{'}}\left(\mu m\right)$, $d_{\gamma_s^{'}}\left(nm\right)$, $d_{\gamma_t^{'}}\left(nm\right)$, $d_{\gamma}\left(\mu m\right)$	3.9, 250, 19, 27.92

5.4.1   Macroscopic Stress-Strain Response

The constitutive model was first calibrated to the tensile stress-strain response at 293 K and at 923 K. The undeformed experimental (EBSD) texture shown in Figure 5.4 in the Appendix (in terms of the (111), (110), and (001) pole figures) was used to generate reduced textures comprised of 512 orientations for each deformation temperature. Preliminary simulations were performed on 3D microstructures, in which an appropriate number of grains were assigned to the primary $\gamma_p^{'}$ precipitates according to their volume fraction, and the rest were the matrix phase. 8 hexahedral elements (with linear interpolation) were used per grain, assuming cube-shaped grains, using the reduced texture shown in Figure 5.4 in the Appendix. Roller boundary conditions were applied on the three adjacent faces of the domain (displacements normal to these three faces were prescribed as zero). The corner node common to these three faces was fixed. Displacement-controlled tensile loading was applied along the y-direction (referred to as Loading Direction (LD) in Figure 5.4) at a prescribed strain rate of 10^{-4} s^{-1}. Comparison of the predicted mechanical response is shown in Figure 5.7, while a comparison of the predicted deformed textures with

their experimental counterparts is shown in Figure 5.4. The deformed experimental (111), (110), and (001) pole figures show that the concentrations of poles along the Normal Direction (ND) as observed in the undeformed pole figure become diffuse after 15% applied strain due to lattice rotation at both temperatures. The model also predicts this behavior qualitatively, although to a smaller extent. Enhanced lattice rotation at elevated temperatures (923 K) results in significant dispersion of the ND || (001) pole, a phenomenon well captured by our model. Enhanced lattice rotation at elevated temperatures (923 K) leads to a more pronounced dispersion of the ND || (001) pole compared to room temperature. The model qualitatively captures this trend as is evident from the Texture Indices reported before and after deformation in Table 5.6 The Texture Index (TI) is generally used as a measure of the anisotropy of texture and is calculated as (Pai et al., 2025):

$$TI = \int f(g)^2 dg \tag{5.14}$$

Where $f(g)$ is the numerical ODF value in a small Euler space segment of dg. As can be seen, the predicted TI is lower after deformation at 923 K, indicating a lower degree of texture anisotropy due to the above mentioned dispersion of the ND || (001) pole, as compared to deformation at room temperature.

However, it should be noted from both experiments and simulations that the texture

TABLE 5.6: Texture Index (TI) before and after tensile deformation as calculated from the experimental and simulated textures.

Temperature (K)	Experiment	Simulation
293 (0%)	1.6650	1.7721
293 (15%)	1.6191	1.6677
923 (0%)	1.3638	1.3276
923 (15%)	1.2382	1.1959

evolution is not significant, as may be expected at a relatively small deformation of 15% applied strain. Comparison of the deformed texture has also been shown in terms of the Inverse Pole Figure (IPF) and Orientation Distribution Function (ODF) plots in the Figure 5.5 and 5.6, respectively.

Figure 5.7(a) and (b) show the comparison of the model-predicted stress-strain response with the experimental counterparts at 293 K and 923 K, respectively. The model predicts the initial yield strength at both 293 K and 923 K with reasonable accuracy. However, the experimental hardening rate at 293 K is initially low, followed by an increase in the hardening rate. The constitutive model is not able to predict this trend, although the flow stress
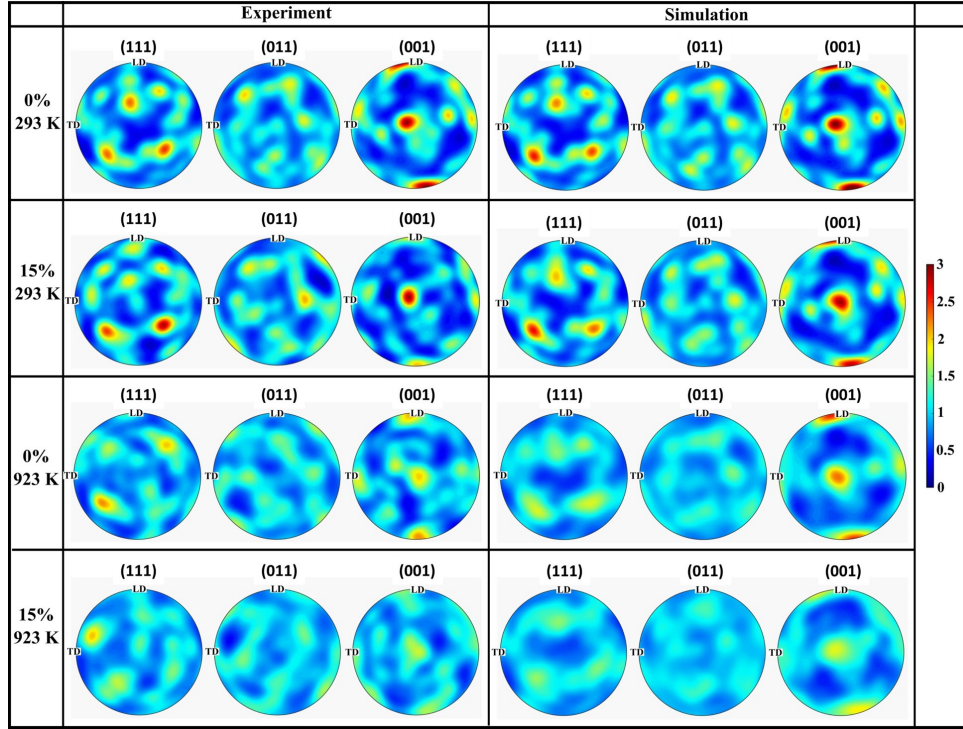
FIGURE 5.4: Comparison of the initial and predicted 512 grain deformed textures with their experimental counterparts at 293 K and 923 K. Here, LD and TD refer to the Loading and Transverse Directions, while the Normal Direction (ND) is out of the plane.

(and hardening) at higher strains (> 0.12) is again predicted with reasonable accuracy. This is discussed later in Section 5.5. However, note that such a non-monotonic hardening is not observed at higher temperatures, where the constitutive model can qualitatively predict the response over the entire range of deformation.

Model predictions of mechanical response at two intermediate temperatures (523 K and 723 K) are used as validation cases (Figure 5.7 (c) and (d), respectively). Although a marginally lower yield stress is predicted at both these temperatures, the simulated mechanical response shows a qualitative comparison with the experiments. This suggests that the constitutive models and associated parameters were able to capture the underlying physics of deformation across a range of temperatures. Further, the root mean square error (RMSE) is given in Table 5.7 to quantify the error between simulation and experimental results. It is calculated as:

$$RMSE = \sqrt{\frac{1}{N}\left(\frac{\sigma_{exp}(\bar{\epsilon}) - \sigma_{sim}(\bar{\epsilon})}{\sigma_{exp}(\bar{\epsilon})}\right)^2} \qquad (5.15)$$

where $\sigma_{exp}(\bar{\epsilon})$ and $\sigma_{sim}(\bar{\epsilon})$ represents the experimental and simulated stress values at
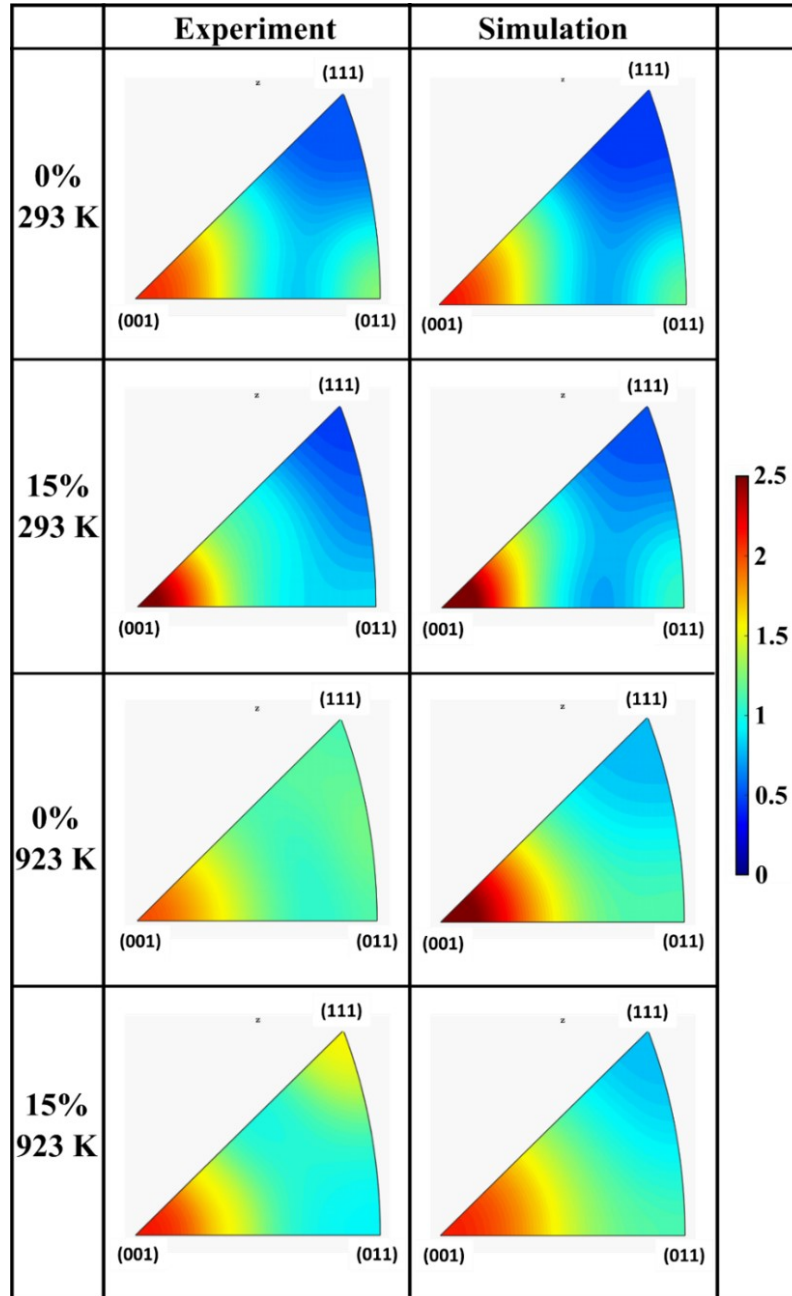
FIGURE 5.5: Comparison of the initial and predicted 512 grain deformed textures with EBSD measurements shown on the Inverse Pole Figure (IPF).
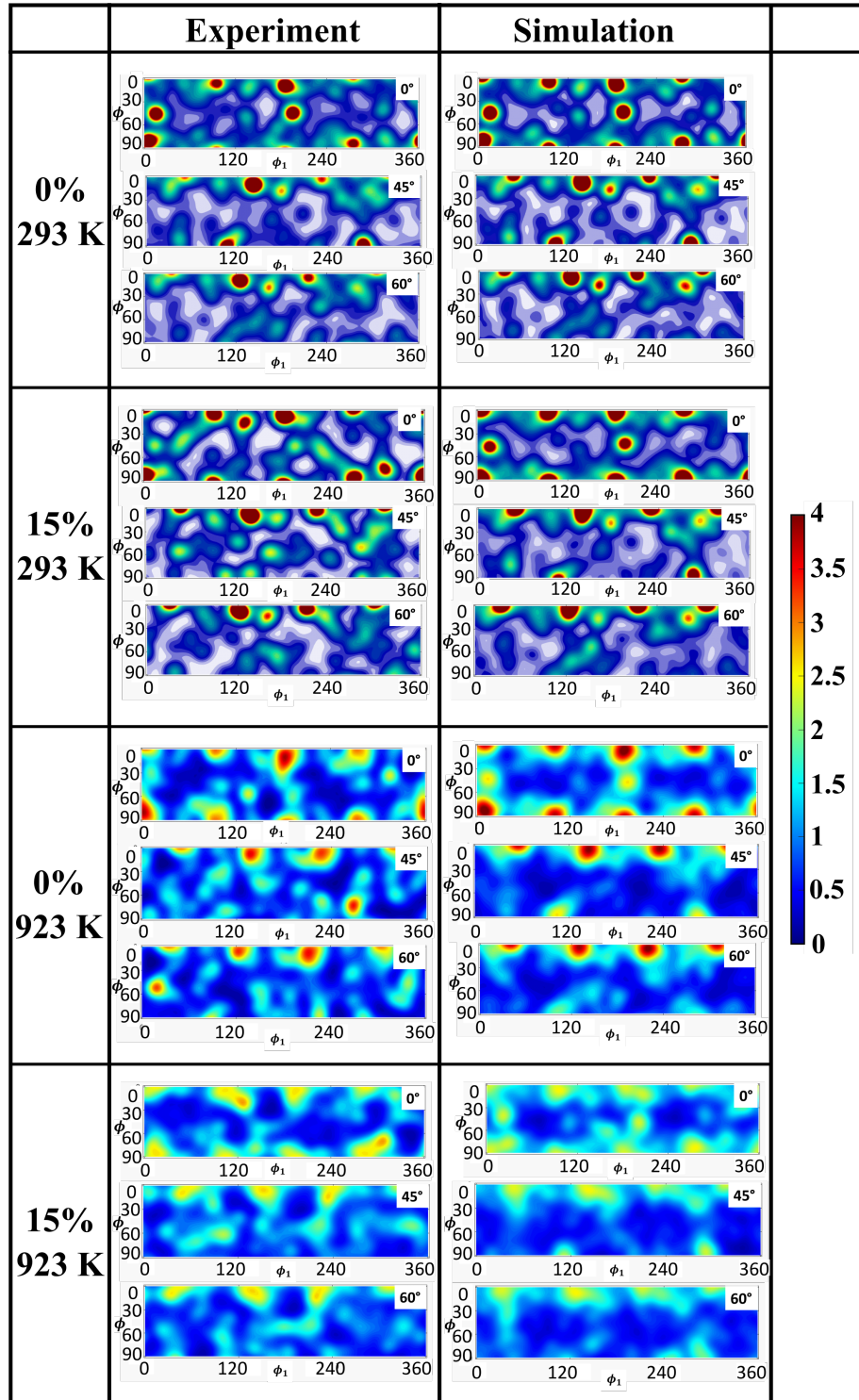
FIGURE 5.6: Comparison of the initial and predicted 512 grain deformed textures with EBSD measurements, shown using Orientation Distribution Function (ODF) plots.

strain= $\bar{\epsilon}$, respectively. N is total number of experimental data points. It can be seen that except for 723 K, the error is less than 10% for all other cases.

TABLE 5.7: RMSE for simulation and experimental results shown in Figure 5.7.

Temperature (K)	293	523	723	923
RMSE(%)	8.38	5.69	12.36	2.27
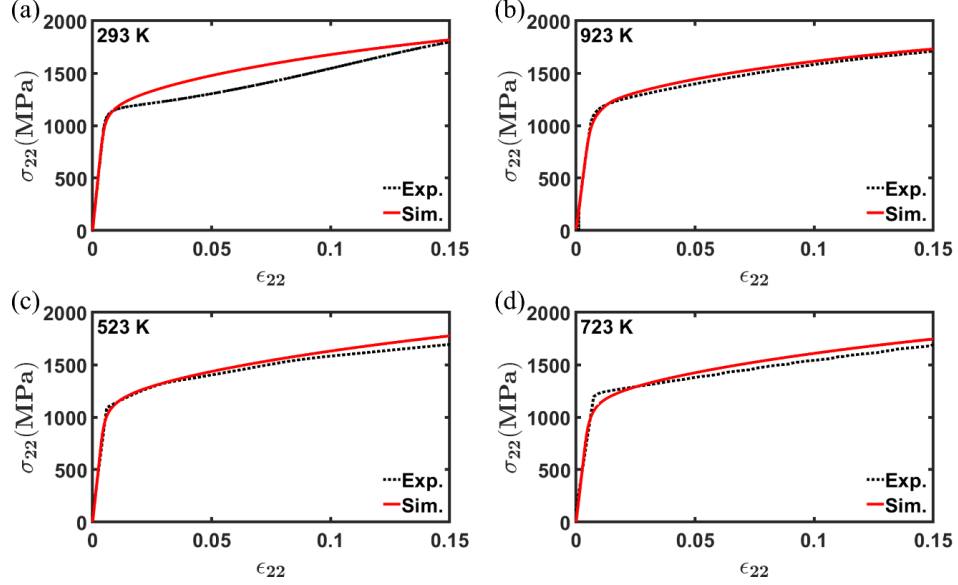
FIGURE 5.7: Comparison of the predicted stress-strain response using a simulation domain comprised of 512 grains (with reduced texture) with the corresponding experimental data at (a) 293 K, (b) 923 K, (c) 523 K, and (d) 723 K, respectively. The model was first fit to the mechanical response at 293 K and 923 K and then validated by predicting the same at 523 K and 723 K.

The temperature-dependent contributions to strength of the superalloy from the different phases are discussed in the following. It should be noted that the initial yield stress and the flow stress of the superalloy are similar and comparable at all deformation temperatures, as seen in both experiments and simulations. However, the underlying strengthening mechanisms are expected to be different. Figure 5.8 shows the 0.2% offset yield strength of the superalloy, matrix, γ'_p precipitate, and individual γ as predicted from the simulations performed at four different temperatures. For these simulations, the same representative texture was used as for the simulations reported in Figure 5.4. Further, the yield strength of the "composite" superalloy is also shown in Figure 5.8. As can be seen, the yield strength of the γ and matrix $(\gamma + \gamma'_s + \gamma'_t)$ phase decreases marginally with increase in temperature. This is due to the temperature sensitivity of the flow rule and is qualitatively similar to conventional metals and alloys, although strengthening due to the γ'_s and γ'_t precipitates does not allow a significant drop in the strength of matrix phase even at higher homologous

temperatures. On the other hand, the yield strength of $\gamma_p^{'}$ phase increases with an increase in temperature. As a result of this strengthening, the yield strength for the polycrystalline superalloy shows little or no decrease with an increase in temperature. This is generally referred to as a yield anomaly in the literature (Westbrooke et al., 2005; Shenoy et al., 2008; Ranjan et al., 2021) and is attributed to the formation of Kear-Wilsdorf locks. The Critical Resolved Shear Stress (CRSS) increases as these locks restrict the dislocation motion on the primary slip plane (Shenoy et al., 2008). This observation motivates the consideration of non-Schmid deformation in the primary $\gamma_p^{'}$ precipitates (cf. Equation 5.8), which would otherwise have demonstrated lower strength at elevated temperatures. It should be noted that a *conventional* crystal plasticity model, which does not account for these material-specific deformation mechanisms, would not be able to predict this anomalous deformation behavior commonly observed in Ni-based superalloys. Other manifestations of non-Schmid effects, such as orientation- and temperature-dependent tension-compression asymmetry Allan (1995); Ghorbanpour et al. (2017); Xu et al. (2023) will be studied using this model in future work.
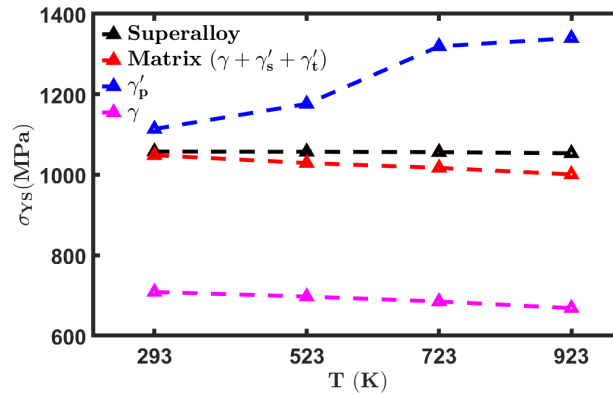
FIGURE 5.8: Effect of temperature on the predicted yield strength of the superalloy, as well as matrix $(\gamma + \gamma_s^{'} + \gamma_t^{'})$, primary $\gamma_p^{'}$ phase and the γ phase. The yield strength of the γ phase was predicted by removing the precipitate strengthening contribution in the model.

The results presented in this section offer qualitative validation of the constitutive model's predictive capabilities for the mechanical response during tensile loading over four different temperatures from 293 K to 923 K. In the following sections, this framework has been used to simulate EBSD microstructures at room temperature and predict the misorientation development during deformation.

5.4.2 Microstructure Evolution during Interrupted Tensile Tests

Interrupted tensile tests were performed on the as-received samples at room temperature. EBSD scans with an area of ($100\mu m \times 100 \ \mu m$) were acquired before the deformation and at regular intervals of 5 % applied strain during the tensile tests. The corresponding Image Quality (IQ), Inverse Pole Figure (IPF), and KAM maps after different applied strains (i.e., 0%, 5%, 10%, and 15%) are shown in Figure 5.9, along with the phase map. The phase map reveals the presence of three major features of interest in these microstructures, namely: phase interfaces, annealing twin boundaries, and grain boundaries. The extent of localized deformation in the vicinity of these features is expected to govern the resistance to crack initiation in these microstructures. Based on visual inspection, our EBSD results indicate that at 15 % applied strain, the localizations are much more concentrated at the grain interiors, especially adjacent to the phase interfaces and annealing twin boundaries.

A majority of these annealing twin boundaries (97%) were observed to be coherent $\Sigma 3$ boundaries. The statistics have not been shown here for brevity. The sharp change in orientation of slip systems across the twin boundary may result in the localization of strain to accommodate incompatible deformation. Another source of misorientation development in the grain interior during deformation is due to the $\gamma_p^{'}$ precipitates. In general, presence of larger $\gamma_p^{'}$ or more number of $\gamma_p^{'}$ precipitates results in larger heterogeneity in deformation. This could be attributed to the obstruction of dislocation glide by the $\gamma_p^{'}$ precipitates. Additionally, misorientation localizations are also visible around triple and quadruple junctions formed between the matrix and the primary $\gamma_p^{'}$ precipitates.

There have been several studies that focus on the orientation dependence of substructure evolution during deformation (Zhang et al., 2019b; Prakash et al., 2022; Pai et al., 2022; Hestroffer et al., 2022). Generally, the softer grains tend to deform more easily and develop more heterogeneities as compared to their hard counterparts. This may lead to the development of grain interior as well as grain boundary localizations in the soft grains. In contrast, the localizations are often restricted to the vicinity of grain boundaries in the hard grains (Mishra et al., 2009; Pai et al., 2022). However, such an effect gets diminished in the presence of solute atoms/precipitates within the grains, irrespective of the grain orientation. This can be seen in Figure 5.9, where the regions surrounding the $\gamma_p^{'}$ precipitates and annealing twins develop more heterogeneities, even within the hard grains.
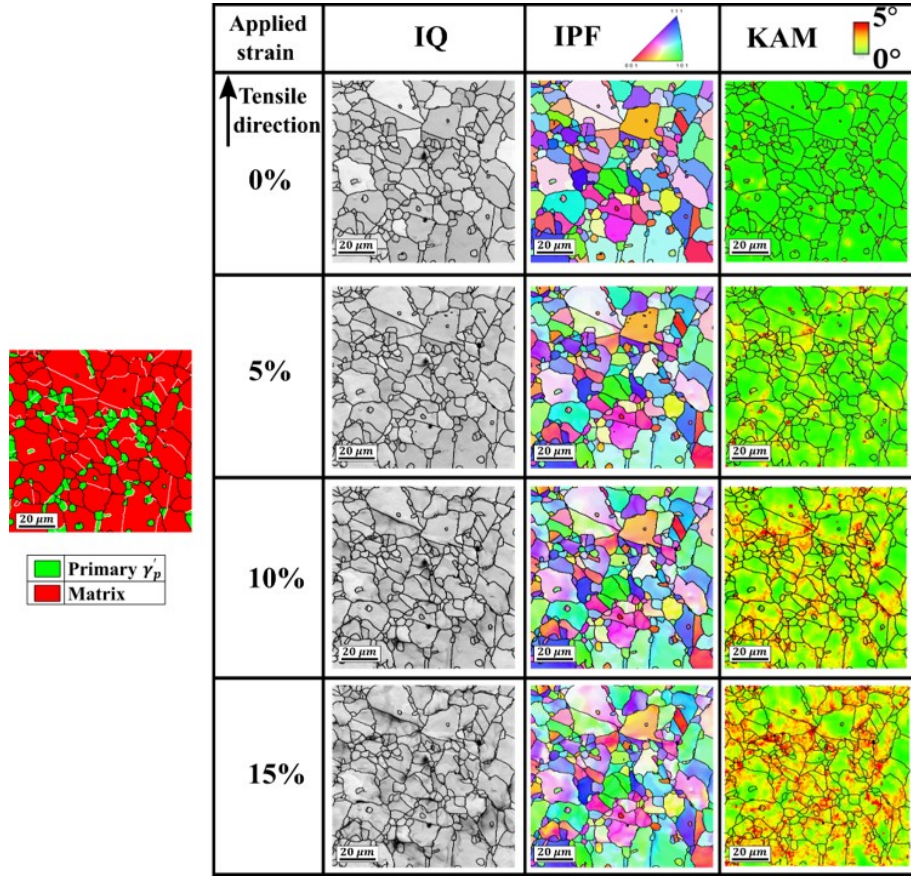
FIGURE 5.9: EBSD measurements from different stages of interrupted tensile deformation (0%, 5%, 10% and 15% applied strains) showing the Image Quality (IQ), Inverse Pole Figure (IPF), and Kernel Average Misorientation (KAM) maps. The phase map on the left shows the Σ3 Coincidence Site Lattice (CSL) twin boundaries marked with white lines, while the grain boundaries are marked with black lines.

5.4.3 Representative deformation contours obtained from simulations

EBSD microstructures were used as input for our CPFE simulations. The EBSD scans were divided into four regions of approximately equal areas of $100\mu m \times 100~\mu m$, which were simulated individually. The microstructures were meshed using 3D hexahedral elements of size 1 μm and with linear interpolation. The loading and boundary conditions employed in our 3D CPFE simulations are shown in Figure 5.10. Displacement normal to the x and y directions was set to zero along the left and bottom faces, respectively. The corner node common to these two faces was fixed. Displacement-controlled tensile loading at a nominal strain rate of $10^{-4}~s^{-1}$ was applied on the top face along the y-direction, while the x-direction and the out-of-plane z-direction were stress-free. These are representative of the axisymmetric boundary conditions. The microstructure has been meshed using 2 layers of elements along the depth/thickness direction (z-direction) as shown in the inset

in Figure 5.10, which also shows the microstructure in terms of the phase map. This is similar to the 3D simulation methodology used in Hestroffer et al. (2022) for studying superalloy deformation and misorientation development.
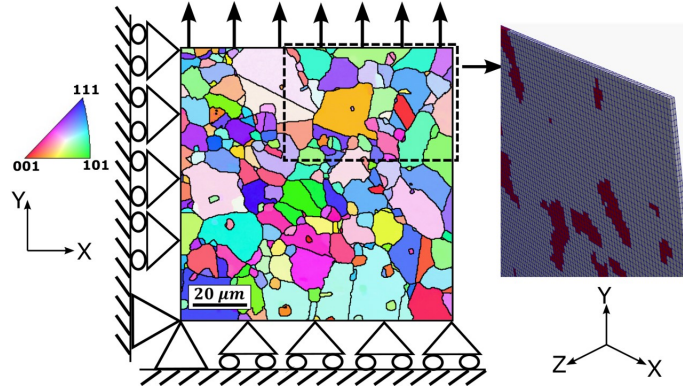
FIGURE 5.10: Simulation setup and boundary conditions overlaid on the IPF map of the EBSD microstructure. The inset shows the corresponding phase map, where the gray color represents the matrix phase and the red color represents the γ_p' precipitates.

Figure 5.11 shows the predicted von Mises effective stress, $\bar{\sigma}$, and effective strain, $\bar{\epsilon}$, contours at 5%, 10%, and 15% applied strains for one of the four simulated microstructures. The phase map indicating the twin boundaries (white lines) and grain boundaries (black lines) is also shown in the same figure. Progressive stress and strain localizations are observed with increasing applied strains. Strain localization in the γ_p' precipitate is comparatively lower than that in the matrix, whereas the stress localization is generally higher in γ_p' precipitate. The flow stress in the matrix $(\gamma + \gamma_s' + \gamma_t')$ is marginally lower than that of γ_p' precipitates (also see Figure 5.9). Higher plastic deformation in the γ phase may have contributed to higher strain concentration. Generally, strain localization in the matrix is observed in the vicinity of γ_p' precipitates. This indicates that γ_p' precipitates might contribute to crack initiation or damage upon further deformation. This hypothesis will be explored further in the following sections.

Annealing twin boundaries are microstructural features that are known to play a vital role in crack initiation for the PM-processed Ni-superalloys (Jiang et al., 2015b; Zhang et al., 2022b), which depends on the elastic stiffness difference between the parent and twin grains and also the length of twin boundaries (Stinville et al., 2016). High maximum Schmid factor (softer grain) along with high twin boundary length and high elastic modulus difference have been correlated with the strain localizations (and eventual crack initiation) in the twin and parent grains. Here, strain localizations are observed in the softer grain and stress localizations in the harder grain between the twin/parent grain pairs (cf. Figure
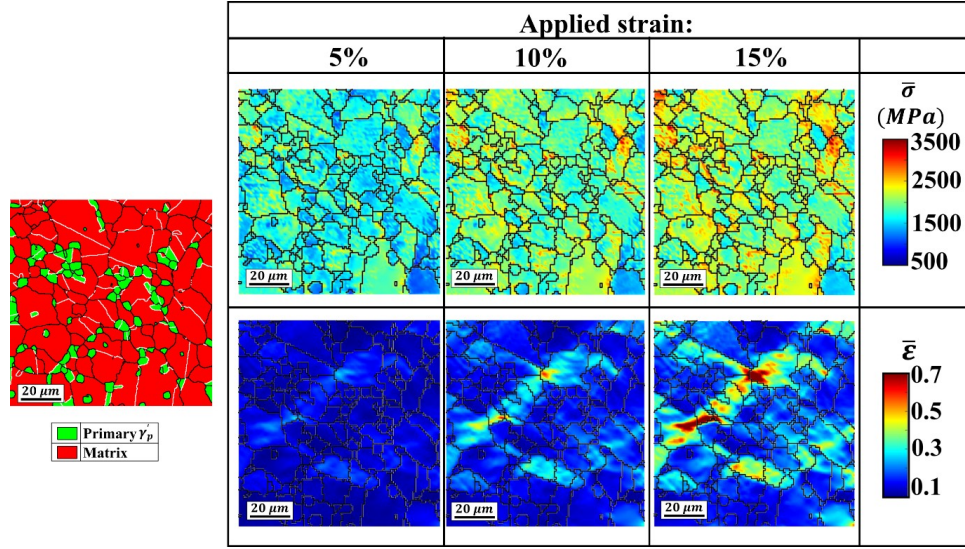
FIGURE 5.11: Evolution of von Mises effective stress, $\bar{\sigma}$, and effective strain, $\bar{\epsilon}$, with increasing applied strain. $\Sigma 3$ Coincidence Site Lattice (CSL) twin boundaries are marked with white lines, and grain boundaries are marked with black lines.

5.11). These results qualitatively indicate that the strain localizations near the twin/parent grain pair are much higher than the strain localization in the proximity of γ'_p precipitates.

5.4.4 Comparison of Misorientation Development between Experiments and Simulations

5.4.4.1 Evolution of KAM Contours with Applied Strain

In order to study the microstructure evolution with deformation, Kernel Average Misorientation (KAM) maps are plotted at different applied strains. KAM is the point-to-point misorientation that represents the average misorientation of a pixel with its immediate neighbours and is generally used as an indicator for deformation localization. Euler angle information extracted from the EBSD measurements and crystal plasticity simulations for each material point was used to calculate KAM using the formulation (Wright et al., 2011, 2016):

$$KAM(^{\circ}) = \frac{1}{n} \sum \Delta g_{ij} \left(g_i g_j \right) \tag{5.16}$$

where, $\sum \Delta g_{ij} \left(g_i g_j \right)$ indicates the misorientation between a pixel i, and its neighbor, j. n here represents the number of neighbors surrounding a pixel. For a square grid, n takes the value of 4 in our EBSD scans. Further, we have restricted the maximum intragranular misorientation to 5°. The local misorientation is known to correlate with the development

of Geometrically Necessary Dislocations (GNDs) (Pai et al., 2022). While our modeling framework does not account for GNDs, misorientations are still expected to develop in the regions of heterogeneous deformation.

Figure 5.12 shows the normalized KAM contours, as obtained from experiments and CPFE simulations at 5%, 10%, and 15% applied strains. These data points are obtained by normalizing the KAMs with the maximum value of KAM observed during that respective stage of the experiment or simulation. Initial Euler angles at $\epsilon = 0\%$ were obtained from the EBSD measurements and used as input to our model. These Euler angles are updated subsequently at every time step in our CPFE model. We then extract the updated Euler angles at 5%,10%, and 15% applied strains, respectively, using an open source library, Sandia Engineering Analysis Code Access System (SEACAS) (Sjaardema, 2017), and plot the crystallographic orientation-based maps, such as IPF and KAM, using the TSL-OIM software.

It can be seen that the average KAM increases with applied strain in both the experimental as well as the simulated microstructure. Local misorientations develop in these heterogeneously deforming microstructures due to different grain orientations, and different microstructure features, such as grain boundaries, twin boundaries, and phase $(\text{matrix}/\gamma_p^{'})$ interfaces. The deformation initiates primarily in the softer matrix phase. The harder $\gamma_p^{'}$ precipitates do not accommodate any significant strains (cf. $\bar{\epsilon}$ contours at 5% applied strains in Figure 5.11). This can also be observed by comparing the experimental and simulated KAM contours (at $\epsilon = 5\%$) with the corresponding phase maps in Figure 5.12, where misorientation localizations are mainly observed near the phase interfaces and twin boundaries. For easier interpretation, we have represented the phase interfaces by blue lines and twin boundaries using white lines in Figure 5.12.

As can be seen from the experimental microstructure, misorientations are more concentrated in the grain interior in regions adjacent to phase interfaces and twin boundaries and less at grain boundaries (see regions marked by black arrows). A similar behavior has also been predicted by our CPFE framework, although the KAM is over-predicted in some regions. Coarse mesh size could be the primary cause for such discontinuities; a lower element/step size of the EBSD microstructure would presumably overcome such an issue, however, leading to higher computational costs. As the deformation progresses, these localizations intensify, especially those along the twins and twin-grain boundary intersections. This can be attributed to the variation in elastic stiffness between the twin/parent grain pairs. Further, no notable misorientation localizations are still observed in the $\gamma_p^{'}$

precipitates, though the localization is higher in the matrix near these precipitates. Similar to the strain localization, higher KAM localization is found to occur on the softer side of the twin and parent grain pair (twin boundaries are represented by white lines) in the predictions.

In general, the favourably oriented grains in the vicinity of primary $\gamma_p^{'}$ precipitates and twin boundaries undergo higher deformation, and thus display more localizations. Further investigation reveals the presence of grain clusters (see markers A-D in Figure 5.12), which show similar deformation behavior between the experiments and simulations. For example, the localizations developing at the twin-grain boundary intersections (see marker C) are well predicted by our modeling framework. The maximum KAM observed in experiments is 3.21° (at the twin-grain boundary intersection (marker C)), which is similar to our predictions, 2.89° at the same location. Additionally, we have also marked grains whose average intragranular KAM is comparable between experiments and simulations (see markers A-B).

To further explore the effect of misorientation development along the annealing twin boundaries, we analyse the deviation of these twin boundaries from the ideal CSL relationship, i.e., $\Sigma 3 =< 111 > 60°$ Kronberg and Wilson (1949). Brandon's criterion defines a tolerance within which these special/CSL boundaries exist Brandon (1966). In the present study, we have calculated the tolerance using the equation: k/Σ^n, where $k = 15°$ (represents the transition from low angle to high angle grain boundary) and $n = 1/2$. The deviation from ideal CSL (in degrees), along with their standard deviation, has been noted in Table 5.8. With increasing applied strains, the deviation increases for both experiment ($2.74 \pm 1.84°$ at $\bar{\epsilon} = 5\%$ to $4.10 \pm 2.29°$ at $\bar{\epsilon} = 15\%$) as well as simulation ($2.46 \pm 2.26°$ at $\bar{\epsilon} = 5\%$ to $4.94 \pm 2.12°$ at $\bar{\epsilon} = 15\%$). This is expected, since crystallites on both sides of the twin boundaries would rotate to accommodate the applied deformation, resulting in deviation from the ideal $< 111 > 60°$ relationship Hestroffer et al. (2022). However, the magnitude of change in the simulation is, to some extent, larger in comparison to our experimental results. This is in coherence with our earlier reported misorientation data, where we observe that our simulations over-predict the misorientations as compared to the experiments. The same contributed to a higher deviation from ideal CSL in the simulations. Nonetheless, our results do indicate that the proposed numerical framework has qualitatively captured the deformation characteristics and misorientation development in the vicinity of annealing twin boundaries.

However, the model does exhibit some discrepancies; the simulated KAM varies significantly in comparison to its experimental counterparts (especially) in the vicinity of a $\gamma_p^{'}$

TABLE 5.8: Deviation from ideal CSL relationship ($\Sigma 3 = < 111 > 60°$) for annealing twins in the deformed microstructures.

	Deviation from $\Sigma 3$ (°)	
$\bar{\epsilon}$	Experiment	Simulation
0%	1.53 ± 1.20	1.53 ± 1.20
5%	2.74 ± 1.84	2.46 ± 2.26
10%	3.40 ± 2.00	3.96 ± 2.06
15%	4.10 ± 2.29	4.94 ± 2.12

precipitate (see markers E-G). Also, KAM accumulates in both twin and parent grains in the simulations. KAM accumulation is higher at grain boundaries than grain interior for some grains in the simulations. This can be attributed to two specific reasons. Firstly, the model does not account for the effect of strain gradients and can lead to an underestimation of deformation heterogeneities. It has been shown that the misorientation development in the vicinity of microstructure heterogeneities may be better predicted using strain gradient plasticity models (Pai et al., 2022), even in superalloys with relatively simple constitutive models for strengthening (Zhang et al., 2014; Bergsmo et al., 2022). Secondly, the simulation domain comprised of only two layers of elements along the thickness, which may have contributed to overestimating the localizations. The prediction accuracy may be increased by considering more number of elements along the thickness (Lim et al., 2014, 2015), although at higher computational costs. Nonetheless, there is qualitative concurrence between the simulated and experimental contour maps of normalized KAM.

5.4.4.2 Statistics of Misorientation Development at Different Microstructural Features

As discussed earlier, crack initiation and micro-crack propagation are expected to be influenced by various grain-scale microstructural features, such as twin boundaries, grain boundaries, and phase (matrix/γ'_p) interfaces. While the role of the former in failure has been studied extensively (Stinville et al., 2015; Charpagne et al., 2021; Hestroffer et al., 2022), there is limited evidence in the literature to suggest that phase interfaces may also be contributing to failure in these PM processed superalloys (Flageolet et al., 2005; Jiang et al., 2015a). In order to explore this further, we have studied the competitive misorientation developments at these three features (grain boundaries, twin boundaries, and phase interfaces) in terms of the distribution of KAM from the experimental and simulated microstructures at different applied strains. These are plotted in Figure 5.13 in terms of

FIGURE 5.12: Normalized KAM contours at different stages of deformation as predicted using the crystal plasticity model and comparison with the experimental contours. $\Sigma 3$ Coincidence Site Lattice (CSL) twin boundaries are marked with white lines, phase interfaces are marked with blue lines, and grain boundaries are marked with black lines. Markers (A-D) represent grains whose average intragranular KAMs are comparable with the experiments, and markers (E-G) represent grains showing discrepancies with experimental results.

the number fraction of the pixels belonging to the respective features. KAM values were extracted at grain boundaries and phase interfaces directly from the TSL-EDX EBSD system, while an in-house MATLAB code was developed to extract the KAM values at the twin boundaries. Broadly speaking, microstructural features with a higher spread of KAM distribution may be correlated with a higher propensity of crack nucleation/propagation.

The spread of KAM values increases with an increase in applied strain for experimental and as well as simulated microstructures (see Figure 5.13). This is for the same microstructure as shown in Figure 5.12. The spread in the KAM histogram is roughly similar for 10% and 15% applied strain for both experiments and simulations. At 5% applied strain, the simulations predict a slightly higher spread as compared to the experiments. This might

be due to higher misorientation developments (in the microstructure discussed above) at the grain interior than at grain/phase/twin boundaries.

FIGURE 5.13: KAM distribution at different applied strains extracted for the grain boundaries, twin boundaries, and phase interfaces from experiments and simulations, and comparison of simulated KAM distributions for the grain boundaries, twin boundaries, and phase interfaces with the experimental data at 5% and 15 % applied strains. Note that the scales are different in each of the plots.

The histograms from the simulated and experimental microstructures were plotted together in Figure 5.13. This figure also shows the comparison of the simulated KAM distributions at 5% and 15% applied strain with the corresponding experimental results for the grain boundaries, twin boundaries, and phase interfaces. While simulations predict a lower spread in the KAM histograms at 5% applied strain, simulation predictions are comparable with the experimental counterparts at higher applied strain (15 %). This implies that CPFE simulations are not able to capture *local* point-to-point misorientations accurately, but they can *statistically* predict misorientation evaluation at various microstructural features. As mentioned earlier, a strain gradient plasticity model is perhaps better suited for capturing the local KAM evolution. In the absence of strain gradient plasticity, the

grain interior may show higher relative deformation (as compared to the grain/phase/twin boundary) in order to accommodate the imposed deformation. Nonetheless, the model predicts qualitatively comparable trends of misorientation development at 15 % applied strain with respect to the experiments. These results highlight the capability of the CPFE framework for predicting heterogeneous deformation characteristics in these superalloy microstructures.

Finally, data has been collected from four different EBSD microstructures of area $100\mu m \times 100 \ \mu m$ to identify the competing role of these microstructural features on heterogeneous deformation. Deformation contours and KAM distributions from the three additional microstructures are given in Figures 5.14, 5.17, 5.20, 5.15, 5.18, and 5.21.

Using a similar exercise as earlier, combined data from all four microstructures are plotted in terms of the KAM distributions for these three microstructural features after 15% strain in Figure 5.23. Note that the number fraction is with respect to the number of pixels belonging to a particular microstructural feature/number of elements in the microstructure. It can clearly be seen that the spread of KAM distribution is higher at twin boundaries, as compared to the grain boundaries and phase interfaces, for both the experimental and simulated microstructures. Further, the KAM at phase interfaces and grain boundaries is observed to have a qualitatively similar distribution, with lower spread, from both experiments and simulations, for the combined data from four microstructures.

These results indicate that twin boundaries have a higher propensity for heterogeneous deformation and strain localization (and potentially failure initiation), as compared to the phase interfaces or grain boundaries. While short crack initiation has indeed been observed at the matrix/$\gamma_p^{'}$ interfaces by Flageolet et al. (2005), competitive deformation between phase interfaces and twin boundaries was not studied in detail. Our observations could be explained based on the fact that there is a higher fraction of points with high misorientation at the twin boundaries in the initial (undeformed) microstructures than at the phase interfaces or grain boundaries (cf. Figure 5.13).

5.5 Discussion

Development of a crystal plasticity constitutive modeling framework, which can predict the mechanical response across a range of deformation temperatures, as well as the microstructure evolution, is the novel contribution of this work. The model is "experimentally informed" in the sense that microstructural information (precipitate sizes and grain sizes,
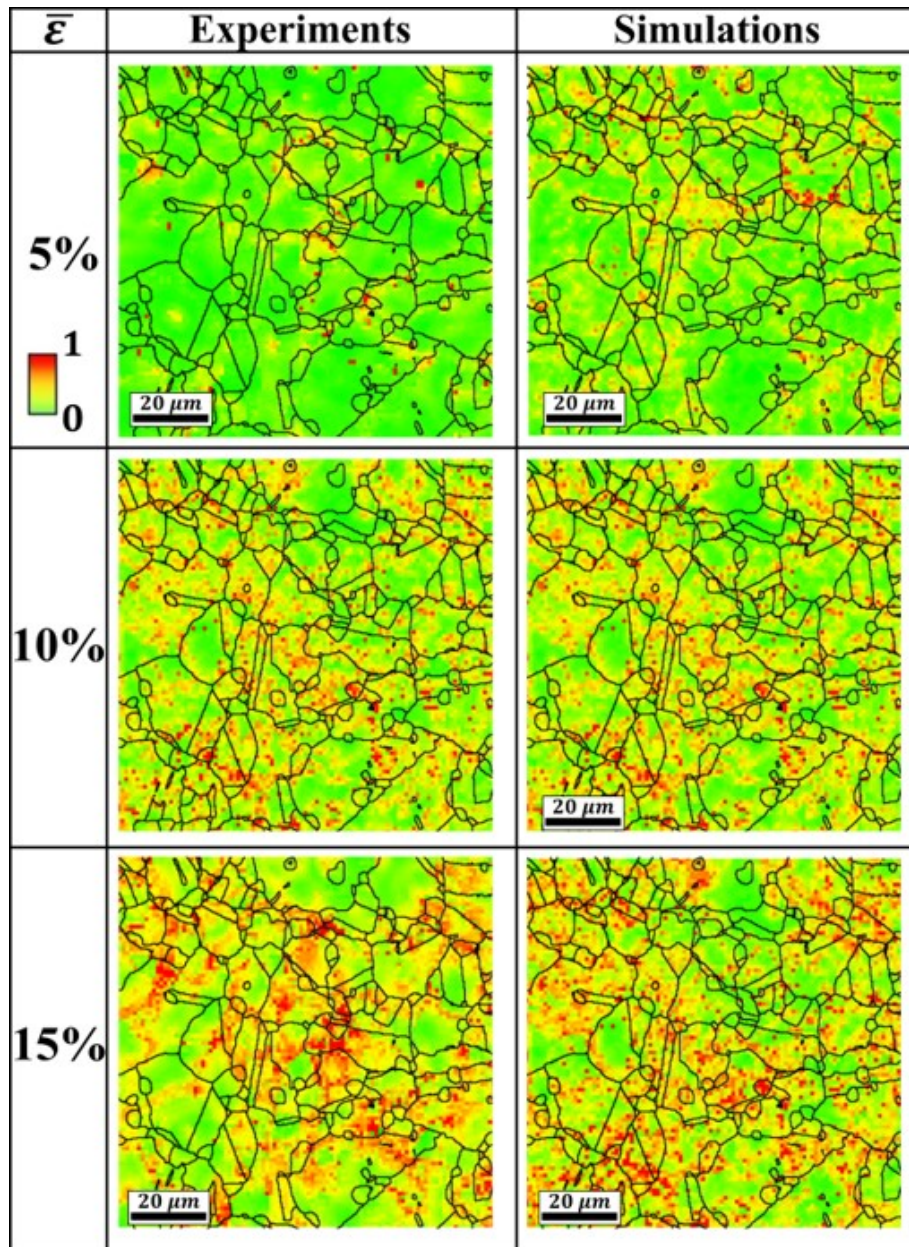
FIGURE 5.14: Normalized KAM contours at different stages of deformation as predicted using the crystal plasticity model and comparison with the experimental contours for Microstructure-2.
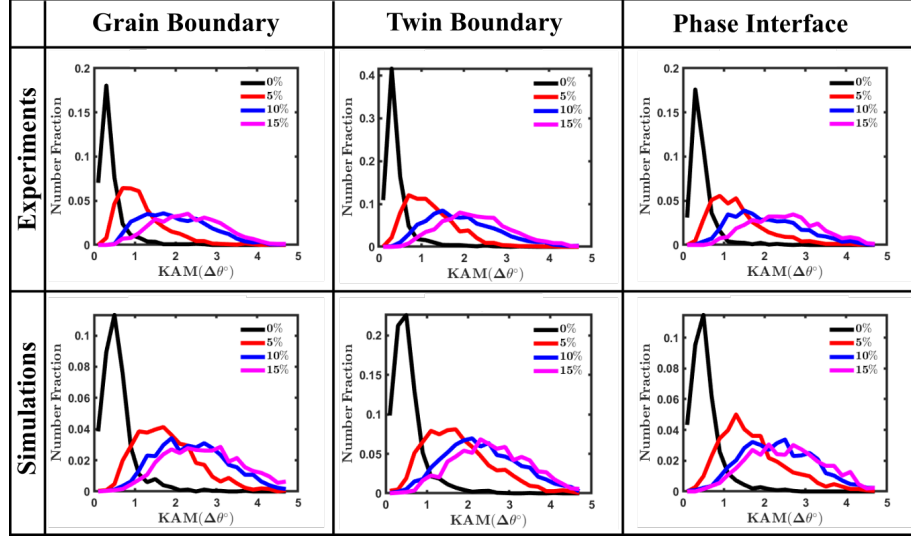
FIGURE 5.15: KAM distribution at different applied strains extracted for the grain boundaries, twin boundaries, and phase interfaces from experiments and simulations for Microstructure-2. Note that the scales are different in each of the plots.
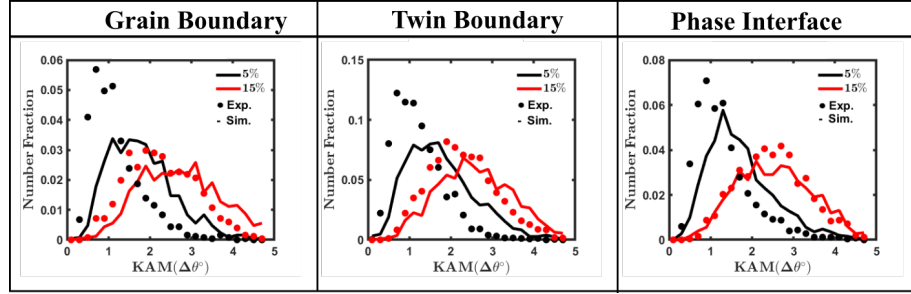
FIGURE 5.16: Comparison of simulated KAM distributions for the grain boundaries, twin boundaries, and phase interfaces with the experimental data at 5% and 15 % applied strains for Microstructure-2. Note that the scales are different in each of the plots.

texture, and most importantly, the solute concentrations) extracted from the experimental measurements across different length scales is directly used in the constitutive model for predicting the material's response. Further, based on the experimentally observed microstructure, we have explicitly considered $\gamma_p^{'}$ precipitates, along with appropriate constitutive models, in our simulations. To the best of our knowledge, prior studies in the literature have not considered this. The methodology adopted here highlights the potential for synergistic experiments and simulations to elucidate deformation mechanisms and pathways in Ni-based superalloys. There are several studies accounting for deformation mechanisms such as non-Schmid effects, temperature- and APB energy-dependent CRSS for single crystal superalloys (Tinga et al., 2009b; Keshavarz et al., 2016; Ranjan et al., 2021). However, there are only a few such studies (Shenoy et al., 2008; Weber and Ghosh, 2016; Ghorbanpour et al., 2017) for polycrystalline superalloys. We have advanced this line
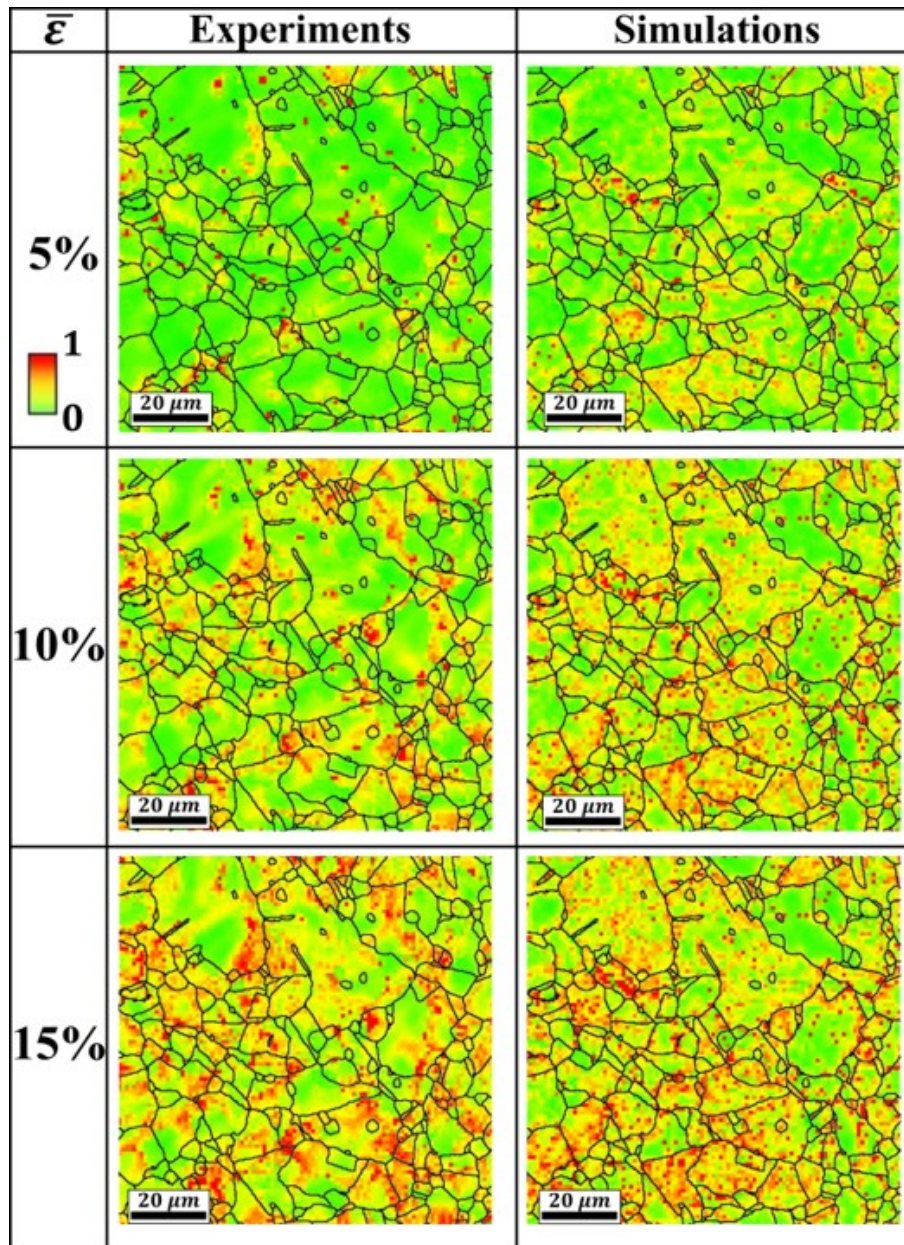
FIGURE 5.17: Normalized KAM contours at different stages of deformation as predicted using the crystal plasticity model and comparison with the experimental contours for Microstructure-3.
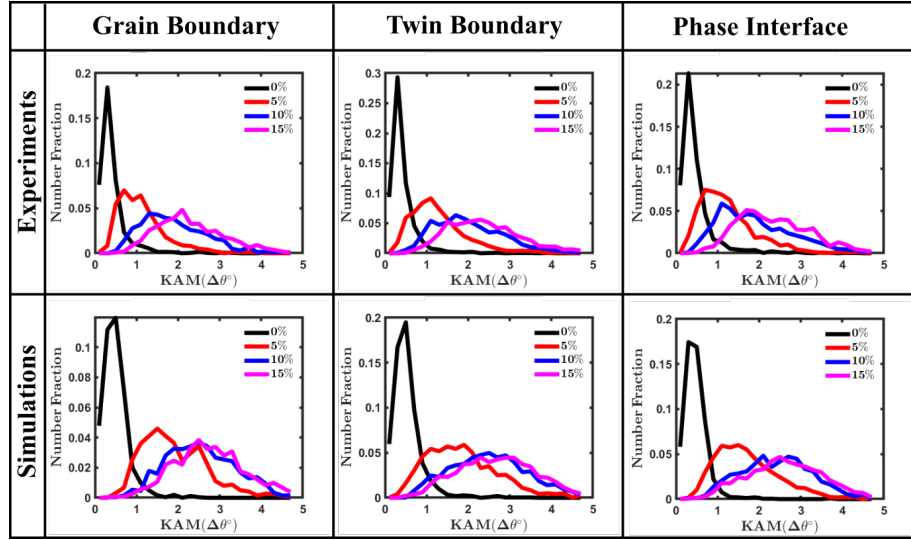
FIGURE 5.18: KAM distribution at different applied strains extracted for the grain boundaries, twin boundaries, and phase interfaces from experiments and simulations for Microstructure-3. Note that the scales are different in each of the plots.
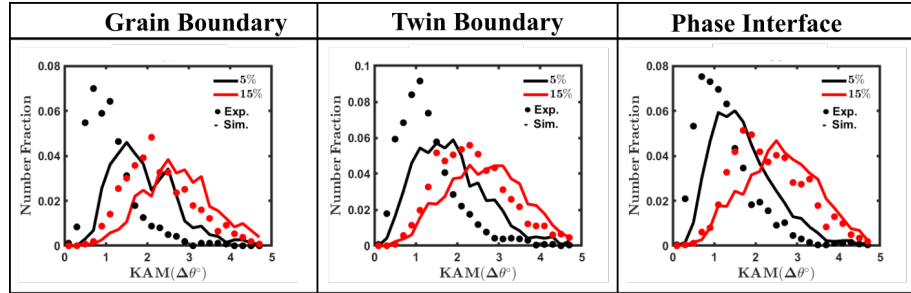
FIGURE 5.19: Comparison of simulated KAM distributions for the grain boundaries, twin boundaries, and phase interfaces with the experimental data at 5% and 15 % applied strains for Microstructure-3. Note that the scales are different in each of the plots.

of study by considering the above-mentioned deformation mechanisms in polycrystalline superalloys and predicting the deformation behavior and texture evolution across a range of temperatures. Further, while there are several crystal plasticity studies in the literature which have predicted and compared misorientations with experimental measurements for Ni-based superalloys (cf. Section 5.1), the competitive role of different microstructural features, especially primary $\gamma_p^{'}$ precipitates, has not been studied in great detail. A statistical study of the same across different microstructures is another novel contribution of our work.

The constitutive model has one shortcoming in that it is not able to accurately predict the stress-strain response at room temperature. Deviation from a non-monotonic hardening behavior in the room temperature experimental response could be due to the transition
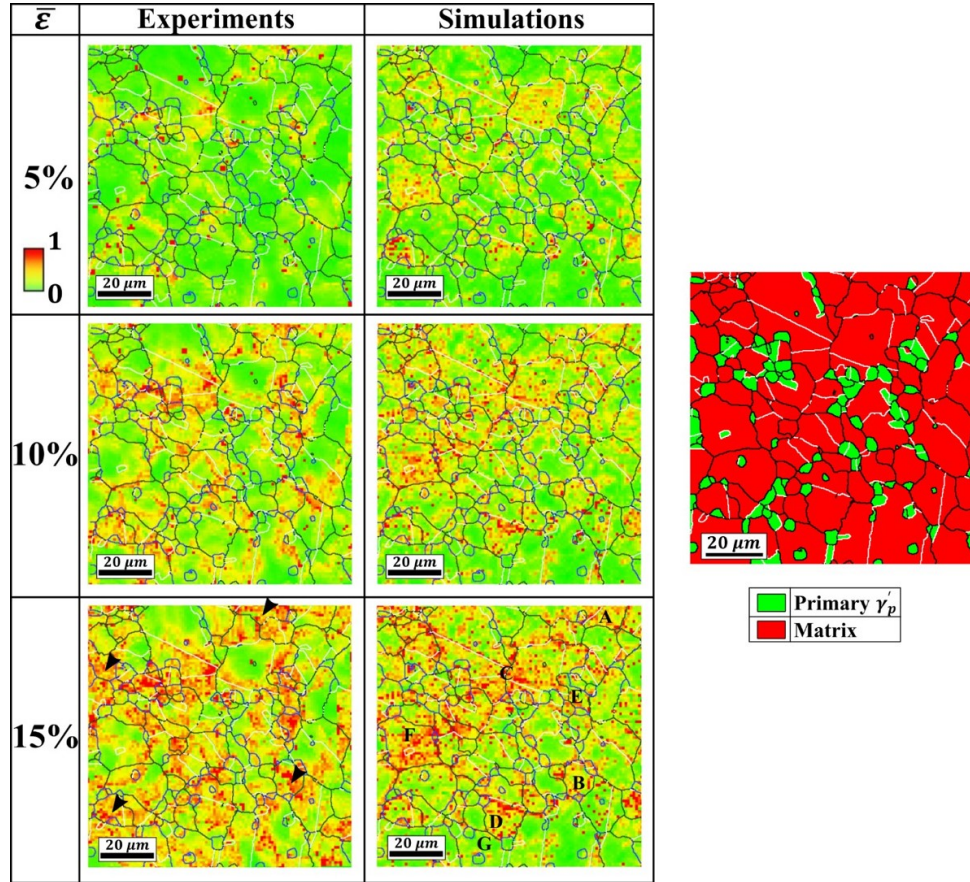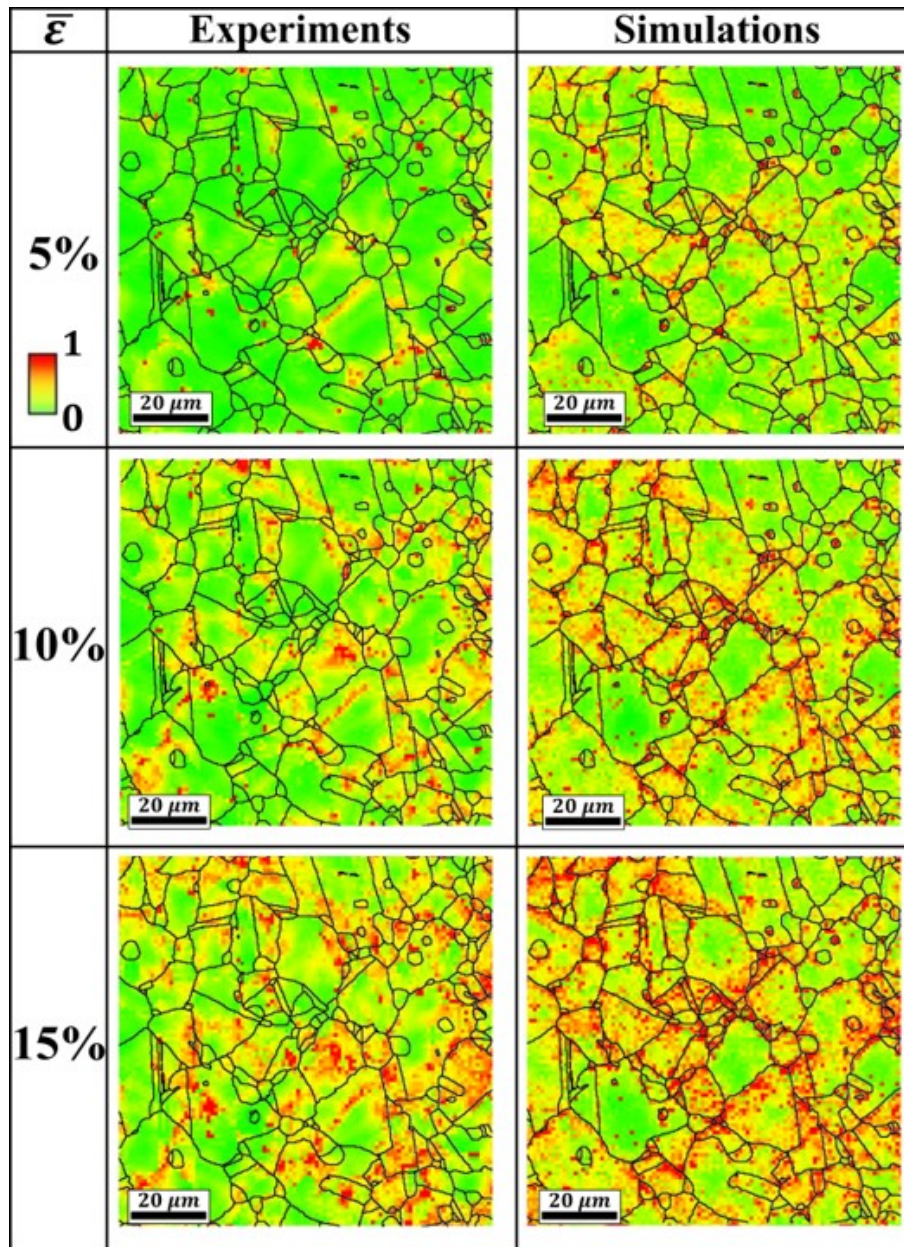
FIGURE 5.20: Normalized KAM contours at different stages of deformation as predicted using the crystal plasticity model and comparison with the experimental contours for Microstructure-4.
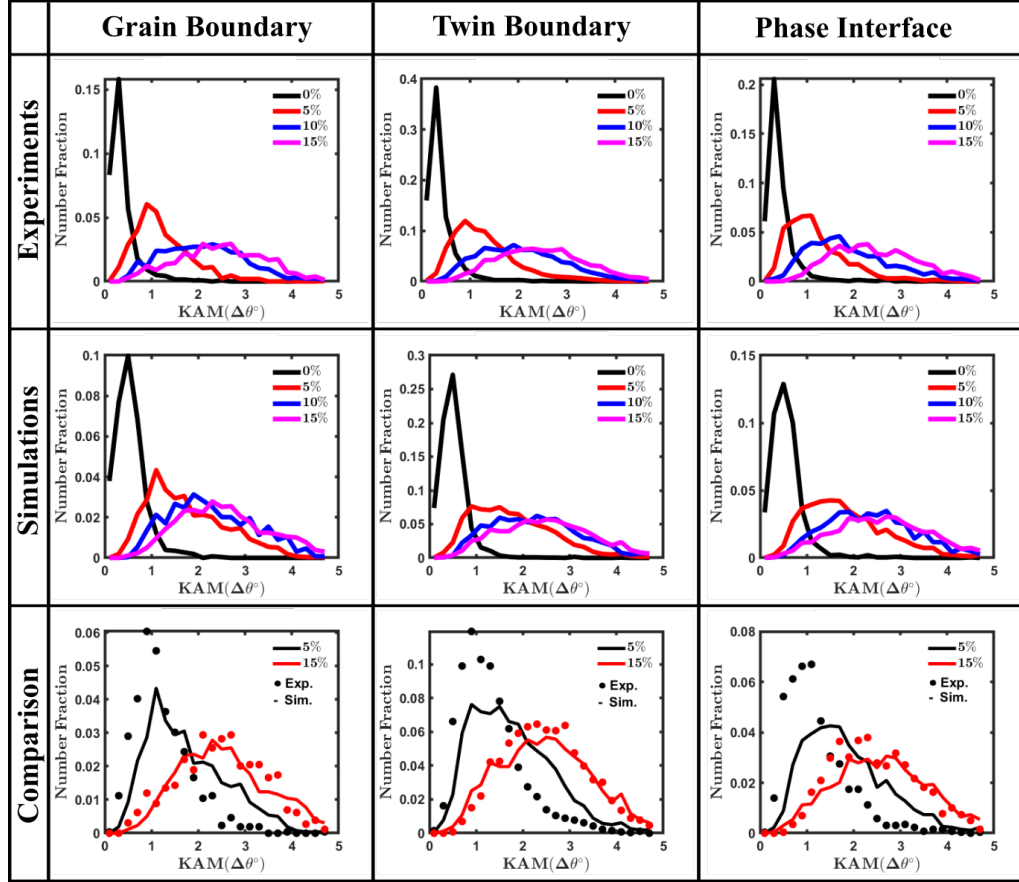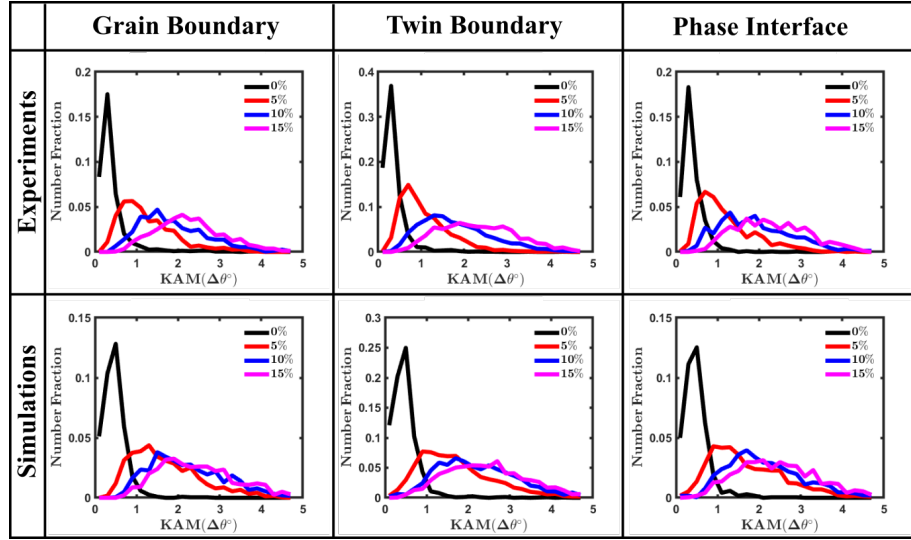
FIGURE 5.21: KAM distribution at different applied strains extracted for the grain boundaries, twin boundaries, and phase interfaces from experiments and simulations for Microstructure-4. Note that the scales are different in each of the plots.
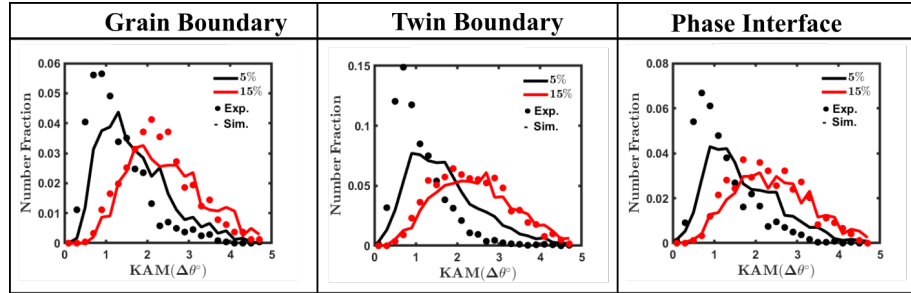
FIGURE 5.22: Comparison of simulated KAM distributions for the grain boundaries, twin boundaries, and phase interfaces with the experimental data at 5% and 15 % applied strains for Microstructure-4. Note that the scales are different in each of the plots.

from single slip to double slip following initial yield. Such a non-monotonic hardening behavior has been attributed to the 'recovery of strain hardening rate' phenomenon in Nickel-Silicon alloys (Yang et al., 2015) and could potentially be active here as well. Rapid activation of secondary slip systems results in a sharp decrease in the dislocation mean free path subsequent to the initial yield. This is also similar to the strain hardening phenomena commonly observed during single crystal deformation (Dieter, 1988). This phenomenon needs to be addressed in future work. Nonetheless, it should be noted that the model predicts the initial yield stress as well as the flow stress at 15% applied strain accurately at room temperature. Hence, the misorientation predictions at 15% applied strain, which are used for comparison with experiments, are not expected to be influenced significantly by this shortcoming. Further, the model predictions are in reasonable agreement with the experimental stress-strain response at other deformation temperatures (cf. Figure 5.7).
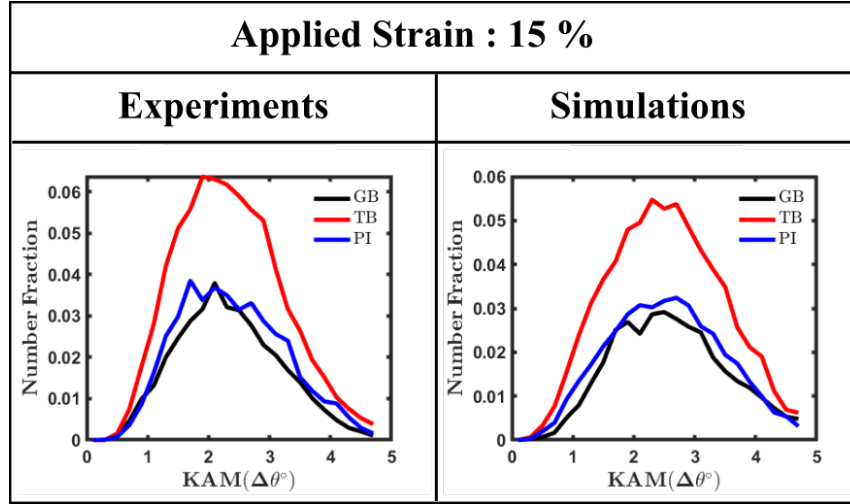
FIGURE 5.23: KAM distributions at grain boundaries (GB), twin boundaries (TB), and phase interfaces (PI) from experiments and simulations for data collected from four different microstructures after 15% applied strain. Individual data for the remaining three microstructures are given in the Supplementary Material.

On the same note, the model predicts the strengths of the individual phases at the different deformation temperatures in Figure 5.8. As mentioned earlier, this non-monotonic strengthening in the γ_p' phase is generally attributed to the anomalous hardening due to KW lock formation. A qualitatively similar behavior has also been recently reported using high-temperature nanoindentation experiments for single-phase Ni-based superalloys Ruzic et al. (2021) and also studied extensively using theoretical models Kozar et al. (2009); Wu et al. (2023). Phase-mapped high-throughput nanoindentation Basu et al. (2023) at elevated temperatures may be used to further validate these model predictions in future work.

5.6 Conclusions

A physically based crystal plasticity constitutive modeling framework was developed for simulating the temperature-dependent tensile deformation of polycrystalline Ni-based superalloys. The framework accounts for the individual deformation of the matrix (γ with embedded γ_s' and γ_t' precipitates) and primary γ_p' phases and their effect on the overall deformation. The concentration of solute atoms present in the matrix and primary γ_p' phases is obtained from the EDS characterization of the experimental microstructures. These concentration values and the EBSD microstructures served as input to the crystal plasticity model. Interrupted tensile testing was performed using the SEM and EBSD

to understand microstructure evolution during deformation. These deformed microstructures were correlated with the simulated EBSD microstructures to identify regions of local misorientation development.

The strength of the superalloy does not reduce noticeably even at elevated deformation temperatures, up to 923 K, as observed from both experiments and the model predictions. This can be attributed to the anomalous deformation behavior of the $\gamma^{'}$ precipitates, as considered appropriately in our constitutive model. Simulated KAM prediction at different microstructural features (grain boundaries, annealing twin boundaries, and phase interfaces) is qualitatively comparable with experiments at higher applied strain (15 %), which validates the model predictions. KAM localization is higher at the twin boundaries as compared to the phase interfaces and grain boundaries. These twin boundaries may be expected to have a higher propensity for heterogeneous deformation (and eventual failure) in the PM processed superalloys, as also found in the literature. Analysis of the competitive misorientation distribution at these microstructural features suggests that this could be due to the fact that the initial (undeformed) microstructures themselves have higher KAM at the twin boundaries as compared to the phase interfaces or grain boundaries.

The results presented in this work highlight the value of synergistic modeling and experiments for elucidating the competitive, microstructure-sensitive deformation mechanisms operative in polycrystalline Ni-based superalloys and their effect on the local and aggregate deformation behavior. This is the novelty of the present work.

Chapter 6

Modeling Cyclic Deformation of Polycrystalline Ni-based Superalloys

6.1 Introduction

Polycrystalline Ni-based superalloys are used in rotating aero-engine turbine disks. These superalloys are commonly manufactured by PM and exhibit superior mechanical properties at elevated temperatures, such as higher strength, creep, and fatigue resistance properties, as compared to their cast and wrought counterparts (Reed, 2008; Zhang et al., 2022b). Turbine disks undergo complex loading, such as thermal and mechanical cyclic loading, due to exposure to harsh environments during service conditions (Agaram et al., 2021; Zhang et al., 2022b). LCF failure is generally a critical issue that restricts the service life of the aero-engine components.

The LCF behavior of Ni-based superalloys has been explored in several studies (Stoltz and Pineau, 1978; Lerch and Gerold, 1987; Sundararaman et al., 1989; Mercer et al., 1999; Risbet et al., 2001; Dunne et al., 2007; Reed, 2009; Zhong et al., 2012; Phillips et al., 2013; Qin et al., 2015; Liu et al., 2018; Wang et al., 2019b; Cui et al., 2020; Barat et al., 2022; Zhang et al., 2022b). However, the majority of these studies focus on understanding the mechanisms of fatigue crack initiation and propagation, rather than the physics of microstructure evolution during cyclic deformation and macroscopic stress-strain response.

---

[1]Significant parts of this chapter have been published in Chaudhary et al. (2025).

140

The primary contributions to the strength of these alloys are due to the interactions of glide dislocations with $\gamma^{'}$ precipitates, which manifest in the form of strong-pair coupling, weak-pair coupling, and anomalous hardening due to cross slip from the {111} planes to {001} planes (Chan, 2021). Initial cyclic hardening in these alloys is generally the result of work hardening as the dislocation density increases with the number of cycles (Phillips et al., 2010). However, depending on the alloy, the initial cyclic hardening may or may not be present (Singh et al., 1991; Ye et al., 2004; Wei et al., 2013; Zhang et al., 2015b; Klotz et al., 2017; Jiang et al., 2021; Sun et al., 2021). More importantly, a commonly observed phenomenon in these precipitate-strengthened alloys is regarding cyclic softening, which refers to the reduction in stress amplitude with the number of cycles (Sundararaman et al., 1989; Singh et al., 1991; Xiao et al., 2008; Phillips et al., 2010; Prasad et al., 2013; León-Cázares et al., 2020b). The physical mechanism for cyclic softening is generally attributed to the shearing of the precipitates due to the interaction between dislocations and precipitates (Xiao et al., 2008; Agaram et al., 2021). The to-and-fro motion of dislocations in the matrix and dislocation pairs in the precipitates leads to the gradual shearing of the precipitates during fully reversed cyclic loading (Yashiro et al., 2006; Xiao et al., 2008; León-Cázares et al., 2020a; Agaram et al., 2021). The size of the precipitates reduces after each cycle, until they no longer offer resistance to dislocation glide (Agaram et al., 2021). Due to the reduction in size of the precipitates, their contribution to the strengthening decreases and manifests in the reduction in the peak stress. It should also be mentioned that generally, there are three types of precipitates in the PM processed superalloys. Primary $\gamma^{'}_{p}$ precipitates are micron-sized, while the cuboidal secondary $\gamma^{'}_{s}$ and tertiary $\gamma^{'}_{t}$ precipitates are distributed within the γ phase. The size of the secondary $\gamma^{'}_{s}$ and tertiary $\gamma^{'}_{t}$ precipitates lies in the range of 200-300 nm and 10-30 nm, respectively (Jiang et al., 2015a, 2021; Chaudhary et al., 2023). Depending on their size, the underlying strengthening mechanisms may vary.

Experimental studies have reported cyclic softening in superalloys for the past several decades. Merrick Merrick (1974) observed cyclic softening in three wrought nickel-based superalloys, Waspaloy, alloy 718, and alloy 901 at ambient and elevated temperatures, and attributed the observed fatigue softening to shearing and subsequent dissolution of the primary, $\gamma^{'}_{p}$, and secondary, $\gamma^{'}_{s}$, precipitates. Further, the effect of the size of the $\gamma^{'}_{s}$ precipitates on the cyclic response was measured by Stoltz and Pineau Stoltz and Pineau (1978). Cyclic hardening followed by saturation was observed due to dislocation looping for the precipitates with size greater than 25 nm, while cyclic softening due to shearing of smaller precipitates was observed for the samples with smaller precipitate sizes ($\approx$ 8 nm) Stoltz and Pineau (1978). Sundara Raman et al. Sundararaman et al. (1989)

observed $\gamma^{'}$ precipitate-free deformation band using TEM analysis and concluded that a localized and repeated shearing of precipitates on {111} planes results in the dissolution of $\gamma^{'}$ precipitates. Further, cyclic softening due to the shearing of fine $\gamma^{'}$ precipitates was also reported in subsequent studies on Waspaloy Lerch et al. (1984), Nimonic 90 Raman and Padmanabhan (1994), Nimonic PE16 Singh et al. (1991), Inconel 718 Kumar et al. (2024) and other polycrystalline nickel-based superalloys Zhang et al. (2015b).

Several crystal plasticity modeling frameworks have been developed for studying the cyclic deformation of Ni-based superalloys (Shenoy, 2006; Shenoy et al., 2008; Cruzado et al., 2017, 2018; Bandyopadhyay and Sangid, 2019; Sun and Yuan, 2019; León-Cázares et al., 2020a; Agaram et al., 2021; Eghtesad and Knezevic, 2021; Zhang and Yuan, 2022; le Graverend, 2023). A phenomenological Voce-type softening model, without explicit consideration for precipitate shearing, has been employed by Cruzado et al. (Cruzado et al., 2017, 2018). Sun and Yang (Sun and Yuan, 2019) have modified the constitutive equation within the Ohno-Wang cyclic plasticity framework to capture the cyclic hardening/softening behavior of Inconel 718. Zhang et al. (Zhang and Yuan, 2022) adopted the crystal plasticity model by Sun and Yang (Sun and Yuan, 2019) to predict the low-cycle fatigue behavior of the laser-melting processed Ni-based superalloy. A phenomenological model for cyclic softening has also been proposed for Inconel 718 by Le Graverend (le Graverend, 2023). Further, cyclic hardening and subsequent softening of Ni-based superalloys have been modeled using visco-plastic constitutive models in several studies (Cornet et al., 2011; Brommesson et al., 2016; Cao et al., 2021; Sun et al., 2022). The Prandtl operator approach has been used by Bartošák et al. (Bartošák et al., 2022) for strain range-dependent cyclic softening. In order to accurately predict cyclic softening with the number of cycles, a new numerical approach of the non-unified constitutive model has been implemented by Cheng et al. Cheng et al. (2021). Chan et al. (Chan, 2021) have developed a physics-based constitutive model for shearing of precipitates and bowing of dislocations to capture the cyclic softening of various wrought Ni-based superalloys at room temperature and further extended the model for high-temperature fatigue behavior (Chan, 2023). However, these approaches are generally phenomenological and do not account for the underlying physics of deformation. To the best of our knowledge, the micromechanics of precipitate shearing has only been considered in (León-Cázares et al., 2020a; Agaram et al., 2021; Kumar et al., 2024) by accounting for the evolution of precipitate size during cyclic deformation and their corresponding contribution to the strength. Agaram et al. (Agaram et al., 2021) have also implemented their proposed model in a crystal plasticity modeling framework. These models are able to predict the drop in peak stress during cyclic loading, following

the initial cyclic hardening. However, these models do not have consideration for different precipitate shapes. The γ' precipitates in Ni-based superalloys may be non-spherical, for example, cuboidal in shape (Chaudhary et al., 2023). Further, the interaction with glide dislocations has not been explicitly considered in these models. In the present work, we propose an alternative micromechanical model for precipitate shearing and precipitate size evolution during cyclic deformation, with appropriate geometrical and mechanistic considerations for different types of precipitate shapes and sizes.

The present work develops and implements constitutive models for microstructure evolution during cyclic deformation of Ni-based superalloys, specifically in terms of the back-stress evolution (contributing to cyclic hardening) and the γ' precipitate shearing due to its interaction with mobile dislocations (contributing to cyclic softening). These models have been implemented in a previously developed dislocation density-based crystal plasticity finite element framework (Chaudhary et al., 2023) that was earlier used for predicting the temperature-dependent tensile response of polycrystalline Ni-based superalloys. The crystal plasticity model considers the individual deformation of the matrix (cuboidal-shaped homogenized γ'_s and γ'_t precipitates in the γ phase) and primary γ'_p precipitates, solute solution strengthening, dislocation strengthening and grain size strengthening. The model has been used to predict the macroscopic stress-strain response during cyclic deformation, especially in terms of the peak stress evolution for two different superalloys, with different initial microstructures having different precipitate sizes, shapes, and volume fractions. This highlights the capability of the microstructure-sensitive model for predicting the cyclic deformation and softening behavior of polycrystalline Ni-based superalloys.

6.2 Crystal Plasticity Framework

The crystal plasticity modeling framework is based on our prior work (Chaudhary et al., 2023) and is summarized briefly in the following. This microstructure-sensitive model can account for the individual deformation of the matrix (homogenized γ'_s and γ'_t precipitates in the γ phase) and primary γ'_p phases to study the heterogeneous deformation behavior of polycrystalline Ni-based superalloys. The micron-sized primary γ'_p precipitates may be formed during the PM processing and have a non-negligible volume fraction (Chaudhary et al., 2023). The secondary, γ'_s, and tertiary, γ'_t, precipitates are generally nanometer-sized (Chaudhary et al., 2023) and contribute to the overall strengthening of the matrix. The dominant strengthening mechanisms considered in the framework are: (a) solute solution strengthening, (b) dislocation strengthening, (c) strengthening due to secondary γ'_s and

tertiary γ_t' precipitates present in the matrix (γ) phase, (d) grain size strengthening, and (e) dislocation strengthening. For substructure evolution, we consider the evolution of the mobile, ρ_m^α, and immobile, ρ_i^α, dislocation densities (α denotes the slip system). The model takes as input microstructural features such as solute concentrations, precipitate sizes, and volume fractions directly from experimental microstructure characterization to predict their effect on the mechanical properties. In the present work, we extend this framework by considering the slip system-level backstress evolution and microstructure evolution (precipitate shearing) during cyclic deformation to predict cyclic softening.

The crystal plasticity constitutive equations for the strengthening mechanisms mentioned above are given in Table 6.1. The crystal plasticity framework assumes the multiplicative dissociation of the finite deformation gradient, $\boldsymbol{F}$, into the elastic, $\boldsymbol{F^e}$ and inelastic, $\boldsymbol{F^i}$ parts, i.e., $\boldsymbol{F} = \boldsymbol{F^e} \cdot \boldsymbol{F^i}$ Asaro and Rice (1977). The elastic part of the deformation gradient is related to the elastic Green strain tensor as, $\boldsymbol{E^e}$ as, $\boldsymbol{E^e} = 1/2\left(\boldsymbol{F^{eT}} \cdot \boldsymbol{F^e} - \boldsymbol{I}\right)$. The second Piola-Kirchoff stress is given as, $\boldsymbol{S} = \boldsymbol{C_{eff}} : \boldsymbol{E^e}$, where $\boldsymbol{C_{eff}}$ denotes the effective elasticity tensor. Further, the Cauchy stress, $\boldsymbol{\sigma}$, is given as, $\boldsymbol{S} = det\left(\boldsymbol{F^e}\right)\boldsymbol{F^{e-1}} \cdot \boldsymbol{\sigma} \cdot \boldsymbol{F^{e-T}}$ in the current configuration. The elasticity tensor for the matrix (secondary γ_s' and tertiary $\gamma^{t'}$ precipitates in γ phase) and the primary γ_p' are given as (Ranjan et al., 2021):

$$C^{ijkl} = \begin{cases} \left(\left(1 - f_{\gamma_s'} - f_{\gamma_t'}\right)C_\gamma^{ijkl-1} + \left(f_{\gamma_s'} + f_{\gamma_t'}\right)C_\gamma^{ijkl-1}\right)^{-1}; matrix \\ C_{\gamma'}^{ijkl}; \gamma_p' \end{cases} \tag{6.1}$$

where, the anisotropic elasticity tensor in the γ and precipitate (γ_p') phase are represented by C_m^{ijkl} and C_p^{ijkl}, respectively. Further, $f_{\gamma_p'}$, $f_{\gamma_s'}$ and $f_{\gamma_t'}$ are the volume fractions of the primary, secondary and tertiary γ' precipitates, respectively. The inelastic velocity gradient, $\boldsymbol{L^i}$ is given as, $\dot{\boldsymbol{F^i}} = \boldsymbol{L^i} \cdot \boldsymbol{F^i}$ and $\boldsymbol{L^i}$ is modeled as the tensor sum of crystallographic shearing rate over all possible deformation systems, i.e.,

$$\boldsymbol{L^i} = \begin{cases} \sum_{\alpha=1}^{N_s} \dot{\gamma}^\alpha \boldsymbol{s}_0^\alpha \otimes \boldsymbol{m}_0^\alpha; matrix \\ \\ \sum_{\alpha=1}^{N_p} \dot{\gamma}^\alpha \boldsymbol{s}_0^\alpha \otimes \boldsymbol{m}_0^\alpha; \gamma_p' \end{cases} \tag{6.2}$$

Here, $\boldsymbol{m}_0^\alpha$ and $\boldsymbol{s}_0^\alpha$ represent unit vectors along the slip plane normal and the slip direction in the reference (and intermediate) configuration, respectively. The total number of slip systems in the matrix is N_s, considering 12 octahedral $\{111\} < 110 >$ slip systems, and the total number of slip systems in the γ' phase is N_p, considering 12 octahedral $\{111\} < 110 >$

slip systems and 6 cube $\{001\} < 110 >$ slip systems. The inelastic shearing rate, $\dot{\gamma}^{\alpha}$, is represented as a function of the driving stress for dislocation glide and internal state variables (ISVs) on slip system α. Given that primary γ'_p precipitates are not present in Alloy 2, the relevant terms are neglected in the above equations for the same.

Dislocation glide is modeled using a Kocks-type thermally activated model Kocks et al. (1975) as given in Equation 6.3. The driving stress for dislocation glide is a function of the Schmid stresses and is given by Equation 6.4. The resistance to dislocation glide due to the long-range stress fields is represented by the athermal slip resistance, s_a^{α} (Equation 6.5). It considers the contribution from different dominant mechanisms: the APB energy-dependent resistance, Hall-Petch effect, dislocation-based Taylor hardening, and precipitate strengthening due to γ' precipitates. The contribution of the deformation mechanism depends on the phase and type of slip system. Further, solute solution strengthening is a dominant mechanism contributing to thermal slip resistance, s_t^{α} (Equation 6.7). This takes the concentration of different elements for matrix and primary γ'_p precipitates. The strengthening coefficients for different alloying elements contributing to solid solution strengthening in nickel have been taken from the literature (Roth et al., 1997).

Constitutive equations for the evolution of mobile dislocation density, ρ^{α}_{Mj} (Equation 6.8) evolves by multiplication of dislocation at pre-existing segments, the annihilation of dislocation dipoles, and trapping of the dislocations at other dislocation segments while immobile dislocation density, ρ^{α}_{Ij} (Equation 6.9) evolves with trapped mobile dislocations and annihilation of dislocations by dynamic recovery.

These constitutive equations are summarized in Table 6.1.

TABLE 6.1: Crystal plasticity constitutive equations

Constitutive Equation		Description

Crystallographic shearing rate due to the glide of mobile dislocations

$$\dot{\gamma}_j^\alpha = \begin{cases} \dot{\gamma}_{0j}^\alpha\, exp\left[-\dfrac{\Delta F_j^\alpha}{kT}\left(1 - \left(\dfrac{\left|\tau_j^\alpha\right| - s_{aj}^\alpha}{s_{tj}^\alpha}\right)^{p_j^\alpha}\right)^{q_j^\alpha}\right] sgn\left(\tau_j^\alpha\right); \left|\tau_j^\alpha\right| > s_{aj}^\alpha,\ \alpha \in oct,cube,\ j \in matrix, \gamma_p' \\[6pt] 0;\ otherwise \end{cases}$$

(6.3)

$\dot{\gamma}_{0j}^\alpha$: Reference strain rate, ΔF_j^α: dislocation glide activation energy, k: Boltzmann constant, T: absolute temperature, τ_j^α: driving stress, s_{aj}^α: athermal slip resistance, s_{tj}^α: thermal resistance, p_j^α and q_j^α: shape parameters the activation energy curve. Here, octahedral slip in the matrix and the primary γ_p' phases are represented by $\alpha \in oct, j \in matrix$ and $\alpha \in oct, j \in \gamma_p'$, respectively, while cube slip in the primary γ_p' phase is represented as $\alpha \in cube, j \in \gamma_p'$

Driving stress for dislocation glide:

$$\tau_j^\alpha = \mathbf{s}^\alpha \cdot \boldsymbol{\sigma} \cdot \mathbf{m}^\alpha;\ \alpha \in oct,cube,\ j \in matrix, \gamma_p'$$

(6.4)

$\mathbf{s}^\alpha$: Slip direction, and $\mathbf{m}^\alpha$: slip plane normal

The athermal slip resistance

$$s_{aj}^\alpha = \begin{cases} \tau_{ps}^\alpha + \dfrac{kH_j}{\sqrt{d_\gamma}} + k_{pj}G_j b_j \sqrt{\left(\sum_{\xi=1}^{N_m} A^{\alpha\xi}\rho_j^\xi\right)};\ \alpha \in oct,\ j \in matrix \\[8pt] \tau_{APB}^\alpha + \dfrac{kH_j}{\sqrt{d'}_{\gamma_p'}} + k_{pj}G_j b_j \sqrt{\left(\sum_{\xi=1}^{N_p} A^{\alpha\xi}\rho_j^\xi\right)};\ \alpha \in oct,\ j \in \gamma_p' \\[8pt] \tau_{0j}^\alpha + \dfrac{kH_j}{\sqrt{d'}_{\gamma_p'}} + k_{pj}G_j b_j \sqrt{\left(\sum_{\xi=1}^{N_p} A^{\alpha\xi}\rho_j^\xi\right)};\ \alpha \in cube,\ j \in \gamma_p' \end{cases}$$

(6.5)

τ_{ps}^α: Precipitate strengthening, τ_{APB}^α: APB dependent strength contribution, τ_{0j}^α: intrinsic strength of the cube slip system, G_j: shear modulus, b_j: Burgers vector magnitude, k_{pj}: dislocation barrier strength, $A^{\alpha\xi}$: matrix of slip system dislocation interaction coefficients, ρ_j^ξ: dislocation density in the slip system ξ

Strengthening of the matrix due to secondary γ_s' and tertiary γ_t' precipitates:

$$\tau_{ps}^\alpha = \tau_{wp}^\alpha + \tau_{sp}^\alpha$$

(6.6)

τ_{wp}^α: Strength due to weak-pair coupling, τ_{sp}^α: Strength due to strong-pair coupling

Thermal slip resistance:

$$s_{tj}^\alpha = \frac{1}{M_j}\Sigma\left(\frac{d\sigma}{\sqrt{dC_i}}\sqrt{C_i}\right);\ \alpha \in oct,cube,\ j \in matrix, \gamma_p'$$

(6.7)

M_j: Taylor factor, C_i: atomic fraction, and $\dfrac{d\sigma}{\sqrt{dC_i}}$: strengthening coefficient for a given element

Mobile dislocation density:

$$\dot{\rho}_{Mj}^\alpha = \frac{k_{Mj}^\alpha}{b_j}\left(\sqrt{\sum_\xi \rho_j^\xi}\right)\left|\dot{\gamma}_j^\alpha\right| - \frac{2R_C}{b_j}\rho_{Mj}^\alpha\left|\dot{\gamma}_j^\alpha\right| - \frac{k_{tj}^\alpha}{b_j\lambda_j^\alpha}\left|\dot{\gamma}_j^\alpha\right|;\ \alpha \in oct,cube,\ j \in matrix, \gamma_p'$$

(6.8)

k_{Mj}^α: associated material parameter associated with dislocation multiplication at pre-existing segments, R_C: critical capture radius for annihilation of dislocation dipoles, k_t^α: material parameter associated with trapping of mobile dislocations at barriers, $\lambda_j^\alpha = \dfrac{1}{\sqrt{\sum_\xi \rho_j^\xi}};\ \alpha \in oct,cube,\ j \in matrix, \gamma_p'$: effective mean free path

Immobile dislocation density:

$$\dot{\rho}_{Ij}^\alpha = \frac{k_{tj}^\alpha}{b_j\lambda_j^\alpha}\left|\dot{\gamma}_j^\alpha\right| - k_{dj}^\alpha\rho_{Ij}^\alpha\left|\dot{\gamma}_j^\alpha\right|;\ \alpha \in oct,cube,\ j \in matrix, \gamma_p'$$

(6.9)

k_{dj}^α: material parameter associated dynamic recovery

As will be shown later, the evolution of precipitate strengthening is one of the main mechanisms contributing to the strengthening and eventual cyclic softening predicted by our model. Here we provide a brief description of the same, while referring the reader to Ref. (Chaudhary et al., 2023) for a more detailed description of the crystal plasticity constitutive equations.

6.2.1 Precipitate Strengthening

The crystal plasticity model considers slip system-level strengthening due to precipitates on slip system α, which is of the form:

$$\tau_{ps}^{\alpha} = \sum_i min(\tau_{sp,i}^{\alpha}, \tau_{wp,i}^{\alpha}), i \in \gamma_s^{'}, \gamma_t^{'} \tag{6.10}$$

where $\tau_{sp,i}^{\alpha}$ represents the strengthening due to strong pair coupling and $\tau_{wp,i}^{\alpha}$ represents the strengthening due to weak pair coupling, and i represents the type of precipitate (secondary or tertiary). Depending on their size, d_i, the strengthening due to precipitates may be either due to the strongly or the weakly coupled dislocation pair contribution, whichever offers lower resistance (Kozar et al., 2009; Collins and Stone, 2014). When the size of the precipitate is larger than a threshold size, d_i^0, strengthening due to strong-pair coupling, $\tau_{sp,i}^{\alpha}$, is expected and this contribution decreases with increase in the precipitate size according to (Collins and Stone, 2014):

$$\tau_{sp,i}^{\alpha} = \frac{1}{2} \left(\frac{G_j b_j}{d_i} \right) f_i^{\frac{1}{2}} 0.72w \left(\frac{\pi d_i \gamma_{APB}}{w G_j b_j^2} - 1 \right)^{\frac{1}{2}}; d_i > d_i^0, i \in \gamma_s^{'}, \gamma_t^{'} \tag{6.11}$$

where, G_j is the shear modulus, b_j is the Burgers vector magnitude, f_i is the volume fraction of the precipitate, γ_{APB} is the APB energy per unit area, and w is the elastic repulsion between the paired dislocations. For smaller-sized precipitates, strengthening due to weak-pair coupling, $\tau_{wp,i}^{\alpha}$, occurs and decreases with a decrease in precipitate size according to (Collins and Stone, 2014):

$$\tau_{wp,i}^{\alpha} = \frac{A}{2} \left(\frac{\gamma_{APB}}{b_j} \right)^{\frac{3}{2}} \left(\frac{2 d_i f_i}{G_j b_j} \right)^{\frac{1}{2}} - \frac{1}{2} \left(\frac{\gamma_{APB}}{b_j} \right) f_i; d_i < d_i^0, i \in \gamma_s^{'}, \gamma_t^{'} \tag{6.12}$$

where, A is a geometric factor. Here, d_i^0 is the threshold precipitate size and can be interpreted as the precipitate size at which the strengthening due to strong-pair coupling

and weak-pair coupling becomes equal, i.e.,

$$d_i^0 = d_i \text{ for } \tau_{sp,i}^\alpha = \tau_{wp,i}^\alpha \tag{6.13}$$

The same strengthening models may be applied to both secondary, $\gamma_s^{'}$, and tertiary, $\gamma_t^{'}$, precipitates, and the subscript i is used to denote the same, i.e., $i \in \gamma_s^{'}, \gamma_t^{'}$. The strength contributions due to these individual mechanisms are shown schematically in Figure 6.1, along with the threshold precipitate size, d_i^0, at which the transition occurs from strong pair coupling to weak pair coupling. Note that we have assumed model parameters based on the values presented later in Table 6.5 for the plots in Figure 6.1.

Note that in this mean field strengthening model, the contribution of precipitates to the strengthening of the matrix is considered in a homogenized sense, and individual interactions between dislocations and precipitates are not considered in this continuum model. Such individual interactions could perhaps be considered in lower-scale models, such as discrete dislocation dynamics models. Further, this is a local crystal plasticity model that does not consider size effects due to strain gradient effects (such effects could arise in the immediate vicinity of matrix-precipitate interfaces).
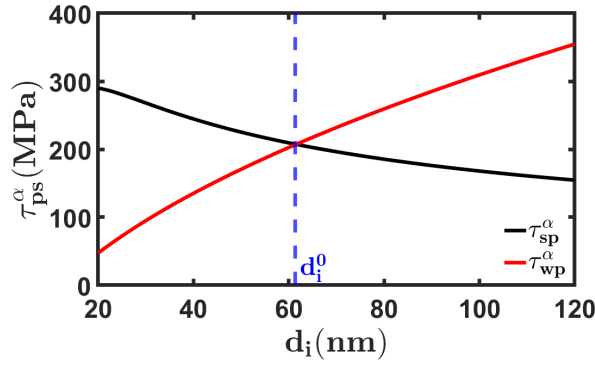
FIGURE 6.1: Contribution of precipitate strengthening, τ_{ps}^α, due to strong pair, τ_{sp}^α, and weak pair, τ_{wp}^α, coupling as a function of the precipitate size, using $f_i = 0.41$ and the material parameters provided in Table 6.5.

6.2.2 Backstress Evolution

Backstresses are expected to develop during cyclic deformation and contribute to directional hardening. In the present work, we have used the slip system-level backstress evolution model given in (Shenoy, 2006; Chaudhary et al., 2022), which is based on an Armstrong-Frederick type kinematic hardening model, and is a function of the total slip

system level dislocation density, $\rho^\alpha = \rho_m^\alpha + \rho_i^\alpha$, i.e.,

$$\chi_j^\alpha = \left(k_{\chi 1}^\alpha G_j b_j \sqrt{\rho_j^\alpha} sgn\left(\tau_j^\alpha - \chi_j^\alpha\right) + k_{\chi 2}^\alpha \chi_j^\alpha \right) \left|\dot{\gamma}_j^\alpha\right|; \alpha \in \text{oct,cube}, j \in matrix, \gamma_p^{'} \quad (6.14)$$

Here, G_j represents the shear modulus, b_j represents the Burgers vector magnitude for deformation mode j, and $k_{\chi 1}^\alpha$, $k_{\chi 2}^\alpha$ are material constants. The first term in this model represents the directional hardening due to the accumulation/pile up of dislocations, while the second term represents a recovery term similar to an Armstrong-Frederick model.

6.2.3 Precipitate Shearing

Precipitate shearing due to dislocation-precipitate interactions is assumed to be the primary contributor to the experimentally observed cyclic softening. As will be discussed later, our experimental microstructure investigation reveals that the $\gamma_s^{'}$ precipitates are sheared during cyclic deformation in a representative superalloy. As discussed earlier (cf. Section 6.1), there have been several experimental studies also reporting the same.

Prior studies (Differt et al., 1987; Agaram et al., 2021) have proposed that glide dislocations shear the precipitates during either phase (tension or compression) of the cyclic loading, leaving an irreversible shift between the upper and lower halves of the precipitates. This could be caused due to the annihilation, trapping, or cross-slip of dislocations onto other planes during reverse loading, thus leaving a permanent shift between the upper and lower halves of the precipitates. Repeated shearing may cause the precipitates to be cut into several smaller volumes.

In the present work, we propose a constitutive model as a mean field approximation of this physical mechanism, which tracks the volume number density, $N_{\gamma'}$, and size, $d_{\gamma'}$, of the precipitates based on their interaction with mobile dislocations and enforces conservation of the volume fraction of the precipitates. This constitutive model for precipitate shearing is adapted from the defect annihilation model proposed earlier Patra and McDowell (2013, 2016) for the annihilation of irradiation-induced defects by mobile dislocations. Recently, Kumar et al. (Kumar et al., 2024) have also developed similar models in a macroplasticity framework for precipitate shearing in Ni-based superalloys.

The schematic of the dislocation shearing the precipitates of different shapes is shown in Figure 6.2. The initial configuration in Figure 6.2(a) shows the unsheared precipitates. In Figure 6.2(b), glide dislocations interact with the precipitates and shear them, eventually leading to the formation of distinct "smaller" precipitates in Figure 6.2(c).
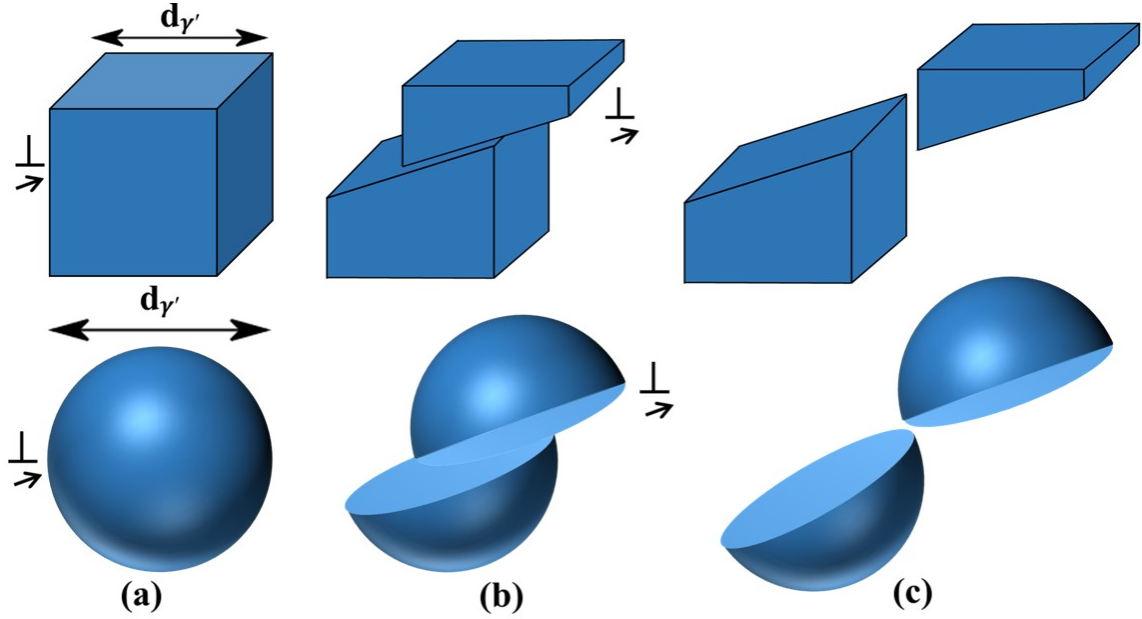
FIGURE 6.2: Schematic of precipitate shearing showing (a) initial configuration, (b) dislocation shearing the precipitate, and (c) sheared precipitates for precipitates with different shapes.

We define $\rho_{\gamma'}$ as the areal density of the precipitates, such that

$$\rho_{\gamma'} = G_a N_{\gamma'} d_{\gamma'} \tag{6.15}$$

where, $N_{\gamma'}$ denotes the volume number density and $d_{\gamma'}$ denotes the precipitate size. G_a is the areal geometric factor and $G_a = 4$ for cuboidal precipitates and $G_a = \pi$ for spherical precipitates. The rate of evolution of the areal density of the precipitates is modeled as a function of $\rho_{\gamma'}$ and the interacting mobile dislocation density, ρ_m^α, summed over all slip systems (Patra and McDowell, 2013), i.e.,

$$\dot{\rho}_{\gamma'} = \sum_{\xi=1}^{N_s} \frac{R_{ann}}{b_j} \left(\rho_{\gamma'}\right)^c (\rho_m^\alpha)^{1-c} \left|\dot{\gamma}_{j,cyclic}^\alpha\right| \tag{6.16}$$

where, R_{ann} is the capture radius for precipitate annihilation and is representative of the distance from the dislocation core within which precipitates may be annihilated, c is the exponent of areal density of the precipitates such that the product of the areal density term and mobile dislocation density term on the right hand side of Equation 6.16 has the units of areal density of the precipitates. Both R_{ann} and c are model parameters estimated by calibrating the model predictions with the experimental counterparts. Further, $\dot{\gamma}_{j,cyclic}^\alpha$ is the cyclic crystallographic shearing rate and is modulated using an input parameter

in our model, such that, $\dot{\gamma}^{\alpha}_{j,cyclic} = \dot{\gamma}^{\alpha}_{j}\Delta(cyclic)$ (Kumar et al., 2024). Here, $\dot{\gamma}^{\alpha}_{j}$ is the crystallographic shearing rate on slip system α and $\Delta(cyclic) = 1$ only for cyclic loading and $\Delta(cyclic) = 0$ elsewise (e.g. uniaxial tension and uniaxial compression) (Kumar et al., 2024). Note that while we have only performed cyclic deformation simulations in the present work and $\Delta(cyclic) = 1$ is used, this parameter can be modulated in case the same constitutive model is used to perform non-cyclic loading simulations.

The volume fraction of the precipitates is given as:

$$f_{\gamma'} = G_v N_{\gamma'} d^3_{\gamma'} \tag{6.17}$$

Here, G_v is a volumetric geometric factor, such that $G_v = 1$ for cuboidal precipitates and $G_v = \pi/6$ for spherical precipitates. Given that the volume fraction of the precipitates does not change with shearing, the time derivative of $f_{\gamma'}$ can be derived as the differential form of Equation 6.17 as:

$$\dot{f}_{\gamma'} = G_v \left(\dot{N}_{\gamma'} d^3_{\gamma'} + 3N_{\gamma'} d^2_{\gamma'} \dot{d}_{\gamma'} \right) = 0 \tag{6.18}$$

As precipitates are sheared, the size of the precipitates decreases and the volume number density of precipitates increases (cf. Figure 6.2(c)). This also follows from Equation 6.18 and the rate of increase in the volume number density of the precipitates is given as:

$$\dot{N}_{\gamma'} = -\frac{3N_{\gamma'} \dot{d}_{\gamma'}}{d_{\gamma'}} \tag{6.19}$$

By taking the time derivative of Equation 6.15, and using appropriate terms from Equations 6.17 and 6.19, we have:

$$\dot{\rho}_{\gamma'} = G_a \left(\dot{N}_{\gamma'} d_{\gamma'} + N_{\gamma'} \dot{d}_{\gamma'} \right) = G_a \left(-\frac{3N_{\gamma'} \dot{d}_{\gamma'}}{d_{\gamma'}} d_{\gamma'} + N_{\gamma'} \dot{d}_{\gamma'} \right) = -2G_a N_{\gamma'} \dot{d}_{\gamma'} = -\frac{2G_a f_{\gamma'}}{d^3_{\gamma'}} \dot{d}_{\gamma'} \tag{6.20}$$

Thus, the rate of precipitate size evolution can be given as:

$$\dot{d}_{\gamma'} = -\frac{\dot{\rho}_{\gamma'} d^3_{\gamma'}}{2G_a f_{\gamma'}} \tag{6.21}$$

Finally, the volume number density and size of precipitates at a given instant of time can be written as:

$$
\begin{aligned}
N_{\gamma'}|_{t+\Delta t} &= N_{\gamma'}|_t + \dot{N}_{\gamma'}\Delta t \\
d_{\gamma'}|_{t+\Delta t} &= d_{\gamma'}|_t + \dot{d}_{\gamma'}\Delta t
\end{aligned}
\tag{6.22}
$$

Further, the updated precipitate size is used to calculate the precipitate strengthening as per Equation 6.10. As the precipitate size decreases, the change in precipitate strength contributes to initial hardening or subsequent softening, depending on whether it is sheared by strongly or weakly coupled dislocation pairs.

Note that our proposed model is different from previous micromechanical models (Differt et al., 1987; León-Cázares et al., 2020a; Agaram et al., 2021) in that these prior works have proposed that the shearing of the precipitates is a function of the number of cumulative irreversible slip steps or the cumulative irreversible slip distance, while our proposed model simply considers the rate of evolution of the areal density of precipitates as a function of the cyclic crystallographic shearing rate, $\dot{\gamma}^{\alpha}_{j,cyclic}$. As will be shown later, despite this simplified first-order approximation, the proposed model for precipitate size evolution, coupled with the precipitate strengthening model (cf. Equation 6.10), can successfully predict the observed cyclic softening behavior for a range of loading conditions in two different polycrystalline Ni-based superalloys. Further, the proposed model is an improvement from the recent work of Kumar et al. (Kumar et al., 2024) in that the conservation equations (cf. Equations 6.18 - 6.22) were not considered previously. Further, our model has explicit consideration for the precipitate shape, via the geometric factors, G_a and G_v, which allows us to simulate different types of precipitates observed in Ni-based superalloys. In the example applications of the model shown later, we have considered cuboidal and spherical precipitates as experimentally observed in two different superalloys. Coupling of this shearing model with the precipitate size-dependent strengthening models described in Section 6.2.1 allows natural consideration for the effect of precipitate size on strength contribution.

Since this precipitate shearing model is implemented in a continuum crystal plasticity model, consideration for discrete/individual interactions between dislocations and precipitates is not possible. Rather, dislocation-precipitate interactions are considered phenomenologically via Equation 6.16 in this mean field model, where the capture radius, R_{ann}, is a parameter that is physically representative of the capture/interaction radius around a dislocation core at which a precipitate may get sheared. Moreover, the geometric factors, G_a and G_v, are based on an implicit assumption of the precipitate shape. This

mean field model is meant to provide a statistical representation of dislocation-precipitate interactions, ultimately leading to precipitate shearing. Having said that, our model is rather simplified and does not account for the dynamics of precipitate shearing, which are still a matter of ongoing research. As discussed in Eggeler et al. (Eggeler et al., 2021), different nanoscale mechanisms may be active depending on the stacking fault energy of the anti-phase boundaries. Accounting for such individual nanoscale mechanisms is perhaps beyond the scope of a continuum constitutive model. Further, given that the stacking fault energy itself is temperature-dependent, precipitate shearing may be expected to be a temperature-dependent phenomenon (Tian et al., 2016; Li et al., 2019b; Wang et al., 2023).

These constitutive equations, along with those listed in the Appendix, have been numerically implemented in the form of a material model that interfaces with the open-source finite element solver, MOOSE (Permann et al., 2020). The time step integration has been performed using a modified version of the fully implicit Newton-Raphson scheme as discussed in (Patra et al., 2023).

6.3 Application of the Model

We have used the constitutive model to predict the low-cycle fatigue behavior of two different polycrystalline Ni-based superalloys. The first one is a PM-processed polycrystalline superalloy, for which detailed mechanical and microstructural characterization has also been performed in the present study. This is referred as Alloy 1 here on. The second one is the superalloy Nimonic-90, for which experimental data have been taken directly from the literature (Raman and Padmanabhan, 1995). This is referred as Alloy 2. As will be discussed in the following, these two superalloys have distinct initial microstructures, with different volume fractions and sizes of precipitates, and the microstructure-sensitive model is used to predict their resulting cyclic deformation behavior.

6.3.1 Model Predictions for Alloy 1

6.3.1.1 Material and Experimental Characterization

Alloy 1 is a PM-processed polycrystalline Ni-based superalloy manufactured by the Defence Metallurgical Research Laboratory (India). The microstructure of this alloy consists

of primary γ_p' precipitates, cuboidal-shaped secondary γ_s' and tertiary γ_t' precipitates homogenized in the γ phase. The mean grain sizes of the γ phase and the primary γ_p' phase are 27.42 μm and 3.8 μm, respectively. The size of secondary γ_s' and tertiary γ_t' precipitates lies in the range of 200-300 nm and 10-30 nm, respectively (Chaudhary et al., 2023). The composition of the matrix and precipitate phases is given in Table 6.2.

TABLE 6.2: Elemental composition (in atomic fraction) of the matrix and primary γ_p' phase of the as-received Alloy 1 (Chaudhary et al., 2023).

	Al	Mo	Ti	Cr	Co	Ni
Matrix	8.75	2.80	5.70	14.68	15.30	52.80
Primary γ_p'	12.78	0.72	9.71	4.68	10.30	61.90

Fatigue specimens extracted from the as-received circular rod were used to study the microstructure evolution after cyclic deformation and had the following initial dimensions: 25 mm gauge length, 6.35 mm diameter, and 100 mm total length. The LCF tests were performed on a closed-loop servo-hydraulic axial fatigue test system, MTS-Landmark, with a 100 kN load cell capacity. Two tests were conducted at 0.9% and 1.8% strain amplitudes in a strain-controlled mode under fully reversed loading (with R = -1) at a nominal strain rate of 2×10^{-3} s^{-1}. The LCF tests were carried out at room temperature, with the sample initially loaded in tension during the 1st cycle. The strain values were measured by a 10 mm extensometer positioned at the gauge section. In this study, we are not interested in simulating failure during LCF, and hence, the cyclic deformation experiments have also not been performed till failure.

The LCF test samples after deformation to 500 cycles at 0.9% strain amplitude were sectioned longitudinally to study the deformed microstructure using electron microscopy. The samples were polished using sub-micron colloidal silica and etched using Collins reagent (composition of 100 ml (38%) Hydrochloric Acid, 100 ml Ethyl Alcohol, and 5 grams Copper (II) Chloride) for SEM. The SEM micrographs were obtained using an FEI Nova-Nano scanning electron microscope. A Struers Tenupol-5 twin-jet electropolishing using a 90:10 ratio of methanol to perchloric acid was used to prepare TEM specimens at 15 V DC, and at a stable temperature below 250 K. A Thermofisher Themis-300 microscope (300 keV operating voltage) with a four-detector ChemiSTEM$^{\text{TM}}$ EDS arrangement was used for TEM analysis. Further, the γ_s' precipitates were also studied using HAADF-STEM.

Figure 6.3 shows the SEM images of the deformed microstructure for Alloy 1. The SEM images in Figure 6.3(a,b) reveal the sheared precipitates, which are relatively smaller in size as compared to their unsheared counterparts (see regions marked by red circles

and arrows). Figure 6.4 shows TEM images of the γ' precipitates in the as-received and deformed specimens. TEM micrographs in Figure 6.4(b,c) reveal that the unsheared secondary γ'_s precipitates exhibit a cuboidal shape. However, as shown in Figure 6.4(b) and (c), the size of the precipitates changes due to shearing during deformation. After shearing, the size of the secondary γ'_s precipitates reduces from $\approx$ 200-300 nm to $\approx$ 91 nm. Presumably, the phenomenon of precipitate shearing contributes to the changes observed in these microstructures. Note that microstructural evidence of precipitate shearing in Ni-based superalloys has also been reported in the literature. There are studies which show the formation of shear bands through the precipitates (Stoltz and Pineau, 1978; Sundararaman et al., 1989; Xiao et al., 2005), while others have shown the morphology of the precipitates after shearing (Ye et al., 2004).
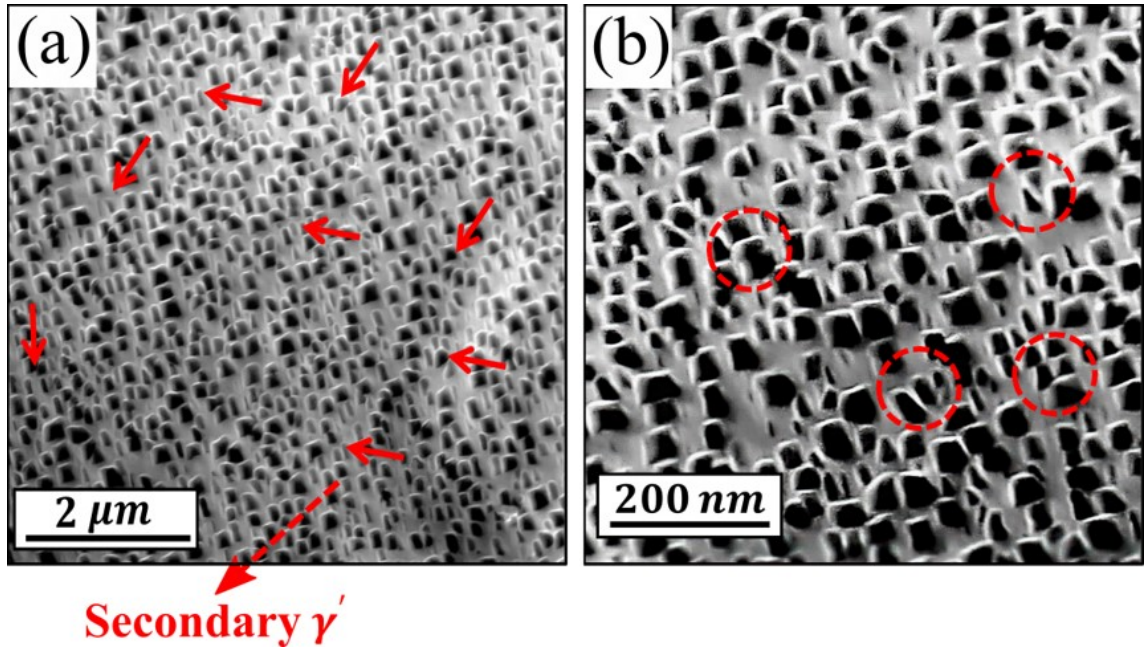
FIGURE 6.3: (a), (b): SEM images of the deformed Alloy 1 showing sheared secondary γ'_s precipitates.

Further note that in the present alloy, the volume fraction of γ' is nearly 50%. The matrix, γ, and the precipitate phase, γ', often brought significant mass-thickness contrast (Williams et al., 1996), which dominated over the diffraction contrast essential for dislocation imaging (Williams et al., 1996; Edington and Edington, 1975). As shown in Figure 6.4(a), revealing the dislocations with diffraction contrast in a highly magnetic Ni-based system was non-trivial and often non-quantitative. The last point is indicated by the lower magnification TEM bright and dark field images in Figure 6.4(b). Though these images are for regions surrounding the unsheared and sheared precipitates, the dislocations are

not revealed effectively. We have hence used TEM-based Precession Electron Diffraction (TEM-PED) and a methodology described in Refs. (Rauch and Veron, 2005; Pai et al., 2024a; Sudhalkar et al., 2024), for bringing out this aspect. However, as suggested by Kiss et al. (Kiss et al., 2016), the correlation coefficient map (c.f. 6.3.1.2) revealed the presence of dislocations around the unsheared and sheared precipitates (Figure 6.4(c)). In particular, microstructural evidence of precipitate shearing was clearly revealed in terms of dislocation activity in the vicinity of γ' precipitates.
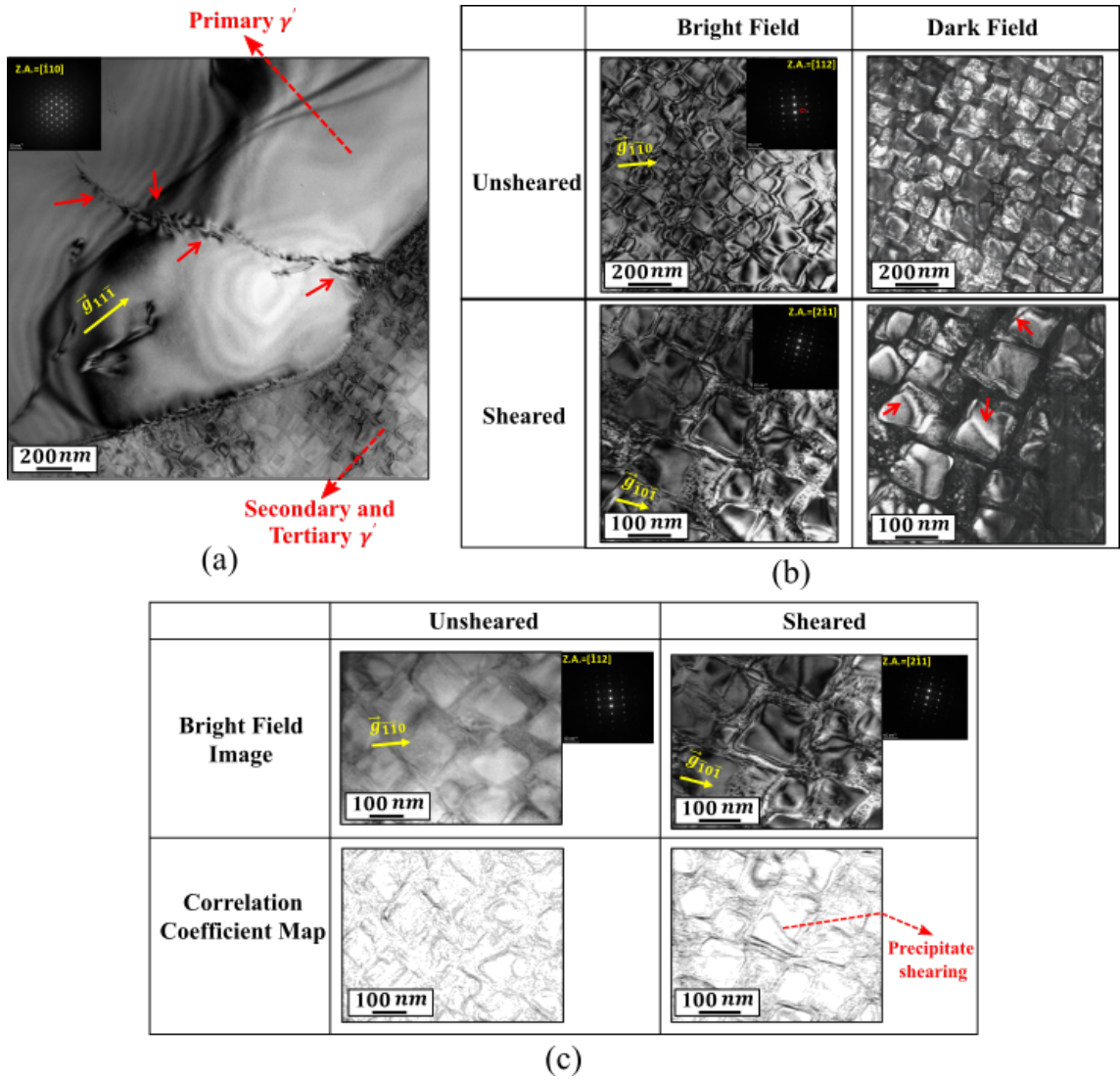
FIGURE 6.4: (a) TEM-based bright field image showing dislocations in primary γ', (b) bright and dark field images showing the unsheared and sheared γ'_s precipitates, (c) TEM bright field and TEM-PED-based correlation coefficient map showing evidence of precipitate shearing.

6.3.1.2 Correlation Coefficient Map

TEM-PED was performed, and a series of diffraction patterns was collected from a region at a particular step size (2 nm). The correlation coefficient $C(i, j)$ was calculated using equation S1 comparing each diffraction pattern in the 144×144 pixel domain with its neighbouring patterns (Kiss et al., 2016):

$$C\left(i, j\right) = \sqrt{\frac{\Sigma_{x,y}\left[P^{i,j}\left(x, y\right) - P^{i+1,j}\left(x, y\right)\right]^2 + \Sigma_{x,y}\left[P^{i,j}\left(x, y\right) - P^{i,j+1}\left(x, y\right)\right]^2}{2N}} \tag{6.23}$$

where $P^{i,j}$ and $P^{i+1,j}$ represent the two successive diffraction patterns from left to right, while $P^{i,j}$ and $P^{i,j+1}$ are from top to bottom. Meanwhile, (x,y) are pixel coordinates within the patterns. $N = 144 \times 144$ is the total number of pixels in the pattern. The $C(i, j)$ were then plotted over the entire domain, and the resulting map is shown in Figure 6.4(c).

6.3.1.3 Model Parameters

The crystal plasticity model parameters were calibrated to predict the macroscopic stress-strain data obtained from the room temperature low-cycle fatigue tests at different strain amplitudes. As discussed in (Chaudhary et al., 2023), the microstructure consisting of the homogenized matrix (γ phase with secondary γ'_s and tertiary γ'_t precipitates), and the micron-sized primary γ'_p precipitate as a separate phase were considered in our model. Accordingly, we have considered 12 octahedral $\{111\} < 110 >$ slip systems in the matrix phase, and 12 octahedral $\{111\} < 110 >$ slip systems along with 6 cube slip systems in the primary γ'_p phase. The individual deformation of the γ'_s and γ'_t precipitates is not considered; rather, their contribution to the strengthening is considered in the form of the precipitate strengthening contributions discussed earlier.

For these predictions, simulations were performed on a 3D cube geometry with 512 cube-shaped grains (with 8 linearly interpolated hexahedral elements per grain). The reduced texture comprising 512 grains/orientations was obtained from the undeformed experimental texture plotted with (111), (011), and (001) pole figures as shown in Figure 6.5. A random texture is observed for the undeformed material, with no significant pole intensities. According to the volume fraction of primary γ'_p precipitates, an appropriate number of grains were assigned to the γ'_p phase, and the rest were assigned to the matrix phase. Displacement-controlled cyclic loading was applied along the y-direction at a nominal strain rate of 2×10^{-3} s^{-1} in simulations. Displacement normal to three adjacent faces of

the 3D microstructure was set to zero by applying roller boundary conditions. The corner
node common to these three faces was fixed to avoid rigid body rotation.
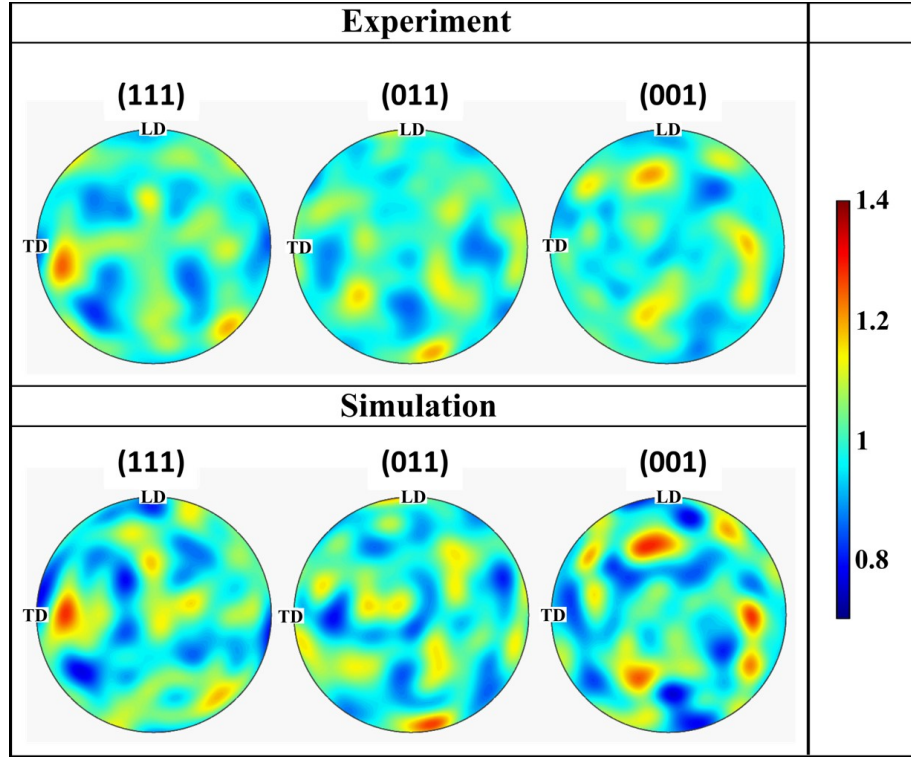
FIGURE 6.5: Comparison of reduced 512 grain texture used for the crystal plasticity
simulations with the undeformed experimental EBSD texture for Alloy 1. Here, LD and
TD represent the loading and transverse directions, respectively.

TABLE 6.3: Temperature-dependent elastic constants for the γ and $\gamma^{'}$ phase (Keshavarz
et al., 2016).

Phase	Value
γ	$C_{11} = 269.87 - 0.096T$ GPa
	$C_{12} = 174.29 - 0.057T$ GPa
	$C_{44} = 128.74 - 0.035T$ GPa
$\gamma^{'}$	$C_{11} = 298.87 - 0.096T$ GPa
	$C_{12} = 192.29 - 0.057T$ GPa
	$C_{44} = 133.74 - 0.035T$ GPa

TABLE 6.4: Strengthening coefficients for different alloying elements contributing to solid
solution strengthening (Roth et al., 1997).

Alloying Element	C	Cr	Co	Mo	Ti	Al	Mn	Si	Fe	Ni
Strength Coefficient (MPa.At.Fraction$^{-\frac{1}{2}}$)	1061	337	39.4	1015	775	225	448	275	153	–

TABLE 6.5: Flow, strengthening and substructure parameters for γ and $\gamma_p^{'}$ phase for Alloy 1.

Parameter	$\alpha \in$ oct, $j \in$ matrix	$\alpha \in$ oct,cube, $j \in \gamma_p^{'}$
Reference strain rate: $\dot{\gamma}_{0j}\left(\mathrm{s}^{-1}\right)$	0.03	10^{-3}
Activation energy for dislocation glide: ΔF_j^{α}	$0.15b^3$	$10Gb^3$
Shape parameters: p_j^{α}, q_j^{α}	0.5, 1.4	0.5, 1.4
Dislocation barrier strength: $k_{\rho j}^{\alpha}$	0.45	0.45
Dislocation interaction coefficients: $A^{\alpha\alpha}$, $A^{\alpha\zeta}$	1, 0	1, 0
Initial dislocation densities: $\rho_M^0\left(\mathrm{m}^{-2}\right)$, $\rho_I^0\left(\mathrm{m}^{-2}\right)$	1×10^{12}, 1×10^{12}	1×10^{12}, 1×10^{12}
Hall–Petch coefficient: $k_{Hj}^{\alpha}\left(\mathrm{MPa}\sqrt{\mu m}\right)$	250	222.22
Dislocation multiplication constant: k_{Mj}^{α}	0.22	0.25
Capture radius for annihilation of mobile dislocations: R_c	$6b$	$6b$
Dislocation trapping constant: k_{tj}^{α}	0.214	0.065
Dynamic recovery constant: k_{dj}^{α}	1000	5
Burgers vector magnitude: $b(\mathrm{nm})$	0.249	0.249
APB energy of polycrystalline superalloy: $\gamma_{APB}\left(\frac{\mathrm{mJ}}{\mathrm{m}^2}\right)$	200	200
APB energy of CMSX-4: $\gamma_{APB}|_{CMSX-4}\left(\frac{\mathrm{mJ}}{\mathrm{m}^2}\right)$	-	111
Geometry parameter: A	0.72	-
Elastic repulsion parameter: w	1	-
Backstress: $k_{\chi1}^{\alpha}$, $k_{\chi2}^{\alpha}$	2000, 1000	1000, 1000
Precipitate shearing parameters: R_{ann} (nm), c	3.78, 0.3	-
Areal geometric factor: G_a	4	-
Volumetric geometric factor: G_v	1	-

Majority of the model parameters used here are based on the values used in Chapter 5. Additionally, parameters related to the cyclic hardening and softening are calibrated to the experimental stress-strain response and are described briefly in the following. The temperature-dependent elastic constants for γ and $\gamma^{'}$ phases were taken from Keshavarz et al. (2016) and are given in Table 6.3. Model parameters related to the activation energy shape parameters, Burgers vector magnitude, and precipitate and grain size strengthening parameters, and the initial microstructural parameters (size and volume fraction of different phases and precipitates), and the solute concentrations and solid solution strengthening coefficients for the matrix and $\gamma_p^{'}$ phases were directly adopted from Roth et al. (1997) and are given in Table 6.4. Parameters related to the dislocation evolution, which contribute to *isotropic hardening*, were slightly modified from our previous study to obtain a better fit of the initial hardening during cyclic deformation as given in Table 6.5. Note that in our previous study, the role of non-Schmid stresses was also considered in the primary $\gamma_p^{'}$ precipitates, while the same has been neglected here to simplify the parameter estimation process. As discussed in (Ranjan et al., 2021), the contribution of non-Schmid stresses to room temperature deformation may be expected to be minimal. While we do not have the exact estimate of the APB energy for this alloy, we have used a value of $\gamma_{APB} = 200\mathrm{mJ/m}^2$. This is in the range of APB energies reported for Ni-based superalloys

reported in the literature (Kozar et al., 2009; Ghorbanpour et al., 2017; Li et al., 2019b; Eggeler et al., 2021). The backstress model parameters, $k_{\chi 1}^{\alpha}$ and $k_{\chi 2}^{\alpha}$, were calibrated to capture the observed kinematic hardening and predict the cyclic stress-strain response. Finally, the model parameters related to cyclic softening, c and R_{ann}, were chosen based on the best fit to the experimental data. As discussed in (Patra and McDowell, 2013), the exponent of the areal density of the precipitates lies between $0 < c < 1$ in the precipitate shearing model, and it controls the rate of shearing. Before moving further, it should be noted that based on the experimental microstructure evidence seen in Figure 6.3, we have only considered shearing of the secondary $\gamma_s^{'}$ precipitates in the matrix phase for Alloy 1 in our model. While tertiary $\gamma_t^{'}$ precipitates may also get sheared, microstructure characterization at such a fine resolution is presently not possible. Hence, we have neglected the contribution of the shearing of tertiary $\gamma_t^{'}$ precipitates, if any, in our present simulations.

6.3.1.4 Prediction of Low Cycle Fatigue Behavior

The predicted hysteresis loops for fully reversed cyclic loading at 0.9% and 1.8% strain amplitudes, along with the cyclic stress-strain response, are plotted in Figure 6.6 and compared with the corresponding experimental data. The predicted cyclic stress-strain responses are compared with the experimental counterparts for the 1st cycle, the cycle with the highest peak stress, and the last cycle up to which the experiments were performed. Note that the experiments were not performed till failure to perform microstructure characterization on the deformed specimens. Moreover, the primary objective of the present work is the prediction of the cyclic softening behavior, and fatigue life prediction will be performed in future work.

Model predictions of the hysteresis loop compare qualitatively with the corresponding experimental counterparts at the different cycles, while over-predicting the elastic-plastic transition for both strain amplitudes. In these simulations, the response in the first cycle was calibrated by fitting the backstress evolution parameters, whereas the predicted response in the following cycles was adjusted using the cyclic softening parameters. The peak stress increased slightly from the 1st cycle to the 30th cycle for the 0.9% strain amplitude test, and up to the 10th cycle for the 1.8% strain amplitude test. Following this, a decrease in the peak stress was observed in both experimental and simulation results. This observed behavior is due to the initial kinematic hardening-induced backstress, followed by subsequent cyclic softening.
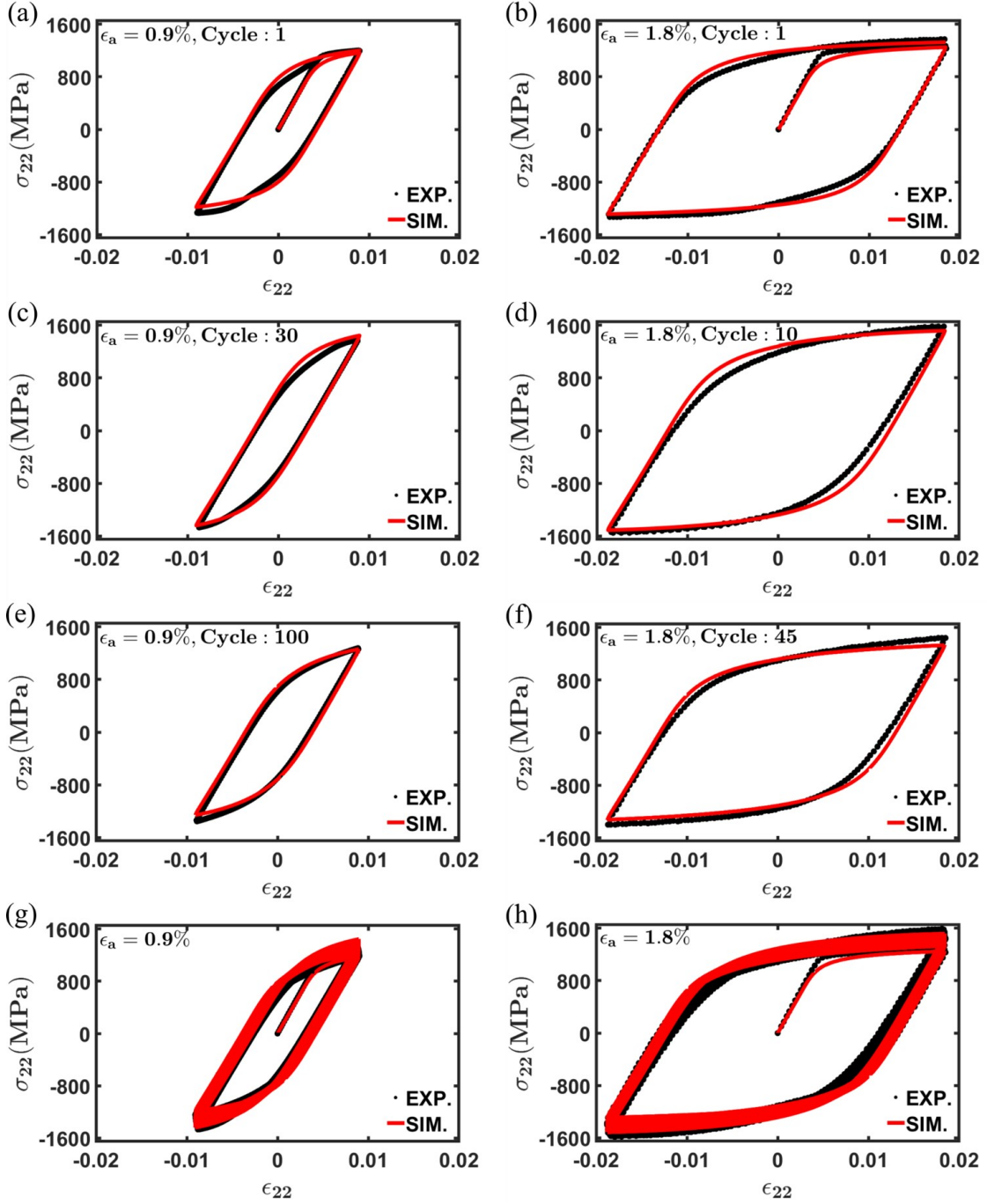
FIGURE 6.6: Comparison of the predicted hysteresis loop for cycles (a) 1, (c) 30, (e) 100, and (g) cyclic stress-strain response at 0.9% strain amplitude, and for cycles (b) 1, (d) 10, (f) 45, and (h) cyclic stress-strain response at 1.8% strain amplitude with the corresponding experimental data for a fully reversed cyclic loading test for Alloy 1.
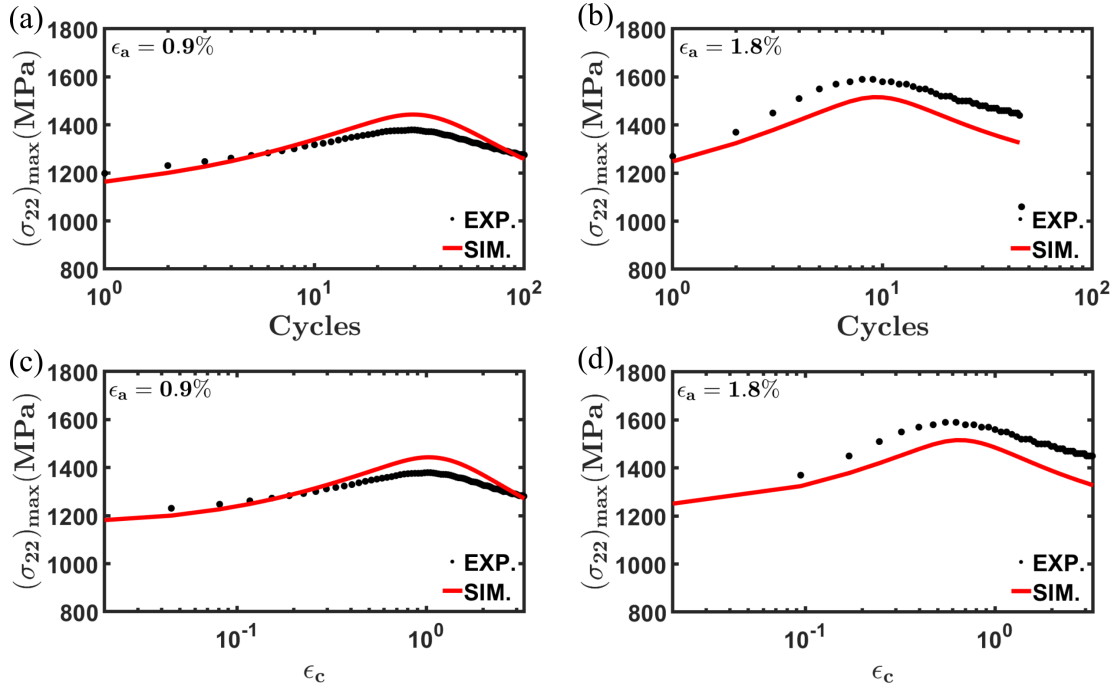
FIGURE 6.7: Comparison of the predicted peak stress with the corresponding experimental values as a function of the number of cycles and total nominal cyclic strain for (a,c) 0.9% and (b,d) 1.8% strain amplitude for Alloy 1.

Figure 6.7 shows a comparison of the peak stress as a function of the number of cycles for 0.9% and 1.8% strain amplitude for Alloy 1. The peak stress plotted as a function of the total nominal cyclic strain, $\epsilon_c = \sum_{i=1}^{n} 2|\epsilon^a|$, additively summed over the number of loading cycles, n, at any instant is also shown to compare the cyclic softening behaviors for the two simulations on the same scale. Here, the first few cycles show hardening followed by a progressive decrease in the peak stress on further cyclic deformation. It is also observed that cyclic softening commences at an approximately similar value of ϵ_c for the two strain amplitudes in both experiments and simulations. The resistance to plastic deformation is primarily due to the work hardening, which results from dislocation-dislocation interactions, and the precipitation strengthening, which results from dislocation-precipitate interaction in these precipitation-hardened systems Raman and Padmanabhan (1995). In the present case, the initial hardening is the result of work hardening, whereas softening after a few cycles is due to a decrease in precipitate strengthening. While noting that there are some quantitative differences ($\approx 5 - 7\%$) in the model predictions of the peak stress, especially for the 1.8% strain amplitude case, as compared with the experimental data, the model is able to qualitatively predict the hardening rate, peak stress and softening rate for both the strain amplitudes.
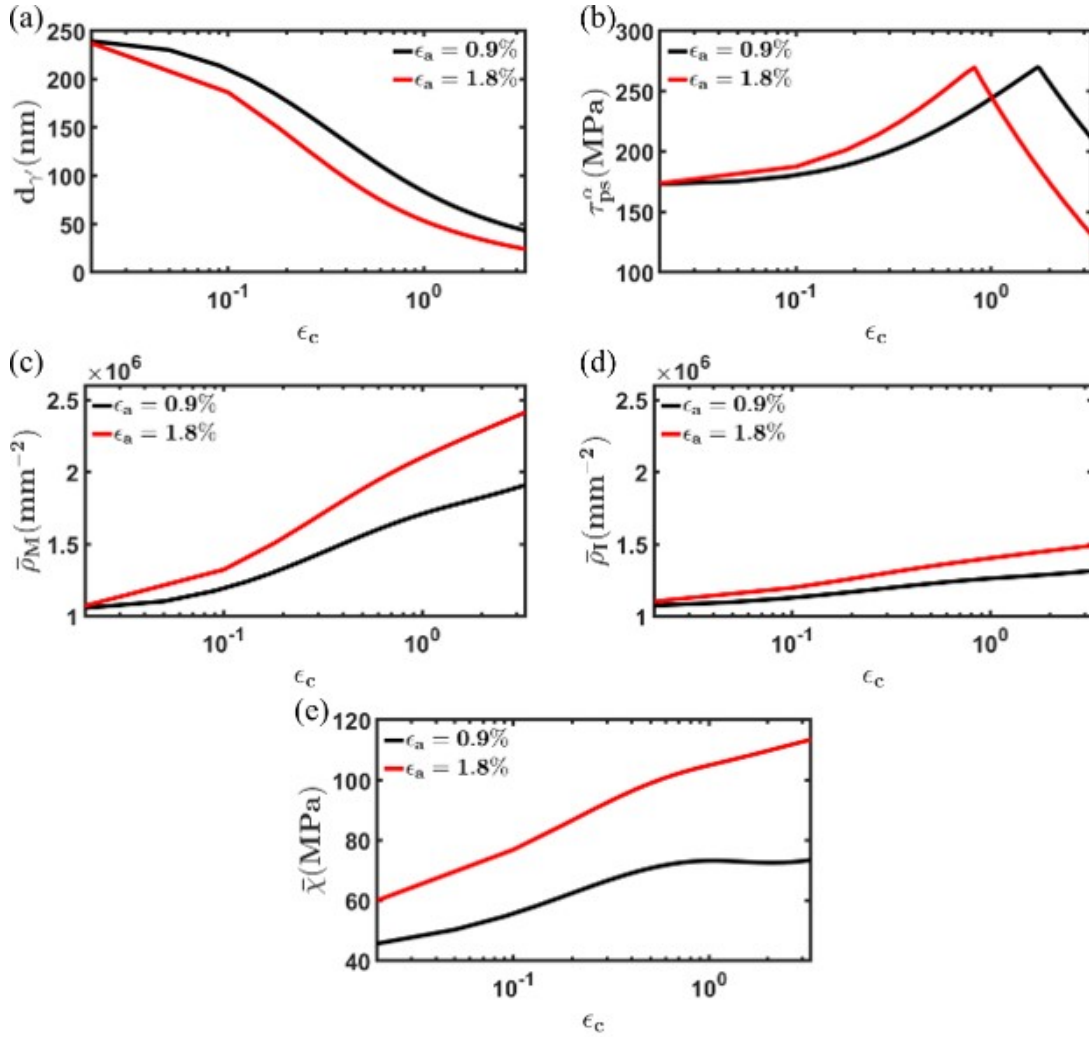
FIGURE 6.8: The evolution of (a) precipitate size, $d_{\gamma'}$, (b) precipitate strengthening, τ_{ps}^{α}, (c) slip system-averaged mobile dislocation densities, $\bar{\rho}_M$, (d) slip system-averaged immobile dislocation densities, $\bar{\rho}_I$, and (e) effective backstress, $\bar{\chi}$, as a function of total nominal cyclic strain, ϵ_c, at 0.9% and 1.8% strain amplitude.

Figure 6.8 shows the predicted evolution of various microstructure and internal state variables as a function of ϵ_c for the two strain amplitudes for Alloy 1. The precipitate size decreases with an increase in ϵ_c due to precipitate shearing as shown in Figure 6.8(a). The predicted mean precipitate size (≈ 50 nm) at the end of the simulation is qualitatively comparable to the TEM measured sheared precipitate size 91 ± 6 nm measured earlier in Figure 6.4. Note that the initial precipitate size, prior to cyclic deformation, was of the order of 250 nm. The corresponding contribution to precipitate strengthening, τ_{ps}^{α}, changes according to Equation 6.10 and is shown in Figure 6.8(b). During the initial cycles, the size of the secondary γ'_s is still larger than the threshold precipitate size, d_i^0, such that the

reduction in the precipitate size leads to an increase in τ_{sp}^{α} according to the Equation 6.11. Subsequently, the weak pair coupling mechanism becomes operative and τ_{wp}^{α} decreases with a reduction in size of the γ_s' precipitates according to Equation 6.12. Further, the evolution of the slip system-averaged mobile and immobile dislocation densities is plotted in Figures 6.8 (c) and (d), respectively, and the evolution of the effective backstress is plotted in Figure 6.8 (e). The effective backstress, $\bar{\chi}$, is calculated as (Evers et al., 2004):

$$\bar{\chi} = \sqrt{\frac{3}{2}\boldsymbol{\chi} : \boldsymbol{\chi}}, \boldsymbol{\chi} = \sum_{\alpha=1}^{N_s} \chi^{\alpha} \boldsymbol{s}_0^{\alpha} \otimes \boldsymbol{m}_0^{\alpha} \tag{6.24}$$

The macroscopic strength of the polycrystalline aggregate is the sum of the individual slip system-level strengthening contributions. As predicted from our simulations, the initial increase in peak stress is due to an increase in the back stress and the isotropic hardening (due to an increase in dislocation densities), and an increase in the precipitate strengthening. On further cyclic deformation, reduction of precipitate size occurs, and the corresponding strengthening due to precipitates decreases, thus resulting in the observed cyclic softening.

For cyclic loading at 1.8% strain amplitude, the material fails much earlier (at around 54 cycles) as compared to 0.9% strain amplitude. This is because of the relatively higher plastic deformation per cycle at 1.8% strain amplitude. As a result, the cyclic softening starts much earlier at 1.8% strain amplitude and the size of the precipitates decreases at a higher rate (with the number of cycles) as compared to 0.9% strain amplitude (see Figure 6.7(a) and (b)). However, it is interesting to note that the values of mobile and immobile dislocation densities and the backstress are relatively higher for 1.8 % strain amplitude at a given ϵ_c, as compared to the 0.9 % strain amplitude predictions (see Figure 6.8). This indicates that although the contributions of dislocation strengthening and backstress increase with an increase in strain amplitude, precipitate strengthening is still the dominant mechanism contributing to the overall strength of the superalloy.

6.3.2 Model Predictions for Alloy 2

The model has been used to predict the cyclic deformation behavior of another polycrystalline Ni-based superalloy, Nimonic-90, and compared with the experimental data at different strain amplitudes (Raman and Padmanabhan, 1995). This is referred as Alloy 2 in the following discussion and its elemental composition is given in Table 6.6. This alloy was selected to show the model's capability to predict the cyclic deformation for

a different initial microstructure, which has a different shape, size, and volume fraction of the precipitates as compared to Alloy 1. The microstructure of Alloy 2 consists of spherical γ' precipitates in the γ matrix (Singh et al., 1991). Since larger, micron-sized γ' precipitates have not been reported, we have assumed a homogenized γ matrix with γ' precipitates in our simulations (i.e., secondary or tertiary precipitates have not been considered separately).

6.3.2.1 Model Parameters

We have considered 12 octahedral $\{111\} < 110 >$ slip systems in the matrix phase. Similar to earlier simulations, a 3D cube geometry with 512 cube-shaped grains (with 8 linearly interpolated hexahedral elements per grain) was used for these simulations. Further, the initial reduced texture obtained for Alloy 1 (cf. Figure 6.5) was used for the Alloy 2 simulations as well. The crystal plasticity model was calibrated to predict the cyclic deformation for different strain amplitudes at room temperature and compared with the corresponding experimental data (Raman and Padmanabhan, 1995).

TABLE 6.6: Elemental composition of Alloy 2. This was converted to an atomic fraction from the wt. % given in Ref. (Raman and Padmanabhan, 1995).

Alloying Element	C	Cr	Co	Mo	Ti	Al	Mn	Si	Fe	Ni
Atomic Fraction	0.37	22.75	13.44	1.78	2.67	3.92	0.04	0.37	1.47	53.19

The undeformed microstructure of Alloy 2 consists of γ' precipitates with an average precipitate size of 25 nm, coherent in the γ matrix, which has an average grain size of $300\pm 30\,\mu$m (Raman and Padmanabhan, 1995). While the volume fraction of the precipitates has not been reported, the heat treatment history for Alloy 2 has been provided. Specifically, solutionizing treatments were applied at 1353 K for 8 hours, followed by aging at 973 K for 16 hours (Raman and Padmanabhan, 1995). We have used the approach given in Dyson et al. (Dyson, 2009) to estimate the volume fraction of precipitates, as a first-order approximation. The γ' volume fraction is calculated using the following equation (Dyson, 2009):

$$f_{\gamma'}\left(T\right) = \frac{c_0 - c_e\left(T\right)}{0.23 - c_e\left(T\right)} \tag{6.25}$$

where c_0 denotes the concentration of γ' forming element of the alloy and $c_e\left(T\right)$ denotes the equilibrium solute concentration in the matrix and is given as (Dyson, 2009)

$$c_e\left(T\right) = 17exp\left(-\frac{7250}{T}\right) \tag{6.26}$$

Thus, for the ageing temperature as T=973 K, $c_e(973\text{K}) = 0.00987$. Further, $c_0 = c_e(T)$ at solvus temperature. At the γ' solvus for Nimonic-90 (1273 K) (Dyson, 2009), $c_0 = c_e(1273\text{K}) = 0.05715$. This gives $f_{\gamma'} = 0.215$. Based on these calculations, $f_{\gamma'} \approx 0.21$ is assumed in our study. Similar volume fractions of $f_{\gamma'} = 0.25$ have also reported by Basoalto et al. (Basoalto et al., 2004) for Nimonic-90.

For Alloy 2, most of the model parameters were assumed to be the same as Alloy 1. The parameters, $\dot{\gamma}_{0j}$ and ΔF_j, were modified to estimate the initial yield strength. Further, the initial hardening and the width of the hysteresis loop were obtained by calibrating k_{dj}^{α} and the backstress evolution parameters. Finally, the cyclic softening parameters were modified to predict the rate of softening accurately. These model parameters are given in Table 6.7.

TABLE 6.7: Model parameters for γ and γ' phase for Alloy 2. In the absence of primary γ'_p precipitates, it was assumed that the nanometer-sized precipitates are distributed in the homogenized γ matrix.

Parameter	$\alpha \in \text{oct}, j \in \text{matrix}$
Reference strain rate: $\dot{\gamma}_{0j}\left(\text{s}^{-1}\right)$	0.5
Activation energy for dislocation glide: ΔF_j^{α}	$0.040Gb^3$
Shape parameters: p_j^{α}, q_j^{α}	0.5, 1.4
Dislocation barrier strength: $k_{\rho j}^{\alpha}$	0.45
Dislocation interaction coefficients: $A^{\alpha\alpha}$, $A^{\alpha\zeta}$	1, 0
Initial dislocation densities: $\rho_M^0\left(\text{m}^{-2}\right)$, $\rho_I^0\left(\text{m}^{-2}\right)$	1×10^{12}, 1×10^{12}
Hall–Petch coefficient: $k_{Hj}^{\alpha}\left(\text{MPa}\sqrt{\mu\text{m}}\right)$	250
Dislocation multiplication constant: k_{Mj}^{α}	0.22
Capture radius for annihilation of mobile dislocations: R_c	$6b$
Dislocation trapping constant: k_{tj}^{α}	0.214
Dynamic recovery constant: k_{dj}^{α}	500
Burgers vector magnitude: b(nm)	0.249
APB energy of polycrystalline superalloy: $\gamma_{APB}\left(\frac{\text{mJ}}{\text{m}^2}\right)$	200
Geometry parameter: A	0.72
Elastic repulsion parameter: w	1
Backstress: $k_{\chi1}^{\alpha}$, $k_{\chi2}^{\alpha}$	2000, 500
Precipitate shearing parameters: R_{ann} (nm), c	0.28, 0.3
Areal geometric factor: G_a	π
Volumetric geometric factor: G_v	$\pi/6$

6.3.2.2 Prediction of Low Cycle Fatigue Behavior

The model was used to predict the deformation for two different types of cyclic loading: incremental step tests and fully reversed constant strain amplitude tests.

For the incremental step test, the loading block is shown in Figure 6.9(a). In these incremental step tests, loading was applied in repeated blocks of cyclic loading with varying strain amplitude (Raman and Padmanabhan, 1995), and the hysteresis loops for one such block were reported at half life. While we have not performed simulations till the end of life, we report the predicted cyclic stress-strain response in Figure 6.9 for the 80th block, assuming that the hysteresis loops have saturated by this point. The predicted cyclic stress-strain response at a nominal strain rate of 3×10^{-3} s^{-1} is shown for block 1 and block 80 in Figure 6.9(b) and compared with the corresponding experimental data (Raman and Padmanabhan, 1995) at half life in Figure 6.9(c). As can be seen, the peak stress as well as the width of the hysteresis loop for each of the cycles in the loading block is predicted by the model with reasonable accuracy.
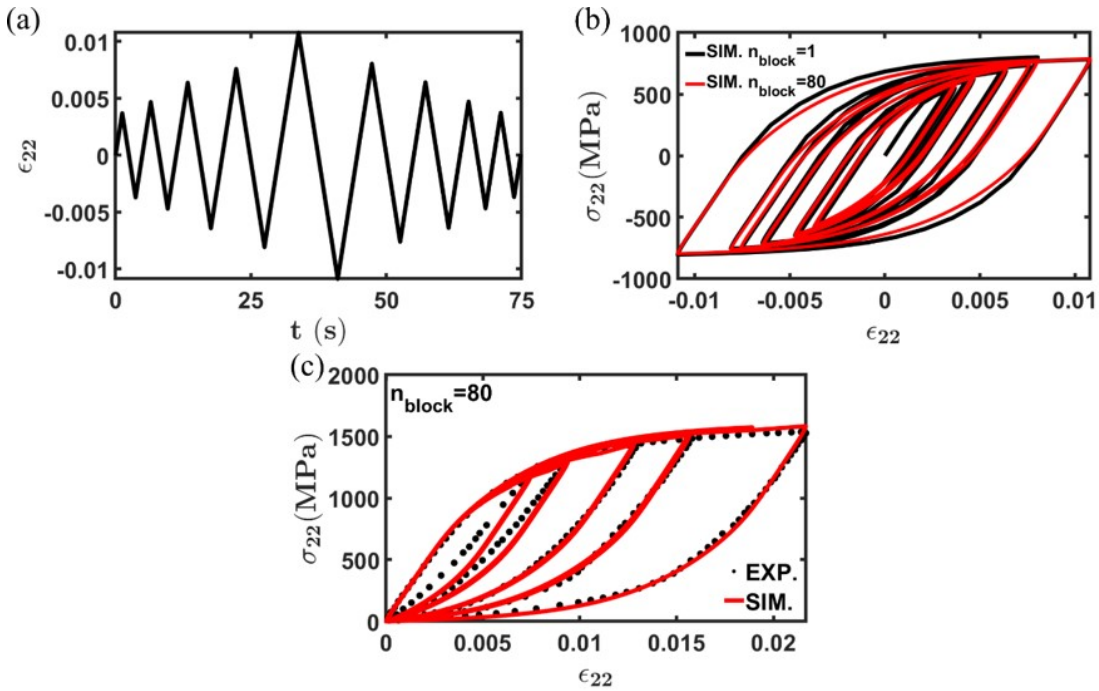
FIGURE 6.9: (a) Strain versus time for each loading block in the incremental step test. (b) Predicted cyclic stress-strain response for blocks 1 and 80, and (c) comparison of superimposed predicted stress-strain response with matched lower tips for block 80 with the corresponding experimental data for Alloy 2 (Raman and Padmanabhan, 1995).

Further, simulations were performed for fully reversed cyclic loading for three different strain amplitudes at a nominal strain rate of 3×10^{-3} s^{-1} at room temperature. While the experimental peak stress data at 1.1% and 0.6% strain amplitudes were used for calibrating the cyclic softening parameters, the model was used to predict the response at 0.85% strain amplitude as a validation test case. The comparison of peak stress for the different strain amplitudes as a function of the number of cycles and ϵ_c with the

corresponding experimental data from (Raman and Padmanabhan, 1995) is plotted for Alloy 2 in Figure 6.10. The peak stress evolution during the first few cycles shows an increase in cyclic hardening for all three strain amplitudes, while a gradual drop in the peak stress is observed on further deformation. For all three strain amplitudes, the peak stress evolution with the number of cycles is predicted relatively well by the model. This provides validation for the model's ability to predict cyclic softening. Further, as can be seen from both experiments and simulations, the peak stress values increase with an increase in strain amplitudes.
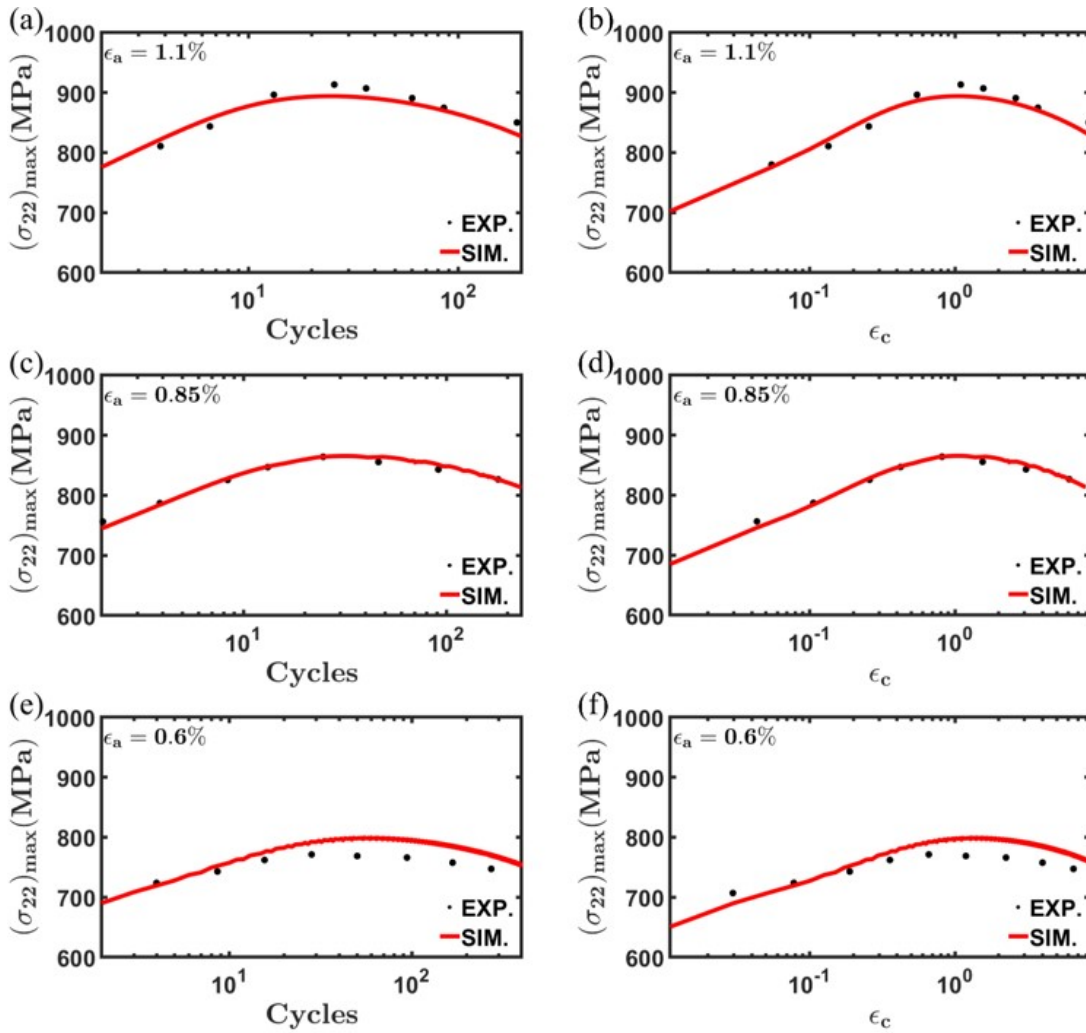
FIGURE 6.10: Comparison of peak stress as a function of the number of cycles and total nominal cyclic strain, ϵ_c, for (a,b) 1.1%, (c,d) 0.85%, and (e,f) 0.6% strain amplitude with the corresponding experimental data for Alloy 2 (Raman and Padmanabhan, 1995).

Figure 6.11 shows the predicted evolution of various microstructure and internal state variables as a function of ϵ_c for the different strain amplitudes for Alloy 2. The initial increase

in peak stress as seen in Figure 6.10 can be correlated with an increase in the dislocation densities and back stress in Figures 6.11 (c), (d), and (e). The dislocation densities and the backstress at any given ϵ_c are higher for a higher strain amplitude. However, as seen in Figure 6.11(a), the precipitate size does not change appreciably during the first few cycles (up to about $\epsilon_c = 1$ for all three strain amplitudes). Subsequently, as the mobile dislocation density increases, the areal density and the precipitate size decrease on further cyclic deformation. Given the relatively small initial precipitate size, the strengthening contribution is due to weakly coupled dislocation pairs (cf. Equation 6.12). As a result, the strength contribution, τ_{ps}^α, decreases with increasing ϵ_c. Note that this is in contrast to the corresponding predictions for Alloy 1, where τ_{ps}^α initially increases and then decreases with increasing ϵ_c (cf. Figure 6.8 (b)).

These results indicate that there is a transition from strong pair coupling to weak pair coupling for Alloy 1, while there is no such transition with cyclic deformation for Alloy 2. Remarkably, the microstructure-sensitive crystal plasticity model is able to predict the experimentally observed cyclic softening behavior for both these alloys by accounting for the underlying physical mechanisms.

6.3.3 Statistics of Precipitate Shearing

The SEM image of sheared precipitates shown in Figure 6.3(b) was analyzed to estimate the fraction of sheared precipitates using a combination of image processing tools. Based on the limited data analyzed, it was found that roughly 45% of the precipitates are sheared. However, we note that a similar fraction of sheared precipitates may not be observed in all grains, and this may also be dependent on the orientation of the grains and the loading conditions.

While a direct comparison of model predictions with experiments is not possible, we have plotted the distribution of the number density of precipitates, $N_{\gamma'}$, for the different simulations for both alloys. This is obtained by extracting the post-deformation, precipitate number density over all material points present in the simulation domain. Model predictions are shown for Alloy 1 and Alloy 2 in Figure 6.12(a) and 6.12(b), respectively. Note that all precipitates were initially assumed to be of the same size in this mean field model, and hence the number fraction of 1 for the undeformed precipitates. It can be seen from the model predictions that the mean number density of the precipitates corresponding to the peak number fraction is approximately 2-4 times the initial number density of the precipitates. This provides a qualitative comparison with the limited analysis of the
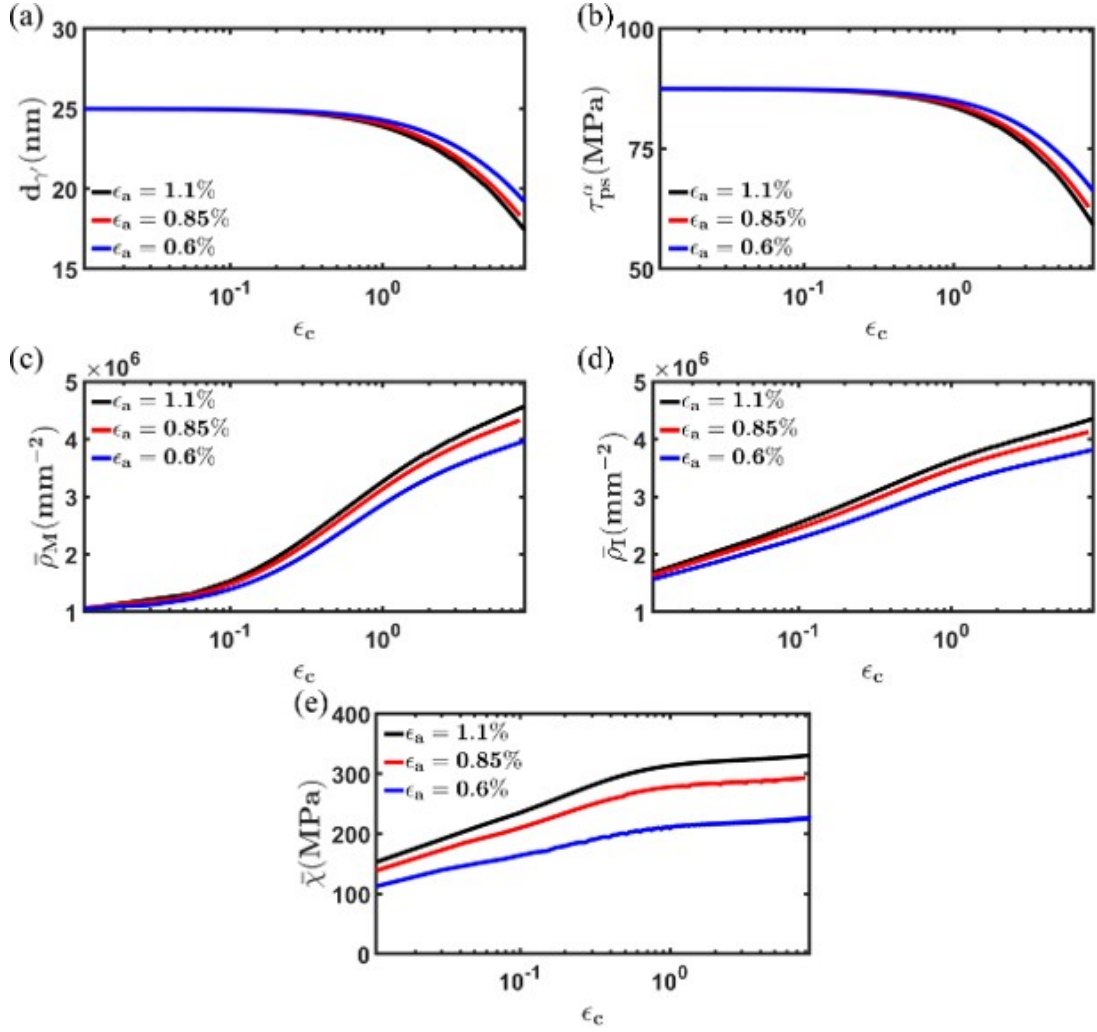
FIGURE 6.11: The evolution of (a) precipitate size, $d_{\gamma'}$, (b) precipitate strengthening, τ_{ps}^{α}, (c) slip system-averaged mobile dislocation densities, $\bar{\rho}_M$, (d) slip system-averaged immobile dislocation densities, $\bar{\rho}_I$, and (e) effective backstress, $\bar{\chi}$, as a function of total nominal cyclic strain, ϵ_c, at 1.1%, 0.85% and 0.6% strain amplitude for Alloy 2.

experimental SEM microstructures. Moreover, these predictions are from a mean field model, which only considers the mean value of precipitate number density and size at a material point. We note that a cluster dynamics-based approach for the prediction of the distribution of precipitate number density and size may be more appropriate as compared to our mean field model.
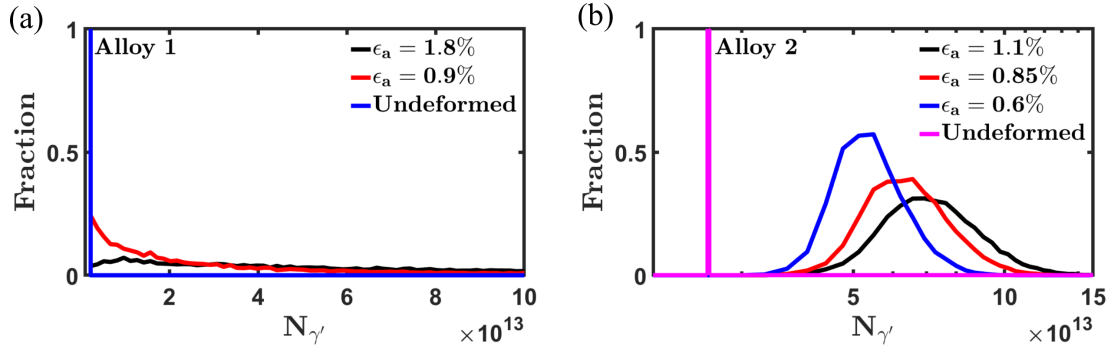
FIGURE 6.12: Distribution of precipitate number density before and after cyclic deformation for (a) Alloy 1 to 44 cycles for 1.8% strain amplitude and 100 cycles for 0.9% strain amplitude, and (b) Alloy 2 to 200 cycles for 1.1% strain amplitude, 234 cycles for 0.85% strain amplitude, and 400 cycles for 0.6% strain amplitude.

6.3.4 Prediction of Cycle Deformation and Softening at High Temperature

Preliminary predictions of the cycle deformation behavior have been made at 923 K and 0.9% strain amplitude for Alloy 1. A comparison of the peak stress evolution as a function of the number of cycles at 923 K with the corresponding room temperature response is shown in Figure 6.13. The flow stress at high temperatures is lower than at room temperature. A qualitatively similar increase in the peak stress with number of cycles, followed by a delay in the initiation of cyclic softening is predicted at 923 K. Gopinath et al. (Gopinath et al., 2009) have performed low cycle fatigue tests at different temperatures and strain amplitude for a powder metallurgy processed Ni-based superalloy, Alloy 720Li, that has a similar microstructure comprised of primary, secondary and tertiary γ' precipitates. Our model predictions of the high-temperature peak stress evolution, as compared to the room temperature behavior, are qualitatively similar to their experimental observations (see Figure 2 in Ref. (Gopinath et al., 2009)). Temperature-dependent elastic constants for γ and γ' phases have been considered for the high-temperature simulations. Further, the model naturally considers thermally activated glide according to the flow rule given in Equation 4.4. It is expected that the APB energy may vary with temperature and also with alloy composition (Manga et al., 2015; Ghorbanpour et al., 2017; Li et al., 2019b). Accordingly, τ_{APB}^{α} is a temperature-dependent term, which has been discussed in prior studies (Ranjan et al., 2021; Chaudhary et al., 2022) and is used to phenomenologically account for the effect of the APB energy on the strength. Lower-scale modeling studies can also be used to estimate the variation of this parameter as a function of alloy composition (Chandran

and Sondhi, 2011; Vamsi and Karthikeyan, 2021; Dodaran et al., 2020). Quantitative comparison of model predictions with the experimentally measured high-temperature cyclic stress-stress response will be performed in future work.
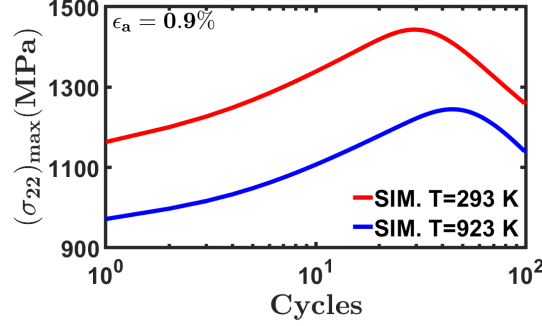
FIGURE 6.13: Prediction of peak stress as a function of the number of cycles at 0.9% strain amplitude at 923 K for Alloy 1.

6.4   Discussion

The micromechanical model for precipitate shearing, coupled with a precipitate strengthening model, implemented in a previously developed crystal plasticity framework, allows prediction of the cyclic deformation behavior, including cyclic softening in polycrystalline Ni-based superalloys. The primary novelty of this model is in its ability to predict cyclic softening in superalloys, with different initial microstructures, both in terms of the mechanical properties (cf. Figures 6.6, 6.7, 6.9, 6.10) and the microstructure evolution (cf. Figures 6.8, 6.11).

Alloy 1 has a microstructure comprising primary (micron-sized), secondary ($\approx$ 250 nm sized, cuboidal-shaped), and tertiary ($\approx$ 30 nm sized) γ' precipitates, for which experimental microstructure and mechanical property characterization were performed in the present study. The crystal plasticity framework was used to predict the cyclic deformation, in terms of the initial cyclic hardening, followed by cyclic softening observed in this alloy during room temperature deformation for 0.9% and 1.8% strain amplitudes. Further, the substructure and microstructure evolution were also predicted in terms of the precipitate size, backstress, and dislocation densities during deformation. The predicted microstructure evolution was qualitatively validated by comparing model predictions of precipitate size with experimental TEM measurements. It was predicted that the observed cyclic softening occurs due to a transition from strong pair coupling to weak pair coupling of

the dislocation-precipitate interactions. We note that the comparison of model predictions with the experimental microstructure measurements for this alloy is rather limited at present. More detailed characterization, including High Resolution Transmission Electron Microscopy (HRTEM) (for example, see (Zenk et al., 2021)), could be performed in future work to validate the model predictions.

Alloy 2 has a microstructure comprising spherical γ' precipitates, with an initial size of ≈ 25 nm. The crystal plasticity model was first calibrated to the cyclic incremental step test and fully reversed cyclic deformation tests at two strain amplitudes (1.1% and 0.6%), while it was validated by predicting the cyclic deformation and softening behavior for another strain amplitude (0.85%). Given that the initial precipitate size was small, the weak pair coupling mechanism was present in this alloy from the beginning of deformation, and the observed cyclic softening was primarily due to the reduction in precipitate size and its contribution to precipitate strengthening.

The model could be improved further by accounting for a distribution of precipitates, rather than a mean field precipitate size and number density. This could be inspired by stochastic cluster dynamics-based models commonly used for studying defect distribution in irradiated materials (Yu et al., 2021). This would also allow consideration of different types of precipitates (secondary and tertiary) within the same shearing model. The detailed precipitate shape anisotropy and local coherency variations arising from interfacial chemistry fluctuations are not explicitly modeled in the present work. While these may play a role on the local deformation behavior, the homogenized macroscopic response is not expected to be affected appreciably. However, the constitutive models for dislocation-precipitate interactions can be improved by taking insights from lower scale discrete dislocation dynamics (DDD) simulations. The model could also be improved by insights from detailed experimental characterization (Zenk et al., 2021). While orientation-dependent anisotropy and heterogeneous deformation is also expected during cyclic loading, this was not studied using direct microstructural observations.

Cyclic deformation and softening at high temperature (which is generally the expected operating temperature of superalloys in gas turbine engines) is an issue of concern not addressed in the present work. While we have predicted and validated the high-temperature tensile deformation using our constitutive model in the previous work (Chaudhary et al., 2023), we intend to study the high-temperature cyclic deformation and softening in future work. Nonetheless, preliminary model predictions of the cyclic deformation of Alloy 1 are shown in Section 6.3.4.

6.5   Conclusions

A micromechanical constitutive model has been developed and implemented in a crystal plasticity framework to simulate microstructure evolution due to precipitate shearing and resultant cyclic softening in polycrystalline Ni-based superalloys. This model accounts for the shearing of γ' precipitates on their interaction with mobile dislocations, which results in a decrease in the areal density of the precipitates. The constitutive model has explicit consideration for the evolution of the volume number density and size of the precipitates, as well as their shapes. This constitutive model has been implemented along with an Armstrong-Frederick type slip system-level backstress evolution model to simulate the mechanical behavior and microstructure evolution during cyclic deformation of two polycrystalline Ni-based superalloys, with different initial microstructures.

The results presented in our work highlight the capability of the model to predict cyclic softening in Ni-based superalloys, with different types of initial microstructures, which may arise due to the processing and heat treatment. This is the primary novelty of the present work. This can potentially aid the design and optimization of heat treatment regimes to tailor the superalloy microstructures (in terms of precipitate size and volume fraction) for optimal strength and life during cyclic deformation. The framework can also be used in future work for fatigue lifing predictions of Ni-based superalloys (cf. Castelluccio and McDowell (2014); McDowell (2007)).

Chapter 7

Predicting Fatigue Indicator Parameters During Cyclic Deformation of Polycrystalline Ni-based Superalloys

7.1 Introduction

Fatigue failure of turbine disks is one of the most critical issues in the design and maintenance of aero-engines. Grain-scale microstructural features, such as the grain size, precipitate size and volume fraction, grain orientation, and presence of grain boundaries, significantly affect the LCF behavior, particularly during crack initiation and micro-crack propagation. Essentially, these microstructural features lead to heterogeneous stress and strain fields (Abuzaid et al., 2013). For example, Miao et al. (2009, 2012) revealed that cracks initiate within grains with high Schmid factors, particularly along planes that are parallel to and slightly offset from coherent twin boundaries in René 88DT alloy under very high cycle fatigue conditions. Crack initiation under low-cycle fatigue behavior has also been reported along twin boundaries in polycrystalline nickel-based superalloys (Miao et al., 2009, 2012; Stein et al., 2012). Heinz and Neumann (1990) suggested that strain localization is more pronounced at twin boundaries compared to general grain boundaries. Furthermore, Flageolet et al. (2005) reported that primary precipitates $\gamma^{'}$ could contribute to the crack initiation of P/M processed N18 alloy. Jiang et al. (2015a) concluded that crack initiation predominantly occurs during cyclic deformation at grain boundaries or

$\gamma/\gamma^{'}$ interfaces, primarily as a result of the formation and eventual rupture of chromium-rich and/or cobalt-rich oxides. Antolovich and Jayaraman (1983); Lerch et al. (1984) explored the effect of precipitate and grain size on the fatigue behavior of Waspaloy and concluded that microstructures with coarse grains and small precipitates show heterogeneous deformation due to precipitate shearing. Thus, gaining insight into the effect of these grain-scale damage mechanisms on crack formation or related parameters is crucial for understanding the contributors to fatigue life.

The EBSD technique is widely used to find misorientation-related parameters such as Grain Reference Orientation Deviation (GROD), KAM, and GND density, which are valuable in examining fatigue, creep, and creep-fatigue deformation (Han et al., 2021; Hu et al., 2021; Rui et al., 2018; Wang et al., 2021). For example, Wang et al. (2021) performed a creep-fatigue damage analysis in the Ni-based superalloy GH4169, using KAM, GROD, and GND. Their findings indicated that these misorientation parameters aligned well with damage parameters predicted by continuum damage mechanics under varying dwell times and strain ratios. Using digital images, Harte et al. (2020) showed a correlation between plastic strain and misorientation parameters. Jiang et al. (2022) studied the crack initiation and strain localization during low-cycle fatigue using SEM-DIC characterization and highlighted that elastic anisotropy near twin boundaries promotes strain localization and correlated the SEM-DIC analysis with crystal plasticity simulation by adding fatigue indicator parameters. Li et al. (2023) investigated the effect of microstructural features on fatigue short crack paths and propagation rates for GH4169 superalloys at room temperature and revealed that intragranular cracks predominantly propagate along activated slip bands within the γ-matrix grains parallel to 111 crystallographic slip planes. It was also observed that low-angle and subgrain boundaries were found to deflect intragranular cracking, whereas high-angle grain boundaries played a more dominant role in blocking short crack growth. Stinville et al. (2017a) investigated strain heterogeneity correlating SEM and DIC analysis during cyclic loading at 650 $^\circ C$ and observed strain localization near twin boundaries, which is associated with the activation of the 111 $\langle 110 \rangle$ and 111 $\langle 112 \rangle$ slip systems. Zhao et al. (2022) studied strain localization using SEM-DIC characterization during cyclic loading at 450 $^\circ C$ for PM-processed superalloys and revealed that strain generally accumulates within slip or strain bands as a result of dislocation slip on the 111 planes and strain bands at grain boundaries either transmit through, deflected by, or get blocked will depended on grain boundary characteristics and the crystallographic orientation of adjacent grains. Mello et al. (2017) studied a deformation mechanism map under cyclic loading at three temperatures using high-resolution DIC with an SEM and EBSD, and found out that at low temperatures, deformation occurs via 111 slip planes,

while higher temperatures activate both 111 and 100 slip planes due to cross-slip within the γ' phase. Moreover, high-resolution EBSD (HR-EBSD) has been used for the measurement of elastic strain and lattice rotation through the image correlation of Kikuchi patterns, and it is useful for validating and comparing simulation outputs (Wilkinson et al., 2006; Zhang et al., 2014, 2018, 2022b).

Several strain-based parameters have been proposed to predict fatigue crack formation, based on the range or amplitude of shear stress, shear strain, or plastic shear strain critical plane (Fatemi and Socie, 1988; Socie, 1993; Bennett and McDowell, 2003). These parameters are generally used to assess fatigue crack initiation, encompassing both the initial crack formation and a limited extent of small crack growth through the microstructure. Bennett and McDowell (2003) included cyclic microplasticity, the Fatemi-Socie parameter, and the Mohr–Coulomb parameter in the crystal plasticity framework to study the role of microstructural heterogeneity on fatigue behavior. Further, FIPs based on computed stress and plastic strain range have been used to predict the probability of formation of micro-fatigue cracks (Manonukul and Dunne, 2004; McDowell and Dunne, 2010). FIP for characterizing fatigue damage can be complex functions of stress and strain and may depend on the failure mechanisms (McDowell and Dunne, 2010). Firstly, Manonukul and Dunne (2004) implemented accumulated plastic slip as an FIP to predict crack initiation and characterize fatigue damage in a crystal plasticity framework for nickel alloy C263. Shenoy et al. (2007) introduced the Fatemi-Socie parameter and the maximum cyclic plastic shear strain parameter in the crystal plasticity framework for a representative volume element (RVE) to predict crack incubation. Following this, the FIP was successfully used to predict fatigue crack initiation for various materials (Shenoy et al., 2007; Castelluccio and McDowell, 2014; Yuan et al., 2020; Zhang et al., 2022b). Castelluccio and McDowell (2014) proposed a crystal plasticity framework to investigate fatigue crack initiation and growth at the mesoscale. The Fatemi-Socie parameter is employed to link local cyclic plasticity to crack nucleation sites (Liu et al., 2023). Yuan et al. (2020) implemented accumulated plastic slip and energy dissipation as FIP in the crystal plasticity model to predict fatigue crack initiation and showed that fatigue cracks generally initiate at triple points and grain boundaries. Zhang et al. (2022b) studied fatigue behavior using EBSD and crystal plasticity simulations of FGH4098 alloy at 650 $^\circ C$ and 750 $^\circ C$. At 750$^\circ C$, the alloy shows larger hysteresis loop areas and shorter fatigue life, and CPFE simulations reveal intense localization of accumulated shear-strain energy dissipation density (ASSEDD) and Fatemi–Socie parameter values, which indicate more rapid and extensive fatigue damage compared to 650 $^\circ C$. However, these studies do not study the competitive role of various microstructure features in fatigue damage initiation.

This study aims to examine the role of various grain-scale features in fatigue crack initiation during low-cycle fatigue deformation. Chapter 5 had focused on detailed microstructural characterization, followed by a qualitative comparison of our model predictions with experimental observations of various substructure-governing variables, namely the secondary precipitate size and local misorientations during tensile loading. Further, a crystal plasticity model for cyclic deformation and softening was developed in Chapter 6. In the present chapter, Fatigue Indicator Parameters (FIPs) proposed in the literature are introduced into the existing framework (Chapter 6) to simulate the microstructure evolution during cyclic deformation and hence identify the potential sites for damage initiation. Further, attempts are also made to correlate the FIPs with the microstructure evolution metrics, such as KAM (if any).

7.2 Prediction of Fatigue Indicator Parameters (FIPs) Using the Crystal Plasticity Model

In our crystal plasticity framework, mesoscale parameters such as CRSS, normal stress on specific slip systems, and shear strain can be correlated to estimate the FIPs. These FIPs characterize the driving forces for both the initiation of fatigue cracks and the growth of microstructurally small cracks (Zhang et al., 2022b). Slip impingement on grain boundaries or other concentrated slip bands is a physically feasible mechanism for fatigue crack formation. This phenomenon is linked to dislocation pileups, which can be quantified at the continuum level by measuring cumulative plastic shear strain, P_r (Shenoy et al., 2007):

$$P_r = max \left(\int_{cyclic} \dot{\epsilon}_{ij}^p m_i^\alpha s_j^\alpha dt \right) \tag{7.1}$$

where, s^α is the slip direction and m^α is the slip plane normal. The maximum value of this parameter is calculated over all possible slip systems for one cycle.

According to the critical plane approach, cracks initiate and propagate along specific planes, with this fatigue crack growth being further influenced by the normal stress acting on those planes (Shenoy et al., 2007). The Fatemi–Socie parameter, P_{fs}, effectively correlates with crack incubation related to slip band cracking and shear-dominated microstructurally small crack growth and is defined by (Shenoy et al., 2007; McDowell and Dunne, 2010; Zhang et al., 2022b):

$$P_{fs} = \frac{\Delta \gamma_{max}^p}{2} \left[1 + k \frac{\sigma_n^{max}}{\sigma_y} \right] \tag{7.2}$$

$$\sigma_n = \boldsymbol{m}^\alpha \cdot \boldsymbol{\sigma} \cdot \boldsymbol{m}^\alpha \tag{7.3}$$

where, $\Delta\gamma^p_{max}$ represents the maximum range of the cyclic plastic shear strain on the specific slip system, σ_y represents the yield strength, σ_n^{max} represents the peak stress normal to the plane associated with this maximum shear range and k is the constant lies between 0.5 to 1 that controls the influence of normal stress and set as 0.5 in this study (Shenoy et al., 2007; Zhang et al., 2022b). The cumulative plastic shear strain FIP, P_r, and the Fatemi–Socie FIP, P_{fs}, have been implemented in the crystal plasticity framework (Chapter 6) to predict the micro-crack formation sites in representative EBSD microstructures in the present chapter.

7.3 Model Predictions

Room temperature cyclic deformation is performed on the four EBSD microstructures studied earlier in Chapter 3 at 0.9 % strain amplitude, and FIPs are calculated at different cycles. The loading and boundary conditions remain the same as shown earlier, with the exception that positive and negative displacements are applied during the respective tensile and compressive loading cycles.

Figures 7.1, 7.2, 7.3 and 7.4 show the P_{fs} and P_r contours after cyclic deformation at cycles 10 and 20 for four different microstructures. P_r considers the accumulated shear strain, whereas P_{fs} considers the combined effect of stress and strain components. It can be seen that both P_{fs} and P_r increase on further cyclic deformation from cycles 10 to 20. However, the regions in which these FIPs develop in the respective microstructures do not change. This indicates that potential failure initiation may occur at these hotspots, which appear in the microstructure after deformation to only 10 cycles.

As discussed in Chapter 4, various grain-scale features, grain boundaries, twin boundaries, and phase interfaces lead to heterogeneous deformation. Higher FIP development is generally observed in the matrix compared to the primary γ'_p precipitates. Although favorably oriented grains in the vicinity of primary γ'_p precipitates and twin boundaries also show FIP localization due to higher deformation (see regions marked by black arrows in the phase map and white arrows in FIP contours). Further, higher FIP localization is generally observed near the twin boundaries (represented by white lines in the phase map). This is due to the sharp change in orientation of slip systems across the twin boundary.

Annealing twin boundaries play a crucial role in crack initiation in PM-processed Ni-based superalloys (Bozzolo et al., 2012; Jiang et al., 2015b). Typically, for smooth specimen
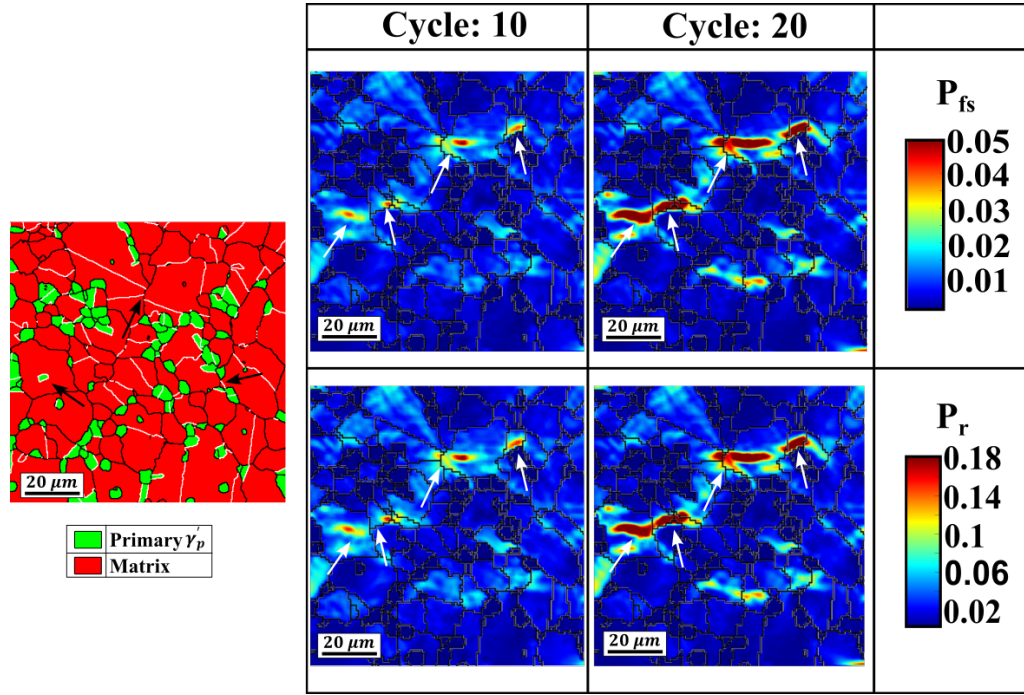
FIGURE 7.1: Evolution of Fatemi–Socie parameter, P_{fs}, and cumulative plastic shear strain, P_r, during the cyclic deformation for ROI-1. $\Sigma3$ Coincidence Site Lattice (CSL) twin boundaries are marked with white lines, and grain boundaries are marked with black lines.
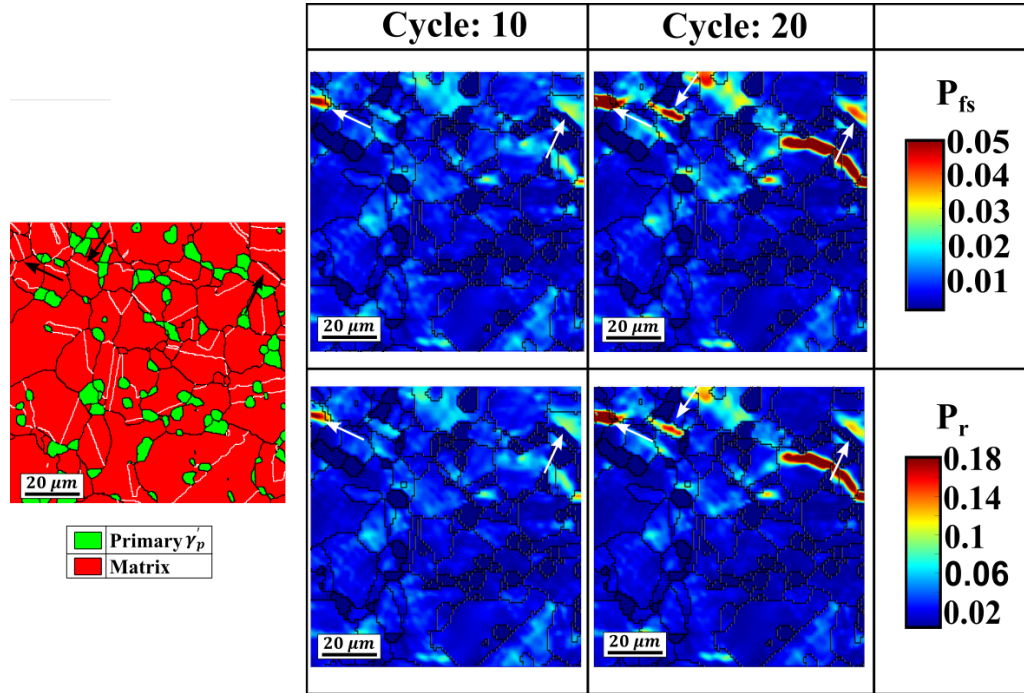
FIGURE 7.2: Evolution of Fatemi–Socie parameter, P_{fs}, and cumulative plastic shear strain, P_r, during the cyclic deformation for ROI-2. $\Sigma3$ Coincidence Site Lattice (CSL) twin boundaries are marked with white lines, and grain boundaries are marked with black lines.
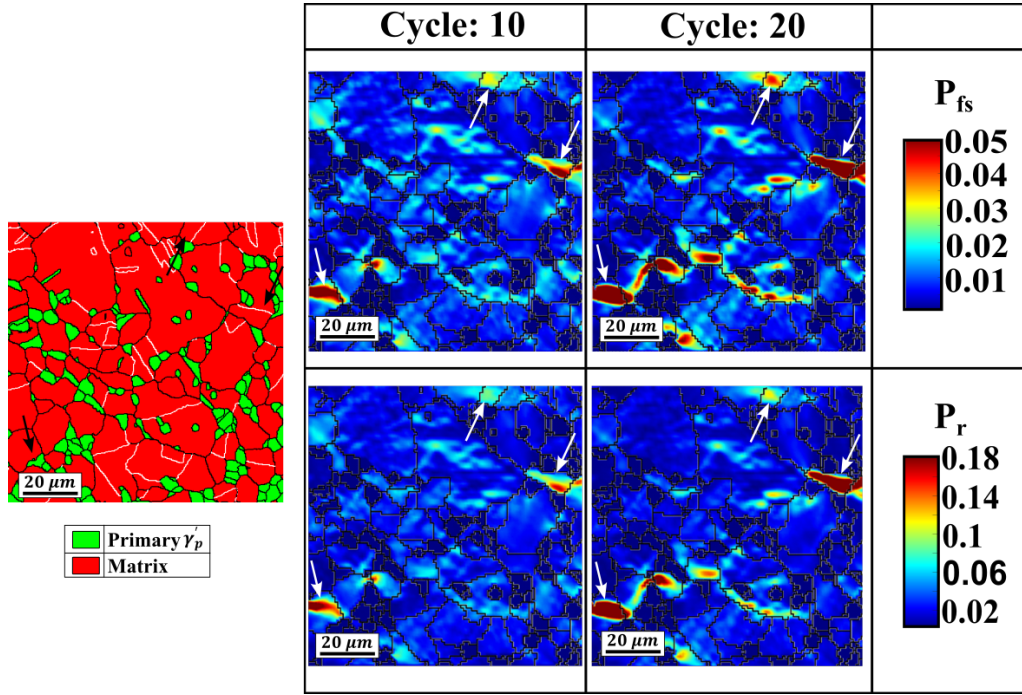
FIGURE 7.3: Evolution of Fatemi–Socie parameter, P_{fs}, and cumulative plastic shear strain, P_r, during the cyclic deformation for ROI-3. $\Sigma3$ Coincidence Site Lattice (CSL) twin boundaries are marked with white lines, and grain boundaries are marked with black lines.
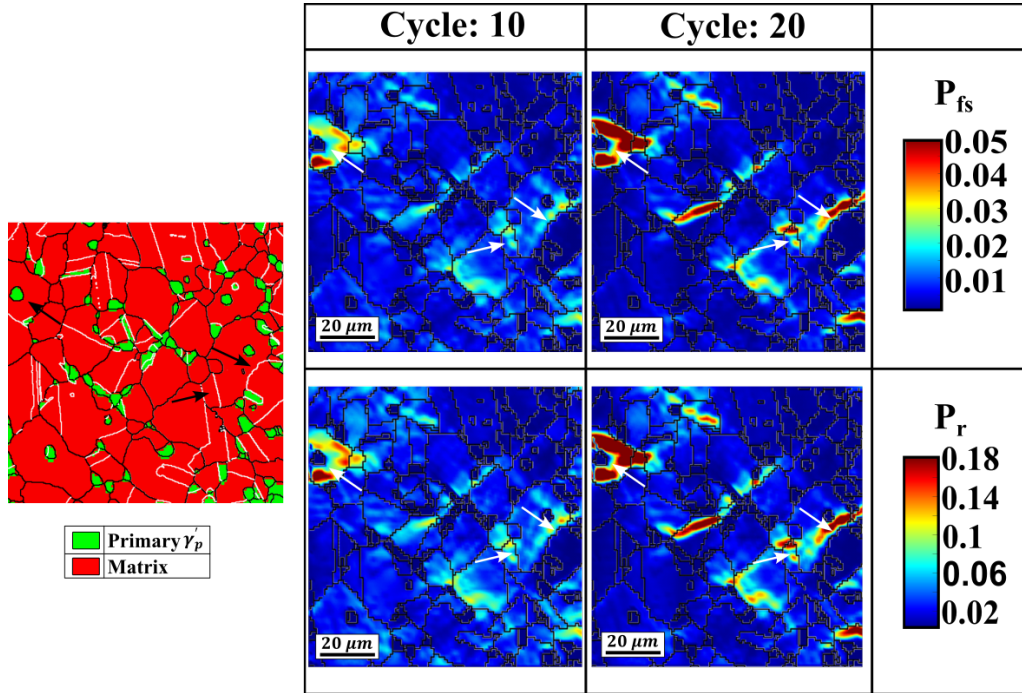
FIGURE 7.4: Evolution of Fatemi–Socie parameter, P_{fs}, and cumulative plastic shear strain, P_r, during the cyclic deformation for ROI-4. $\Sigma3$ Coincidence Site Lattice (CSL) twin boundaries are marked with white lines, and grain boundaries are marked with black lines.

fatigue, without the presence of inclusions or manufactured micro-notches, cracks are likely to form in favorably oriented grains near annealing twin boundaries (Miao et al., 2009, 2012; Jiang et al., 2017). The localization near twin boundaries marked with a white arrow is observed in all the microstructures in favorably oriented twin-parent grain pairs. The $\Sigma 3$ twin boundary, which is aligned with the {111} slip plane, along with the elastic anisotropy between the twin and parent grain pairs, contributes to stress and strain concentration, potentially leading to fatigue failure. Thus, the probability of the fatigue crack initiation in the vicinity of twin boundaries and primary γ_p' precipitates is higher and can contribute to the crack initiation or damage.

Data from all four microstructures have been collected to find the distribution of FIPs and misorientation at the different microstructure features. Figure 7.5 shows the distribution of Fatemi–Socie parameter, P_{fs}, cumulative plastic shear strain, P_r and kernel average misorientation (KAM) histograms at three critical microstructural features, i.e., grain boundaries, twin boundaries, and phase interfaces after the 10th and 20th loading cycles. The peak of the FIPs increases from cycle 10 to cycle 20, as well as cycle 20 also shows a slightly narrower FIP distribution with a longer tail at all three microstructure features. Initially, localization is more diffuse in cycle 10 according to the grain orientation, and during further deformation due to rotation of the grains, localization is more intense at cycle 20. This suggests a redistribution of deformation across the microstructure, where certain interfaces become more dominant crack initiation sites, while others become less dominant in contributing to damage accumulation. In addition, KAM represents local lattice rotation and can be used as an indicator of plastic deformation. A peak at low KAM values ($\sim 0.5°$)is observed, which indicates low plastic deformation during cyclic deformation. The distribution for cycle 20 shows a slightly broader tail towards higher KAM values compared to cycle 10, highlighting the progressive development of deformation localization. Further, a higher fraction of FIPs and KAMs is observed near twin boundaries compared to grain boundaries and phase interfaces, which indicates the role of twin boundaries in deformation localizations. This indicates twin boundaries have a higher propensity for failure compared to grain boundaries and phase interfaces for both Cycle 10 and 20.

The Pearson's correlation coefficient is calculated to explore the statistical correlation between P_{fs}, P_r, and KAM, if any. The PCC ($r(x,y)$) for two variables x and y is computed as (Adler and Parmryd, 2010):

$$r(x,y) = \frac{\sum_i (x_i - x_{av})(y_i - y_{av})}{\sqrt{\sum_i (x_i - x_{av})^2 \sum_i (y_i - y_{av})^2}} \tag{7.4}$$
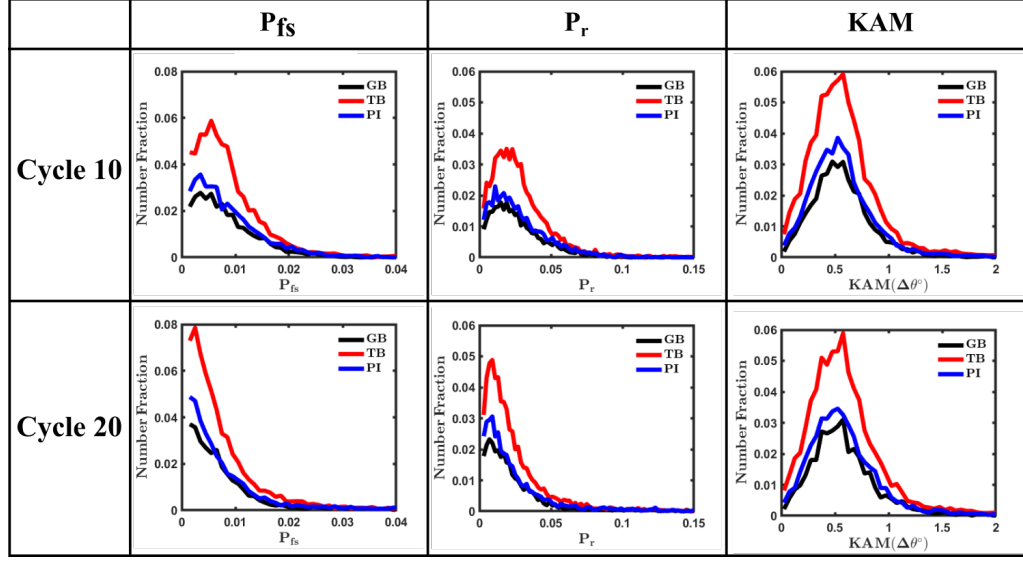
FIGURE 7.5: Distribution of Fatemi–Socie parameter, P_{fs}, cumulative plastic shear strain, P_r, and kernel average misorientation (KAM) at twin boundaries, grain boundaries, and phase interfaces after cycle 10 and cycle 20.

where i is summed over all the material points, x_{av} and y_{av} is mean of x and y data. For highly correlated variables, $r(x, y) \to 1$.

The correlation between P_{fs}, P_r, and KAM is plotted in Figure 7.6 for all material points and also separately at grain boundaries, twin boundaries, and phase interfaces. The correlation coefficient ($r > 0.99$) between P_r and P_{fs} indicates a linear positive correlation, which indicates that both FIPs predict a similar heterogeneous localization. This is observed for all material points, as well as the different microstructural features. Further, the correlation coefficient, $r = 0.3695$ between P_r and KAM, and $r = 0.3821$ between P_{fs} and KAM, indicates a moderate positive linear correlation. Similarly, moderate positive correlation is observed at all three microstructure features between P_r and KAM and P_{fs} and KAM. Here, the FIPs serve as a localized indicator for fatigue damage accumulation, typically influenced by cyclic plastic strain, whereas KAM is commonly used as a measure for local plastic deformation. The Figure 7.6 shows that the region of higher P_r and P_{fs} has higher KAM values as well. However, there are also material points where higher KAM values are observed in some regions, which have low P_r and P_{fs} values.

In Chapter 5, it has been shown that simulated KAM prediction shows a discrepancy in some regions compared to experimental KAM values. The over-estimation of KAM was largely attributed to the lack of strain gradient effects in the model and the consideration of only two layers of elements along the thickness direction. Similarly, considering the strain gradients effects in the model, the actual 3D grain structure and coarser mesh might predict
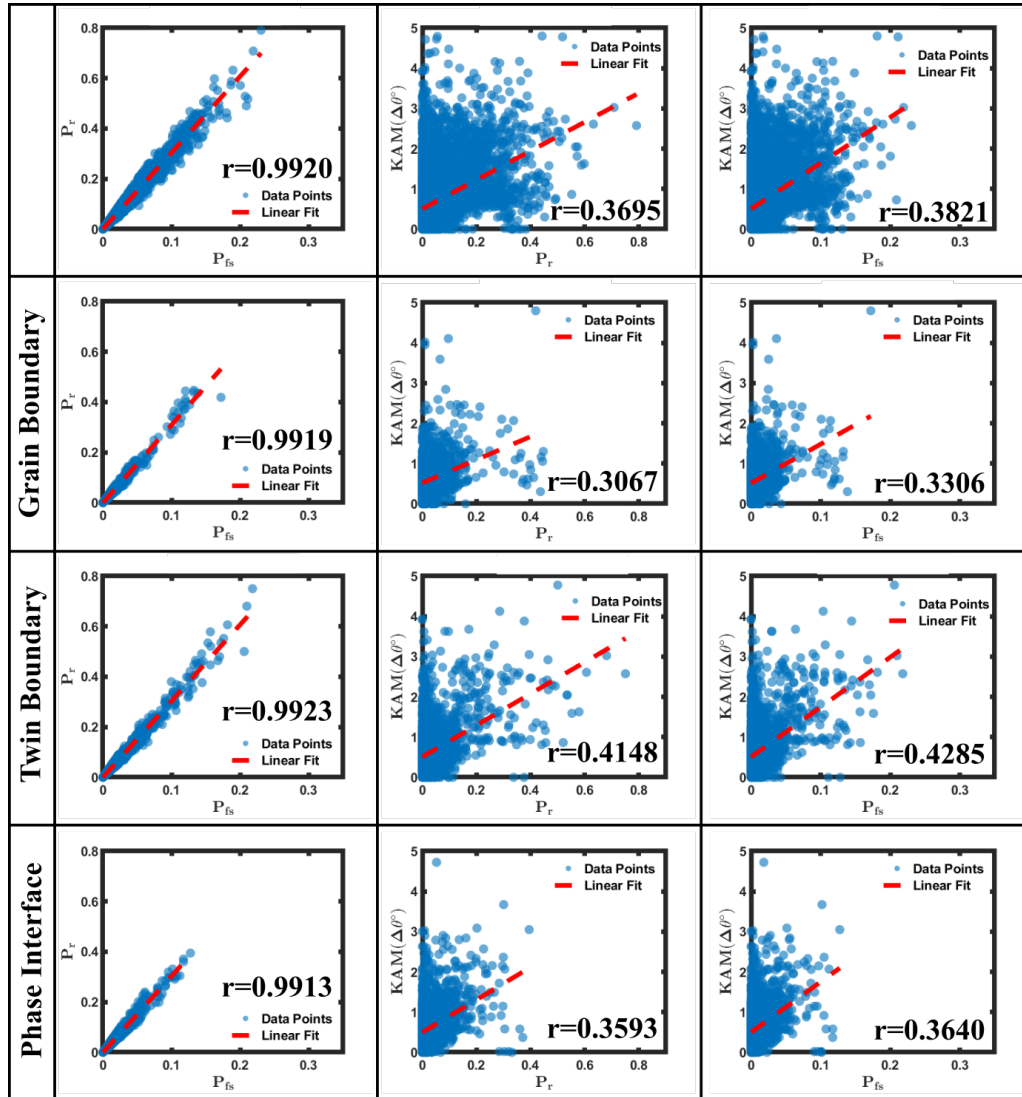
FIGURE 7.6: Statistical correlation between P_{fs}, P_r, and KAM at all the pixels, grain boundaries, twin boundaries, and phase interfaces. r is the value of Pearson's correlation coefficient.

a better correlation between the KAM and FIPs. Though this work highlights the higher localization of both KAM and FIPs along twin boundaries, and correlation coefficient is also higher at twin boundaries compared to grain boundaries and phase interfaces.

In this study, two FIPs, the Fatemi–Socie (FS) parameter and the cumulative plastic shear strain were evaluated for their effectiveness in predicting fatigue damage under cyclic loading conditions. The Fatemi–Socie parameter, which combines the shear strain amplitude with the maximum normal stress on the critical plane, is particularly effective in capturing the influence of both shear and tensile stresses on crack initiation. This makes it especially suitable for loading conditions where non-proportional multiaxial stresses are present. On

the other hand, the cumulative plastic shear strain based FIP provides a computationally efficient approach by summing the plastic shear strain over the fatigue life. This parameter is particularly useful for ductile materials, where fatigue damage is predominantly governed by shear deformation and cyclic plasticity. It is useful for large-scale simulations or when computational resources are limited. However, it may not fully capture the effects of normal stress, which can be critical in certain loading scenarios, leading to an underestimation of fatigue damage in some cases.

7.4   Conclusions

The present chapter focuses on the effect of the subgrain features, e.g., grain boundaries, twin boundaries, and phase interfaces, as potential sites for fatigue crack nucleation during cyclic deformation. Two FIPs were introduced into our crystal plasticity framework in order to predict possible sites of crack nucleation and were also correlated with predicted KAM data. Further, statistical analysis of FIPs and KAM at different microstructure features has been done to find the competitive roles of these features in fatigue deformation.

It can be concluded from these model predictions that:

- The two FIPs, namely the Fatemi–Socie parameter, P_{fs}, and cumulative plastic shear strain, P_r, showed that significant localizations develop in the vicinity of annealing twins, grain and phase boundaries.

- Statistical analysis reveals higher misorientation and FIPs near twin boundaries compared to grain boundaries and phase interfaces, which suggests that twin boundaries have a higher tendency for damage initiation and accumulation.

- The spatial location of the predicted FIP hotspots does not change from cycle 5 to cycle 10, and potential crack initiation may be expected to occur at these sites on loading to a higher number of cycles.

Chapter 8

Summary and Conclusions

8.1 Summary of the Thesis

This thesis focused on developing mesoscale constitutive modeling tools for predicting the processing-microstructure-mechanical property correlations in Ni-based superalloys. To achieve this, different chapters of the thesis have developed constitutive models for predicting such correlations in either single crystal or polycrystalline superalloys. The models for microstructure evolution and mechanical properties have been experimentally validated either with literature data or using experimental data generated for this thesis work. These physically-based modeling frameworks can serve as powerful tools for research in optimizing the microstructures of Ni-based superalloys, with improved mechanical properties and performance.

This thesis presents the following key advancements in terms of model development and implementation:

1. Coupled phase field-crystal plasticity framework for single crystal superalloys for predicting the microstructure evolution during heat treatment and resultant mechanical properties (see Chapter 3).

2. Development of physically-based crystal plasticity framework for single crystal superalloys, considering crystallographic dislocation climb around the precipitates, Orowan looping around precipitates, grain/phase size dependent hardening, substructure evolution in the form of mobile and immobile dislocation densities, backstress evolution, and constitutive equations for microstructure evolution due to rafting (see Chapter 4).

3. Development of crystal plasticity framework for polycrystalline superalloys, considering individual deformation of the matrix (comprised of secondary $\gamma_s^{'}$ and tertiary $\gamma_t^{'}$ precipitates homogenized in the γ phase) and primary $\gamma_p^{'}$ precipitates, dislocation strengthening, strengthening due secondary $\gamma_s^{'}$ and tertiary $\gamma_t^{'}$ precipitates, solute solution strengthening due to various alloying elements, and grain size strengthening (see Chapter 5).

4. Development of a micromechanical constitutive model for the shearing of $\gamma^{'}$ precipitates due to their interaction with mobile dislocations and the resultant mechanical properties during cyclic loading (see Chapter 6).

5. Implementation of fatigue indicator parameters in the crystal plasticity framework for studying cyclic deformation in two-phase microstructures of polycrystalline superalloys (see Chapter 7).

8.2 Conclusions

The key findings from the research conducted in the various chapters are summarized as follows:

Chapter 3: Coupled Phase Field Plasticity Model for Heat Treatment and Deformation of Single Crystal Ni-based Superalloys

Chapter 3 studied the microstructure evolution during aging and the effect of microstructure on the mechanical properties of single crystal Ni-based superalloys using a coupled phase field-crystal plasticity framework. This has been performed using a phase field model, coupled with a crystal plasticity framework, to simulate the microstructure evolution during heat treatment processes. Further, the phase-field generated microstructure is provided as input to crystal plasticity model to predict mechanical properties of CMSX-4. The following are the main conclusions:

- The $\gamma^{'}$ precipitate morphology changes from spherical (3D)/circular (2D) to cubodial (3D)/square (2D) during the initial stages of precipitate growth.

- The kinetics of precipitate growth are temperature-dependent, with significantly smaller precipitate sizes at lower temperatures as compared to aging at higher temperatures.

- The morphology of the precipitates does not change appreciably with or without consideration for plasticity in the model.

Chapter 4: Crystal Plasticity Constitutive Modeling of Tensile, Creep and Cyclic Deformation in Single Crystal Ni-based Superalloys

Chapter 4 focused on the development and implementation of a crystal plasticity framework to simulate the temperature- and orientation-dependent deformation of single crystal Ni-based superalloys. We have used the framework to simulate the cyclic and creep responses of single crystal Ni-based superalloys for various orientations and temperatures. Specifically, the constitutive model was used to predict the tensile, cyclic and creep deformation of two single crystal Ni-based superalloys, CMSX-4 and PWA-1484. The following are the main conclusions from the results presented in this chapter:

- The crystal plasticity framework successfully predicted the orientation- and temperature-dependent tensile, cyclic, and creep response for two different superalloys, CMSX-4 and PWA-1484.

- The model was validated by the prediction of creep-fatigue interactions in these alloys.

- The model also predicted the loading orientation-dependent microstructure evolution due to rafting, with no microstructure evolution observed during creep loading of the $[\bar{1}11]$ single crystal.

- Octahedral slip in the matrix phase was found to be dominant during [0 0 1] loading, while cube slip in the precipitate phase was found to be dominant during $[\bar{1}11]$ tensile loading of the single crystals.

Chapter 5: Modeling Heterogeneous Deformation of Polycrystalline Ni-based Superalloys

In Chapter 5, a physically based, microstructure-sensitive crystal plasticity constitutive framework has been developed for simulating the temperature-dependent tensile response of polycrystalline Ni-based superalloys. The model accounts for the individual deformation for γ and primary γ' phases and their effect on overall deformations. EBSD microstructures were used as inputs to the model, and the microstructure evolution during tensile deformation has been compared with experiments. The model has been used to study the

misorientation developments at various microstructural features of interest, such as grain boundaries, twin boundaries and phase interfaces. The following are the main conclusions:

- Stress localization was found to be generally comparable or higher in the $\gamma_p^{'}$ precipitates, and strain localization was higher in the matrix phase in the vicinity of the primary $\gamma_p^{'}$ precipitates.

- Strain localization was observed in the softer grain and stress localization in the harder grain between the twin/parent grain pairs.

- Higher misorientation development was found to occur near the twin boundaries as compared to the grain boundaries and phase interfaces, suggesting a higher tendency for localized or heterogeneous deformation in these regions.

Chapter 6: Modeling Cyclic Deformation and Softening of Polycrystalline Ni-based Superalloys

Chapter 6 focused on studying the precipitate shearing-induced cyclic softening in polycrystalline superalloys. . A dislocation density-based crystal plasticity model has been developed to simulate cyclic hardening followed by precipitate-induced cyclic softening for polycrystalline superalloys. Shearing of the secondary $\gamma^{'}$ precipitates during cyclic deformation is assumed to be the primary mechanism for the observed cyclic softening and a micromechanical constitutive model has been developed for the same. A slip system level backstress model is adopted to account for initial kinematic hardening behavior. The developed model has been used to simulate the cyclic deformation at two strain amplitudes at room temperature. The model predicts the cyclic stress-strain curve and a peak stress vs. number of cycles with reasonable accuracy for both strain amplitudes. The following are the main conclusions:

- Microstructure characterization using SEM and TEM analysis revealed shearing of secondary $\gamma_s^{'}$ precipitates.

- The slip system-level backstress model, along with a micromechanical model for precipitate shearing, was able to predict the initial cyclic hardening, followed by cyclic softening in two different superalloys, with different precipitate morphologies.

- The precipitate shearing model, along with the strengthening model, predicted the transition from strong pair coupling to weak pair coupling during the cyclic deformation-induced shearing of the precipitates.

Chapter 7: Predicting Fatigue Indicator Parameters of Polycrystalline Ni-based Superalloys

Chapter 7 focused on predicting the fatigue indicator parameters during cyclic deformation of the polycrystalline nickel superalloy specimens. As seen in Chapter 4, the annealing twins, grain and phase boundaries displayed the presence of large strain localizations, and were hence noted to be possible sources for crack initiation. Different fatigue indicator parameters (FIPs) were implemented within the crystal plasticity framework to predict the potential sites for micro-crack initiation and propagation for PM-processed Ni-based superalloys. Cyclic deformation simulations have been performed for four EBSD microstructures at 0.9% strain amplitudes at room temperature. FIP localization near the microstructure feature has been studied. The following are the main conclusions:

- FIP localizations were observed in the matrix phase in the vicinity of the annealing twin boundaries, grain boundaries, and phase interfaces.

- Higher misorientation and FIPs near the annealing twin boundaries could be indicative of a higher propensity for failure during cyclic deformation as compared to the phase interfaces and grain boundaries.

8.3 Future Work

The following are the recommendations for future work that could be pursued as extensions of the work performed in this thesis:

- The phase field model used in Chapter 3 can be extended for multi-component systems and coupled with CALPHAD databases to obtain temperature-dependent material parameters, thus allowing prediction of microstructure evolution during non-isothermal heat treatments.

- The crystal plasticity model in Chapter 4 can be further improved by consideration of mechanisms pertaining to rafting in alloys with positive misfit.

- Evolution of $\gamma^{'}$ precipitate volume fraction can also be considered by coupling with phase field models.

- Strain gradient plasticity can be considered in the model used in Chapter 5 for enhanced prediction of misorientation developments and heterogeneous deformation in polycrystalline alloys.

- The model used in Chapter 6 can be improved by considering the effects of lattice misfit, coherency stresses, and anti-phase boundary (APB) energy to understand their influence on the precipitate shearing and cyclic softening.

- The models developed in this thesis can be used in an Integrated Computational Materials Engineering (ICME) framework for computational design of superalloy microstructures with enhanced mechanical properties and performance.

8.4 Significant Contributions of the Thesis

8.4.1 Journal Publications

- Chaudhary S, Guruprasad PJ, Patra A, "Crystal plasticity constitutive modeling of tensile, creep and cyclic deformation in single crystal Ni-based superalloys", Mechanics of Materials, Vol. 174, 2022, 104474.

- Chaudhary S, Pai N, Rao GA, Alam Z, Sankarasubramanian R, Guruprasad PJ, Samajdar I, Patra A, "Competitive role of primary $\gamma^{'}$ precipitates and annealing twins on the heterogeneous deformation of a polycrystalline Ni-based superalloy: crystal plasticity modeling and experiments", Journal of Alloys and Compounds, Vol. 967, 2023, 171783.

- Chaudhary S, Sudhalkar B, Pai N, Palit M, Alam Z, Sankarasubramanian R, Samajdar I, Patra A, "A crystal plasticity-based micromechanical model for precipitate shearing: Application to cyclic softening of polycrystalline Ni-based superalloys", International Journal of Fatigue, Vol. 190, 2025, 108582.

- Chaudhary S, Patra A, "Integrated Phase Field - Crystal Plasticity Framework for Simulating Heat Treatment and Deformation of Single Crystal Ni-based Superalloys", Modelling and Simulation in Materials Science and Engineering, 2025, DOI: 10.1088/1361-651X/ae1e1c.

8.4.2 Conference Presentations

- Chaudhary, S.*, Guruprasad, P.J., Patra, A., "Crystal plasticity modeling of creep and fatigue deformation in Ni-based superalloy single crystals", 8th International Conference on Creep, Fatigue and Creep-Fatigue Interaction (CF-8), Virtual Conference, IGCAR, Kalpakkam, August 24-27, 2021.

- Chaudhary, S.*, Guruprasad, P.J., Patra, A., "Crystal plasticity constitutive modeling of thermo- mechanical deformation in Ni-based superalloy single crystals", 4th European Symposium on Superalloys and their Applications (EuroSuperalloys 2022), Bamberg, Germany, September 18-22, 2022.

- Chaudhary, S.*, Pai, N., Appa Rao, G., Alam, Z., Sankarasubramanian, R., Guruprasad, P.J., Samajdar, I., Patra, A., "Experimentally informed crystal plasticity model for predicting the deformation of a polycrystalline Ni-based superalloy", Indian Institute of Metals - Annual Technical Meeting (IIM-ATM) 2022, Hyderabad, November 14-16, 2022.

- Chaudhary, S.*, Pai, N., Sudhalkar, B., Alam, Z., Sankarasubramanian, R., Guruprasad, P.J., Samajdar, I., Patra, A., "Crystal plasticity model for cyclic softening of a polycrystalline Ni-based superalloy", 29th International Conference on Processing and Fabrication of Advanced Materials, Indian Institute of Technology Tirupati, September 6-8, 2023.

- Chaudhary, S.*, Sudhalkar, B., Pai, N., Guruprasad, P.J., Samajdar, I., Patra, A., "Crystal plasticity constitutive model for cyclic deformation and softening in polycrystalline Ni-based superalloys", 8th International Conference on Material Modelling, Loughborough University, London, UK, July 15-17, 2024.

References

Abdul-Latif, A., Ferney, V., Saanouni, K., 1999. Fatigue damage initiation in waspaloy under complex cyclic loading .

Aburakhia, A., Bonakdar, A., Molavi-Zarandi, M., Kelleher, J., Abdolvand, H., 2022. Deformation mechanisms of additively manufactured hastelloy-x: A neutron diffraction experiment and crystal plasticity finite element modeling. Materials & Design 222, 111030.

Abuzaid, W., Sehitoglu, H., Lambros, J., 2013. Plastic strain localization and fatigue micro-crack formation in hastelloy x. Materials Science and Engineering: A 561, 507–519.

Acharya, M., Fuchs, G., 2004. The effect of long-term thermal exposures on the microstructure and properties of cmsx-10 single crystal ni-base superalloys. Materials Science and Engineering: A 381, 143–153.

Adams, D., Irfan, S., Cramer, J., Miles, M.P., Homer, E.R., Brown, T., Mishra, R.K., Fullwood, D.T., 2020. Digital image correlation of forescatter detector images for simultaneous strain and orientation mapping. Microscopy and Microanalysis 26, 641–652.

Adler, J., Parmryd, I., 2010. Quantifying colocalization by correlation: the pearson correlation coefficient is superior to the mander's overlap coefficient. Cytometry Part A 77, 733–742.

Agaram, S., Kanjarla, A.K., Bhuvaraghan, B., Srinivasan, S.M., 2021. Dislocation density based crystal plasticity model incorporating the effect of precipitates in in718 under monotonic and cyclic deformation. International Journal of Plasticity 141, 102990.

Ahmad, U., Murr, L., 1976. Surface free energy of nickel and stainless steel at temperatures above the melting point. Journal of Materials Science 11, 224–230.

Ai, C., Xi, L., Wang, B., Sun, Y., Zhang, J., Su, H., Yang, W., Liu, L., Sun, Z., Chen, Y., 2020. Investigation on solution heat treatment response and $\gamma^{'}$ solvus temperature of a mo-rich second generation ni based single crystal superalloy. Intermetallics 125, 106896.

Akca, E., Gürsel, A., et al., 2015. A review on superalloys and in718 nickel-based inconel superalloy. Period. Eng. Nat. Sci 3, 15–27.

Ali, M.A., Amin, W., Shchyglo, O., Steinbach, I., 2020a. 45-degree rafting in ni-based superalloys: A combined phase-field and strain gradient crystal plasticity study. International Journal of Plasticity 128, 102659.

Ali, M.A., López-Galilea, I., Gao, S., Ruttert, B., Amin, W., Shchyglo, O., Hartmaier, A., Theisen, W., Steinbach, I., 2020b. Effect of $\gamma^{'}$ precipitate size on hardness and creep properties of ni-base single crystal superalloys: experiment and simulation. Materialia 12, 100692.

Ali, M.A., Shchyglo, O., Stricker, M., Steinbach, I., 2023. Coherency loss marking the onset of degradation in high temperature creep of superalloys: phase-field simulation coupled to strain gradient crystal plasticity. Computational Materials Science 220, 112069.

Allan, C.D., 1995. Plasticity of nickel base single crystal superalloys. Ph.D. thesis. Massachusetts Institute of Technology.

Amaro, R., Antolovich, S., Neu, R., 2012. Mechanism-based life model for out-of-phase thermomechanical fatigue in single crystal ni-base superalloys. Fatigue & Fracture of Engineering Materials & Structures 35, 658–671.

Ammar, K., Appolaire, B., Cailletaud, G., Forest, S., 2009. Combining phase field approach and homogenization methods for modelling phase transformation in elastoplastic media. European Journal of Computational Mechanics/Revue Européenne de Mécanique Numérique 18, 485–523.

Ammar, K., Appolaire, B., Cailletaud, G., Forest, S., 2011. Phase field modeling of elasto-plastic deformation induced by diffusion controlled growth of a misfitting spherical precipitate. Philosophical magazine letters 91, 164–172.

Antolovich, B.F., 1996. Fatigue and fracture of nickel-base superalloys. ASM International, Member/Customer Service Center, Materials Park, OH 44073-0002, USA, 1996. , 854–868.

Antolovich, S.D., 2015. Microstructural aspects of fatigue in ni-base superalloys. Philosophical Transactions of the Royal Society A: Mathematical, Physical and Engineering Sciences 373, 20140128.

Antolovich, S.D., Jayaraman, N., 1983. The effect of microstructure on the fatigue behavior of ni base superalloys, in: Fatigue: environment and temperature effects. Springer, pp. 119–144.

Antolovich, S.D., Rosa, E., Pineau, A., 1981. Low cycle fatigue of rené 77 at elevated temperatures. Materials Science and Engineering 47, 47–57.

Ardell, A., 1968. An application of the theory of particle coarsening: The $\gamma^{'}$ precipitate in ni-al alloys. Acta Metallurgica 16, 511–516.

Ardell, A.J., 2021. Temperature dependence of the $c/c^{'}$ interfacial energy in binary ni–al alloys .

Arsenlis, A., Parks, D.M., 2002. Modeling the evolution of crystallographic dislocation density in crystal plasticity. Journal of the Mechanics and Physics of Solids 50, 1979–2009.

Asaro, R.J., 1983. Micromechanics of crystals and polycrystals. Advances in applied mechanics 23, 1–115.

Asaro, R.J., Rice, J., 1977. Strain localization in ductile single crystals. Journal of the Mechanics and Physics of Solids 25, 309–338.

Asim, U.B., Zhan, Z., Radovic, M., Srivastava, A., 2022. Modeling the non-schmid crystallographic slip in max phases. International Journal of Plasticity , 103399.

Atabay, S.E., Sanchez-Mata, O., Muñiz-Lerma, J.A., Brochu, M., 2021. Effect of heat treatment on the microstructure and elevated temperature tensile properties of rene 41 alloy produced by laser powder bed fusion. Journal of Alloys and Compounds 858, 157645.

Attallah, M.M., Jennings, R., Wang, X., Carter, L.N., 2016. Additive manufacturing of ni-based superalloys: The outstanding issues. MRS bulletin 41, 758–764.

Austin, R.A., McDowell, D.L., 2011. A dislocation-based constitutive model for viscoplastic deformation of fcc metals at very high strain rates. International Journal of Plasticity 27, 1–24.

Babamiri, B.B., Mayeur, J.R., Hazeli, K., 2022. Synchronous involvement of topology and microstructure to design additively manufactured lattice structures. Additive Manufacturing 52, 102618.

Baldan, A., 2002. Review progress in ostwald ripening theories and their applications to nickel-base superalloys part i: Ostwald ripening theories. Journal of materials science 37, 2171–2202.

Balikci, E., Raman, A., Mirshams, R., 1997. Influence of various heat treatments on the microstructure of polycrystalline in738lc. Metallurgical and Materials Transactions A 28, 1993–2003.

Bandyopadhyay, R., Mello, A.W., Kapoor, K., Reinhold, M.P., Broderick, T.F., Sangid, M.D., 2019. On the crack initiation and heterogeneous deformation of ti-6al-4v during high cycle fatigue at high r ratios. Journal of the Mechanics and Physics of Solids 129, 61–82.

Bandyopadhyay, R., Sangid, M.D., 2019. Crystal plasticity assessment of inclusion-and matrix-driven competing failure modes in a nickel-base superalloy. Acta Materialia 177, 20–34.

Bandyopadhyay, R., Sangid, M.D., 2021. A probabilistic fatigue framework to enable location-specific lifing for critical thermo-mechanical engineering applications. Integrating Materials and Manufacturing Innovation 10, 20–43.

Barat, K., Ghosh, A., Doharey, A., Mukherjee, S., Karmakar, A., 2022. Crystallographic evaluation of low cycle fatigue crack growth in a polycrystalline Ni-based superalloy. International Journal of Plasticity 149, 103174.

Barba, D., Alabort, E., Garcia-Gonzalez, D., Moverare, J., Reed, R., Jérusalem, A., 2018. A thermodynamically consistent constitutive model for diffusion-assisted plasticity in ni-based superalloys. International Journal of Plasticity 105, 74–98.

Bartošák, M., Nagode, M., Klemenc, J., Doubrava, K., Šeruga, D., 2022. Use of Prandtl operators in simulating the cyclic softening of Inconel 718 under isothermal low-cycle fatigue loading. International Journal of Mechanical Sciences 222, 107182.

Basoalto, H., Sondhi, S., Dyson, B., McLean, M., 2004. A generic microstructure-explicit model of creep in nickel-base superalloys. Superalloys 1, 897–906.

Basu, S., Jaya, B.N., Seekala, H., Phani, P.S., Patra, A., Ganguly, S., Dutta, M., Samajdar, I., 2023. Correlative characterization and plasticity modeling of microscopic strain localizations in a dual phase steel. Materials Characterization 197, 112704.

Bennett, V., McDowell, D., 2003. Polycrystal orientation distribution effects on microslip in high cycle fatigue. International Journal of Fatigue 25, 27–39.

Bergsmo, A., Xu, Y., Poole, B., Dunne, F.P., 2022. Twin boundary fatigue crack nucleation in a polycrystalline nickel superalloy containing non-metallic inclusions. Journal of the Mechanics and Physics of Solids 160, 104785.

Betteridge, W., Heslop, J., et al., 1974. The nimonic alloys and other nickel-base high-temperature alloys .

Bhaskar, M., Abinandanan, T., 2018. Effect of different solute diffusivities on precipitate coarsening in ternary alloys. Computational Materials Science 146, 73–83.

Bhattacharyya, S., Abinandanan, T., 2009. Evolution of multivariant microstructures with anisotropic misfit: A phase field study. Acta Materialia 57, 646–656.

Bhowal, P., Wright, E., Raymond, E., 1990. Effects of cooling rate and γ' morphology on creep and stress-rupture properties of a powder metallurgy superalloy. Metallurgical Transactions A 21, 1709–1717.

Bhure, S., Nalajala, D., Choudhury, A., 2025. Single-crystalline ni-based superalloy builds using laser-directed energy deposition (l-ded): A multi-scale modeling and experimental approach. Acta Materialia 286, 120703.

Boittion, G., Gallerneau, F., Locq, D., Kanoute, P., Cailletaud, G., 2010. Numerical modelling of the microstructure effect on fatigue behaviour of ni-base superalloys for turbine disk. Technische Mechanik-European Journal of Engineering Mechanics 30, 15–28.

Bozzolo, N., Souaï, N., Logé, R.E., 2012. Evolution of microstructure and twin density during thermomechanical processing in a γ-γ'nickel-based superalloy. Acta materialia 60, 5056–5066.

Brandon, D., 1966. The structure of high-angle grain boundaries. Acta metallurgica 14, 1479–1484.

Brehm, H., Glatzel, U., 1999. Material model describing the orientation dependent creep behavior of single crystals based on dislocation densities of slip systems. International journal of plasticity 15, 285–298.

Brenne, F., Taube, A., Pröbstle, M., Neumeier, S., Schwarze, D., Schaper, M., Niendorf, T., 2016. Microstructural design of ni-base alloys for high-temperature applications: impact of heat treatment on microstructure and mechanical properties after selective laser melting. Progress in Additive Manufacturing 1, 141–151.

Brommesson, R., Ekh, M., Persson, C., 2016. Experimental observations and modelling of cyclic and relaxation behaviour of the Ni-based superalloy Haynes 282. International Journal of Fatigue 87, 180–191.

Cahn, J.W., 1962. The impurity-drag effect in grain boundary motion. Acta metallurgica 10, 789–798.

Cao, D., Ta, N., Zhang, L., 2017. Unit-cell design for two-dimensional phase-field simulation of microstructure evolution in single-crystal ni-based superalloys during solidification. Progress in Natural Science: Materials International 27, 678–686.

Cao, W., Yang, J., Zhang, H., 2021. Unified constitutive modeling of Haynes 230 including cyclic hardening/softening and dynamic strain aging under isothermal low-cycle fatigue and fatigue-creep loads. International Journal of Plasticity 138, 102922.

Caron, P., Khan, T., 1983. Improvement of creep strength in a nickel-base single-crystal superalloy by heat treatment. Materials Science and Engineering 61, 173–184.

Caron, P., Ohta, Y., Nakagawa, Y., Khan, T., 1988. Creep deformation anisotropy in single crystal superalloys, in: Superalloys 1988 (Sixth International Symposium), TMS. pp. 215–224.

Castelluccio, G.M., McDowell, D.L., 2014. Mesoscale modeling of microstructurally small fatigue cracks in metallic polycrystals. Materials Science and Engineering: A 598, 34–55.

Castelluccio, G.M., McDowell, D.L., 2016. Microstructure-sensitive small fatigue crack growth assessment: Effect of strain ratio, multiaxial strain state, and geometric discontinuities. International Journal of Fatigue 82, 521–529.

Castelluccio, G.M., Musinski, W.D., McDowell, D.L., 2014. Recent developments in assessing microstructure-sensitive early stage fatigue of polycrystals. Current Opinion in Solid State and Materials Science 18, 180–187.

Cerrone, A., Spear, A., Tucker, J., Stein, C., Rollett, A., Ingraffea, A., 2013. Modeling crack nucleation at coherent twin boundaries in nickel—modeling crack nucleation at coherent twin boundaries in nickel-based superalloys. Mater Sci Technol (MS&T) 1649.

Cervellon, A., Cormier, J., Mauget, F., Hervier, Z., 2017. Vhcf life evolution after microstructure degradation of a ni-based single crystal superalloy. International Journal of Fatigue 104, 251–262.

Chaboche, J.L., Gaubert, A., Kanoute, P., Longuet, A., Azzouz, F., Mazière, M., 2013. Viscoplastic constitutive equations of combustion chamber materials including cyclic hardening and dynamic strain aging. International journal of plasticity 46, 1–22.

Chafle, R., Mukherjee, R., 2020. Anomalous coarsening behaviour in ni-al alloys: insights from phase-field simulations. Materials Letters 279, 128444.

Chan, K.S., 2021. Mechanistic modeling of cyclic softening and slip localization in ni-based superalloys. Metallurgical and Materials Transactions A 52, 1759–1776.

Chan, K.S., 2023. Mechanistic modeling of cyclic softening in Ni-based superalloys at elevated temperatures. Metallurgical and Materials Transactions A 54, 106–120.

Chandra, S., Samal, M., Kapoor, R., Kumar, N.N., Chavan, V., Raghunathan, S., 2018. Deformation behavior of nickel-based superalloy su-263: Experimental characterization and crystal plasticity finite element modeling. Materials Science and Engineering: A 735, 19–30.

Chandran, M., Sondhi, S., 2011. First-principle calculation of APB energy in Ni-based binary and ternary alloys. Modelling and Simulation in Materials Science and Engineering 19, 025008.

Chang, J.C., Allen, S.M., 1991. Elstic energy changes accompanying gamma-prime rafting in nickel-base superalloys. Journal of materials research 6, 1843–1855.

Charpagne, M., Hestroffer, J., Polonsky, A., Echlin, M., Texier, D., Valle, V., Beyerlein, I., Pollock, T., Stinville, J., 2021. Slip localization in inconel 718: a three-dimensional and statistical perspective. Acta Materialia 215, 117037.

Charpagne, M., Stinville, J., Callahan, P., Texier, D., Chen, Z., Villechaise, P., Valle, V., Pollock, T., 2020. Automated and quantitative analysis of plastic strain localization via multi-modal data recombination. Materials Characterization 163, 110245.

Charpagne, M.A., Billot, T., Franchet, J.M., Bozzolo, N., 2016. Heteroepitaxial recrystallization: A new mechanism discovered in a polycrystalline γ-$\gamma^{'}$ nickel based superalloy. Journal of Alloys and Compounds 688, 685–694.

Chaudhary, S., Guruprasad, P., Patra, A., 2022. Crystal plasticity constitutive modeling of tensile, creep and cyclic deformation in single crystal ni-based superalloys. Mechanics of Materials 174, 104474.

Chaudhary, S., Pai, N., Rao, G.A., Alam, Z., Sankarasubramanian, R., Guruprasad, P., Samajdar, I., Patra, A., 2023. Competitive role of primary $\gamma^{'}$ precipitates and annealing twins on the heterogeneous deformation of a polycrystalline ni-based superalloy: Crystal plasticity modeling and experiments. Journal of Alloys and Compounds , 171783.

Chaudhary, S., Patra, A., 2025. Integrated phase field-crystal plasticity framework for simulating heat treatment and deformation of single crystal ni-based superalloys. Modelling and Simulation in Materials Science and Engineering .

Chaudhary, S., Sudhalkar, B., Pai, N., Palit, M., Alam, Z., Sankarasubramanian, R., Samajdar, I., Patra, A., 2025. A crystal plasticity-based micromechanical model for precipitate shearing: Application to cyclic softening of polycrystalline ni-based superalloys. International Journal of Fatigue 190, 108582.

Chen, B., Jiang, J., Dunne, F.P., 2018. Is stored energy density the primary meso-scale mechanistic driver for fatigue crack nucleation? International Journal of Plasticity 101, 213–229.

Chen, Q., Ma, N., Wu, K., Wang, Y., 2004. Quantitative phase field modeling of diffusion-controlled precipitate growth and dissolution in ti–al–v. Scripta Materialia 50, 471–476.

Chen, S., He, Z., Xiao, J., Gai, S., Wang, Z., Li, J., 2023. Modified heat treatment and related microstructure-mechanical property evolution of arc melting additively manufactured gh4169 ni-based superalloy. Journal of Alloys and Compounds 947, 169449.

Chen, W., Voisin, T., Zhang, Y., Forien, J.B., Spadaccini, C.M., McDowell, D.L., Zhu, T., Wang, Y.M., 2019. Microscale residual stresses in additively manufactured stainless steel. Nature communications 10, 4338.

Cheng, K., Jo, C., Kim, D., Jin, T., Hu, Z., 2009. Influence of local chemical segregation on the $\gamma^{'}$ directional coarsening behavior in single crystal superalloy cmsx-4. Materials Characterization 60, 210–218.

Cheng, L.Y., Wang, R.Z., Wang, J., Zhu, S.P., Zhao, P.C., Miura, H., Zhang, X.C., Tu, S.T., 2021. Cycle-dependent creep-fatigue deformation and life predictions in a nickel-based superalloy at elevated temperature. International Journal of Mechanical Sciences 206, 106628.

Clement, N., Couret, A., Caillard, D., 1991. An in situ study of cube glide in the $\gamma^{'}$-phase of a superalloy: I. the controlling mechanism. Philosophical Magazine A 64, 669–695.

Collins, D., Stone, H., 2014. A modelling approach to yield strength optimisation in a nickel-base superalloy. International Journal of Plasticity 54, 96–112.

Cormier, J., Cailletaud, G., 2010. Constitutive modeling of the creep behavior of single crystal superalloys under non-isothermal conditions inducing phase transformations. Materials Science and Engineering: A 527, 6300–6312.

Cornet, C., Zhao, L., Tong, J., 2011. A study of cyclic behaviour of a nickel-based superalloy at elevated temperature using a viscoplastic-damage model. International Journal of Fatigue 33, 241–249.

Cottura, M., Appolaire, B., Finel, A., Le Bouar, Y., 2016. Coupling the phase field method for diffusive transformations with dislocation density-based crystal plasticity: Application to ni-based superalloys. Journal of the Mechanics and Physics of Solids 94, 473–489.

Cottura, M., Le Bouar, Y., Finel, A., Appolaire, B., Ammar, K., Forest, S., 2012. A phase field model incorporating strain gradient viscoplasticity: application to rafting in ni-base superalloys. Journal of the Mechanics and Physics of Solids 60, 1243–1256.

Cruzado, A., Gan, B., Jiménez, M., Barba, D., Ostolaza, K., Linaza, A., Molina-Aldareguia, J., Llorca, J., Segurado, J., 2015. Multiscale modeling of the mechanical behavior of in718 superalloy based on micropillar compression and computational homogenization. Acta Materialia 98, 242–253.

Cruzado, A., LLorca, J., Segurado, J., 2017. Modeling cyclic deformation of inconel 718 superalloy by means of crystal plasticity and computational homogenization. International Journal of Solids and Structures 122, 148–161.

Cruzado, A., Lucarini, S., LLorca, J., Segurado, J., 2018. Crystal plasticity simulation of the effect of grain size on the fatigue behavior of polycrystalline inconel 718. International Journal of Fatigue 113, 236–245.

Cui, C., Gu, Y., Ping, D., Harada, H., 2009. Microstructural evolution and mechanical properties of a ni-based superalloy, tmw-4. Metallurgical and Materials Transactions A 40, 282–291.

Cui, L., Liu, J., Peng, R.L., Yu, J., Moverare, J., Sun, X., 2020. Low cycle fatigue behavior and microstructural evolution of nickel-based superalloy M951G at elevated temperatures. Materials Characterization 163, 110241.

Cuitino, A., Ortiz, M., 1993. Constitutive modeling of l12 intermetallic crystals. Materials Science and Engineering: A 170, 111–123.

Cullity, B.D., 1956. Elements of X-ray Diffraction. Addison-Wesley Publishing.

Dan, W., Lixi, T., Chaoli, M., 2015. Effect of aging time at high temperature on microstructural evolution behavior of a nickel-based single crystal superalloy. Rare Metal Materials and Engineering 44, 1345–1350.

Deng, W., Zhang, D., Wu, H., Huang, Z., Zhou, K., Jiang, L., 2020. Prediction of yield strength in a polycrystalline nickel base superalloy during interrupt cooling. Scripta Materialia 183, 139–143.

Deshpande, A., Deb Nath, S., Atre, S., Hsu, K., 2020. Effect of post processing heat treatment routes on microstructure and mechanical property evolution of haynes 282 ni-based superalloy fabricated with selective laser melting (slm). Metals 10, 629.

Desmorat, R., Mattiello, A., Cormier, J., 2017. A tensorial thermodynamic framework to account for the γ'rafting in nickel-based single crystal superalloys. International Journal of Plasticity 95, 43–81.

Dieter, G., 1988. Mechanical metallurgy (2001). SI Metric Edition .

Differt, K., Essmann, U., Mughrabi, H., 1987. Models of particle destruction in fatigued precipitation-hardened alloys. physica status solidi (a) 104, 95–106.

Ding, Q., Bei, H., Yao, X., Zhao, X., Wei, X., Wang, J., Zhang, Z., 2021. Temperature effects on deformation substructures and mechanisms of a ni-based single crystal superalloy. Applied Materials Today 23, 101061.

Dodaran, M., Ettefagh, A.H., Guo, S., Khonsari, M., Meng, W., Shamsaei, N., Shao, S., 2020. Effect of alloying elements on the $\gamma^{'}$ antiphase boundary energy in Ni-base superalloys. Intermetallics 117, 106670.

Du, B., Sheng, L., Hu, Z., Cui, C., Yang, J., Sun, X., 2018. Investigation on the microstructure and tensile behavior of a ni-based in792 superalloy. Advances in Mechanical Engineering 10, 1687814017752167.

Du, Y., Yang, Y., Diao, A., Li, Y., Wang, X., Zhou, Y., Li, J., Sun, X., 2021. Effect of solution heat treatment on creep properties of a nickel-based single crystal superalloy. Journal of Materials Research and Technology 15, 4702–4713.

Dunne, F., Wilkinson, A., Allen, R., 2007. Experimental and computational studies of low cycle fatigue crack nucleation in a polycrystal. International Journal of Plasticity 23, 273–295.

Dyson, B., 2009. Microstructure based creep constitutive model for precipitation strengthened alloys: theory and application. Materials Science and Technology 25, 213–220.

Edington, J.W., Edington, J., 1975. Electron diffraction in the electron microscope. Springer.

Eggeler, Y., Vamsi, K., Pollock, T., 2021. Precipitate shearing, fault energies, and solute segregation to planar faults in Ni-, CoNi-, and Co-base superalloys. Annual Review of Materials Research 51, 209–240.

Eghtesad, A., Knezevic, M., 2021. A full-field crystal plasticity model including the effects of precipitates: Application to monotonic, load reversal, and low-cycle fatigue behavior of inconel 718. Materials Science and Engineering: A 803, 140478.

Emokpaire, S.O., Wang, N., Liu, J., Zhu, C., Wang, X., Li, J., Zhou, Y., 2023. Effect of ru on deformation mechanism and microstructure evolution of single-crystal superalloys under medium-temperature and high-stress creep. Materials 16, 2732.

Epishin, A., Link, T., Klingelhöffer, H., Fedelich, B., Brückner, U., Portella, P.D., 2009. New technique for characterization of microstructural degradation under creep: Application to the nickel-base superalloy cmsx-4. Materials Science and Engineering: A 510, 262–265.

Epishin, A., Link, T., Portella, P.D., Brückner, U., 2000. Evolution of the γ/γ' microstructure during high-temperature creep of a nickel-base superalloy. Acta materialia 48, 4169–4177.

Essmann, U., Mughrabi, H., 1979. Annihilation of dislocations during tensile and cyclic deformation and limits of dislocation densities. Philosophical Magazine A 40, 731–756.

Everitt, S., Starink, M., Pang, H., Wilcock, I., Henderson, M., Reed, P., 2007. A comparison of high temperature fatigue crack propagation in various subsolvus heat treated turbine disc alloys. Materials Science and Technology 23, 1419–1423.

Evers, L., Brekelmans, W., Geers, M., 2004. Scale dependent crystal plasticity framework with dislocation density and grain boundary effects. International Journal of Solids and Structures 41, 5209–5230.

Fan, Y., Tan, L., Yang, X., Huang, W., Shi, D., 2024. Monotonic tensile and cyclic deformation of a ni-based single crystal superalloy with anisotropic microstructural rafting patterns at high temperature: Experiment and constitutive modelling. International Journal of Plasticity 179, 104031.

Fan, Y.N., Shi, H.J., Qiu, W.H., 2015. Constitutive modeling of creep behavior in single crystal superalloys: Effects of rafting at high temperatures. Materials Science and Engineering: A 644, 225–233.

Fatemi, A., Socie, D.F., 1988. A critical plane approach to multiaxial fatigue damage including out-of-phase loading. Fatigue & Fracture of Engineering materials & structures 11, 149–165.

Fedelich, B., Epishin, A., Link, T., Klingelhöffer, H., Künecke, G., Portella, P.D., 2012. Rafting during high temperature deformation in a single crystal superalloy: experiments and modeling. Superalloys 2012 6, 491.

Fedelich, B., Künecke, G., Epishin, A., Link, T., Portella, P., 2009. Constitutive modelling of creep degradation due to rafting in single-crystalline ni-base superalloys. Materials Science and Engineering: A 510, 273–277.

Feng, Z., Wen, Z., Li, M., Zhao, Y., Yue, Z., 2021. Effect of aging heat treatment on microstructure of ni-based single crystal superalloys. AIP Advances 11.

Fernandez-Zelaia, P., Lee, Y., Dryepondt, S., Kirka, M.M., 2022. Creep anisotropy modeling and uncertainty quantification of an additively manufactured ni-based superalloy. International Journal of Plasticity , 103177.

Fischer, T., Werner, E., Munz, O., et al., 2019. Crystal plasticity modeling of polycrystalline ni-base superalloy honeycombs under combined thermo-mechanical loading. Continuum Mechanics and Thermodynamics 31, 703–713.

Flageolet, B., Jouiad, M., Villechaise, P., Mendez, J., 2005. On the role of γ particles within γ' precipitates on damage accumulation in the p/m nickel-base superalloy n18. Materials Science and Engineering: A 399, 199–205.

Flageolet, B., Villechaise, P., Jouiad, M., Mendez, J., 2004. Ageing characterization of the powder metallurgy superalloy n18. Superalloys 2004 , 371–379.

Fleck, M., Schleifer, F., Holzinger, M., Glatzel, U., 2018. Phase-field modeling of precipitation growth and ripening during industrial heat treatments in ni-base superalloys. Metallurgical and Materials Transactions A 49, 4146–4157.

Flinn, P.A., 1960. Theory of deformation in superlattices. Transactions of the American Institute of Mining and Metallurgical Engineers 218, 145–154.

Fuchs, G., 2002. Improvement of creep strength of a third generation, single-crystal ni-base superalloy by solution heat treatment. Journal of materials engineering and performance 11, 19–25.

Fullwood, D., 2020. Openxy. `https://github.com/BYU-MicrostructureOfMaterials/OpenXY`.

Fullwood, D., Vaudin, M., Daniels, C., Ruggles, T., Wright, S.I., 2015. Validation of kinematically simulated pattern hr-ebsd for measuring absolute strains and lattice tetragonality. Materials Characterization 107, 270–277.

Furrer, D., Fecht, H., 1999. Ni-based superalloys for turbine discs. Jom 51, 14–17.

Furrer, D., Shankar, R., White, C., 2003. Optimizing the heat treatment of ni-based superalloy turbine discs. Jom 55, 32–34.

Gabb, T., Kantzos, P., Telesman, J., Gayda, J., Sudbrack, C., Palsa, B., 2011. Fatigue resistance of the grain size transition zone in a dual microstructure superalloy disk. International Journal of Fatigue 33, 414–426.

Gabb, T.P., Gayda, J., Telesman, J., Kantzos, P.T., 2005. Thermal and mechanical property characterization of the advanced disk alloy LSHR. Technical Report.

Gai, Y., Zhang, R., Yang, J., Cui, C., Qu, J., 2022. Effects of heat treatment on γ' precipitates and tensile properties of a ni-base superalloy. Materials Science and Engineering: A 842, 143079.

Galpin, S.J., 2022. A review of microstructure phenomena during manufacture of polycrystalline ni-based superalloys. Materials Science and Technology 38, 1315–1331.

Gao, J., Li, H., Zhang, X., Shao, G., Xiang, Z., Sun, X., 2025. Decoupling the nonthermal effect of current by electrically assisted crystal plasticity modeling of ni-based single crystal superalloys. Journal of Materials Science & Technology 204, 91–103.

Gao, S., Ali, M.A., Hartmaier, A., 2019. Influence of rafted microstructures on creep in ni-base single crystal superalloys: a 3d discrete dislocation dynamics study. Modelling and Simulation in Materials Science and Engineering 28, 025001.

Gaston, D., Newman, C., Hansen, G., Lebrun-Grandie, D., 2009. Moose: A parallel computational framework for coupled systems of nonlinear equations. Nuclear Engineering and Design 239, 1768–1778.

Gaubert, A., Finel, A., Le Bouar, Y., Boussinot, G., 2008. Viscoplastic phase field modellling of rafting in ni base superalloys. Collection Sciences de la matière , 161–166.

Gaubert, A., Jouiad, M., Cormier, J., Le Bouar, Y., Ghighi, J., 2015. Three-dimensional imaging and phase-field simulations of the microstructure evolution during creep tests of< 011>-oriented ni-based superalloys. Acta Materialia 84, 237–255.

Gaubert, A., Le Bouar, Y., Finel, A., 2010. Coupling phase field and viscoplasticity to study rafting in ni-based superalloys. Philosophical Magazine 90, 375–404.

Geddes, B., Leon, H., Huang, X., 2010. Superalloys: alloying and performance. Asm International.

Geers, M., Cottura, M., Appolaire, B., Busso, E.P., Forest, S., Villani, A., 2014. Coupled glide-climb diffusion-enhanced crystal plasticity. Journal of the Mechanics and Physics of Solids 70, 136–153.

Gell, M., Duhl, D., 1986. The development of single crystal superalloy turbine blades. Advanced high-temperature alloys: Processing and properties , 41–49.

Ghassemi-Armaki, H., Chen, P., Bhat, S., Sadagopan, S., Kumar, S., Bower, A., 2013. Microscale-calibrated modeling of the deformation response of low-carbon martensite. Acta Materialia 61, 3640–3652.

Ghorbanpour, S., Alam, M.E., Ferreri, N.C., Kumar, A., McWilliams, B.A., Vogel, S.C., Bicknell, J., Beyerlein, I.J., Knezevic, M., 2020. Experimental characterization and crystal plasticity modeling of anisotropy, tension-compression asymmetry, and texture evolution of additively manufactured inconel 718 at room and elevated temperatures. International Journal of Plasticity 125, 63–79.

Ghorbanpour, S., Zecevic, M., Kumar, A., Jahedi, M., Bicknell, J., Jorgensen, L., Beyerlein, I.J., Knezevic, M., 2017. A crystal plasticity model incorporating the effects of precipitates in superalloys: application to tensile, compressive, and cyclic deformation of inconel 718. International Journal of Plasticity 99, 162–185.

Ghosh, R., Curtis, R., McLean, M., 1990. Creep deformation of single crystal superalloys—modelling the crystallographic anisotropy. Acta Metallurgica et Materialia 38, 1977–1992.

Ghosh, S., Kumar, H., Brandl, C., Choudhury, A.N., Bhattacharyya, S., Mukherjee, R., 2024. Effect of molybdenum addition on precipitate coarsening kinetics in inconel 740h: A phase-field study. Intermetallics 175, 108513.

Glicksman, M., Fradkov, V., 1995. Kinetics of diffusional droplet growth in a liquid/liquid two-phase system. Final Technical Report Rensselaer Polytechnic Inst .

Gopinath, K., Gogia, A., Kamat, S., Balamuralikrishnan, R., Ramamurty, U., 2009. Low cycle fatigue behaviour of a low interstitial Ni-base superalloy. Acta Materialia 57, 3450–3459.

Grafe, U., Böttger, B., Tiaden, J., Fries, S., 2000. Coupling of multicomponent thermodynamic databases to a phase field model: application to solidification and solid state transformations of superalloys. Scripta Materialia 42, 1179–1186.

Grant, B.M., Francis, E.M., da Fonseca, J.Q., Preuss, M., Daymond, M.R., 2013. The effect of $\gamma^{'}$ size and alloy chemistry on dynamic strain ageing in advanced polycrystalline nickel base superalloys. Materials Science and Engineering: A 573, 54–61.

le Graverend, J.B., 2023. Crystal-plasticity modeling of monotonic and cyclic softening in inconel 718 superalloy. International Journal of Mechanical Sciences 239, 107871.

Grosdidier, T., Hazotte, A., Simon, A., 1998. Precipitation and dissolution processes in $\gamma/\gamma^{'}$ single crystal nickel-based superalloys. Materials Science and Engineering: A 256, 183–196.

Guo, X., Shi, S.Q., Ma, X., 2005. Elastoplastic phase field model for microstructure evolution. Applied Physics Letters 87.

Guo, Z., Huang, D., Yan, X., 2021. Physics-based modeling of $\gamma/\gamma^{'}$ microstructure evolution and creep constitutive relation for single crystal superalloy. International Journal of Plasticity 137, 102916.

Gupta, S., Bronkhorst, C.A., 2021. Crystal plasticity model for single crystal ni-based superalloys: capturing orientation and temperature dependence of flow stress. International Journal of Plasticity 137, 102896.

Gururajan, M., Abinandanan, T., 2005. A phase field study of microstructural evolution in elastically inhomogeneous systems. Proceedings of solid-solid phase transformations in inorganic materials , 747.

Gururajan, M., Abinandanan, T., 2007. Phase field study of precipitate rafting under a uniaxial stress. Acta Materialia 55, 5015–5026.

Han, G., Yu, J., Hu, Z., Sun, X., 2013. Creep property and microstructure evolution of a nickel-base single crystal superalloy in [011] orientation. Materials characterization 86, 177–184.

Han, Q., Lei, X., Yang, H., Yang, X., Su, Z., Rui, S.S., Wang, N., Ma, X., Cui, H., Shi, H., 2021. Effects of temperature and load on fretting fatigue induced geometrically necessary dislocation distribution in titanium alloy. Materials Science and Engineering: A 800, 140308.

Hao, Z., Tian, T., Peng, S., Ge, C., Li, X., Jia, C., Guo, C., Zhu, Q., 2020. Effect of heat treatment on microstructure and properties of fgh4096m superalloy processed by selective laser melting. Metals and Materials International 26, 1270–1285.

Hardy, M., Detrois, M., McDevitt, E., Argyrakis, C., Saraf, V., Jablonski, P., Hawk, J., Buckingham, R., Kitaguchi, H., Tin, S., 2020. Solving recent challenges for wrought ni-base superalloys. Metallurgical and Materials Transactions A 51, 2626–2650.

Harikrishnan, R., le Graverend, J.B., 2018. A creep-damage phase-field model: Predicting topological inversion in ni-based single crystal superalloys. Materials & Design 160, 405–416.

Harte, A., Atkinson, M., Preuss, M., Da Fonseca, J.Q., 2020. A statistical study of the relationship between plastic strain and lattice misorientation on the surface of a deformed ni-based superalloy. Acta Materialia 195, 555–570.

He, R., Li, M., Han, X., Feng, W., Zhang, H., Xie, H., Liu, Z., 2023. Experimental study of as-cast and heat-treated single-crystal ni-based superalloy interface using tem. Nanomaterials 13, 608.

Heaney, J., Lasonde, M., Powell, A., Bond, B., O'Brien, C., 2014. Development of a new cast and wrought alloy (rene 65) for high temperature disk applications, superalloys 718, 625,706 and various derivatives, ed. Banik, et al, TMS .

Heinz, A., Neumann, P., 1990. Crack initiation during high cycle fatigue of an austenitic steel. Acta metallurgica et materialia 38, 1933–1940.

Henderson, P., Berglin, L., Jansson, C., 1998. On rafting in a single crystal nickel-base superalloy after high and low temperature creep. Scripta materialia 40.

Heredia, F., Pope, D., 1991a. Effect of boron additions on the ductility and fracture behavior of ni3al single crystals. Acta metallurgica et materialia 39, 2017–2026.

Heredia, F., Pope, D., 1991b. The plastic flow of binary ni3al single crystals. Acta metallurgica et materialia 39, 2027–2036.

Hestroffer, J.M., Latypov, M.I., Stinville, J.C., Charpagne, M.A., Valle, V., Miller, M.P., Pollock, T.M., Beyerlein, I.J., 2022. Development of grain-scale slip activity and lattice rotation fields in inconel 718. Acta Materialia 226, 117627.

Hu, X., Ye, W., Zhang, L., Jiang, R., Song, Y., 2021. Investigation on creep properties and microstructure evolution of gh4169 alloy at different temperatures and stresses. Materials Science and Engineering: A 800, 140338.

Huang, J., Shi, D.Q., Yang, X.G., 2016. A physically based methodology for predicting anisotropic creep properties of ni-based superalloys. Rare Metals 35, 606–614.

Huang, J., Yang, X., Shi, D., Yu, H., Dong, C., Hu, X., 2014. Systematic methodology for high temperature lcf life prediction of smooth and notched ni-based superalloy with and without dwells. Computational materials science 89, 65–74.

Huang, S., An, K., Gao, Y., Suzuki, A., 2018. Determination of $\gamma/\gamma^{'}$ lattice misfit in ni-based single-crystal superalloys at high temperatures by neutron diffraction. Metallurgical and Materials Transactions A 49, 740–751.

Huang, Y., Wang, X., Cui, C., Li, J., Ye, L., Hou, G., Yang, Y., Liu, J., Liu, J., Zhou, Y., et al., 2020. The effect of coarsening of $\gamma^{'}$ precipitate on creep properties of ni-based single crystal superalloys during long-term aging. Materials Science and Engineering: A 773, 138886.

Humphreys, F.J., Hatherly, M., 2012. Recrystallization and related annealing phenomena. Elsevier.

Hüther, W., Reppich, B., 1979. Order hardening of mgo by large precipitated volume fractions of spinel particles. Materials Science and Engineering 39, 247–259.

Ignat, M., Buffiere, J.Y., Chaix, J., 1993. Microstructures induced by a stress gradient in a nickel-based superalloy. Acta metallurgica et materialia 41, 855–862.

Jackson, M., Reed, R., 1999. Heat treatment of udimet 720li: the effect of microstructure on properties. Materials Science and Engineering: A 259, 85–97.

Jacome, L.A., Nörtershäuser, P., Heyer, J.K., Lahni, A., Frenzel, J., Dlouhy, A., Somsen, C., Eggeler, G., 2013. High-temperature and low-stress creep anisotropy of single-crystal superalloys. Acta Materialia 61, 2926–2943.

Jiang, R., Everitt, S., Gao, N., Soady, K., Brooks, J., Reed, P.A., 2015a. Influence of oxidation on fatigue crack initiation and propagation in turbine disc alloy n18. International Journal of Fatigue 75, 89–99.

Jiang, R., Karpasitis, N., Gao, N., Reed, P., 2015b. Effects of microstructures on fatigue crack initiation and short crack propagation at room temperature in an advanced disc superalloy. Materials Science and Engineering: A 641, 148–159.

Jiang, R., Pierron, F., Octaviani, S., Reed, P., 2017. Characterisation of strain localisation processes during fatigue crack initiation and early crack propagation by sem-dic in an advanced disc alloy. Materials Science and Engineering: A 699, 128–144.

Jiang, R., Zhang, L., Zhang, W., Zhang, Y., Chen, Y., Liu, J., Zhang, Y., Song, Y., 2021. Low cycle fatigue and stress relaxation behaviours of powder metallurgy Ni-based superalloy FGH4098. Materials Science and Engineering: A 817, 141421.

Jiang, R., Zhang, W., Zhang, L., Zhao, Y., Zhang, L., Song, Y., 2022. Strain localization and crack initiation behavior of a pm ni-based superalloy: Sem-dic characterization and crystal plasticity simulation. Fatigue & Fracture of Engineering Materials & Structures 45, 1635–1651.

Jiang, X., Wang, D., Xie, G., Li, H., Lou, L., Zhang, J., 2014. The effect of long-term thermal exposure on the microstructure and stress rupture property of a directionally solidified ni-based superalloy. Metallurgical and Materials Transactions A 45, 6016–6026.

Jogi, T., Shenoy, S., Sankarasubramanian, R., Choudhury, A., Bhattacharyya, S., 2024. Splitting instability in superalloys: A phase-field study. arXiv preprint arXiv:2401.13151 .

Joseph, C., Persson, C., Colliander, M.H., 2017. Influence of heat treatment on the microstructure and tensile properties of ni-base superalloy haynes 282. Materials Science and Engineering: A 679, 520–530.

Karunaratne, M., Cox, D., Carter, P., Reed, R., 2000. Modelling of the microsegregation in cmsx-4 superalloy and its homogenisation during heat treatment .

Kashinga, R., Zhao, L., Silberschmidt, V.V., Farukh, F., Barnard, N., Whittaker, M., Proprentner, D., Shollock, B., McColvin, G., 2017. Low cycle fatigue of a directionally solidified nickel-based superalloy: Testing, characterisation and modelling. Materials Science and Engineering: A 708, 503–513.

Kearsey, R., Tsang, J., Oppenheimer, S., McDevitt, E., 2012. Microstructural effects on the mechanical properties of ati 718plus® alloy. Jom 64, 241–251.

Keefe, P., Mancuso, S., Maurer, G., 1992. Effects of heat treatment and chemistry on the long-term phase stability of a high strength nickel-based superalloy, in: Superalloys 1992 (Seventh International Symposium), TMS. pp. 487–496.

Keshavarz, S., Campbell, C.E., Reid, A.C., 2022. Multi-scale crystal plasticity model of creep responses in nickel-based superalloys. Materials 15, 4447.

Keshavarz, S., Ghosh, S., 2015a. A crystal plasticity finite element model for flow stress anomalies in ni3al single crystals. Philosophical Magazine 95, 2639–2660.

Keshavarz, S., Ghosh, S., 2015b. Hierarchical crystal plasticity fe model for nickel-based superalloys: sub-grain microstructures to polycrystalline aggregates. International Journal of Solids and Structures 55, 17–31.

Keshavarz, S., Ghosh, S., Reid, A.C., Langer, S.A., 2016. A non-schmid crystal plasticity finite element approach to multi-scale modeling of nickel-based superalloys. Acta Materialia 114, 106–115.

Kim, S.G., Kim, W.T., Suzuki, T., 1999. Phase-field model for binary alloys. Physical review e 60, 7186.

Kim, Y.K., Kim, D., Kim, H.K., Yoon, E.Y., Lee, Y., Oh, C.S., Lee, B.J., 2018. A numerical model to predict mechanical properties of ni-base disk superalloys. International Journal of Plasticity 110, 123–144.

Kiss, Á.K., Rauch, E.F., Lábár, J.L., 2016. Highlighting material structure with transmission electron diffraction correlation coefficient maps. Ultramicroscopy 163, 31–37.

Klotz, T., Blas, S., Lévesque, M., Brochu, M., 2017. 1d cyclic yield model independent of load spectrum characteristics and its application to Inconel 718. Mechanics of Materials 109, 34–41.

Kobayashi, R., 1993. Modeling and numerical simulations of dendritic crystal growth. Physica D: Nonlinear Phenomena 63, 410–423.

Kocks, U.F., AS, A., MF, A., 1975. Thermodynamics and kinetics of slip. Progress in Materials Science 19, 1.

Konno, T., Hiraga, K., Kawasaki, M., 2001. Guinier-preston (gp) zone revisited: atomic level observation by haadf-tem technique. Scripta materialia 44, 2303–2307.

Koslowski, M., Cuitino, A.M., Ortiz, M., 2002. A phase-field theory of dislocation dynamics, strain hardening and hysteresis in ductile single crystals. Journal of the Mechanics and Physics of Solids 50, 2597–2635.

Kozar, R., Suzuki, A., Milligan, W., Schirra, J., Savage, M., Pollock, T., 2009. Strengthening mechanisms in polycrystalline multimodal nickel-base superalloys. Metallurgical and materials transactions A 40, 1588–1603.

Krausz, A., Krausz, K., 1996. Unified Constitutive Laws of Plastic Deformation. Elsevier Science. URL: `https://books.google.co.in/books?id=OA9PxDRYpUoC`.

Kronberg, M., Wilson, u.F., 1949. Secondary recrystallization in copper. JOM 1, 501–514.

Krueger, D.D., Kissinger, R.D., Menzies, R.G., Wukusick, C.S., 1990. Fatigue crack growth resistant nickel-base article and alloy and method for making. US Patent 4,957,567.

Kumar, C., Reddy, S., Eswaramoorthy, N.K., Ravanappa, P., Chintapenta, V., Srinivasan, D., Kumar, P., 2025. Microstructure optimization for improving creep resistance of additively manufactured ni-based superalloy in939 through heat treatment. Journal of Materials Science 60, 1545–1560.

Kumar, S., Patra, A., Sahu, J., 2024. Dislocation density-based constitutive model for cyclic deformation and softening of Ni-based superalloys. Fatigue & Fracture of Engineering Materials & Structures 47, 3264–3284. doi:`https://doi.org/10.1111/ffe.14367`.

Kundin, J., Mushongera, L., Goehler, T., Emmerich, H., 2012. Phase-field modeling of the γ'-coarsening behavior in ni-based superalloys. Acta materialia 60, 3758–3772.

Kuo, C.M., Yang, Y.T., Bor, H.Y., Wei, C.N., Tai, C.C., 2009. Aging effects on the microstructure and creep behavior of inconel 718 superalloy. Materials Science and Engineering: A 510, 289–294.

Laberge, C., Fratzl, P., Lebowitz, J., 1997. Microscopic model for directional coarsening of precipitates in alloys under external load. Acta materialia 45, 3949–3962.

Lamm, M., Singer, R., 2007. The effect of casting conditions on the high-cycle fatigue properties of the single-crystal nickel-base superalloy pwa 1483. Metallurgical and Materials Transactions A 38, 1177–1183.

Lapin, J., Gebura, M., Bajana, O., Pelachová, T., Nazmy, M., 2009. Effect of size and volume fraction of cuboidal $\gamma^{'}$ precipitates on mechanical properties of single crystal nickel–based superalloy cmsx-4. Kovove Mater 47, 129–138.

Lapin, J., Gebura, M., Pelachová, T., Nazmy, M., 2008. Coarsening kinetics of cuboidal γ'precipitates in single crystal nickel base superalloy cmsx-4. Kovove Mater 46, 313–322.

Latypov, M.I., Stinville, J.C., Mayeur, J.R., Hestroffer, J.M., Pollock, T.M., Beyerlein, I.J., 2021. Insight into microstructure-sensitive elastic strain concentrations from integrated computational modeling and digital image correlation. Scripta Materialia 192, 78–82.

Le Bouar, Y., Finel, A., Appolaire, B., Cottura, M., 2022. Phase field models for modeling microstructure evolution in single-crystal ni-base superalloys, in: Nickel Base Single Crystals Across Length Scales. Elsevier, pp. 379–399.

Le Graverend, J.B., 2019. A hardening-based damage model for fast-evolving microstructures: Application to ni-based single crystal superalloys. International Journal of Plasticity 123, 1–21.

Le Graverend, J.B., Cormier, J., Gallerneau, F., Villechaise, P., Kruch, S., Mendez, J., 2014. A microstructure-sensitive constitutive modeling of the inelastic behavior of single crystal nickel-based superalloys at very high temperature. International Journal of Plasticity 59, 55–83.

Le Graverend, J.B., Cormier, J., Jouiad, M., Gallerneau, F., Paulmier, P., Hamon, F., 2010. Effect of fine $\gamma^{'}$ precipitation on non-isothermal creep and creep-fatigue behaviour of nickel base superalloy mc2. Materials Science and Engineering: A 527, 5295–5302.

Le Graverend, J.B., Harikrishnan, R., 2019. Finite-element crystal plasticity on phase-field microstructures: Predicting mechanical response variations in ni-based single-crystal superalloys. JOM 71, 2600–2611.

Le Graverend, J.B., Harikrishnan, R., 2021. A lattice-misfit-dependent micromechanical approach in ni-based single crystal superalloys. International Journal of Mechanical Sciences 195, 106229.

Lebensohn, R.A., Hartley, C.S., Tomé, C.N., Castelnau, O., 2010. Modeling the mechanical response of polycrystals deforming by climb and glide. Philosophical Magazine 90, 567–583.

Lee, H.s., Kim, D.h., Kim, D.s., Yoo, K.b., 2013. Microstructural changes by heat treatment for single crystal superalloy exposed at high temperature. Journal of alloys and compounds 561, 135–141.

Lei, Y., Li, X., Sun, R., Tang, Y., Niu, W., 2020. Effect of sintering temperature and heat treatment on microstructure and properties of nickel-based superalloy. Journal of Alloys and Compounds 818, 152882.

Leidermark, D., Moverare, J., Johansson, S., Simonsson, K., Sjöström, S., 2010. Tension/-compression asymmetry of a single-crystal superalloy in virgin and degraded condition. Acta Materialia 58, 4986–4997.

León-Cázares, F., Monni, F., Jackson, T., Galindo-Nava, E., Rae, C., 2020a. Stress response and microstructural evolution of nickel-based superalloys during low cycle fatigue: Physics-based modelling of cyclic hardening and softening. International Journal of Plasticity 128, 102682.

León-Cázares, F.D., Schlütter, R., Jackson, T., Galindo-Nava, E.I., Rae, C., 2020b. A multiscale study on the morphology and evolution of slip bands in a nickel-based superalloy during low cycle fatigue. Acta Materialia 182, 47–59.

Lerch, B., Gerold, V., 1987. Cyclic hardening mechanisms in NIMONIC 80A. Metallurgical Transactions A 18, 2135–2141.

Lerch, B.A., Jayaraman, N., Antolovich, S.D., 1984. A study of fatigue damage mechanisms in waspaloy from 25 to 800 c. Materials Science and Engineering 66, 151–166.

Li, C., Seyring, M., Li, X., Zhong, Y., Ren, Z., Rettenmayr, M., 2019a. Effect of heat treatment combined with an alternating magnetic field on microstructure and mechanical properties of a ni-based superalloy. Metallurgical and Materials Transactions A 50, 1837–1850.

Li, H., Sun, J., Hardy, M., Evans, H., Williams, S., Doel, T., Bowen, P., 2015. Effects of microstructure on high temperature dwell fatigue crack growth in a coarse grain pm nickel based superalloy. Acta Materialia 90, 355–369.

Li, J., Ding, R., Guo, Q., Li, C., Liu, Y., Wang, Z., Li, H., Liu, C., 2021. Effect of solution cooling rate on microstructure evolution and mechanical properties of ni-based superalloy ati 718plus. Materials Science and Engineering: A 812, 141113.

Li, J., Huang, Q., Wang, Z., Zhang, N., Chen, G., Qian, G., 2023. Microstructural insights into fatigue short crack propagation resistance and rate fluctuation in a ni-based superalloy manufactured by laser powder bed fusion. International Journal of Plasticity 171, 103800.

Li, K.S., Wang, R.Z., Cheng, L.Y., Lu, T.W., Zhang, X.C., Tu, S.T., Zhang, G.D., Fan, Z.C., 2022a. Dislocation-based crystal plasticity modelling of a nickel-based superalloy under dwell-fatigue: From life prediction to residual life assessment. International Journal of Fatigue 159, 106569.

Li, W., Ma, J., Kou, H., Shao, J., Zhang, X., Deng, Y., Tao, Y., Fang, D., 2019b. Modeling the effect of temperature on the yield strength of precipitation strengthening ni-base superalloys. International Journal of Plasticity 116, 143–158.

Li, Y., Wang, L., He, Y., Zheng, W., Lou, L., Zhang, J., 2022b. Role of interfacial dislocation networks during secondary creep at elevated temperatures in a single crystal ni-based superalloy. Scripta Materialia 217, 114769.

Liang, X.f., Zhao, Y.t., Jia, Z.h., Zhang, C., 2016. Preparation and tensile properties of dd5 single crystal castings. International Journal of Minerals, Metallurgy, and Materials 23, 683–690.

Lim, H., Carroll, J., Battaile, C.C., Buchheit, T., Boyce, B., Weinberger, C., 2014. Grain-scale experimental validation of crystal plasticity finite element simulations of tantalum oligocrystals. International Journal of Plasticity 60, 1–18.

Lim, H., Carroll, J.D., Battaile, C.C., Boyce, B.L., Weinberger, C.R., 2015. Quantitative comparison between experimental measurements and cp-fem predictions of plastic deformation in a tantalum oligocrystal. International Journal of Mechanical Sciences 92, 98–108.

Lin, B., Zhao, L., Tong, J., 2011. A crystal plasticity study of cyclic constitutive behaviour, crack-tip deformation and crack-growth path for a polycrystalline nickel-based superalloy. Engineering Fracture Mechanics 78, 2174–2192.

Lin, Y., Li, G., Wei, M., Gao, J., Zhang, L., 2019. Effect of different cooling media after solid solution on the microstructure and yield strength in a ni-al alloy during aging:

experimental measurement and computational modeling. Metallurgical and Materials Transactions A 50, 4920–4930.

Lindström, T., Nilsson, D., Simonsson, K., Eriksson, R., Lundgren, J.E., Leidermark, D., 2022. Constitutive model for thermomechanical fatigue conditions of an additively manufactured combustor alloy. Mechanics of Materials 168, 104273.

Liu, G., Tong, J., Xie, G., Zhao, W., Duan, H., Zhang, J., Du, K., 2025. Microstructure evolution of single-crystal nickel-base superalloy during the rafting process under thermomechanical fatigue. Journal of Materials Science , 1–15.

Liu, J., Jin, T., Sun, X., Zhang, J., Guan, H., Hu, Z., 2008. Anisotropy of stress rupture properties of a ni base single crystal superalloy at two temperatures. Materials Science and Engineering: A 479, 277–284.

Liu, J., Jin, T., Yu, J., Sun, X., Guan, H., Hu, Z., 2010. Effect of thermal exposure on stress rupture properties of a re bearing ni base single crystal superalloy. Materials Science and Engineering: A 527, 890–897.

Liu, J., Vanderesse, N., Stinville, J.C., Pollock, T., Bocher, P., Texier, D., 2019. In-plane and out-of-plane deformation at the sub-grain scale in polycrystalline materials assessed by confocal microscopy. Acta Materialia 169, 260–274.

Liu, K., Wang, J., Wang, B., Mao, P., Yang, Y., Zhou, Y., 2022. Quantifying the influences of carbides and porosities on the fatigue crack evolution of a ni-based single-crystal superalloy using x-ray tomography. Acta Metallurgica Sinica (English Letters) 35, 133–145.

Liu, X., Huang, T., Zhang, J., Wang, D., Zhang, J., Hu, R., Zhang, J., Liu, L., 2021. Influence of thermal exposure on microstructure and stress rupture property of a re-containing ni-based single crystal superalloy. Intermetallics 136, 107237.

Liu, Y., Kang, M., Wu, Y., Wang, M., Li, M., Yu, J., Gao, H., Wang, J., 2018. Crack formation and microstructure-sensitive propagation in low cycle fatigue of a polycrystalline nickel-based superalloy with different heat treatments. International Journal of Fatigue 108, 79–89.

Liu, Y., Zhang, X., Oskay, C., 2023. A comparative study on fatigue indicator parameters for near-α titanium alloys. Fatigue & Fracture of Engineering Materials & Structures 46, 271–294.

Liu, Y.Z., Shi, Z.L., Zhang, Y.B., Qin, M., Hu, S.P., Song, X.G., Fu, W., Lee, B.J., 2024. Effect of temperature on the mechanical properties of ni-based superalloys via molecular dynamics and crystal plasticity. Journal of Materials Science & Technology 203, 126–142.

Locq, D., Caron, P., 2011. On some advanced nickel-based superalloys for disk applications. Aerospace Lab , p–1.

Lorentzen, T., Daymond, M., Clausen, B., Tomé, C., 2002. Lattice strain evolution during cyclic loading of stainless steel. Acta materialia 50, 1627–1638.

Lu, P., Jin, X., Li, P., Sun, Y., Fan, X., 2023. Crystal plasticity constitutive model and thermodynamics informed creep-fatigue life prediction model for ni-based single crystal superalloy. International Journal of Fatigue 176, 107829.

Lu, X., Dunne, F.P., Xu, Y., 2020. A crystal plasticity investigation of slip system interaction, gnd density and stored energy in non-proportional fatigue in nickel-based superalloy. International Journal of Fatigue 139, 105782.

Luccarelli, P., Rabbolini, S., Beretta, S., Foletti, S., 2019. Crack-closure simulations of ni-based super-alloy polycrystal, a comparison between experiments and crystal plasticity. Materials Science and Engineering: A 740, 368–380.

Lukáš, P., Čadek, J., Šustek, V., Kunz, L., 1996. Creep of cmsx-4 single crystals of different orientations in tension and compression. Materials Science and Engineering: A 208, 149–157.

Lund, A.C., Voorhees, P.W., 2002. The effects of elastic stress on coarsening in the ni-al system. Acta materialia 50, 2085–2098.

Luo, L., Chen, F., Chen, T., Zeng, J., Qin, J., Li, Y., 2022. Microstructural evolution and elastic–plastic accommodation of misfit strain in a $\gamma^{'}$-richen ni-based superalloy during ultra-high temperature thermal cycle. Applied Physics A 128, 197.

Ma, A., Dye, D., Reed, R., 2008. A model for the creep deformation behaviour of single-crystal superalloy cmsx-4. Acta Materialia 56, 1657–1670.

MacLachlan, D., Knowles, D., 2000. Creep-behavior modeling of the single-crystal superalloy cmsx-4. Metallurgical and materials transactions A 31, 1401–1411.

MacLachlan, D.W., Wright, L.W., Gunturi, S., Knowles, D.M., 2001. Constitutive modelling of anisotropic creep deformation in single crystal blade alloys srr99 and cmsx-4. International Journal of Plasticity 17, 441–467.

Manga, V.R., Shang, S.L., Wang, W.Y., Wang, Y., Liang, J., Crespi, V.H., Liu, Z.K., 2015. Anomalous phonon stiffening associated with the (1 1 1) antiphase boundary in L12 Ni3Al. Acta Materialia 82, 287–294.

Mann, T., Fahrmann, M.G., Koslowski, M., Titus, M.S., 2024. Phase field dislocation dynamics modeling of shearing modes in ni2 (cr, mo, w)-containing haynes® 244® superalloy. Acta Materialia 281, 120453.

Manonukul, A., Dunne, F., 2004. High–and low–cycle fatigue crack initiation using polycrystal plasticity. Proceedings of the Royal Society of London. Series A: Mathematical, Physical and Engineering Sciences 460, 1881–1903.

Marchese, G., Atzeni, E., Salmi, A., Biamino, S., 2021. Microstructure and residual stress evolution of laser powder bed fused inconel 718 under heat treatments. Journal of Materials Engineering and Performance 30, 565–574.

Masoumi, F., Jahazi, M., Shahriari, D., Cormier, J., 2016. Coarsening and dissolution of γ' precipitates during solution treatment of ad730 ni-based superalloy: Mechanisms and kinetics models. Journal of Alloys and Compounds 658, 981–995.

Matan, N., Cox, D., Carter, P., Rist, M., Rae, C., Reed, R., 1999a. Creep of cmsx-4 superalloy single crystals: effects of misorientation and temperature. Acta materialia 47, 1549–1563.

Matan, N., Cox, D., Rae, C., Reed, R., 1999b. On the kinetics of rafting in cmsx-4 superalloy single crystals. Acta Materialia 47, 2031–2045.

McDowell, D., Dunne, F., 2010. Microstructure-sensitive computational modeling of fatigue crack formation. International journal of fatigue 32, 1521–1542.

McDowell, D.L., 2007. Simulation-based strategies for microstructure-sensitive fatigue modeling. Materials Science and Engineering: A 468, 4–14.

Mello, A.W., Nicolas, A., Sangid, M.D., 2017. Fatigue strain mapping via digital image correlation for ni-based superalloys: The role of thermal activation on cube slip. Materials Science and Engineering: A 695, 332–341.

Mercer, C., Soboyejo, A., Soboyejo, W., 1999. Micromechanisms of fatigue crack growth in a forged Inconel 718 nickel-based superalloy. Materials Science and Engineering: A 270, 308–322.

Me´ric, L., Poubanne, P., Cailletaud, G., 1991. Single crystal modeling for structural calculations: part 1—model presentation. Journal of Engineering Materials and Technology 113, 162.

Merrick, H., 1974. The low cycle fatigue of three wrought nickel-base alloys. Metallurgical and Materials Transactions B 5, 891–897.

Merrick, H., Floreen, S., 1978. The effects of microstructure on elevated temperature crack growth in nickel-base alloys. Metallurgical Transactions A 9, 231–236.

Mesarovic, S.D., 2017. Dislocation creep: Climb and glide in the lattice continuum. Crystals 7. URL: `https://www.mdpi.com/2073-4352/7/8/243`, doi:10.3390/`cryst7080243`.

Meyers, M.A., Chawla, K.K., 2008. Mechanical behavior of materials. Cambridge university press.

Miao, J., Pollock, T.M., Jones, J.W., 2009. Crystallographic fatigue crack initiation in nickel-based superalloy rené 88dt at elevated temperature. Acta materialia 57, 5964–5974.

Miao, J., Pollock, T.M., Jones, J.W., 2012. Microstructural extremes and the transition from fatigue crack initiation to small crack growth in a polycrystalline nickel-base superalloy. Acta Materialia 60, 2840–2854.

Milenkovic, S., Sabirov, I., LLorca, J., 2012. Effect of the cooling rate on microstructure and hardness of mar-m247 ni-based superalloy. Materials Letters 73, 216–219.

Miller, V.M., Johnson, A.E., Torbet, C.J., Pollock, T.M., 2016. Recrystallization and the development of abnormally large grains after small strain deformation in a polycrystalline nickel-based superalloy. Metallurgical and Materials Transactions A 47, 1566–1574.

Mishra, S., Pant, P., Narasimhan, K., Rollett, A., Samajdar, I., 2009. On the widths of orientation gradient zones adjacent to grain boundaries. Scripta materialia 61, 273–276.

Mitchell, R., Preuss, M., Tin, S., Hardy, M., 2008. The influence of cooling rate from temperatures above the $\gamma^{'}$ solvus on morphology, mismatch and hardness in advanced polycrystalline nickel-base superalloys. Materials Science and Engineering: A 473, 158–165.

MIURA, N., KONDO, Y., MATSUO, T., 2003. Relation between creep rate during accelerating creep stage and γ channel thickness in single crystal nickel-based superalloy, cmsx-4. Tetsu-to-hagané 89, 1240–1247.

Moshtaghin, R., Asgari, S., 2003. Growth kinetics of γ' precipitates in superalloy in-738lc during long term aging. Materials & design 24, 325–330.

Mostafaei, A., Behnamian, Y., Krimer, Y.L., Stevens, E.L., Luo, J.L., Chmielus, M., 2016. Effect of solutionizing and aging on the microstructure and mechanical properties of powder bed binder jet printed nickel-based superalloy 625. Materials & Design 111, 482–491.

Mughrabi, H., 2009. Cyclic slip irreversibilities and the evolution of fatigue damage. Metallurgical and Materials Transactions B 40, 431–453.

Mughrabi, H., 2013a. Cyclic slip irreversibility and fatigue life: A microstructure-based analysis. Acta materialia 61, 1197–1203.

Mughrabi, H., 2013b. Microstructural fatigue mechanisms: Cyclic slip irreversibility, crack initiation, non-linear elastic damage analysis. International Journal of Fatigue 57, 2–8.

Mughrabi, H., 2014. The importance of sign and magnitude of γ/γ' lattice misfit in superalloys—with special reference to the new γ'-hardened cobalt-base superalloys. Acta materialia 81, 21–29.

Mughrabi, H., Ott, M., Tetzlaff, U., 1997. New microstructural concepts to optimize the high-temperature strength of γ'-hardened monocrystalline nickel-based superalloys. Materials Science and Engineering: A 234, 434–437.

Mughrabi, H., Tetzlaff, U., 2000. Microstructure and high-temperature strength of monocrystalline nickel-base superalloys. Advanced Engineering Materials 2, 319–326.

Mukherjee, R., Abinandanan, T., Gururajan, M., 2009. Phase field study of precipitate growth: Effect of misfit strain and interface curvature. Acta Materialia 57, 3947–3954.

Mukherjee, R., Abinandanan, T., Gururajan, M., 2013. Phase field models as computer experiments: Growth kinetics of anisotropic precipitates, in: Materials Science Forum, Trans Tech Publ. pp. 1–12.

Murakumo, T., Kobayashi, T., Koizumi, Y., Harada, H., 2004. Creep behaviour of ni-base single-crystal superalloys with various γ' volume fraction. Acta Materialia 52, 3737–3744.

Mushongera, L.T., Fleck, M., Kundin, J., Wang, Y., Emmerich, H., 2015. Effect of re on directional $\gamma^{'}$-coarsening in commercial single crystal ni-base superalloys: a phase field study. Acta Materialia 93, 60–72.

Musinski, W.D., McDowell, D.L., 2015. On the eigenstrain application of shot-peened residual stresses within a crystal plasticity framework: Application to ni-base superalloy specimens. International Journal of Mechanical Sciences 100, 195–208.

Nabarro, F.R., 1996. Rafting in superalloys. Metallurgical and Materials transactions A 27, 513–530.

Nembach, E., Neite, G., 1985. Precipitation hardening of superalloys by ordered $\gamma^{'}$-particles. Progress in Materials Science 29, 177–319.

Nestler, B., Choudhury, A., 2011. Phase-field modeling of multi-component systems. Current opinion in solid state and Materials Science 15, 93–105.

Nestler, B., Garcke, H., Stinner, B., 2005. Multicomponent alloy solidification: phase-field modeling and simulations. Physical Review E—Statistical, Nonlinear, and Soft Matter Physics 71, 041609.

Nowell, M.M., Wright, S.I., Rampton, T., de Kloe, R., 2014. Advances in scattered electron intensity distribution imaging for microstructural visualization and correlations with ebsd measurements. Microscopy and Microanalysis 20, 856–857.

Ohashi, T., Hidaka, K., Imano, S., 1997. Elastic stress in single crystal ni-base superalloys and the driving force for their microstructural evolution under high temperature creep conditions. Acta materialia 45, 1801–1810.

Ohring, M., 1998. Reliability and failure of electronic materials and devices. Elsevier.

Okunishi, E., Ishikawa, I., Sawada, H., Hosokawa, F., Hori, M., Kondo, Y., 2009. Visualization of light elements at ultrahigh resolution by stem annular bright field microscopy. Microscopy and Microanalysis 15, 164–165.

Osinkolu, G., Onofrio, G., Marchionni, M., 2003. Fatigue crack growth in polycrystalline in 718 superalloy. Materials Science and Engineering: A 356, 425–433.

Österle, W., Bettge, D., Fedelich, B., Klingelhöffer, H., 2000. Modelling the orientation and direction dependence of the critical resolved shear stress of nickel-base superalloy single crystals. Acta materialia 48, 689–700.

Pai, N., Manda, S., Sudhalkar, B., Syphus, B., Fullwood, D., de Kloe, R., Wright, S., Patra, A., Samajdar, I., 2024a. Diffraction-based multiscale residual strain measurements. Microscopy and Microanalysis 30, 236–252.

Pai, N., Prakash, A., Samajdar, I., Patra, A., 2022. Study of grain boundary orientation gradients through combined experiments and strain gradient crystal plasticity modeling. International Journal of Plasticity 156, 103360.

Pai, N., Samajdar, I., Patra, A., 2024b. Microstructural and mechanistic insights into the tension-compression asymmetry of rapidly solidified fe-cr alloys: A phase field and strain gradient plasticity study. Journal of the Mechanics and Physics of Solids , 105695.

Pai, N., Samajdar, I., Patra, A., 2025. Study of orientation-dependent residual strains during tensile and cyclic deformation of an austenitic stainless steel. International Journal of Plasticity 185, 104228.

Paidar, V., Pope, D., Vitek, V., 1984. A theory of the anomalous yield behavior in l12 ordered alloys. Acta Metallurgica 32, 435–448.

Pang, H., Reed, P., 2007. Microstructure effects on high temperature fatigue crack initiation and short crack growth in turbine disc nickel-base superalloy udimet 720li. Materials Science and Engineering: A 448, 67–79.

Pang, H., Reed, P., 2009. Microstructure variation effects on room temperature fatigue threshold and crack propagation in udimet 720li ni-base superalloy. Fatigue & Fracture of Engineering Materials & Structures 32, 685–701.

Patra, A., Chaudhary, S., Pai, N., Ramgopal, T., Khandelwal, S., Rao, A., McDowell, D.L., 2023. ρ-cp: Open source dislocation density based crystal plasticity framework for simulating temperature-and strain rate-dependent deformation. Computational Materials Science 224, 112182.

Patra, A., McDowell, D.L., 2012. Crystal plasticity-based constitutive modelling of irradiated bcc structures. Philosophical Magazine 92, 861–887.

Patra, A., McDowell, D.L., 2013. Continuum modeling of localized deformation in irradiated bcc materials. Journal of Nuclear Materials 432, 414–427.

Patra, A., McDowell, D.L., 2016. Crystal plasticity investigation of the microstructural factors influencing dislocation channeling in a model irradiated bcc material. Acta Materialia 110, 364–376.

Patra, A., Zhu, T., McDowell, D.L., 2014. Constitutive equations for modeling non-schmid effects in single crystal bcc-fe at low and ambient temperatures. International Journal of Plasticity 59, 1–14.

Peach, M., Koehler, J., 1950. The forces exerted on dislocations and the stress fields produced by them. Physical Review 80, 436.

Pei, H., Yang, Y., Gu, S., Zhao, Y., Yao, X., Wen, Z., Yue, Z., 2022. Study on oxidation-creep behavior of a ni-based single crystal superalloy based on crystal plasticity theory. Materials Science and Engineering: A 839, 142834.

Permann, C.J., Gaston, D.R., Andrš, D., Carlsen, R.W., Kong, F., Lindsay, A.D., Miller, J.M., Peterson, J.W., Slaughter, A.E., Stogner, R.H., Martineau, R.C., 2020. Moose: Enabling massively parallel multiphysics simulation. SoftwareX 11, 100430. URL: `https://www.sciencedirect.com/science/article/pii/S2352711019302973`, doi:`https://doi.org/10.1016/j.softx.2020.100430`.

Phan, V.T., Zhang, X., Li, Y., Oskay, C., 2017. Microscale modeling of creep deformation and rupture in nickel-based superalloy in 617 at high temperature. Mechanics of Materials 114, 215–227.

Phillips, P., Unocic, R.R., Mills, M.J., 2013. Low cycle fatigue of a polycrystalline ni-based superalloy: Deformation substructure analysis. International journal of fatigue 57, 50–57.

Phillips, P.J., Unocic, R.R., Kovarik, L., Mourer, D., Wei, D., Mills, M.J., 2010. Low cycle fatigue of a ni-based superalloy: non-planar deformation. Scripta materialia 62, 790–793.

Pilgar, C.M., Fernandez, A.M., Lucarini, S., Segurado, J., 2022. Effect of printing direction and thickness on the mechanical behavior of slm fabricated hastelloy-x. International Journal of Plasticity 153, 103250.

Pinomaa, T., McKeown, J.M., Wiezorek, J.M., Provatas, N., Laukkanen, A., Suhonen, T., 2020. Phase field modeling of rapid resolidification of al-cu thin films. Journal of Crystal Growth 532, 125418.

Plotnikov, E.Y., Mao, Z., Noebe, R.D., Seidman, D.N., 2014. Temporal evolution of the γ (fcc)/$\gamma^{'}$ (l12) interfacial width in binary ni–al alloys. Scripta Materialia 70, 51–54.

Pokharel, R., Patra, A., Brown, D.W., Clausen, B., Vogel, S.C., Gray III, G.T., 2019. An analysis of phase stresses in additively manufactured 304l stainless steel using neutron

diffraction measurements and crystal plasticity finite element simulations. International Journal of Plasticity 121, 201–217.

Pollock, T., Argon, A., 1992. Creep resistance of cmsx-3 nickel base superalloy single crystals. Acta Metallurgica et Materialia 40, 1–30.

Pollock, T., Argon, A., 1994. Directional coarsening in nickel-base single crystals with high volume fractions of coherent precipitates. Acta metallurgica et materialia 42, 1859–1874.

Pollock, T.M., Tin, S., 2006. Nickel-based superalloys for advanced turbine engines: chemistry, microstructure and properties. Journal of propulsion and power 22, 361–374.

Porter, D.A., Easterling, K.E., 2009. Phase transformations in metals and alloys (revised reprint). CRC press.

Prakash, A., Tak, T.N., Anand, A., Pai, N.N., Narayana Murty, S., Singh, C.V., Guruprasad, P., Samajdar, I., 2022. Mechanistic origin of orientation-dependent substructure evolution in aluminum and aluminum-magnesium alloys. Metallurgical and Materials Transactions A 53, 2689–2707.

Prasad, K., Sarkar, R., Ghosal, P., Kumar, V., Sundararaman, M., 2013. High temperature low cycle fatigue deformation behaviour of forged in 718 superalloy turbine disc. Materials Science and Engineering: A 568, 239–245.

Prevéy, P.S., 1986. X-ray diffraction residual stress techniques. volume 10. American Society for Metals, Metals Park, OH.

Prithivirajan, V., Sangid, M.D., 2020. Examining metrics for fatigue life predictions of additively manufactured in718 via crystal plasticity modeling including the role of simulation volume and microstructural constraints. Materials Science and Engineering: A 783, 139312.

Qi, D., Yan, X., Tang, X., Peng, J., Yu, Q., Feng, L., Yuan, G., Zhang, A., Chen, Y., Yuan, J., et al., 2020. Epidemiological and clinical features of 2019-ncov acute respiratory disease cases in chongqing municipality, china: a retrospective, descriptive, multiple-center study. MedRxiv .

Qin, H.y., Chen, G., Zhu, Q., Wang, C.j., Zhang, P., 2015. High temperature low cycle fatigue behavior of GH4742 alloy. Journal of Iron and Steel Research International 22, 551–556.

Qin, Q., Bassani, J.L., 1992. Non-schmid yield behavior in single crystals. Journal of the Mechanics and Physics of Solids 40, 813–833.

Qin, R., Bhadeshia, H., 2009. Phase-field model study of the effect of interface anisotropy on the crystal morphological evolution of cubic metals. Acta Materialia 57, 2210–2216.

Radis, R., Schaffer, M., Albu, M., Kothleitner, G., Pölt, P., Kozeschnik, E., 2009. Multimodal size distributions of $\gamma^{'}$ precipitates during continuous cooling of udimet 720 li. Acta Materialia 57, 5739–5747.

Rahul, M., Agilan, M., Mohan, D., Phanikumar, G., 2022. Integrated experimental and simulation approach to establish the effect of elemental segregation in inconel 718 welds. Materialia 26, 101593.

Raju, S., Oni, A., Godwal, B., Yan, J., Drozd, V., Srinivasan, S., LeBeau, J., Rajan, K., Saxena, S., 2015. Effect of b and cr on elastic strength and crystal structure of ni3al alloys under high pressure. Journal of Alloys and Compounds 619, 616–620.

Raman, S.G.S., Padmanabhan, K., 1994. Room-temperature low-cycle fatigue behaviour of a ni-base superalloy. International journal of fatigue 16, 209–215.

Raman, S.G.S., Padmanabhan, K., 1995. A comparison of the room-temperature behaviour of AISI 304LN stainless steel and Nimonic 90 under strain cycling. International Journal of Fatigue 17, 271–277.

Ranjan, D., Narayanan, S., Kadau, K., Patra, A., 2021. Crystal plasticity modeling of non-schmid yield behavior: from ni3al single crystals to ni-based superalloys. Modelling and Simulation in Materials Science and Engineering 29, 055005.

Rauch, E., Veron, M., 2005. Coupled microstructural observations and local texture measurements with an automated crystallographic orientation mapping tool attached to a TEM. Materialwissenschaft und Werkstofftechnik: Entwicklung, Fertigung, Prüfung, Eigenschaften und Anwendungen technischer Werkstoffe 36, 552–556.

Reed, P., 2009. Fatigue crack growth mechanisms in superalloys: overview. Materials Science and Technology 25, 258–270.

Reed, R.C., 2008. The superalloys: fundamentals and applications. Cambridge university press.

Rettig, R., Ritter, N.C., Müller, F., Franke, M.M., Singer, R.F., 2015. Optimization of the homogenization heat treatment of nickel-based superalloys based on phase-field simulations: numerical methods and experimental validation. Metallurgical and Materials Transactions A 46, 5842–5855.

Risbet, M., Feaugas, X., Clavel, M., 2001. Study of the cyclic softening of an under-aged gamma'-precipitated nickel-base superalloy (Waspaloy). Le Journal de Physique IV 11, Pr4–293.

Rodas, E.A.E., Neu, R.W., 2018. Crystal viscoplasticity model for the creep-fatigue interactions in single-crystal ni-base superalloy cmsx-8. International Journal of Plasticity 100, 14–33.

Rodney, D., Finel, A., 2000. Phase field methods and dislocationss. MRS Online Proceedings Library 652, 1–6.

Roth, H., Davis, C., Thomson, R., 1997. Modeling solid solution strengthening in nickel alloys. Metallurgical and Materials Transactions A 28, 1329–1335.

Rui, S.S., Shang, Y.B., Fan, Y.N., Han, Q.N., Niu, L.S., Shi, H.J., Hashimoto, K., Komai, N., 2018. Ebsd analysis of creep deformation induced grain lattice distortion: A new method for creep damage evaluation of austenitic stainless steels. Materials Science and Engineering: A 733, 329–337.

Ruzic, J., Goto, K., Watanabe, I., Osada, T., Wu, L., Ohmura, T., 2021. Temperature-dependent deformation behavior of γ and γ' single-phase nickel-based superalloys. Materials Science and Engineering: A 818, 141439.

Sabnis, P.A., Forest, S., Arakere, N.K., Yastrebov, V.A., 2013. Crystal plasticity analysis of cylindrical indentation on a ni-base single crystal superalloy. International Journal of Plasticity 51, 200–217.

Sahu, S.K., Mishra, D.K., Behera, A., Dalai, R.P., 2021. An overview on the effect of heat-treatment and cooling rates on ni-based superalloys. Materials Today: Proceedings 47, 3309–3312.

Saleh, A.A., Pereloma, E.V., Clausen, B., Brown, D.W., Tomé, C.N., Gazder, A.A., 2013. On the evolution and modelling of lattice strains during the cyclic loading of twip steel. Acta Materialia 61, 5247–5262.

Satyanarayana, D., Eswara Prasad, N., 2016. Nickel-based superalloys, in: Aerospace Materials and Material Technologies: Volume 1: Aerospace Materials. Springer, pp. 199–228.

Schwen, D., Jiang, C., Aagesen, L., 2021. A sublattice phase-field model for direct calphad database coupling. Computational Materials Science 195, 110466.

Selvaraj, S.K., Sundaramali, G., Jithin Dev, S., Srii Swathish, R., Karthikeyan, R., Vijay Vishaal, K., Paramasivam, V., 2021. Recent advancements in the field of ni-based superalloys. Advances in Materials Science and Engineering 2021, 9723450.

Semiatin, S., Levkulich, N., Saurber, A., Mahaffey, D., Payton, E., Senkov, O., 2017. The kinetics of precipitate dissolution in a nickel-base superalloy. Metallurgical and Materials Transactions A 48, 5567–5578.

Sengupta, A., Putatunda, S., Bartosiewicz, L., Hangas, J., Nailos, P., Peputapeck, M., Alberts, F., 1994. Tensile behavior of a new single-crystal nickel-based superalloy (cmsx-4) at room and elevated temperatures. Journal of materials engineering and performance 3, 73–81.

Serin, K., Göbenli, G., Eggeler, G., 2004. On the influence of stress state, stress level and temperature on γ-channel widening in the single crystal superalloy cmsx-4. Materials Science and Engineering: A 387, 133–137.

Shang, Z., Niu, H., Wei, X., Song, D., Zou, J., Liu, G., Liang, S., Nie, L., Gong, X., 2022. Microstructure and tensile behavior of nickel-based single crystal superalloys with different re contents. Journal of Materials Research and Technology 18, 2458–2469.

Sharma, S., Ko, G., Li, F., Kang, K., 2008. Oxidation and creep failure of alloy 617 foils at high temperature. Journal of nuclear materials 378, 144–152.

Shenoy, M., Gordon, A., McDowell, D., Neu, R., 2005. Thermomechanical fatigue behavior of a directionally solidified ni-base superalloy. J. Eng. Mater. Technol 127, 325–336.

Shenoy, M., Tjiptowidjojo, Y., McDowell, D., 2008. Microstructure-sensitive modeling of polycrystalline in 100. International Journal of Plasticity 24, 1694–1730.

Shenoy, M., Zhang, J., McDowell, D.L., 2007. Estimating fatigue sensitivity to polycrystalline ni-base superalloy microstructures using a computational approach. Fatigue & Fracture of Engineering Materials & Structures 30, 889–904.

Shenoy, M.M., 2006. Constitutive modeling and life prediction in nickel-base superalloys. Georgia Institute of Technology.

Shi, Z., Li, J., Liu, S., 2012. Effect of long term aging on microstructure and stress rupture properties of a nickel based single crystal superalloy. Progress in Natural Science: Materials International 22, 426–432.

Shin, K.Y., Kim, J.H., Terner, M., Kong, B.O., Hong, H.U., 2019. Effects of heat treatment on the microstructure evolution and the high-temperature tensile properties of haynes 282 superalloy. Materials Science and Engineering: A 751, 311–322.

Simmons, J., Wen, Y., Shen, C., Wang, Y., 2004. Microstructural development involving nucleation and growth phenomena simulated with the phase field method. Materials Science and Engineering: A 365, 136–143.

Sims, C.T., Stoloff, N.S., Hagel, W.C., 1987. superalloys II. volume 8. Wiley New York.

Singh, V., Sundararaman, M., Chen, W., Wahi, R., 1991. Low-cycle fatigue behavior of nimonic pe16 at room temperature. Metallurgical Transactions A 22, 499–506.

Sinharoy, S., Virro-Nic, P., Milligan, W.W., 2001. Deformation and strength behavior of two nickel-base turbine disk alloys at 650° c. Metallurgical and Materials Transactions A 32, 2021–2032.

Sjaardema, G.D., 2017. Sandia Engineering Analysis Code Access System v. 2.0. 1. Technical Report. Sandia National Lab.(SNL-NM), Albuquerque, NM (United States).

Smith, B.D., Shih, D.S., McDowell, D.L., 2016. Fatigue hot spot simulation for two widmanstätten titanium microstructures. International Journal of Fatigue 92, 116–129.

Socie, D., 1993. Critical plane approaches for multiaxial fatigue damage assessment. Advances in multiaxial fatigue .

Spanos, G., Rowenhorst, D., Lewis, A., Geltmacher, A., 2008. Combining serial sectioning, ebsd analysis, and image-based finite element modeling. Mrs Bulletin 33, 597–602.

Staroselsky, A., Cassenti, B.N., 2010. Combined rate-independent plasticity and creep model for single crystal. Mechanics of materials 42, 945–959.

Staroselsky, A., Cassenti, B.N., 2011. Creep, plasticity, and fatigue of single crystal superalloy. International Journal of Solids and Structures 48, 2060–2075.

Stein, C., Lee, S., Rollett, A., 2012. An analysis of fatigue crack initiation using 2d orientation mapping and full-field simulation of elastic stress response. Superalloys 2012 , 439–444.

Stein, C.A., Cerrone, A., Ozturk, T., Lee, S., Kenesei, P., Tucker, H., Pokharel, R., Lind, J., Hefferan, C., Suter, R.M., et al., 2014. Fatigue crack initiation, slip localization and twin boundaries in a nickel-based superalloy. Current Opinion in Solid State and Materials Science 18, 244–252.

Steinbach, I., 2009. Phase-field models in materials science. Modelling and simulation in materials science and engineering 17, 073001.

Steinbach, I., Pezzolla, F., 1999. A generalized field method for multiphase transformations using interface fields. Physica D: Nonlinear Phenomena 134, 385–393.

Steinbach, I., Pezzolla, F., Nestler, B., Seeßelberg, M., Prieler, R., Schmitz, G.J., Rezende, J.L., 1996. A phase field concept for multiphase systems. Physica D: Nonlinear Phenomena 94, 135–147.

Steuer, S., Villechaise, P., Pollock, T., Cormier, J., 2015. Benefits of high gradient solidification for creep and low cycle fatigue of am1 single crystal superalloy. Materials Science and Engineering: A 645, 109–115.

Stinville, J., Lenthe, W., Miao, J., Pollock, T., 2016. A combined grain scale elastic–plastic criterion for identification of fatigue crack initiation sites in a twin containing polycrystalline nickel-base superalloy. Acta Materialia 103, 461–473.

Stinville, J., Vanderesse, N., Bridier, F., Bocher, P., Pollock, T., 2015. High resolution mapping of strain localization near twin boundaries in a nickel-based superalloy. Acta Materialia 98, 29–42.

Stinville, J.C., Echlin, M.P., Callahan, P.G., Miller, V.M., Texier, D., Bridier, F., Bocher, P., Pollock, T.M., 2017a. Measurement of strain localization resulting from monotonic and cyclic loading at 650° c in nickel base superalloys. Experimental Mechanics 57, 1289–1309.

Stinville, J.C., Lenthe, W.C., Echlin, M.P., Callahan, P.G., Texier, D., Pollock, T.M., 2017b. Microstructural statistics for fatigue crack initiation in polycrystalline nickel-base superalloys. International Journal of Fracture 208, 221–240.

Stinville, J.C., Martin, E., Karadge, M., Ismonov, S., Soare, M., Hanlon, T., Sundaram, S., Echlin, M.P., Callahan, P.G., Lenthe, W.C., et al., 2018. Fatigue deformation in a polycrystalline nickel base superalloy at intermediate and high temperature: Competing failure modes. Acta Materialia 152, 16–33.

Stoltz, R., Pineau, A., 1978. Dislocation-precipitate interaction and cyclic stress-strain behavior of a $\gamma^{'}$ strengthened superalloy. Materials Science and Engineering 34, 275–284.

Stouffer, D.C., Dame, L.T., 1996. Inelastic deformation of metals: models, mechanical properties, and metallurgy. John Wiley & Sons.

Strutt, V.C.I., Jenkins, B., Woolrich, J., Appleton, M., Moody, M., Bagot, P., 2023. Effect of microsegregation and heat treatment on localised γ and $\gamma^{'}$ compositions in single crystal ni-based superalloys. Journal of Alloys and Compounds 949, 169861.

Su, X., Xu, Q., Wang, R., Xu, Z., Liu, S., Liu, B., 2018. Microstructural evolution and compositional homogenization of a low re-bearing ni-based single crystal superalloy during through progression of heat treatment. Materials & Design 141, 296–322.

Su, Y., Han, Q.N., Qiu, W., He, Z., Shang, Y.B., Shi, H.J., Niu, L.S., 2020. High temperature in-situ sem observation and crystal plasticity simulation on fretting fatigue of ni-based single crystal superalloys. International Journal of Plasticity 127, 102645.

Sudhalkar, B.R., Pai, N., Patra, A., Kapoor, K., Kapoor, R., Agarwal, A., Samajdar, I., 2024. Grain boundary localized damage in hexagonal titanium. Materials Science and Engineering: A 902, 146608.

Sun, J., Yuan, H., 2019. Cyclic plasticity modeling of nickel-based superalloy Inconel 718 under multi-axial thermo-mechanical fatigue loading conditions. International Journal of Fatigue 119, 89–101.

Sun, L., Bao, X.G., Guo, S.J., Wang, R.Z., Zhang, X.C., Tu, S.T., 2021. The creep-fatigue behavior of a nickel-based superalloy: Experiments study and cyclic plastic analysis. International Journal of Fatigue 147, 106187.

Sun, L., Liu, L.Q., Wang, R.Z., Wang, X.W., Tan, J.P., Guo, S.J., Wang, J., Zhang, D.W., Zhang, X.C., Tu, S.T., 2022. A modified damage-coupled viscoplastic constitutive model for capturing the asymmetric behavior of a nickel-based superalloy under wide creep-fatigue loadings. International Journal of Fatigue 164, 107160.

Sun, S., Li, L., Yue, Z., Yang, W., Zhao, Z., Cao, R., Li, S., 2020. Experimental and numerical investigation on fretting fatigue behavior of nickel-based single crystal superalloy at high temperature. Mechanics of Materials 150, 103595.

Sun, Y., Hazzledine, P., 1996. Geometry of dislocation glide in ll2$\gamma^{'}$-phase: Tem observations, in: Dislocations in solids. Elsevier. volume 10, pp. 27–68.

Sun, Y., Wang, Z., Du, M., Du, Y., Zhang, W., 2023. First-principles study on si atom diffusion behavior in ni-based superalloys. Materials 16, 5989.

Sundararaman, M., Chen, W., Wahi, R., 1989. Interpretation of fatigue softening at room temperature in a superalloy. Scripta metallurgica 23, 1795–1800.

Svoboda, J., Lukas, P., 1996. Modelling of kinetics of directional coarsening in ni-superalloys. Acta materialia 44, 2557–2565.

Szeliga, D., Kubiak, K., Motyka, M., Sieniawski, J., 2016. Directional solidification of ni-based superalloy castings: thermal analysis. Vacuum 131, 327–342.

Ta, N., Zhang, L., Du, Y., 2014. Design of the precipitation process for ni-al alloys with optimal mechanical properties: a phase-field study. Metallurgical and Materials Transactions A 45, 1787–1802.

Ta, N., Zhang, L., Tang, Y., Chen, W., Du, Y., 2015. Effect of temperature gradient on microstructure evolution in ni–al–cr bond coat/substrate systems: A phase-field study. Surface and Coatings Technology 261, 364–374.

Tan, K., Wang, X., Liang, J., Meng, J., Zhou, Y., Sun, X., 2021. Effects of rejuvenation heat treatment on microstructure and creep property of a ni-based single crystal superalloy. Journal of Materials Science & Technology 60, 206–215.

Tan, L., Li, Y., Deng, W., Liu, Y., Liu, F., Nie, Y., Jiang, L., 2019. Tensile properties of three newly developed ni-base powder metallurgy superalloys. Journal of Alloys and Compounds 804, 322–330.

Texier, D., Cormier, J., Villechaise, P., Stinville, J.C., Torbet, C.J., Pierret, S., Pollock, T.M., 2016. Crack initiation sensitivity of wrought direct aged alloy 718 in the very high cycle fatigue regime: the role of non-metallic inclusions. Materials Science and Engineering: A 678, 122–136.

Thellaputta, G.R., Chandra, P.S., Rao, C., 2017. Machinability of nickel based superalloys: a review. Materials Today: Proceedings 4, 3712–3721.

Theska, F., Tse, W.F., Schulz, B., Buerstmayr, R., Street, S.R., Lison-Pick, M., Primig, S., 2023. Review of microstructure–mechanical property relationships in cast and wrought ni-based superalloys with boron, carbon, and zirconium microalloying additions. Advanced Engineering Materials 25, 2201514.

Thool, K., Patra, A., Fullwood, D., Krishna, K.M., Srivastava, D., Samajdar, I., 2020. The role of crystallographic orientations on heterogeneous deformation in a zirconium alloy: a combined experimental and modeling study. International Journal of Plasticity 133, 102785.

Thornton, E.L., Zannoun, H., Vomero, C., Caudill, D., Schoop, J., 2023. A review of constitutive models and thermal properties for nickel-based superalloys across machining-specific regimes. Journal of Manufacturing Science and Engineering 145, 080801.

Tian, S., Wu, J., Shu, D., Su, Y., Yu, H., Qian, B., 2014. Influence of element re on deformation mechanism within γ' phase of single crystal nickel-based superalloys during creep at elevated temperatures. Materials Science and Engineering: A 616, 260–267.

Tian, S., Xia, D., Li, T., Meng, F., Wang, M., Yu, X., 2008. Influence of element w and microstructure evolution on lattice parameters and misfits of nickel-base superalloys. Journal of Aeronautical Materials 28, 12–16.

Tian, S., Zhu, X., Wu, J., Yu, H., Shu, D., Qian, B., 2016. Influence of temperature on stacking fault energy and creep mechanism of a single crystal nickel-based superalloy. Journal of Materials Science & Technology 32, 790–798.

Tinga, T., Brekelmans, W., Geers, M., 2008. Incorporating strain gradient effects in a multiscale constitutive framework for nickel-base superalloys. Philosophical Magazine 88, 3793–3825.

Tinga, T., Brekelmans, W., Geers, M., 2009a. Directional coarsening in nickel-base superalloys and its effect on the mechanical properties. Computational materials science 47, 471–481.

Tinga, T., Brekelmans, W., Geers, M.G., 2009b. Cube slip and non-schmid effects in single crystal ni-base superalloys. modelling and simulation in materials science and engineering 18, 015005.

Titus, M.S., Suzuki, A., Pollock, T.M., 2012. Creep and directional coarsening in single crystals of new γ–γ' cobalt-base alloys. Scripta Materialia 66, 574–577.

Tóth, L.S., Estrin, Y., Lapovok, R., Gu, C., 2010. A model of grain fragmentation based on lattice curvature. Acta Materialia 58, 1782–1794.

Toursangsaraki, M., Du, D., Wang, H., Dong, A., 2024. Crystal plasticity quantification of anisotropic tensile and fatigue properties in laser powder bed fused inconel 718 superalloy. Additive Manufacturing 89, 104300.

Tsukada, Y., Murata, Y., Koyama, T., Miura, N., Kondo, Y., 2011. Creep deformation and rafting in nickel-based superalloys simulated by the phase-field method using classical flow and creep theories. Acta materialia 59, 6378–6386.

Ubachs, R.L.J.M., 2005. Thermomechanical modelling of microstructure evolution in solder alloys .

Uehara, T., Tsujino, T., Ohno, N., 2007. Elasto-plastic simulation of stress evolution during grain growth using a phase field model. Journal of Crystal Growth 300, 530–537.

Vaithyanathan, V., Chen, L., 2002. Coarsening of ordered intermetallic precipitates with coherency stress. Acta Materialia 50, 4061–4073.

Vamsi, K., Karthikeyan, S., 2021. Modeling apb energies in multicomponent ni-base superalloys. Intermetallics 132, 107124.

Varma, A., Pant, P., Gururajan, M., 2023. Dislocation assisted phase separation: a phase field study. Acta Materialia 244, 118529.

Varma, A.R., Pant, P., Gururajan, M., 2024. Dislocation assisted coarsening of coherent precipitates: a phase field study. Philosophical Magazine 104, 1230–1255.

Vattré, A., 2009. Strength of single crystal superalloys: from dislocation mechanisms to continuum micromechanics. PhD These. ONERA The French Aerospace Lab , 155.

Vattré, A., Devincre, B., Roos, A., Feyel, F., 2010. Predicting size effects in nickel-base single crystal superalloys with the discrete-continuous model. European Journal of Computational Mechanics/Revue Européenne de Mécanique Numérique 19, 65–76.

Vattré, A., Fedelich, B., 2011. On the relationship between anisotropic yield strength and internal stresses in single crystal superalloys. Mechanics of materials 43, 930–951.

Vaunois, J.R., Cormier, J., Villechaise, P., Devaux, A., Flageolet, B., 2010. Influence of both $\gamma^{'}$ distribution and grain size on the tensile properties of udimet 720li at room temperature. Proceedings of the 7th International Symposiumon Superalloy 718.

Voorhees, P.W., 1985. The theory of ostwald ripening. Journal of Statistical Physics 38, 231–252.

Wan, Z., Hu, L., Sun, Y., Wang, T., Li, Z., Zhang, Y., 2018. Effect of solution treatment on microstructure and tensile properties of a u720li ni-based superalloy. Vacuum 156, 248–255.

Wanderka, N., Glatzel, U., 1995. Chemical composition measurements of a nickel-base superalloy by atom probe field ion microscopy. Materials Science and Engineering: A 203, 69–74.

Wang, A., Lv, J., Chen, C., Xu, W., Zhang, L., Mao, Y., Zhao, Y., 2019a. Effects of heat treatment on microstructure and high-temperature tensile properties of nickel-based single-crystal superalloys. Materials Research Express 6, 126527.

Wang, B., Pan, B., 2015. Random errors in digital image correlation due to matched or overmatched shape functions. Experimental Mechanics 55, 1717–1727.

Wang, C., Umair, M., Jiang, Y., Nerella, D.K., Ali, M.A., Steinbach, I., 2025a. Morphological evolution of γ' and γ'' precipitation in a model superalloy: Insights from 3d phase-field simulations. Computational Materials Science 256, 113972.

Wang, G., Tian, S., Tian, N., Zhu, X., Zhang, S., Zhang, S., 2023. Stacking fault energy and creep mechanism of a single-crystal nickel-based superalloy. Materials Science and Technology 39, 1393–1401.

Wang, J., Guo, W.G., Su, Y., Zhou, P., Yuan, K., 2016a. Anomalous behaviors of a single-crystal nickel-base superalloy over a wide range of temperatures and strain rates. Mechanics of Materials 94, 79–90.

Wang, L., Wang, S., Song, X., Liu, Y., Xu, G., 2014a. Effects of precipitated phases on the crack propagation behaviour of a ni-based superalloy. International Journal of Fatigue 62, 210–216.

Wang, M., Wang, X., Sun, P., Li, H., Liu, Z., Yang, G., Liu, Y., 2024. Multi-scale investigation on grain size effect of a powder metallurgy ni-based superalloy based on simulation and experimental characterization. Intermetallics 173, 108429.

Wang, R.Z., Cheng, L.Y., Zhu, S.P., Zhao, P.C., Miura, H., Zhang, X.C., Tu, S.T., 2021. Semi-quantitative creep-fatigue damage analysis based on diffraction-based misorientation mapping and the correlation to macroscopic damage evolutions. International Journal of Fatigue 149, 106227.

Wang, R.Z., Zhu, S.P., Wang, J., Zhang, X.C., Tu, S.T., Zhang, C.C., 2019b. High temperature fatigue and creep-fatigue behaviors in a Ni-based superalloy: Damage mechanisms and life assessment. International Journal of Fatigue 118, 8–21.

Wang, T., Wang, X., Zhao, Z., Zhang, Z., 2016b. Dissolution behaviour of the γ' precipitates in two kinds of ni-based superalloys. Materials at High Temperatures 33, 51–57.

Wang, W., Liu, H., Zhu, C., Wei, P., Tang, J., 2019c. Effects of microstructure on rolling contact fatigue of a wind turbine gear based on crystal plasticity modeling. International Journal of Fatigue 120, 73–86.

Wang, X., Liu, J., Jin, T., Sun, X., 2014b. Tensile behaviors and deformation mechanisms of a nickel-base single crystal superalloy at different temperatures. Materials Science and Engineering: A 598, 154–161.

Wang, X.Y., Li, M., Wen, Z.X., 2020. The effect of the cooling rates on the microstructure and high-temperature mechanical properties of a nickel-based single crystal superalloy. Materials 13, 4256.

Wang, Y., Banerjee, D., Su, C.C., Khachaturyan, A., 1998. Field kinetic model and computer simulation of precipitation of l12 ordered intermetallics from fcc solid solution. Acta materialia 46, 2983–3001.

Wang, Y., Liu, Z.K., Chen, L.Q., 2004. Thermodynamic properties of al, ni, nial, and ni3al from first-principles calculations. Acta Materialia 52, 2665–2671.

Wang, Y., Zhu, Z., Wang, S., Yu, Z., Wang, X., 2025b. Effects of the loading conditions on rafting behaviour in ni-based single crystal superalloys: a phase-field study. Materials at High Temperatures , 1–18.

Wang, Y.U., Jin, Y., Cuitino, A., Khachaturyan, A., 2001. Nanoscale phase field microelasticity theory of dislocations: model and 3d simulations. Acta materialia 49, 1847–1857.

Warnken, N., Ma, D., Drevermann, A., Reed, R.C., Fries, S., Steinbach, I., 2009. Phase-field modelling of as-cast microstructure evolution in nickel-based superalloys. Acta Materialia 57, 5862–5875.

Weber, G.R., Ghosh, S., 2016. Thermo-mechanical deformation evolution in polycrystalline ni-based superalloys by a hierarchical crystal plasticity model. Materials at High Temperatures 33, 401–411.

Webster, G., Sullivan, C., 1967. Some effects of temperature cycling on the creep behavior of a nickel-base alloy. INST METALS J 95, 138–142.

Wei, B., Lin, Y., Huang, Z., Huang, L., Zhou, K., Zhang, L., Zhang, L., 2022. A novel re-free ni-based single-crystal superalloy with enhanced creep resistance and microstructure stability. Acta Materialia 240, 118336.

Wei, D.S., Shi, L., Wang, Y.R., 2013. Experimental study of the cyclic mechanical behaviour of two Ni-based superalloys at evaluated temperature. Materials Science and Engineering: A 569, 124–131.

Wen, D.X., Lin, Y., Chen, J., Chen, X.M., Zhang, J.L., Liang, Y.J., Li, L.T., 2015. Work-hardening behaviors of typical solution-treated and aged ni-based superalloys during hot deformation. Journal of alloys and compounds 618, 372–379.

Wen, W., Capolungo, L., Patra, A., Tomé, C., 2017. A physics-based crystallographic modeling framework for describing the thermal creep behavior of fe-cr alloys. Metallurgical and Materials Transactions A 48, 2603–2617.

Wen, W., Kohnert, A., Kumar, M.A., Capolungo, L., Tomé, C.N., 2020. Mechanism-based modeling of thermal and irradiation creep behavior: An application to ferritic/martensitic ht9 steel. International Journal of Plasticity 126, 102633.

Wen, Y., Simmons, J., Shen, C., Woodward, C., Wang, Y., 2003. Phase-field modeling of bimodal particle size distributions during continuous cooling. Acta materialia 51, 1123–1132.

Wen, Y., Wang, B., Simmons, J., Wang, Y., 2006. A phase-field model for heat treatment applications in ni-based alloys. Acta materialia 54, 2087–2099.

Wen, Y., Wang, Y., Chen, L.Q., 1999. Effect of elastic interaction on the formation of a complex multi-domain microstructural pattern during a coherent hexagonal to orthorhombic transformation. Acta materialia 47, 4375–4386.

Westbrook, J., 1957. Temperature dependence of the hardness of secondary phases common in turbine bucket alloys. JOM 9, 898–904.

Westbrooke, E.F., Forero, L.E., Ebrahimi, F., 2005. Slip analysis in a ni-base superalloy. Acta Materialia 53, 2137–2147.

Wilkinson, A.J., Meaden, G., Dingley, D.J., 2006. High-resolution elastic strain measurement from electron backscatter diffraction patterns: New levels of sensitivity. Ultramicroscopy 106, 307–313.

Williams, D.B., Carter, C.B., Williams, D.B., Carter, C.B., 1996. Imaging in the TEM. Transmission Electron Microscopy: A Textbook for Materials Science , 349–366.

Williams, J.C., Starke Jr, E.A., 2003. Progress in structural materials for aerospace systems. Acta materialia 51, 5775–5799.

Wilson, B., Hickman, J., Fuchs, G., 2003. The effect of solution heat treatment on a single-crystal ni-based superalloy. JOM 55, 35–40.

Wise, G., Church, N., Talbot, C., Mignanelli, P., Hardy, M., Jones, N., Stone, H., 2024. Microstructural stability and evolution in a new polycrystalline ni-base superalloy. Metallurgical and Materials Transactions A 55, 38–53.

Wright, D., Smith, D., 1986. Forging of blades for gas turbines. Materials science and technology 2, 742–747.

Wright, S.I., Nowell, M.M., Field, D.P., 2011. A review of strain analysis using electron backscatter diffraction. Microscopy and microanalysis 17, 316–329.

Wright, S.I., Nowell, M.M., de Kloe, R., Camus, P., Rampton, T., 2015. Electron imaging with an ebsd detector. Ultramicroscopy 148, 132–145.

Wright, S.I., Suzuki, S., Nowell, M.M., 2016. In situ ebsd observations of the evolution in crystallographic orientation with deformation. Jom 68, 2730–2736.

Wu, H., Zhuang, X., Nie, Y., Li, Y., Jiang, L., 2019a. Effect of heat treatment on mechanical property and microstructure of a powder metallurgy nickel-based superalloy. Materials Science and Engineering: A 754, 29–37.

Wu, K., Chang, Y., Wang, Y., 2004. Simulating interdiffusion microstructures in ni–al–cr diffusion couples: a phase field approach coupled with calphad database. Scripta materialia 50, 1145–1150.

Wu, L., Osada, T., Yokokawa, T., Chang, Y., Kawagishi, K., 2023. The temperature dependence of strengthening mechanisms in ni-based superalloys: A newly re-defined cuboidal model and its implications for strength design. Journal of Alloys and Compounds 931, 167508.

Wu, R., Sandfeld, S., 2016a. Insights from a minimal model of dislocation-assisted rafting in single crystal nickel-based superalloys. Scripta Materialia 123, 42–45.

Wu, R., Sandfeld, S., 2016b. Some steps towards modelling of dislocation assisted rafting: A coupled 2d phase field—continuum dislocation dynamics approach, in: TMS 2016: 145th Annual Meeting & Exhibition: Supplemental Proceedings: Supplemental Proceedings, Wiley Online Library. pp. 641–648.

Wu, R., Sandfeld, S., 2017. A dislocation dynamics-assisted phase field model for nickel-based superalloys: The role of initial dislocation density and external stress during creep. Journal of Alloys and Compounds 703, 389–395.

Wu, R., Yue, Z., Wang, M., 2019b. Effect of initial γ/γ' microstructure on creep of single crystal nickel-based superalloys: A phase-field simulation incorporating dislocation dynamics. Journal of Alloys and Compounds 779, 326–334.

Wu, R., Zaiser, M., Sandfeld, S., 2017. A continuum approach to combined γ/γ' evolution and dislocation plasticity in nickel-based superalloys. International Journal of Plasticity 95, 142–162.

Wu, R., Zhao, Y., Liu, Y., Ai, X., 2020. High temperature creep mechanisms of a single crystal superalloy: A phase-field simulation and microstructure characterization. Progress in Natural Science: Materials International 30, 366–370.

Wu, W.P., Li, S.Y., Li, Y.L., 2019c. An anisotropic elastic–plastic model for predicting the rafting behavior in ni-based single crystal superalloys. Mechanics of Materials 132, 9–17.

Xia, P., Xie, K., Cui, H., Yu, J., 2018. Influence of heat treatment on γ' phase and property of a directionally solidified superalloy. High Temperature Materials and Processes 37, 271–276.

Xia, P., Yu, J., Sun, X., Guan, H., Hu, Z., 2007. Influence of thermal exposure on γ' precipitation and tensile properties of dz951 alloy. Materials characterization 58, 645–651.

Xia, W., Zhao, X., Yue, L., Zhang, Z., 2020. Microstructural evolution and creep mechanisms in ni-based single crystal superalloys: A review. Journal of Alloys and Compounds 819, 152954.

Xiao, L., Chen, D., Chaturvedi, M., 2005. Shearing of γ'' precipitates and formation of planar slip bands in Inconel 718 during cyclic deformation. Scripta Materialia 52, 603–607.

Xiao, L., Chen, D., Chaturvedi, M., 2008. Cyclic deformation mechanisms of precipitation-hardened inconel 718 superalloy. Materials Science and Engineering: A 483, 369–372.

Xu, J., Zhang, M., Tang, X., Yang, G., Chen, J., Li, Q., Xiao, C., 2018. Influence of solution treatment on microstructure and stress rupture properties of k439 nickel-base superalloy. Atlas Journal of Materials Science , 78–82.

Xu, Z., Li, G., Zhou, Y., Guo, C., Huang, Y., Hu, X., Li, X., Zhu, Q., 2023. Tension-compression asymmetry of nickel-based superalloys: A focused review. Journal of Alloys and Compounds , 169313.

Yabansu, Y.C., Iskakov, A., Kapustina, A., Rajagopalan, S., Kalidindi, S.R., 2019. Application of gaussian process regression models for capturing the evolution of microstructure statistics in aging of nickel-based superalloys. Acta Materialia 178, 45–58.

Yamanaka, A., Takaki, T., Tomita, Y., 2008. Elastoplastic phase-field simulation of self- and plastic accommodations in cubic→ tetragonal martensitic transformation. Materials Science and Engineering: A 491, 378–384.

Yang, C., Xia, H., Xu, Q., Liu, B., 2021. Multiphase-field simulation of the solution heat treatment process in a ni-based superalloy. Computational Materials Science 196, 110550.

Yang, H., Bao, R., Zhang, J., Peng, L., Fei, B., 2011. Crack growth behaviour of a nickel-based powder metallurgy superalloy under elevated temperature. International Journal of Fatigue 33, 632–641.

Yang, H., Huang, M., Li, Z., 2015. The influence of vacancies diffusion-induced dislocation climb on the creep and plasticity behaviors of nickel-based single crystal superalloy. Computational Materials Science 99, 348–360.

Yang, S., Zhang, Z., Zhuo, J., Long, H., Li, Y., 2024. Phase-field simulation of precipitation kinetics and creep properties of ni-al-cr/ta superalloys. Science China Technological Sciences 67, 1139–1150.

Yang, X., Cui, X., Yuan, H., 2020. Correlations between microstructure evolution and mechanical behavior of a nickel-based single crystal superalloy with long-term aging effects. Materials Characterization 169, 110652.

Yashiro, K., Kurose, F., Nakashima, Y., Kubo, K., Tomita, Y., Zbib, H., 2006. Discrete dislocation dynamics simulation of cutting of $\gamma^{'}$ precipitate and interfacial dislocation network in ni-based superalloys. International Journal of Plasticity 22, 713–723.

Ye, D., Ping, D., Wang, Z., Xu, H., Mei, X., Xu, C., Chen, X., 2004. Low cycle fatigue behavior of nickel-based superalloy GH4145/SQ at elevated temperature. Materials Science and Engineering: A 373, 54–64.

Yıldız, G., Gursel, A., Akca, E., 2017. Effects of cooling rate on strength and microstructure of powder metallurgy superalloys. Balance 100, K5.

You, X., Tan, Y., Shi, S., Yang, J.M., Wang, Y., Li, J., You, Q., 2017. Effect of solution heat treatment on the precipitation behavior and strengthening mechanisms of electron

beam smelted inconel 718 superalloy. Materials Science and Engineering: A 689, 257–268.

Yu, H., Su, Y., Tian, N., Tian, S., Li, Y., Yu, X., Yu, L., 2013. Microstructure evolution and creep behavior of a [111] oriented single crystal nickel-based superalloy during tensile creep. Materials Science and Engineering: A 565, 292–300.

Yu, H., Xu, W., van der Zwaag, S., 2020a. Microstructure and dislocation structure evolution during creep life of ni-based single crystal superalloys. Journal of Materials Science & Technology 45, 207–214.

Yu, J., Sun, X., Zhao, N., Jin, T., Guan, H., Hu, Z., 2007. Effect of heat treatment on microstructure and stress rupture life of dd32 single crystal ni-base superalloy. Materials Science and Engineering: A 460, 420–427.

Yu, Q., Chatterjee, S., Roche, K.J., Po, G., Marian, J., 2021. Coupling crystal plasticity and stochastic cluster dynamics models of irradiation damage in tungsten. Modelling and Simulation in Materials Science and Engineering 29, 055021.

Yu, Z., Wang, X., Yang, F., Yue, Z., Li, J.C., 2020b. Review of γ'rafting behavior in nickel-based superalloys: crystal plasticity and phase-field simulation. Crystals 10, 1095.

Yu, Z., Wang, X., Yue, Z., 2020c. The effect of stress state on rafting mechanism and cyclic creep behavior of ni-base superalloy. Mechanics of Materials 149, 103563.

Yuan, G.J., Zhang, X.C., Chen, B., Tu, S.T., Zhang, C.C., 2020. Low-cycle fatigue life prediction of a polycrystalline nickel-base superalloy using crystal plasticity modelling approach. Journal of Materials Science & Technology 38, 28–38.

Yuan, S., Huang, M., Zhu, Y., Li, Z., 2018. A dislocation climb/glide coupled crystal plasticity constitutive model and its finite element implementation. Mechanics of Materials 118, 44–61.

Yue, Q., Liu, L., Yang, W., He, C., Sun, D., Huang, T., Zhang, J., Fu, H., 2019. Stress dependence of the creep behaviors and mechanisms of a third-generation ni-based single crystal superalloy. Journal of Materials Science & Technology 35, 752–763.

Zeng, Z., Li, X., Xu, D., Lu, L., Gao, H., Zhu, T., 2016. Gradient plasticity in gradient nano-grained metals. Extreme Mechanics Letters 8, 213–219.

Zenk, C.H., Feng, L., McAllister, D., Wang, Y., Mills, M.J., 2021. Shearing mechanisms of co-precipitates in IN718. Acta Materialia 220, 117305.

Zhang, C., Hu, W., Wen, Z., Zhang, H., Yue, Z., 2016. Influence of hot isostatic pressing on fatigue performance of k403 nickel-based superalloy. Journal of Alloys and Compounds 655, 114–123.

Zhang, C., Wang, P., Wen, Z., Xu, Z., He, P., Yue, Z., 2022a. Study on creep properties of nickel-based superalloy blades based on microstructure characteristics. Journal of Alloys and Compounds 890, 161710.

Zhang, H., Gu, D., Ma, C., Guo, M., Yang, J., Wang, R., 2019a. Effect of post heat treatment on microstructure and mechanical properties of ni-based composites by selective laser melting. Materials Science and Engineering: A 765, 138294.

Zhang, H., Qin, S., Li, H., Liu, J., Lv, Y., Wang, Y., Zhang, P., Zhou, H., Wu, T., 2019b. Ebsd study of strain dependent microstructure evolution during hot deformation of a typical nickel-based superalloy. Journal of Materials Research 34, 321–334.

Zhang, K.S., Ju, J.W., Li, Z., Bai, Y.L., Brocks, W., 2015a. Micromechanics based fatigue life prediction of a polycrystalline metal applying crystal plasticity. Mechanics of Materials 85, 16–37.

Zhang, L., Zhao, L., Roy, A., Silberschmidt, V., Mccolvin, G., 2019c. Low-cycle fatigue of single crystal nickel-based superalloy–mechanical testing and tem characterisation. Materials Science and Engineering: A 744, 538–547.

Zhang, P., Zhu, Q., Hu, C., Wang, C.j., Chen, G., Qin, H.y., 2015b. Cyclic deformation behavior of a nickel-base superalloy under fatigue loading. Materials & Design 69, 12–21.

Zhang, T., Collins, D.M., Dunne, F.P., Shollock, B.A., 2014. Crystal plasticity and high-resolution electron backscatter diffraction analysis of full-field polycrystal ni superalloy strains and rotations under thermal loading. Acta materialia 80, 25–38.

Zhang, T., Yuan, H., 2022. Multiscale plasticity behavior and fatigue performance of laser melting multi-layer nickel-based superalloys upon heat treatments. International Journal of Plasticity 158, 103404.

Zhang, W., Jiang, R., Zhao, Y., Zhang, L., Zhang, L., Zhao, L., Song, Y., 2022b. Effects of temperature and microstructure on low cycle fatigue behaviour of a pm ni-based superalloy: Ebsd assessment and crystal plasticity simulation. International Journal of Fatigue 159, 106818.

Zhang, X., Stinville, J.C., Pollock, T.M., Dunne, F.P., 2021. Crystallography and elastic anisotropy in fatigue crack nucleation at nickel alloy twin boundaries. Journal of the Mechanics and Physics of Solids 155, 104538.

Zhang, Y., Ding, K., Gu, Y., Chen, W., Wang, Y.M., El-Awady, J., McDowell, D.L., Zhu, T., 2022c. Modeling of microscale internal stresses in additively manufactured stainless steel. Modelling and Simulation in Materials Science and Engineering 30, 074001.

Zhang, Y., Yang, C., Xu, Q., 2020. Numerical simulation of microstructure evolution in ni-based superalloys during p-type rafting using multiphase-field model and crystal plasticity. Computational Materials Science 172, 109331.

Zhang, Z., Lunt, D., Abdolvand, H., Wilkinson, A.J., Preuss, M., Dunne, F.P., 2018. Quantitative investigation of micro slip and localization in polycrystalline materials under uniaxial tension. International Journal of Plasticity 108, 88–106.

Zhao, Y., Jiang, R., Harte, A., Bull, D.J., Reed, P., 2022. Characterisation of strain localisation under cyclic loading at 450° c by sem-dic in a pm ni-based superalloy. Materials Science and Engineering: A 849, 143464.

Zhao, Y., Zhang, H., Wei, H., Zheng, Q., Jin, T., Sun, X., 2014. Progress of phase-field investigations of $\gamma^{'}$ rafting in nickel-base single-crystal superalloys. Chinese Science Bulletin 59, 1684–1695.

Zheng, Z., Balint, D.S., Dunne, F.P., 2016. Dwell fatigue in two ti alloys: an integrated crystal plasticity and discrete dislocation study. Journal of the Mechanics and Physics of Solids 96, 411–427.

Zhipeng, W., Lianxi, H., Yu, S., et al., 2018. Effect of solution treatment on microstructure and tensile properties of a u720li ni-based superalloy [j]. Vacuum 156, 248–255.

Zhixun, W., Haiqing, P., Shaofei, W., Zhenwei, L., Zhufeng, Y., 2015. Effects of long-term aging on the microstructures and tensile properties of ni-based single crystal superalloy. Rare Metal Materials and Engineering 44, 1873–1878.

Zhong, Z., Gu, Y., Yuan, Y., Yokokawa, T., Harada, H., 2012. On the low cycle fatigue behavior of a Ni-base superalloy containing high Co and Ti contents. Materials Science and Engineering: A 552, 434–443.

Zhou, N., Shen, C., Mills, M., Wang, Y., 2007. Phase field modeling of channel dislocation activity and $\gamma^{'}$ rafting in single crystal ni–al. Acta Materialia 55, 5369–5381.

Zhou, N., Shen, C., Mills, M., Wang, Y., 2010. Large-scale three-dimensional phase field simulation of $\gamma^{'}$-rafting and creep deformation. Philosophical Magazine 90, 405–436.

Zhou, X., 2022. Numerical Simulation of Dendrites Growth in Continuous Casting by Using Open Source Software. Master's thesis. Purdue University.

Zhou, Z., Lei, Q., Zhang, L., Cui, Z., Shang, Y., Qi, H., Li, Y., Jiang, L., Nadimpalli, V.K., Huang, L., 2022. Microstructural evolution of nickel-based single crystal superalloy fabricated by directed energy deposition during heat treatment. Journal of Alloys and Compounds 904, 163943.

Zhu, J., Liu, Z., Vaithyanathan, V., Chen, L., 2002. Linking phase-field model to calphad: application to precipitate shape evolution in ni-base alloys. Scripta Materialia 46, 401–406.

Zhu, J., Wang, T., Ardell, A., Zhou, S., Liu, Z., Chen, L., 2004. Three-dimensional phase-field simulations of coarsening kinetics of $\gamma^{'}$ particles in binary ni–al alloys. Acta materialia 52, 2837–2845.

Zhu, Z., Basoalto, H., Warnken, N., Reed, R., 2012. A model for the creep deformation behaviour of nickel-based single crystal superalloys. Acta Materialia 60, 4888–4900.

Acknowledgments

I wanted to express my deepest gratitude to my supervisor, Prof. Anirban Patra, for his invaluable guidance, motivation, and continuous support throughout my PhD research. His patience and belief in me have always motivated me to go beyond my own capabilities. I count myself among the luckiest ones to have worked under the guidance of Professor Patra. I am also grateful to my co-supervisor, Prof. PJ Guruprasad. He has supported me throughout my PhD work with his unmatched technical expertise and invaluable feedback. I am indebted to both my supervisors for their time and effort during my thesis work.

I am thankful to Prof. Indradev Samajdar for allowing me to use his lab resources and his experimental suggestions in my work. I am also grateful to the members of the Research Progress Committee (RPC), Prof. Nagamani Jaya Balila, Prof. M.P. Gururajan, and Prof. Krishnendu Haldar, and my PMRF review committee members for their constructive comments and suggestions, which have greatly enhanced the quality of this work.

I would like to thank my colleagues, Dr. Namit Pai, Lopamudra Singh, Bhargav Sudhalkar, Mahesh Alanka, Suryakant Priyadarshi, Dr. Gopi Gulivindala, Dr. Aditya Prakash, Dr. Tawqeer Tak, and all of the people I have interacted with, for their collaboration, discussions, and for creating a motivating and friendly research environment. I would also like to thank Prof. Sushil Mishra and his group, who helped me perform deformation experiments. I am deeply thankful to all my friends, especially Gaurav Kumar and Sulipta Sarkar, for always standing beside me and motivating me through the course of my PhD.

Above all, I owe my deepest gratitude to my family for their unconditional love, patience, and encouragement throughout this journey. Their faith in me has been a constant source of strength and inspiration.

Finally, I dedicate this thesis to all those who have stood by me through the challenges and triumphs of my doctoral journey.